Non-Destructive Evaluation of Damage in Concrete with Applications in Shallow Foundations

by

Sabah Hassan Lafta Fartosy

A thesis

presented to the University of Waterloo

in fulfillment of the

thesis requirement for the degree of

Doctor of Philosophy

In

Civil Engineering

Waterloo, Ontario, Canada, 2018

Examining Committee Membership

The following served on the Examining Committee for this thesis. The decision of the Examining Committee is by majority vote.

External Examiner	DR. HAYDAR AL-SHUKRI Professor
Supervisor(s)	DR. GIOVANNI CASCANTE Professor
	DR. DIPANJAN BASU Associate Professor
Internal Member	DR. HASSAN BAAJ Associate Professor
Internal Member	DR. ADIL AL-MAYAH Assistant Professor
Internal-external Member	DR. MAURICE B. DUSSEAULT Professor

Author’s Declaration

I hereby declare that I am the sole author of this thesis. This is a true copy of the thesis, including any required final revisions, as accepted by my examiners.

I understand that my thesis may be made electronically available to the public.

Abstract

The most widely used material for civil infrastructure is reinforced concrete. The concrete deteriorates over time because of several reasons, and therefore, inspection of concrete is necessary to ensure its compliance with the design requirements. Decision makers often have insufficient data to implement the appropriate corrective measures in the face of infrastructure failure. Better assessment methods are essential to obtain comprehensive and reliable information about the concrete elements. Although, different methods exist to inspect concrete members, there is no comprehensive technique available for condition assessment of concrete of shallow foundations. To ensure the integrity of shallow foundations during construction and during its service life, it is necessary to monitor their conditions periodically. To achieve this goal a new NDT methodology is developed to reliably evaluate the conditions of new shallow foundations without changing their future performances.

Recently, there is a trend to overcome coupling issues between the transducers and the object under investigation, by installing sensor networks in concrete to assess its integrity. Although many NDT approaches are designed to evaluate the integrity of concrete structural elements, shallow foundations, which are concrete elements embedded in soil, have received less attention. The challenging aspect of characterizing shallow foundations is limited accessibility for in-service foundation inspections because of structural restrictions. Even when accessibility is possible, the NDT methods (ultrasonic pulse velocity, UPV) used may produce measurements with high uncertainties because of inconsistent coupling between the transducer and the surface of the material being tested.

In the current research project, a new NDT procedure is developed based on design of new transducers embedded at the base of lab-scale concrete foundation models, and these transducers are waterproof and used as receivers. The transducers consist of radial-mode piezoceramics that can detect waves from different orientations. The developed methodology relies mainly on two methods to emit the transmission pulse; either using a direct contact method by gluing the transducer to the concrete surface or using a plastic tube partially embedded in concrete and filled with water. The first procedure is used when the accessibility to the top surface of the foundations is possible; otherwise, the second option is employed to reach the concrete surface of foundations. The new methodology can be used in different stages: during construction of foundations to monitor the uniformity and quality of the concrete, and during in-service life to periodically assess the condition of the foundations, specifically after an event that may cause severe damage in concrete such as earthquake and overloading. To verify the applicability of the methodology, unreinforced and reinforced shallow foundation lab-scale concrete

models were tested in the laboratory under uniaxial compression loads. In this work, all ultrasonic measurements are averaged 16 times to ensure the consistency of the results and to eliminate high frequency noise. The average coefficient of variance obtained is less than 3.5%; which is considered acceptable in this type of measurements (typical measurement error ~5%). Also, different tests were repeated more than three times by removing and putting back all the ultrasonic transducers to enhance the statistical significance of the results.

The main contributions of the research presented in this thesis are:

- Characterization of low and high frequency transducers using laser vibrometer to characterize their responses for better ultrasonic measurements.
- Characterization of a single fracture growth in a homogenous material based on wave velocity and wave attenuation.
- Characterization of cement-based materials using ultrasonic pulse velocity and laser vibrometer methods.
- Evaluation of freeze/thaw damage and monitoring progressive damage in concrete specimens subjected to uniaxial compression load using ultrasonic pulse velocity and laser vibrometer methods.
- Fabrication of thirty-six new radial ultrasonic transducers to embed in concrete models for quality control purposes and to monitor progressive damage using new transmission pulse methodology.

Acknowledgment

I would like to express my deepest thanks to my supervisors, Professor Giovanni Cascante and Associate Professor Dipanjan Basu for their valuable support and for giving me the opportunity to study in the Ph.D. program under their supervision at the University of Waterloo. My thanks are extended to the thesis committee members, Professor Maurice B. Dusseault, Dr. Adil Al-Mayah, Dr. Hassan Baaj, and Professor Haydar Al-Shukri.

I gratefully acknowledgment the financial support for this research provided by Ministry of Higher Education and Scientific Research/ The University of Al-Mustansiriyah, Iraq.

I would like to acknowledge the technical and editorial supervision of Edward Ginzel throughout my Ph.D. study.

A warm thanks goes out to the technical staff at the Civil and Environmental Engineering Department, Richard Morrison, Terry Ridgway, Dough Hirst, and Peter, for helping me in fabricating the transducers and helping in the tests related to my research.

I am also thankful for the technical help that I received from Mark Kuntz and Jorge Cruz, who provided me with the materials for the experimental program of my research.

Finally, I would like to express my special thanks to my colleagues in the NDT group and in the Geotechnical group for all the good and difficult situations shared during these years.

Dedication

To my beloved brother Salah, rest in peace.

To my parents, brothers and sisters for unconditional support.

To my wife and my children who always support me.

To Iraq heroes how scarified their souls to protect our homeland and people.

Table of Contents

List of Figures xiv

List of Tables xv

List of Symbols xxviii

Chapter 1 Overview 1

1.1 Research needs 1

1.2 Research objectives 4

General objective 4

Specific objective 4

1.3 Research methodology 5

1.4 Contribution of the research 5

1.5 Thesis organization 6

Chapter 2 Background and Literature Review 8

2.1 Introduction 8

2.2 Characterization of ultrasonic transducers 8

2.3 Fracture characterization in homogenous medium 9

2.4 Characterization of concrete using ultrasonic techniques 10

Ultrasonic pulse velocity 10

Laser vibrometer 12

2.5 Generalities in reinforced concrete 13

2.6 Mechanisms of deterioration in concrete 14

2.6.1 Effect of load application 14

2.6.2 Effect of freeze-thaw process 16

2.7 Condition assessment for concrete structural elements 18

2.7.1 Typical defects in shallow foundations 19

2.7.2 Nondestructive testing (NDT) methods for concrete 21

Stress-wave methods 22

2.8 Theoretical Background 24

2.8.1 Fundamentals of wave propagation 24

2.9 Wave velocities and material parameters calculations 29

2.10 Ultrasonic wave attenuation 30

2.10.1 The cause of wave attenuation 33

Intrinsic attenuation 33

Extrinsic attenuation 35

2.11 Ultrasonic pulse velocity method 37

2.12 Basic principles of laser Doppler vibrometer 39

2.13 Summary 41

Chapter 3 Characterization of ultrasonic transducers 42

3.1 Introduction 42

3.2 Experimental program 43

3.2.1 Ultrasonic transducers 43

3.2.2 Instrumentation setup 44

Conventional methods 44

Laser Doppler vibrometer method 46

3.3 Results and discussion 47

3.3.1 Effect of coupling 47

3.3.2 Determination of the time delay 50

3.3.3 Characterization using laser Doppler vibrometer 51

3.4 Summary 58

Chapter 4 Fracture evaluation in homogenous medium 59

4.1 Introduction 59

4.2. UPV test background 61

4.3. Specimen preparation 63

4.4 Test setup 65

4.5 Testing methodology 69

4.6 Results and discussion 69

4.6.1 Laser characterization of the transducer 68

4.6.2 Stress-strain response of PMMA specimens 70

4.6.3 Fracture interaction with wave velocity 74

4.6.4 Fracture interaction with wave attenuation in time domain 75

4.6.5 Fracture interaction with wave attenuation in frequency domain 77

4.7 Summary 83

Chapter 5 Characterization of cement-based specimens using

Ultrasonic methods 84

5.1 Introduction 84

5.2 Experimental procedure 86

5.2.1 Test methodology and equipment 86

Immersion through-transmission setup 86

Laser vibrometer setup 89

5.2.2 Specimen preparations 89

5.3 Experimental results 91

5.3.1 Immersion test results 91

Pulse velocity of immersion test 93

Material acoustic parameters 94

Material elastic moduli 96

Attenuation measurements of immersion test 97

5.3.2 Laser test results 99

Pulse velocity of laser test 100

Attenuation measurements of laser test 101

5.4 Summary 103

Chapter 6 Study of ultrasonic techniques sensitivity to internal damage 104

6.1 Introduction 104

6.2 Experimental procedure 107

6.2.1 Specimen preparations 107

6.2.2 Equipment description 108

Freeze-thaw chamber 108

Compression machine test 109

Laser vibrometer setup 110

Ultrasonic pulse velocity setup 111

6.2.3 Testing methodology 112

6.3 Experimental results 115

6.3.1 Freeze-thaw results 115
Pulse velocity results 115
Attenuation measurements 116
6.3.2 Laser vibrometer results 119
6.3.3 Compression test results 124
Pulse velocity results 124
Attenuation measurements 125
Single testing measurements 125
Multi-testing measurements 127
Laser vibrometer results 131
6.4 Summary 137
Chapter 7 Health monitoring of concrete shallow foundation lab-scale models 138
7.1 Introduction 138
7.2 Experimental procedure 140
7.2.1 Model preparations 140
7.2.2 Transducer fabrication 140
7.2.3 Equipment description 142
Compression machine test 142
Ultrasonic pulse velocity setup 143
7.2.4 Testing methodology 148
7.3 Experimental results 149
7.3.1 Quality control phase 149
P-wave velocity 149

Frequency content 152

7.3.2 Damage evaluation under compression load..... 153

7.4 Summary 167

Chapter 8 Conclusions and recommendations 158

References 173

APPENDIX A: 190

APPENDIX B: 210

APPENDIX C: 218

APPENDIX D: 246

List of Tables:

Table 2-1: Main deterioration mechanisms, consequences and required information ..... (after Breysse, 2010) 15

Table 2-2: Advantages and disadvantages of stress-wave methods for structures (after Rodríguez Roblero, 2017) 23

Table 2-3: Typical values for the acoustic impedance (ACI 228.2R-13) 28

Table 2-4: Attenuation relationship governs by different scattering regimes ..... (after Ensminger and Bond 2012) 34

Table 3-1: Details of characterized ultrasonic transducers 43

Table 3-2: Sizes of calibration standard rods employed 46

Table 3-3 Details of laser characterization parameters. 48

Table 3-4: Comparison of the delay times of the characterized transducers. 51

Table 3-5: Comparison of delay times of characterized transducers 55

Table 4-1: List of PMMA specimens tested and their corresponding bonding conditions 65

Table 4-2: Details of different tests performed on PMMA specimens 70

Table 4-3: Elastic moduli of specimens tested under strain-controlled load tests 73

Table 5-1: Mix proportions of cement-based specimens 90

Table 5-2: Wavelength results of immersion and laser measurements 93

Table 5-3: Attenuation results of immersion and Laser measurements 102

Table 6-1: Mix proportions of concrete specimens 108

Table 6-2: Excitation parameters of UPV procedure 114

Table 7-1: Attenuation results of immersion and Laser measurements 140

List of Figures

Figure 2-1: Standard calibration reference blocks(https://www.nde-ed.org)..... 9

Figure 2-2: Evaluation of concrete components (after ACI 365.1R-17)..... 19

Figure 2-3: Shrinkage cracking (ACI201.1R-08)..... 21

Figure 2-4: Surface air voids (also known bug holes, ACI 201.1R-08)..... 21

Figure 2-5: Concrete surface with medium spalling (ACI 201.1R-08)..... 21

Figure 2-6: Concrete surface with medium popout (ACI 201.1R-08) 21

Figure 2-7: Concrete surface with severe scaling (ACI 201.1R-08)..... 21

Figure 2-8: Concrete surface with honeycombing (ACI 201.1R-08)..... 21

Figure 2-9: Type of waves in solids 26

Figure 2-10: Influence of different ratios between transducer diameter *d* and wavelength λ of wave pressure at different angles (after Krautkrämer and Krautkrämer, 1990)..... 35

Figure 2-11: The relationship between the relative pressure wave $p(x)/p_o$ and the distance related to transducer diameter x/d at different diameter to wavelength d/λ. The dotted lines are the approximated relative pressure (after Punurai, 2006) 37

Figure 2-12: Schematic diagram of pulse velocity test circuit (after Malhotra, 2004) 38

Figure 2-13: Polytec laser Doppler vibrometer instrumentation (after Martarelli, 2001)..... 40

Figure 3-1: Types of the characterized ultrasonic transducers..... 44

Figure 3-2: Characterization testing setup, for (a) face to face technique and (b) reference bar technique 45

Figure 3-3: Instrumentation of Laser characterization technique 47

Figure 3-4: Influence of coupling on signal strength using a low frequency transducer (54 kHz). (a) signals of aluminum cylinder. (b) signals of mortar cylinder. Signal amplitudes are normalized to highest peak of gel coupling 49

Figure 3-5: Characterization results of 54 kHz transducer (54N). (a) using aluminum rods, (b) using steel rods. where V*p* is wave velocity (m/s), d is delay time, and R2 is correction factor..... 50

Figure 3-6: Typical characterization results of 54N and 54O transducers. (a) time displacement history of 54N and corresponding Fourier spectrum, (b) time displacement history of 54O and corresponding Fourier spectrum..... 52

Figure 3-7: Typical characterization results of 150N and 250N transducers. (a) displacement time history of 150N and corresponding Fourier spectrum, (b) displacement time history of 250N and corresponding Fourier spectrum. Pulsed with 100 volts 53

Figure 3-8: Typical characterization results of 500Oy and 1MSN transducers. (a) displacement time history of 500Oy and corresponding Fourier spectrum, (b) displacement time history of 1MSN and corresponding Fourier spectrum. Pulsed with 100 volts. f_r is resonance frequency 54

Figure 3-9: Typical vibration P-modes of 54N and 54O transducers. (a) perspective and side views of 54N, (b) perspective and side views of 54O. 56

Figure 3-10: Typical vibration modes of 1MPO and 1MSN transducers. (a) perspective and side views of 1MPO vibration, (b) perspective and side views of 1MSN vibration 57

Figure 4-1: Effect of amplification in the determination of travel times. (a) original time signal, (b) amplified signal by a factor of 10. Δt represents the error in the arrival time due to wave attenuation 62

Figure 4-2: (a) Schematic of a general fracture during a compression test, (b) schematic of PMMA specimen, hole and fracture during a compression test 65

Figure 4-3: PMMA specimen (152 mm x 100) with a hole at the centre, fraction location, and transducers glued to the specimen in a uniaxial compressive test. Displacement rate 0.01mm/min 66

Figure 4-4: Ultrasonic pulse velocity instrumentation setup with 3D printed holders 67

Figure 4-5: Laser vibrometer characterization setup 68

Figure 4-6: Typical time and Fourier spectra plots: (a) time signal with two selected time windows w1, and w2 (Tukey windows with time decay exponents **0.1** and **0.3** respectively, Alexander and Poularikas, 1998), (b) Fourier spectra of original and windowed signals. 69

Figure 4-7: Laser characterization results: (a) normalized time signal (maximum displacement = 5.15 nm)**,** (b) corresponding Fourier spectrum 71

Figure 4-8: Typical stress-strain curves for fused (PA16, PA17) and solid (PS1, PS2) PMMA specimens 72

Figure 4-9: Stress-strain curve showing two distinct zones (za, zb) for the evaluation of the average elastic Young's modulus (E*za* and E*zb*) 72

Figure 4-10: Fracture propagation in four specimens, two fused (PA) and two solid (PS) specimens during the strain-controlled load test 77

Figure 4-11: Average ultrasonic wave velocities for different specimens tested under three conditions (intact A, with hole B, with fracture C): (a) 25.4 mm thick specimen, and (b) 12.7 mm thick specimen. Fractures measured for 25.4 mm and 12.7 mm are (42-82 mm) and (51-

63 mm), respectively. The corresponding loads measured are (120-180 kN) and (48.3-55.8 kN). 75

Figure 4-12: Effect of fracture propagation on ultrasonic P-wave velocity for (a) fused specimen (PA16), and (b) solid (intact) specimen (PS1) 76

Figure 4-13: Typical time signals for three specimen conditions (intact, with a stress hole concentrator, and fractured) for two specimen thicknesses (a) 12.7 mm, and (b) 25.4 mm 77

Figure 4-14. Typical time signals measured at three different compression loads, 25.4mm thick specimens, (a). solid specimen, (b). fused specimen. (P = load, L = fracture length) 78

Figure 4-15: Typical Fourier spectra at three conditions (intact, with a stress hole concentrator, and fractured), (a) 12.7 mm thickness specimen, (b) 25.4 mm thickness specimen. Note, spectra of case A (black) and case B (blue) are shifted by 0.75 and 0.35, respectively..... 79

Figure 4-16: Typical Fourier spectra at three different compression loads for (a) solid specimen, and (b) fused specimen (Az is the normalized spectral area with respect to the case of zero load, and L is the fracture length) 80

Figure 4-17: Effect of fracture propagation on spectral areas for (a) solid specimens and (b) fused specimens. A_{Tot} = total area of spectrum, A_{High} = area under high frequency bandwidth range, and A_{Low} = area under low frequency bandwidth range..... 82

Figure 5-1: immersion through-transmission testing setup (adapted from Ginzel and Turnbull, 2016)..... 87

Figure 5-2: Determination of reference time points of immersion test signal 88

Figure 5-3: Rotating specimen to obtain shear mode in through-transmission immersion setup (after Ginzel and Turnbull, 2016) 88

Figure 5-4: Laser Doppler vibrometer testing setup 90

Figure 5-5: Typical waveforms of mortar and concrete specimens. (a) time signals and corresponding Fourier spectra of mortar, (b) time signals and corresponding Fourier spectra of concrete 91

Figure 5-6: Typical waveforms of mortar containing 15% & 50% glass beads. (a) time signals and corresponding Fourier spectra of mortar with 15% glass beads, (b) time signals and corresponding Fourier spectra of mortar with 50% glass beads 92

Figure 5-7: Wave velocities of specimens (a) P-wave velocities, (b) S-wave velocities. Acr & Nyl are acrylic and nylon abbreviations..... 94

Figure 5-8: Results of acoustic impedances of cement-based specimens..... 95

Figure 5-9: Transmission and reflection results of specimens (a) transmission coefficient, (b) reflection coefficient 95

Figure 5-10: Results of Poisson's ratio of cement-based specimens 97

Figure 5-11: Elastic moduli of cement-based specimens (a) Young's modulus, (b) Shear modulus 97

Figure 5-12: Results of attenuation coefficients of cement-based specimens 98

Figure 5-13: Typical laser waveforms of mortar and concrete specimens. (a) time signals and corresponding Fourier spectra of mortar, (b) time signals and corresponding Fourier spectra of concrete 99

Figure 5-14: Typical laser waveforms of mortar containing 15% & 50% glass beads specimens. (a) time signals and corresponding Fourier spectra of mortar with 15% glass beads, (b) time signals and corresponding Fourier spectra of mortar with 50% glass beads 100

Figure 5-15: P-wave velocities of specimens obtained from laser measurements..... 101

Figure 5-16: Laser results of attenuation coefficients of cement-based specimens..... 102

Figure 6-1: Temperature variation recorded during one freeze-thaw cycle (24 hours)..... 109

Figure 6-2: Modified commercial freezer used as freeze-thaw chamber..... 109

Figure 6-3: Compression machine MTS600KN. (a) the main frame of the machine, (b) the control station..... 110

Figure 6-4: Laser Doppler vibrometer testing setup 111

Figure 6-5: UPV instrumentation testing setup (single measurement setup)..... 112

Figure 6-6: UPV instrumentation testing setup (Multi-measurement setup) 112

Figure 6-7: Typical outline of concrete specimen with distribution of aluminum discs and transducers. Red arrows are the triggering directions..... 114

Figure 6-8: Typical variations of ultrasonic velocity for concrete specimens with and without air-entrained. (a) using 54 kHz probe, (b) using 500 kHz probe 115

Figure 6-9: Typical waveforms of untreated cylinder concrete specimen before and at the end of the period of study. (a) time signals and corresponding Fourier spectra of 54 kHz transducer, (b) time signals and corresponding Fourier spectra of 250 kHz 116

Figure 6-10: Typical waveforms of treated cylinder concrete specimen with 0.1% air-entrained before and at the end of the period study. (a) time signals and corresponding Fourier spectra of 54 kHz transducer, (b) time signals and corresponding Fourier spectra of 250 kHz..... 117

Figure 6-11: Typical total attenuation of cylinder concrete specimens using 54 kHz transducer. (a) amplitude method, (b) spectrum area method 118

Figure 6-12: Typical total attenuation of cylinder concrete specimens using 250 kHz transducer. (a) amplitude method, (b) spectrum area method 119

Figure 6-13: Typical vibration modes of untreated cylinder specimen using 54 kHz. (a) before freeze-thaw process, (b) after 56 freeze-thaw cycles 120

Figure 6-14: Typical contour lines of total attenuation results of untreated cylinder specimen scanned with laser using 54 kHz. (a) using peak amplitude, (b) using spectrum area..... 121

Figure 6-15: Typical contour lines of total attenuation results of treated cylinder specimen with 0.1% air-entrained scanned with laser using 54 kHz. (a) using peak amplitude, (b) using spectrum area..... 122

Figure 6-16: Typical contour lines of peak amplitude results of untreated prismatic specimen scanned with laser using 54 kHz. (a) before freeze-thaw, (b) after 56 freeze-thaw cycles.... 123

Figure 6-17: Typical variations of ultrasonic velocity for cylinder specimens. (a) using 54 kHz probe, (b) using 250 kHz probe..... 124

Figure 6-18: Typical variations of relative ratio of ultrasonic velocity for cylinder specimens using all transducers (54 kHz, 150 kHz, 250 kHz, and 500 kHz)..... 125

Figure 6-19: Typical waveforms of untreated cylinder specimen before and after compression load. (a) time signals and corresponding Fourier spectra of 54 kHz transducer, (b) time signals and corresponding Fourier spectra of 250 kHz transducer 126

Figure 6-20: Typical results of treated cylinder specimen with 20% silica fume before and after compression load. (a) time signals and corresponding Fourier spectra of 54 kHz transducer, (b) time signals and corresponding Fourier spectra of 250 kHz..... 127

Figure 6-21: Typical total attenuation results of cylinder concrete specimens test parallel to the load direction. (a) amplitude method, (b) spectrum area method 128

Figure 6-22: Typical waveform results of untreated cylinder specimen subjected to compression load and using 54 kHz transduces at different load steps. (a) in time domain, (b)in frequency domain. P is the applied load 129

Figure 6-23: Typical waveform results of untreated cylinder specimen subjected to compression load and tested using 150 kHz transduces at different load steps. (a) in time domain, (b) in frequency domain..... 129

Figure 6-24: Typical total attenuation results of untreated cylinder specimen subjected to compression load and tested using different orientations. (a) using 54 kHz as transmitter, (b) using 150 kHz as transmitter..... 130

Figure 6-25: Typical vibration modes of untreated cylinder specimen using 54 kHz. (a) before applying the load, (b) after applying the load. Note that the displacement scale of the pre-load condition is nearly five times greater..... 132

Figure 6-26: Typical vibration modes of treated cylinder specimen with 5% silica fume using 250 kHz. (a) before applying the load, (b) after applying the load 133

Figure 6-27: Typical contour lines of total attenuation results of untreated cylinder specimen scanned with laser using 54 kHz. (a) using peak amplitude, (b) using spectrum area..... 134

Figure 6-28: Typical contour lines of total attenuation results of treated cylinder specimen with 10% silica fume and scanned with laser using 250 kHz. (a) using peak amplitude, (b) using spectrum area..... 135

Figure 6-29: Typical contour lines of total attenuation results of untreated prismatic specimen scanned with laser using 54 kHz. (a) using peak amplitude, (b) using spectrum area..... 136

Figure 7-1: Sketches plan of the concrete models. (a) Square plain concrete model, (b) square light reinforced concrete model, (b) dense reinforced concrete model, (c) circular light reinforced concrete model. All dimensions are in cm..... 141

Figure 7-2: Locations of the tubes that used to send the excitation pulse..... 142

Figure 7-3: Typical fabricated radial transducers. (a) before coating, (b) after coating, (c) cross-section of the fabricated transducer..... 143

Figure 7-4: Typical waveform signals of the fabricated radial transducers (model MA-SP transdcuers). (a) in time domian, (b) in frequency domain. P1-P9 refer to nine fabircated transducers. 144

Figure 7-5: Typical waveform signals of the fabricated radial transducers embedded in concrete model MA-SP. (a) in time domian, (b) in frequency domain.145

Figure 7-6: Typical distribution of transducers based on expected cracks location. (a) side section, (b) head section 146

Figure 7-7: Typical load-displacement curves obtained from testing concrete models MA-SP and MC-SDR under compression load..... 147

Figure 7-8: Ultrasonic testing setup 147

Figure 7-9: Typical distribution of transducers based on expected cracks location. (a) side section with expected crack locations, (b) Top view with transducer distribution outline.... 148

Figure 7-10: Typical outline of concrete model showing the locations of tubes and aluminum discs..... 149

Figure 7-11: Typical P-wave velocities computed using the embedded transducers in concrete model MA-SP, (a) sending pulse using acrylic tube (A), (b) sending pulse using nylon tube (B). 150

Figure 7-12: Typical P-wave velocities computed using the embedded transducers in concrete model MA-SP, (a) sending pulse using acrylic tube (A), (b) sending pulse using nylon tube (B). 151

Figure 7-13: Typical waveform signals received at the centre transducer embedded in Model MA-SP during the curing period, (a) in time domain, (b) in frequency domain. AmpR is the maximum amplitude ratio with respect week 4. 152

Figure 7-14: Typical waveform signals received at the centre transducer embedded in Model MA-SDR during the curing period, (a) in time domain, (b) in frequency domain. 154

Figure 7-15: Typical amplitude gain ratio results of the waveforms received at the embedded transducers in concrete model MA-SP during curing period. (a) sending pulse through acrylic tube (A), (b) sending pulse through nylon tube (B). Transducers are arranged based on the distance from the excitation source. 155

Figure 7-16: Typical amplitude gain ratio results of the waveforms received at the embedded transducers in concrete model MC-SDR during curing period. (a) sending pulse through acrylic tube (A), (b) sending pulse through nylon tube (B). 156

Figure 7-17: Picture of the model MA-SP shown a crack marked with blue color underneath the location of transducer (P6). 157

Figure 7-18: Typical waveform signals send using nylon tube (B) with 40 kHz and received at transducer (P6) embedded in Model MA-SP during compression load, (a) in time domain, (b) in frequency domain. P is applied load. ApR is the spectrum area ratio with respect week 4.158

Figure 7-19: Typical waveform signals using aluminum disc with 54 kHz (C) and received at transducer (P6) embedded in Model MA-SP during compression load, (a) in time domain, (b) in frequency domain. L_o and L_f are initial and final load steps. 159

Figure 7-20: Picture of the model MC-SDR shown a crack marked with blue color beside the location of transducer (P2). 160

Figure 7-21: Typical waveform signals send using acrylic tube (A) with 52 kHz and received at transducer (P2) embedded in Model MC-SDR during compression load, (a) in time domain, (b) in frequency domain. 161

Figure 7-22: Typical waveform signals using aluminum disc with 54 kHz (D) and received at transducer (P2) embedded in Model MC-SDR during compression load, (a) in time domain, (b) in frequency domain. 162

Figure 7-23: Typical attenuation results of model MA-SP computed based on peak amplitude of the waveform signals received using the nine embedded transducers during compression load, (a) using acrylic tube with 52 kHz (location A), (b) using direct contact with 54 kHz (location C).163

Figure 7-24: Typical Attenuation results of model MC-SDR computed based on peak amplitude of the waveform signals received using the embedded transducers during compression load, (a)using acrylic tube with 52 kHz (location A), (b) using direct contact with 54 kHz (location C). 164

Figure 7-25: Typical Attenuation results of model MA-SP computed based on spectrum area of the waveform signals received using the nine embedded transducers during compression load, (a) using acrylic tube with 52 kHz (location A), (b) using direct contact with 54 kHz (location C)..... 165

Figure 7-26: Typical Attenuation results of model MC-SDR computed based on spectrum area of the waveform signals received using the nine embedded transducers during compression load, (a) using acrylic tube with 52 kHz (location A), (b) using direct contact with 54 kHz (location C)..... 166

Figure A-1: Characterization results of 54 kHz transducer (54O). (a) using aluminum rods, (b) using steel rods. where V_p is wave velocity (m/s), d is delay time, and R^2 is correlation coefficient. 190

Figure A-2: Characterization results of 150 kHz transducer (150N). (a) using aluminum rods, (b) using steel rods. where V_p is wave velocity (m/s), d is delay time, and R^2 is correlation coefficient. 191

Figure A-3: Characterization results of 250 kHz transducer (250N). (a) using aluminum rods, (b) using steel rods. where V_p is wave velocity (m/s), d is delay time, and R^2 is correlation coefficient. 192

Figure A-4: Characterization results of 500 kHz transducer (500Oy). (a) using aluminum rods, (b) using steel rods. where V_p is wave velocity (m/s), d is delay time, and R^2 is correlation coefficient. 193

Figure A-5: Characterization results of 500 kHz transducer (500Ut). (a) using aluminum rods, (b) using steel rods. where V_p is wave velocity (m/s), d is delay time, and R^2 is correlation coefficient. 194

Figure A-6: Characterization results of 500 kHz immersion transducer (500MN). (a) using aluminum rods, (b) using steel rods. where V_p is wave velocity (m/s), d is delay time, and R^2 is correlation coefficient. 195

Figure A-7: Characterization results of 1 MHz S-wave transducer (1MSN). (a) using aluminum rods, (b) using steel rods. where V_p is wave velocity (m/s), d is delay time, and R^2 is correlation coefficient. 196

Figure A-8: Characterization results of 1 MHz P-wave transducer (1MPO). (a) using aluminum rods, (b) using steel rods. where V_p is wave velocity (m/s), d is delay time, and R^2 is correlation coefficient. 197

Figure A-9: Characterization results of 1 MHz S-wave transducer (1MSO). (a) using aluminum rods, (b) using steel rods. where V_p is wave velocity (m/s), d is delay time, and R^2 is correlation coefficient. 198

Figure A-10: Distribution laser points scheme of 54 kHz transducer (arrows represent the direction of scanning). 199

Figure A-11: Distribution laser points scheme of other transducers. 199

Figure A-12: Perspective and side views of 54 kHz transducer (54O) vibration modes. (a) under 5 volts excitation, (b) under 10 volts excitation, (c) under 150 volts excitation. 200

Figure A-13: Perspective and side views of 54 kHz transducer (54N) vibration modes. (a) under 5 volts excitation, (b) under 10 volts excitation, (c) under 150 volts excitation. 201

Figure A-14: Perspective and side views of 150 kHz transducer (150N) vibration modes. (a) under 10 volts excitation, (b) under 100 volts excitation, (c) under 200 volts excitation. 202

Figure A-15: Perspective and side views of 250 kHz transducer (250N) vibration modes. (a) under 10 volts excitation, (b) under 100 volts excitation, (c) under 200 volts excitation. 203

Figure A-16: Perspective and side views of 500 kHz transducer (500Oy) vibration modes. (a) under 100 volts excitation, (b) under 200 volts excitation. 204

Figure A-17: Perspective and side views of 500 kHz transducer (500Ut) vibration modes. (a) under 100 volts excitation, (b) under 200 volts excitation. 205

Figure A-18: Perspective and side views of 500 kHz transducer (500MN) vibration modes. (a) under 100 volts excitation, (b) under 200 volts excitation. 206

Figure A-19: Perspective and side views of 1 MHz transducer (1MSN) vibration modes. (a) under 100 volts excitation, (b) under 200 volts excitation. 207

Figure A-20: Perspective and side views of 1MHz transducer (1MPO) vibration modes. (a) under 100 volts excitation, (b) under 200 volts excitation. 208

Figure A-21: Perspective and side views of 1MHz transducer (1MSO) vibration modes. (a) under 100 volts excitation, (b) under 200 volts excitation. 209

Figure B-1: Typical P-wave waveforms of water, acrylic and nylon. (a) time signals, (b) Fourier spectra. 210

Figure B-2: Typical P-wave waveforms of water and mortar with 35%gb specimens. (a) time signals, (b) Fourier spectra. 211

Figure B-3: Typical S-wave waveforms of water, acrylic and nylon. (a) time signals, (b) Fourier spectra. 212

Figure B-4: Typical S-wave waveforms of water and mortar specimens. (a) time signals, (b) Fourier spectra. 213

Figure B-5: Typical S-wave waveforms of water and concrete specimens. (a) time signals, (b) Fourier spectra. 214

Figure B-6: Typical S-wave waveforms of water and mortar with 35%gb specimens. (a) time signals, (b) Fourier spectra. 215

Figure B-7: Typical P-wave waveforms of water, acrylic and nylon. (a) time signals, (b) Fourier spectra. 216

Figure B-8: Typical P-wave waveforms of water and mortar with 35%gb specimens. (a) time signals, (b) Fourier spectra. 217

Figure C-1: Typical waveforms of untreated cylinder concrete specimen before and at the end of the period of study using 150 kHz. (a) time signals, (b) Fourier spectra. 218

Figure C-2: Typical waveforms of treated cylinder concrete specimen with 0.1% air-entrained before and at the end of the period study using 150 kHz. (a) time signals, (b) Fourier spectra 219

Figure C-3: Typical waveforms of treated cylinder concrete specimen with 0.1% air-entrained before and at the end of the period study using 250 kHz. (a) time signals, (b) Fourier spectra 220

Figure C-4: Typical waveforms of treated cylinder concrete specimen with 0.1% air-entrained before and at the end of the period study using 250 kHz. (a) time signals, (b) Fourier spectra 221

Figure C-5: Typical total attenuation of cylinder concrete specimens using 500 kHz transducer. (a) amplitude method, (b) spectrum area method. 222

Figure C-6: Typical vibration modes of untreated cylinder specimen using 250 kHz. (a) before freeze-thaw process, (b) after 56 freeze-thaw cycles. 223

Figure C-7: Typical vibration modes of treated cylinder specimen with 0.1% air-entrained scanned with laser using 54 kHz. (a) before freeze-thaw process, (b) after 56 freeze-thaw cycles. 224

Figure C-8: Typical vibration modes of treated cylinder specimen with 0.1% air-entrained scanned with laser using 250 kHz. (a) before freeze-thaw process, (b) after 56 freeze-thaw cycles. 225

Figure C-9: Typical vibration modes of treated cylinder specimen with 0.25% air-entrained scanned with laser using 54 kHz. (a) before freeze-thaw process, (b) after 56 freeze-thaw cycles. 226

Figure C-10: Typical vibration modes of treated cylinder specimen with 0.25% air-entrained scanned with laser using 150 kHz. (a) before freeze-thaw process, (b) after 56 freeze-thaw cycles. 227

Figure C-11: Typical contour lines of total attenuation results of untreated cylinder specimen scanned with laser using 150 kHz. (a) using peak amplitude, (b) using spectrum area..... 228

Figure C-12: Typical contour lines of total attenuation results of treated cylinder specimen with 0.25% air-entrained scanned with laser using 54 kHz. (a) using peak amplitude, (b) using spectrum area..... 229

Figure C-13: Typical waveforms of treated prism concrete specimen with 0.1% air-entrained before and at the end of the period study using 150 kHz. (a) time signals, (b) Fourier spectra..... 230

Figure C-14: Typical contour lines of total attenuation results of untreated prismatic specimen scanned with laser using 500 kHz. (a) using peak amplitude, (b) using spectrum area..... 231

Figure C-15: Typical waveforms of untreated cylinder concrete specimen before and after compression load using 150 kHz. (a) time signals, (b) Fourier spectra. 232

Figure C-16: Typical waveforms of treated cylinder concrete specimen with 20% air-entrained before and at the end of the period study using 54 kHz. (a) time signals, (b) Fourier spectra..... 233

Figure C-17: Typical waveform results of untreated cylinder specimen subjected to compression load and using 150 kHz transduces at different load steps. (a) in time domain, (b) in frequency domain..... 234

Figure C-18: Typical total attenuation results of treated cylinder specimen with 20% silica fume subjected to compression load and tested using different orientations. (a) using 54 kHz as transmitter, (b) using 250 kHz as transmitter. 235

Figure C-19: Typical vibration modes of untreated cylinder specimen using 250 kHz. (a) before applying the load, (b) after applying the load. 236

Figure C-20: Typical vibration modes of treated cylinder specimen with 5% silica fume using 54 kHz. (a) before applying the load, (b) after applying the load. 237

Figure C-21: Typical vibration modes of treated cylinder specimen with 10% silica fume using 150 kHz. (a) before applying the load, (b) after applying the load. 238

Figure C-22: Typical contour lines of total attenuation results of untreated cylinder specimen scanned with laser using 500 kHz. (a) using peak amplitude, (b) using spectrum area..... 239

Figure C-23: Typical contour lines of total attenuation results of treated cylinder specimen with 5% silica fume and scanned with laser using 54 kHz. (a) using peak amplitude, (b) using spectrum area..... 240

Figure C-24: Typical waveforms of untreated prism concrete specimen before and after compression load using 54 kHz. (a) time signals, (b) Fourier spectra. 241

Figure C-25: Typical waveforms of untreated prism concrete specimen before and after compression load using 150 kHz. (a) time signals, (b) Fourier spectra. 242

Figure C-26: Typical waveform results of untreated prismatic specimen subjected to compression load and using 54 kHz - 250 kHz transduces at different load steps. (a) in time domain, (b) in frequency domain. 243

Figure C-27: Typical vibration modes of untreated prismatic specimen using 54 kHz. (a) before applying the load, (b) after applying the load. 244

Figure C-28: Typical contour lines of total attenuation results of untreated prismatic specimen scanned with laser using 150 kHz. (a) using peak amplitude, (b) using spectrum area..... 245

Figure D-1: Typical waveform signals of the fabricated radial transducers (model MC-SDR transdcuers). (a) in time domian, (b) in frequency domain. 246

Figure D-2: Typical laser characterization results of Langevin 52 kHz transducer. (a) time signal, (b) Fourier spectrum, (c) 3D view perspective. fr is resonance frequency..... 247

Figure D-3: Typical laser characterization results of Langevin 40 kHz transducer. (a) time signal, (b) Fourier spectrum, (c) 3D view perspective. 248

Figure D-4: Typical P-wave velocities computed for selected transducers in concrete model MA-SLR reinforced with light rebar, (a) excitation from tube A (acrylic) (b) excitation from tube B (nylon)..... 249

Figure D-5: Typical waveform signals received at the transducer P7 embedded in Model MA-SP during the curing period using 52 kHz through acrylic tube (B), (a) in time domain, (b) in frequency domain. 250

Figure D-6: Typical waveform signals received at the transducer P7 embedded in Model MA-SDR during the curing period using 54 kHz through aluminum disc (C), (a) in time domain, (b) in frequency domain. 251

Figure D-7: Typical maximum amplitude gain of selected embedded transducers in concrete models during curing period. (a) model MA-SP excited from tube B (nylon), (b) model MB-SLR excited from tube A (acrylic). 252

Figure D-8: Typical waveform signals obtained at transducer P5 embedded in concrete model MA-SP by exciting from tube B (nylon) using Langevin 40 kHz transducer. (a) in time domain, (b)in frequency domain. L0 and LF are initial and failure loads. 253

Figure D-9: Typical waveform signals obtained at transducer P9 embedded in concrete model MA-SP by exciting from tube A (acrylic) using Langevin 52 kHz transducer. (a) in time domain, (b) in frequency domain. 254

Figure D-10: Typical waveform signals obtained at transducer P7 embedded in concrete model MA-CLR by exciting from tube B (nylon) using Langevin 40 kHz transducer. (a) in time domain, (b) in frequency domain. 255

Figure D-11: Typical attenuation results of model MB-SLR computed based on peak amplitude of the waveform signals received at the embedded transducers during compression load, (a)using nylon tube with 40 kHz (location B), (b) using direct contact with 54 kHz (location D). 256

Figure D-12: Typical Attenuation results of model MB-SLR computed based on spectrum area of the waveform signals received at the embedded transducers during compression load, (a)using nylon tube with 40 kHz (location B), (b) using direct contact with 54 kHz (location D). 257

List of Symbols

A	=	amplitude of a propagated wave at the distance z1
A_o	=	amplitude of a propagated wave at the distance zo
c	=	phase velocity
d	=	thickness of specimen
dV	=	relative velocity ratio of propagated wave
D	=	the average grain diameter
E	=	Young's modulus of elasticity
f	=	frequency of the wave
FFT	=	Fourier spectrum of the corresponding time signal
G	=	shear modulus
k	=	wave number
L	=	fracture length of PMMA material
p(z)	=	pressure of a propagated wave
P	=	applied static load
Pk_o	=	peak amplitude of a propagated wave at the distance zo
Pk_z	=	peak amplitude of a propagated wave at the distance z1
R_c	=	coefficient of reflection
SA_o	=	spectrum area of a propagated wave at the distance zo
SA_z	=	spectrum area of a propagated wave at the distance z1
t_s	=	reference time of in a material
t_w	=	time reference of wave propagated in water
T	=	time period
T_w	=	temperature of water
T_c	=	coefficient of transmission
V	=	wave velocity
V_b	=	P-wave velocity of the material before the damage
V_f	=	P-wave velocity of the material after the damage
V_l	=	longitudinal wave velocity
V_p	=	velocity of the P-wave computed from the ultrasonic pulse velocity test
V_s	=	shear wave velocity
V_w	=	wave speed in water
z	=	propagation distance

Z	=	acoustic impedance of a material which is the product of the density and the wave velocity
λ	=	wavelength of the ultrasonic wave
v	=	Poisson's ratio
ρ	=	density of material
ω	=	angular frequency
θ_t	=	incident angle determined by the goniometer rotation
α	=	spatial coefficient of wave attenuation caused by the material damping

Chapter 1: Overview

1.1 Research Needs

The most widely used material for infrastructure (e.g. shallow foundations) is reinforced concrete. The concrete deteriorates over time because of serval reasons and therefore inspection of concrete is necessary to ensure its compliance with the design requirements. Decision makers often have insufficient data to implement the appropriate corrective measures in the face of infrastructure failure. Therefore, better assessment methods are essential to obtain comprehensive and reliable information about the concrete elements. Although different methods exist in the market to inspect concrete members, there is no comprehensive technique for reinforced concrete in shallow foundations. To ensure the integrity of shallow foundations during construction and during service life, it is necessary to monitor their condition periodically. To achieve this goal a new NDT methodology is developed to reliably evaluate the condition of new shallow foundations without changing their future performance. This is the main objective of this research project.

Different methods have been developed to assess the integrity of in-service concrete elements. The scope of inspection and resources available are the important aspects considered in selecting a particular method. The techniques that are used to detect flaws, to determine the material properties, or to evaluate the integrity of elements are known as nondestructive testing (NDT) methods and these methods are noninvasive to the component characteristics under inspection. One of the NDT techniques that is used commonly in concrete and depends primarily on wave propagation is called stress-wave methods. Under this category lies the ultrasonic pulse velocity (UPV) technique, which is used in this research work. The term ultrasonic refers to sound waves with frequency above 16 kHz, i.e., above the hearing range of the average person (Ensminger & Bond, 2012).

Determination of propagation velocity of the primary waves (P-waves) through the element being tested is the main principle behind the most common ultrasonic tests. Typically, two probes are placed at opposite ends of the element. These probes are known as piezoelectric transducers and are used to convert an electrical pulse into a mechanical wave and vice versa (Blitz & Simpson, 1996). One of the transducers is

used to produce the electrical pulse, while the other is used as a receiver. The time period between emission of the signal and the detection of the first arrival of the P-waves at the receiver is the time of flight, which is used to compute the ultrasonic pulse velocity based on the distance between the transducers.

The main issue in NDT that causes a variability in ultrasonic measurements is the coupling between the transducer and the object under investigation. To overcome this issue, a trend becomes more attractive recently by installing sensor networks in concrete to determine the dynamic signature of the concrete elements. Several attempts (Dumoulin et al., 2012, 2015, and 2016; Gu et al., 2010; Cheng et al., 2010; Fröjd and Ulriksen, 2016; Lu and Li, 2010; Zongjin et al., 2000; Xu et al., 2018; Dixit and Bahalla, 2018; When et al., 1998; Turner and Arif, 1991) have been made to embed low-cost piezoelectric transducers in concrete to estimate the P-wave velocity in fresh concrete and to evaluate damage development. The existence of transducers inside concrete may have different purposes, such as to improve the interpretation of the test results, to obtain more reliable and consistent measurements, and to adjust the impact of a specific parameter in the measurements. All the proposed procedures that are described in the aforementioned studies are developed to inspect the concrete condition of the structure. For concrete elements embedded in soil, these procedures are impractical to use for several reasons, such as limited accessibility to send the excitation pulse, and incompatibility of the transducers with concrete due to their metal shell and poor waterproof performance.

Although many NDT approaches are designed to evaluate the integrity of concrete superstructure elements, shallow foundations, which are concrete elements embedded in soil, have received less attention. The challenging aspect of characterizing shallow foundations is limited accessibility for in-service foundation inspections because of structural restrictions. Even when accessibility is possible, the NDT methods (UPV) used may produce measurements with high uncertainties because of inconsistent coupling between the transducer and the material being tested.

In the current research project, a new NDT procedure is developed based on design of new transducers embedded at the base of lab-scale concrete foundation models, and these transducers are waterproof and used as receivers. The transducers consist of radial-mode piezoceramics that are able to detect waves from different orientations —

these are cheap and their sizes smaller than other piezoelectric transducers of similar center-frequencies. The developed methodology also includes two proposed procedures to emit the pulse from different locations; either using a transducer coupled to an aluminum plate glued to the concrete surface or using a plastic tube filled with distilled water and embedded partially in concrete. The first procedure is used when the accessibility is possible to the top surface of the foundations, otherwise, the second option is employed to reach the concrete surface of foundations. The new methodology can be used in different stages: during construction of foundations to monitor the uniformity and quality of the concrete, and during in-service life to periodically assess the condition of the foundations, specifically after an event that may cause severe damage in concrete such as earthquake and overloading.

The execution of the tests using an array of transducers is the innovation of the proposed new methodology compared to the conventional procedure that uses only two probes. The measurements of the common ultrasonic testing technique rely generally on a localized single test. In most cases, the selection of test orientation or the size of a defect may not allow the test to identify defects. The advantage of embedding transducers in concrete lies in the ability to scan different orientations from a single location. On the other hand, the measurements obtained using this methodology can provide reliable results because the coupling is better when the transducer is in direct contact with the concrete surface. Nevertheless, this methodology cannot be used to evaluate existing shallow foundations.

The evaluation of damage using ultrasonic measurements of wave velocity and wave attenuation is another contribution of this project. Many researchers (Gaydecki et al., 1992; Basu and Aydin, 2005; Aggelis et al. 2009; Chai et al., 2011; Chai et al. 2011; Yim et al. 2012; Kirlangic, 2013; Fereidooni & Khajevand, 2018) reported that wave attenuation can be more sensitive to damage than wave velocity. It is in fact essential to consider wave attenuation as a complementary parameter to evaluate a material when a degradation or loss of material strength can be indicated by a reduction in the wave amplitude (Ensminger & Bond, 2012). However, use of wave attenuation in the field is limited because the measurements obtained are often not consistent. In the field it is difficult to obtain a consistent coupling, which is the transfer of particle motion between transducers and the concrete elements. To overcome this limitation, a new field-testing technique is proposed.

In this work, all ultrasonic measurements are averaged 16 times to ensure the consistency of the results and to eliminate high frequency noise. The average coefficient of variance obtained is less than 3.5%; which is considered acceptable in this type of measurements (typical measurement error ~5%). Also, different tests were repeated more than three times by removing and putting back all the ultrasonic transducers to enhance the statistical significance of the results.

The main goal of this research study is to improve the NDT technique for evaluating potential damage in concrete shallow foundations. The research study is divided into three parts: first, characterization of the ultrasonic transducers using laser vibrometer technique; second, evaluation of the internal conditions of homogenous and heterogeneous specimens using different NDT techniques in the laboratory; and third, development of a new NDT application for monitoring the integrity of shallow concrete foundation models.

1.2 Research objectives

General objective

The main objective of this research study is to develop a new testing methodology for evaluating the condition of reinforced concrete shallow foundations based on ultrasonic techniques that implement wave attenuation as a complementary parameter to the wave velocity. The novelty of the proposed technique lies on the fabricated transducers that are embedded in concrete and the consistent coupling for better assessment of damage in reinforced concrete of shallow foundations.

Specific objectives

a. To review the literature of the state-of-the art in inspection methods of concrete members, emphasizing the advantages and limitations of the stress-wave methods under study and the improvements required.

b. To characterize the ultrasonic transducers using a laser vibrometer for understanding the actual response of these transducers and identifying their resonance frequencies.

c. To characterize the properties of concrete specimens using two different configuration tests: immersion and laser vibrometer.

d. To study the reliability of using ultrasonic pulse velocity and attenuation measurements for evaluating the internal defects in polymethylmethacrylate (PMMA) and concrete specimens.

e. To assess the reliability of the newly developed ultrasonic procedure for measuring the uniformity and quality of lab-scale concrete models of shallow foundations during curing period.

f. To investigate the functionality of the newly developed ultrasonic procedure by testing lab-scale concrete models of shallow foundations under compression loads.

1.3 Research methodology

The research methodology is divided into two components: literature review and laboratory testing. The literature review is conducted to understand the current inspection methods that are used for concrete members, highlighting the drawbacks of the methods and improvements needed. Laboratory study includes transducer characterization using a laser vibrometer, assessment of fracture in PMMA specimens, evaluation of damage in concrete specimens induced under freeze-thaw cycles and static load using laser vibrometer and UPV methods. Moreover, fabricating and embedding 36 ultrasonic transducers in four lab-scale concrete models (three square shapes and one circular shape models) are parts of the laboratory work. Further, these models are tested in different phases: phase one during curing period to monitor the integrity of the concrete, and phase two under static load to evaluate the damage induced inside concrete. In both the phases, wave attenuation was considered along with wave velocity to assess the internal condition of the concrete.

1.4 Contribution of the research

This research work is expected to contribute with six journal publications that are currently in progress:

1- “Evaluation of the response of ultrasonic transducers for non-destructive material evaluation”. Authors: Fartosy, S., Cascante, G., Basu, this paper illustrates the characterization of ultrasonic transducers using a laser vibrometer (Chapter 3).

2- “Effects of a Fracture on Ultrasonic Wave Velocity and Attenuation in a Homogeneous Medium”. Authors: Fartosy, S., Gomez Roderiguez, D.,

Cascante, G., Basu, D, Dusseault M.. This paper presents the study of using ultrasonic pulse velocity and wave attenuation to monitor the propagation of fracture in homogenous material (Chapter 4). This paper has been submitted to the ASTM Journal of Geotechnical Testing.

3- "Comparison of immersion and laser-vibrometer ultrasonic measurements for characterization of concrete specimens". Authors: Fartosy, S., Cascante, G., Basu, D. This paper presents the study of using different configuration testing methods to characterize concrete specimens (Chapter 5).
4- "Damage evaluation in concrete specimens using nondestructive techniques". Authors: Fartosy, S., Cascante, G., Basu, D. This paper presents the study of using different configuration testing methods to evaluate damage in concrete specimens induced under static load (Chapter 6).
5- "Early evaluation of freeze-thaw damage in concrete specimens using nondestructive techniques". Authors: Fartosy, S., Cascante, G., Basu, D. This paper presents the study of using different configuration testing methods to evaluate damage in concrete specimens induced under freeze-thaw cycles (Chapter 6).
6- "A new NDT approach to monitor damage in concrete shallow foundation - laboratory scale models". Authors: Fartosy, S., Cascante, G., Basu, D. This paper presents the results of the new testing methodology to monitor the quality control and to evaluate the damage in lab-scale concrete models of shallow foundations using fabricated ultrasonic transducers imbedded in models (Chapter 7).

1.5 Thesis organization

Chapter 1 presents the problem statement, the objectives and the expected contributions from current research.

In Chapter 2, the literature review and a brief description of the deterioration mechanics of concrete are presented. Also, the theoretical background is included in which the main concepts of the ultrasonic testing techniques used in this study are summarized.

Chapter 3 describes the results of the characterization of the ultrasonic transducers.

Chapter 4 summarizes the results of a study on the evaluation of fracture in a homogenous material (PMMA specimens) using ultrasonic pulse velocity method.

Chapter 5 describes the results of characterizing concrete specimens using two different configurations: immersion setup and laser vibrometer.

Chapter 6 explains the results of testing concrete specimens under freeze-thaw cycles and static load by using laser vibrometer and ultrasonic pulse velocity methods. This study illustrates the different configurations of testing that were implemented to evaluate the damage in concrete specimens.

Chapter 7 presents the results of testing laboratory-scale concrete models during curing period and under static load using the ultrasonic method. This study illustrates the fabrication of ultrasonic transducers that were embedded in the concrete models and used as receivers, and the effectiveness of the transmitter pulse procedures.

Chapter 8 summarizes the conclusions and recommendations of the research work.

Chapter 2 Background and Literature Review

2.1 Introduction

The purpose of this chapter is to summarize the available information about characterization of ultrasonic transducers, fracture characterization in PMMA material, reinforced concrete as a material and the deterioration mechanisms of reinforced concrete members embedded in soil. The main nondestructive testing techniques used to inspect reinforced concrete are discussed. The fundamentals of elastic wave propagation and attenuation mechanisms are also summarized.

2.2 Characterization of ultrasonic transducers

In ultrasonic testing, transducer characteristics play an important role in evaluating the internal conditions of the medium being tested. According to ASTM-E1316-11b, it is essential in non-destructive testing (NDT) to calibrate the measuring instrument to ensure a reliable measurement. Calibration of electronic equipment is an essential part of this process which is usually done by the equipment manufacturer. On the other hand, different methods have been developed over the years to characterize ultrasonic transducers (Ono, 2017). For example, Schmerr *et al.* (2006) and Dang *et al*. (2002) used a pitch-catch system to characterize the transducers' transmitting and receiving properties. In this characterization, the transducer sensitivity and its electrical impedance are characterized using a simplified procedure by analyzing a signal that is transmitted and received in water. Hatano *et al.* (1998) characterized contact acoustic emission transducers using reciprocity calibration methods in which the reversibility behavior of a pair of transducers (transmitter and receiver) are examined. A laser vibrometer technique is also reported (Ono, 2016) to be a potential procedure to characterize the sensitivity parameters of acoustic emission sensors, and this relies only on one-point measurement.

For the ultrasonic pulse velocity (UPV) method, the common procedure used to characterize ultrasonic transducers is measuring the arrival time based on reference standard bars and blocks. This technique determines the internal system time delay, which is subtracted from the travel time of wave propagation to calculate the wave velocity in the material. This standard procedure is necessary in ultrasonic testing to ensure a general level of consistency in measurements, and this allows for a better

interpretation of the information conveyed by the recorded signal. Moreover, standard references are used to ensure that the setup and the equipment generate similar measurements at different periods of time. These reference objects are manufactured in different shapes and sizes based on the NDT application and on the geometry of the specimens being tested (Figure 2-1).

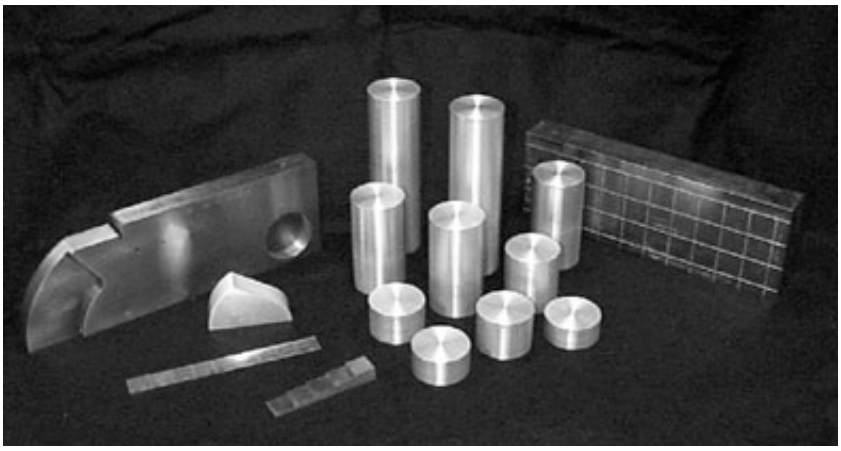

Figure 2-1: Standard reference blocks
(https://www.nde-ed.org)

The common reference standards used in UPV method are the aluminum and steel cylinder blocks manufactured per the requirements of ASTM E127 and ASTM E428, respectively. However, the reference block method is not sufficient to characterize the ultrasonic transducer in terms of frequency response, which requires a complementary procedure to obtain a reliable characterization. In this research project, a state-of-the-art laser vibrometer method is used to characterize and evaluate the characteristics of different ultrasonic transducers.

2.3 Fracture characterization in homogenous medium

Fracture propagation is typically studied to better understand material failure undergoing crack nucleation, growth, and coalescence. Macroscale physical tests have been carried out in various homogenous and heterogeneous materials, such as concrete, metals, ceramics, and, to a lesser extent, plastics to study fracture propagation (Ayatollahi et al. 2015; Haeri *et al*. 2013; Jiefan *et al*. 1990; Yang 2011). Standard procedures, such as the three-point test and four-point tests, are used to characterize fracture toughness of materials like concrete (Gerstle 2010; Tattersall and Tappin 1966; ASTM 2010). In metals, the tear test is a standard procedure to measure fracture toughness (ASME 2001), and the Charpy test is also widely used (Tattersall and Tappin

1966). However, unstable fracture growth remains a major limitation of these test procedures; fracture propagation is unstable and only peak-load measurements become meaningful. On the other hand, in rock mechanics, the generation of tensile stresses during compressive loading has been used for many years to evaluate fracture toughness (Ulusay, 2015). Yang (2011), and Haeri *et al*. (2013) tested sandstone and rock-like specimens in a cylindrical mold containing two artificially created flaws to study fracture coalescence under uniaxial compressive load. Ayatollahi *et al*. (2015) used polymethylmethacrylate (PMMA) specimens to study fracture development in brittle material with a V-notch as a stress concentrator within a specimen under compression; a fracture developed from the tip of the notch and eventually reached the other end of the specimen. All these were attempts to quantitatively observe fracture propagation under quasi-static conditions.

2.4 Characterization of concrete using ultrasonic techniques

Ultrasonic pulse velocity

Quantitative nondestructive assessments of concrete infrastructure rely substantially on the determination of cement-based material properties. Over the years, more attention has paid to characterize cement-based materials (Kozolv et al,1988; Jacobs and Owino, 2000; Anugonda et al, 2001; Popovics et al, 2000; Punurai, 2006; Treiber et al, 2010; Ahn et al., 2017) by implementing experimental programs and studying ultrasonic wave propagation in cementitious media. The research motivations came from two major aspects: developing a better understanding of the microstructure role and proposing an on-site non-destructive technique to assess the remaining service life of concrete members.

Wave propagation methods are commonly used in nondestructive testing (NDT) of concrete materials. At low strains, wave propagation parameters depend on the elastic material properties (Santamarina *et al*., 2001; Breysse, 2012; Slawinski, 2010). Among the NDT methods, the UPV method is most commonly used in practice (ACI 228.2R-13, 2013; Bungey *et al*., 2006) in the areas of medicine, chemistry, physics, biology, and engineering. The UPV technique is generally used in accordance with the ASTM C 597-16 and American Concrete Institute standard ACI 228.2R-13 to assess the quality

of natural rocks and concrete elements (Hertlein, 2013; Malek and Kaouther, 2014), to quantify the environmental impacts on geomaterials and concrete (Chen *et al*., 2015; Duan *et al*., 2011), and to determine material elastic properties (Ensminger and Bond, 2011).

Although wave velocity can be reliably used under certain conditions, it is not well-suited to identify heterogeneities such as cracks generated from loading conditions or environmental factors. In the case of such small-scale internal damage, wave attenuation from UPV test results is a more reliable parameter (Basu and Aydin, 2005; Chai et al., 2011; Kirlangic, 2013). Attenuation is sensitive to heterogeneities at many scales, and is used to characterize defects and heterogeneities in different materials (Aggelis et al. 2009; Chai et al. 2011; Yim et al. 2012; Fereidooni and Khajevand, 2018). As a further development, Gaydecki et al. (1992) proposed frequency-dependent attenuation studies to determine aggregate particle distribution in a concrete specimen; therefore, attenuation and frequency dependent approaches might be used to assess an array of inhomogeneities such as several cracks.

The relationship between wave amplitude and mechanical damage is studied by Nogueria and Willam (2001) to estimate the evolution of micro-cracks in concrete. Philippidis and Aggelis (2005) reported that wave velocity is significantly affected by aggregate quantity, while attenuation is more influenced by aggregate geometry. Chaix et al. (2003) evaluated thermal damage (micro-cracking) in concrete from wave attenuation data. Cerrillo *et al*. (2014) used both ultrasonic P- and S-waves on granite specimens to investigate the feasibility of wave attenuation in quantifying the physical-mechanical properties of the medium. They pointed out the reliability of wave attenuation in assessing properties such as apparent density, compressive strength, and dynamic elastic parameters.

Although, attenuation measurement to determine concrete properties is studied by many researchers, this type of material requires a more careful analysis approach. When an ultrasonic wave propagates through cementitious materials, it exhibits a significant loss because of absorption and scattering (material attenuation losses) so that the amplitude of the recorded waveform decreases due to the propagation of ultrasonic waves with increase in travel path. Therefore, recording and interpretation of actual waveform amplitude coupled into and out of the specimens being tested becomes a

challenging task. Previous research studies have highlighted the difficulty of measuring attenuation experimentally (Philippidis and Aggelis, 2005). The measurement of the waveform amplitude is influenced by several external factors such as system configuration and coupling layer between specimen being tested and ultrasonic transducer.

The components of cement-based materials including concrete, mortar, paste, cracks, and voids require further understanding for the characterization of cementitious materials when using the ultrasonic approach. Many investigators have made efforts to measure attenuation and dispersion in cementitious materials. Gaydeck et al. (1992) and Li (1992) conducted research based on the analysis of frequency spectrum of the primary waveform that propagates in concrete. Li. (1992) tested different types of concrete including loose concrete, dense concrete, and concrete with voids and studied the measured data using the frequency spectrum of the primary waveform. The research results reveal the advantage of using the shifted peak observed in the frequency domain of the examined specimens to characterize different conditions in concrete specimens. As a further development, Gaydecki et al. (1992) proposed frequency-dependent attenuation studies to assess aggregate distribution in a concrete specimen; thus, attenuation and frequency dependent approaches might be used to assess an array of inhomogeneities in concrete materials. The relationship between aggregate and attenuation losses are studied by other researchers as well (Landis and Shah, (1995); Schichert, (2002), Jacobs and Owino, (2000); Popovics et al., (2000). Even though these researchers used different test approaches and specimens.

Laser vibrometer

Laser Doppler vibrometer (LDV) offers a non-contact procedure to measure the vibration in the out-of-plane surface based on the Doppler shift phenomenon, which allows for determination of velocity of the object surface under study. It is designed and used widely in several engineering applications to measure vibrations in inaccessible areas and harsh environments. Modal analysis is one of the applications (Sriram et al., 1992; Stanbridge and Ewins, 1999; Ewins, 2000; MacPherson et al., 2007; Yang and Allen, 2012) along with damage detection based on vibrations (Pai and Lee, 2002; Waldron et al., 2002; Ostachowicz et al., 2010; Adams et al., 2014; Malekjafarian et al., 2018; Maio et al., 2018). Moreover, the laser approach is used to

detect hidden delamination in multi-layer composite materials (Sohn et al., 2010; Kudela, 2017).

LDV is a very useful approach for analyzing the interaction between elastic waves and discontinuities in a medium. It was used effectively to study the interaction of guided waves with cracks (Staszewski et al., 2004; Longo et al., 2010; Owens et al., 2011; Flynn, 2012), and fissures and holes (Ruzzene, 2005) in metallic plates. Also, it has been used to detect simulated deterioration in pipes (Flynn, 2012). Several researchers (Obrien et al., 2016; Flintsch et al., 2012; Malekjafarian et al., 2018) used the LDV technique to detect localized damage in concrete bridges. In the aforementioned researches, a testing methodology was proposed based on a passing vehicle to scan bridge surface with a laser vibrometer, the collected data were analyzed using relative velocities to locate damage.

2.5 Generalities of reinforced concrete

Concrete is presently the most preferred construction material used for different applications because it offers durable engineering properties at affordable cost and has low impact on the environment (Mehta & Monteiro, 1993). It is a heterogenous material primarily consisting of cement, water, and granular materials. Concrete may also contain materials with cementing characteristics (such as fly ash, natural pozzolans, or silica fume), fibers, and chemical additives. Concrete is brittle and has low resistance to tensile stresses. A reinforcement material is added to the concrete matrix which includes bars, strands, fibers, and wires. Aggregates in a typical hydraulic cement concrete are considered the main component that, by volume, consist of between 70% to 80% of concrete mixture (Lamond & Pielert, 2006), while cement paste (water, cement, additives, other cementitious substances) and air voids account for the rest of the volume. The aggregates can be found either naturally such as gravel, crushed stones, and sand or made artificially by broken down hydraulic cement concrete or iron blast furnace slag. Aggregate is classified into two categories: coarse aggregates (retained in the 4.75 mm mesh sieve) and fine aggregates (passing through the 4.75 mm sieve) (ACI CT-13).

The durability of reinforced concrete is mainly characterized by the suitable selection of the materials (proportion and properties) which may not be sufficient to guarantee the expected durability of the concrete members. The desired quality of concrete

elements can be influenced by many factors such as production, handling, placing and curing. These factors, beside the potential deterioration mechanisms, need to be analyzed with care at the design phase to ensure that the concrete member integrity during service life would meet the intended requirements of use. The deterioration of reinforced concrete is the main topic of relevance to the current research and is described briefly in the next section.

2.6 Mechanisms of deterioration in concrete

Many external factors can cause deterioration in concrete such as exposure to environmental and overloading conditions while, in some cases, the cause of deterioration can be internal. The mechanisms behind deterioration can be divided into two categories: (i) physical and mechanical damages and (ii) chemical reactions. The physical or mechanical damages originate from fire, freeze-thaw cycles, abrasion, restraining effects (temperature and shrinkage) and imposed strain or overloading. Chemical processes initiated in the concrete mixture or in the environment can cause damage as well (Breysse, 2010; Neville, 2011). Chloride penetration, carbonation, alkali-silica reaction, leaching, and sulfate attack are the main causes of chemical damage.

The selection of appropriate inspections methods and choosing adequate repair procedures rely essentially on understanding the deterioration mechanisms. Table 2-1 demonstrates the common deterioration processes and the corresponding data regarding inspection methods.

Common defects that are observed in concrete members, and the impact of concrete deterioration on the function and integrity of the elements are given in Table 2-1. It is essential for every infrastructure owner to evaluate the condition of concrete elements. Therefore, based on the nature of interest and the inspection type, assessment of hardened concrete can be achieved by using different methods.

2.6.1 Effect of load application

Several types of loads can cause degradation or deterioration in concrete such compression loading, low-level fatigue cycling, and thermal loading.

Table 2-1: Main deterioration mechanisms, consequences and required information (after Breysse, 2010)

Mechanism	Consequences in concrete	Required information
Overloading Restraining effects (temperature, shrinkage)	Damage, cracking	• If distributed damage: crack density, residual stiffness and strength • If localized cracking: location, width, depth
Freeze-thaw cycles	Scaling, spalling, delamination	• Affected areas • Depth of defect
Fire	Strength decrease, spalling	• Depth reached by fire effects • Residual strengths at different depths
Abrasion-erosion	Material loss	• Residual strength of surface layer
Carbonation	Increase in density, of steel, thus, rebar corrosion	• Carbonation depth • If corrosion: localization of active corrosion areas and corrosion rate
Chloride attack	Rebar corrosion	• Chloride content, chloride profile • If corrosion: localization of active corrosion areas and corrosion rate
Alkali-aggregate reaction Sulphate attack	Internal expansion, generalized cracking	• Potential for future volume change • Residual stiffness and strength
Leaching	Cement paste dissolution increase in porosity	• Residual strength • Porosity
Ammonium nitrate attack	Deterioration of cement paste, spalling, rebar corrosion	• Depth of the attack • If corrosion: localization of active corrosion areas and corrosion rate

Compression loading normally deteriorates concrete and produces distributed microscopic damage. This type of damage often leads to large defects such as scaling, delamination, spalling, and cracks, which can lead to loss of concrete integrity (Selleck et al., 1998; Shah and Ribakov, 2009). The occurrence of cracks can be initiated near the end of material life, and once started, a catastrophic failure can occur due to relatively fast crack growth. Therefore, it is recommended that investigation of cracks

in concrete is done at an early stage and this can be done even before crack initiation (Meyendorf et al., 2013).

Conventional acoustic non-destructive testing methods such as UPV, pulse-echo, and acoustic emission has been successfully applied to evaluate damage in concrete under compression loads. The most common of these methods is the ultrasonic pulse velocity (UPV) technique (Malhotra and Carino, 2004). It is traditionally known that the UPV is used as an indicator to quantify damage in concrete and this parameter is used extensively as a baseline for equipment used to inspect concrete structures in the field. Nevertheless, many researchers have pointed out that velocity alone cannot provide a complete of damage in concrete (Santhanam, 2010; Kirlangic, 2013; Rodríguez Roblero, 2017). Therefore, using another ultrasonic parameter such as wave attenuation is essential for a reliable procedure for detecting damage in concrete.

Knab et al., (1983) evaluated the ability of ultrasonic methods to detect cracks in concrete by performing laboratory experiments. They employed wave velocity and signal amplitude to evaluate concrete conditions in two orientations: parallel and perpendicular to the plane of crack. Both the parameters provided useful information about the degree of damage. Other studies (Tharmaratnam and Tan, 1990; Popovics et al., 1990; Qasrawi and Marie, 2003; Sanathanam, 2010; Rodríguez Roblero, 2017) reported that wave attenuation is more sensitive to damage than wave velocity in concrete specimens subjected to uniaxial compression load. Although the findings of previous studies have provided important information about using wave attributes to detect damage, these research studies focused on using pairs of ultrasonic transducers, which may not be enough to study the damage level in concrete because damage in these studies is estimated using a single wavelength value. It is essential to understand the behavior of cracking under compression load using an array of transducers with different nominal frequencies (different wavelengths), which is rarely reported in the literature.

2.6.2 Effect of freeze-thaw process

For decades, the freeze-thaw process in concrete has been studied thoroughly to understand its effect on the mechanical properties such as strength and stiffness of concrete. Because concrete is a porous medium, it allows water to be absorbed by the intrinsic pores and shrinkage cracks formed previously due to the hydration process.

This causes concrete to be susceptible to freeze-thaw cycles and deterioration of its mechanical properties occurs. The process of freeze-thaw in concrete can be considered as a complex form of fatigue loading. Therefore, the damage that accompanies the freeze-thaw cycles in concrete could be accelerated in the presence of significant external loading (Miao et al., 2002).

The main mechanism relevant to freeze-thaw process is the hydraulic pressure which causes internal cracking in concrete (Detwiller et al., 1989). When the temperature approaches freezing point, water in the capillary pores starts to freeze and expand. This produces a hydraulic pressure that exceeds the tensile strength of the cement paste in concrete and forms distributed cracks inside the concrete medium. During the thawing stage, more water enters these cracks and, by repeating this cycle, more deterioration occurs in concrete.

Different procedures, such as, air entrainment, decreasing water-cement ratio, and increasing curing time are used to reduce the effect of freeze-thaw cycles on the mechanical properties of concrete (Saboori, 2015). The most important procedure identified in the literature and shows significant impact on concrete durability is adding an air entraining agent. More air bubbles are produced in concrete when an air-entraining agent is added. This causes concrete to be more durable against the freeze-thaw cycle effects. The outcome of this procedure is reduction of hydraulic pressure that accompanies the freeze-thaw process. The more the bubbles developed in concrete, the more the capillary pores generated in concrete, and this causes the water to freeze and thaw without building up excessive pressure (Shang and Song, 2008).

Several researchers (Hasan et al., 2004; Shang and Song 2006; Hasan et al., 2008; Duan et al., 2011; Liu and Wang, 2012) quantitatively studied the influence of freeze-thaw cycles on the mechanical properties of concrete. Shang and Song (2006) reported the impact of number of freeze-thaw cycles (25, 50, and 75) on the strength, stiffness, and deformation performance of concrete specimens under biaxial compression. To make concrete more resistive against the freeze-thaw process, ACI E4-16 recommends adding an air-entraining agent to concrete within a range of 0.015-0.13% by cement mass. Several researchers (Shang and Song, 2008: Shang et al., 2009; Wong et al., 2011; Shang and Yi, 2013; Sonia et al., 2015) investigated the effect of adding different percentages (0.1-0.5) of air-entraining agent to concrete subjected to freeze-thaw

cycles. The experimental data of these studies demonstrate that the durability of concrete enhanced significantly against freeze-thaw process when more air-entraining agent is added, while the strength of concrete reduced.

2.7 Condition assessment for concrete structural elements

Concrete structures are designed to perform well during their service life. As with any material, the concrete members, specifically the shallow foundations, deteriorate with time due to aging of the material, excessive use, overloading, climatic conditions, and difficulties faced in suitable diagnostic methods. The outcomes in many situations can result in more repair work, reduced service life and, even in extreme scenarios, collapse of the structure. Moreover, many errors can arise during fabrication; for instance, the concrete mix may not be appropriate, the formwork may not be strong enough, or the estimation of the concrete conditions may be too optimistic. A structure is constructed by multiple people and errors can happen. After a structure is constructed, mistakes may also occur during its usage. Essentially, the normal decay process starts as a result of physical effects and aggressive chemical reactions. To ensure the integrity of concrete members during construction and service life, it is necessary to monitor their conditions periodically. To achieve this goal, many evaluation applications are developed based on different evaluation procedures. Figure (2-2) illustrates the essential components for concrete evaluation, which are visual inspections, documentation examination, laboratory and field testing, and structural analysis.

In addition, the ACI report emphasizes that the concrete components and its integrity need to be tested under many situations like

- Insufficient handling or curing of concrete,
- Exposure to physical (freeze-thaw, explosion, fire, overload, fatigue, abrasion) or chemical deterioration,
- When the structure is overloaded,
- When the operation and maintenance need to be optimized, or to verify models, materials, and environmental factors in the design phase to predict structure service life.

The aforementioned list illustrates the significance of condition evaluation methods, and the corresponding broad range of circumstances that can be applied for. Therefore, it is important to highlight that for this research work, only the conditions corresponding

to the deteriorations of shallow foundations are considered. The conditions studied are detailed in the following section.

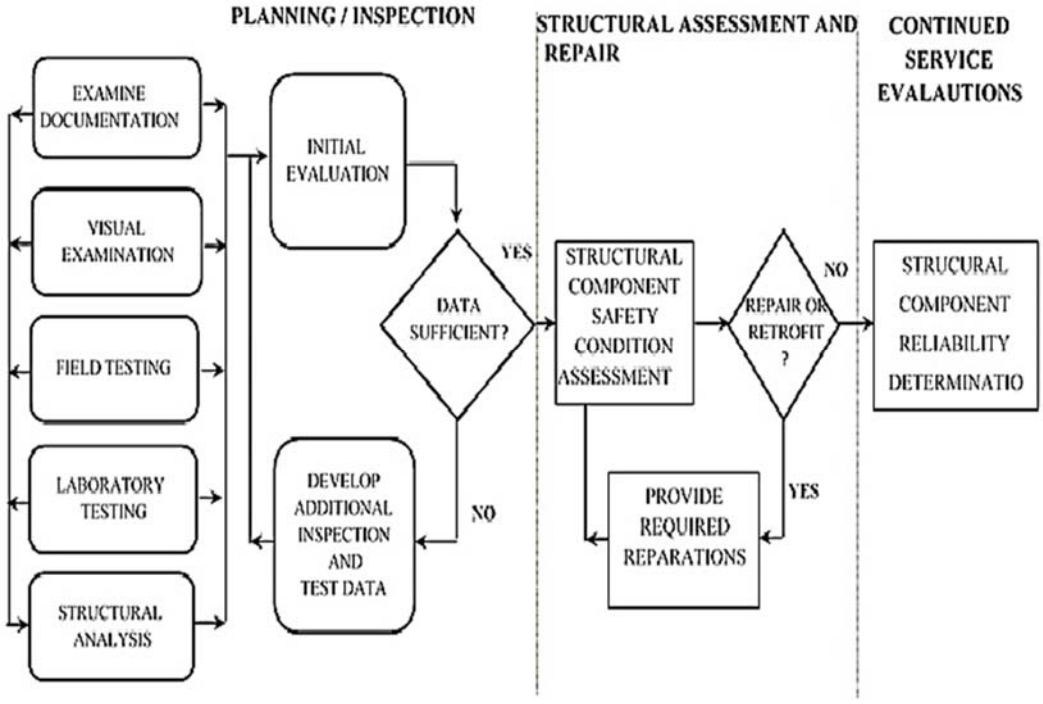

Figure 2-2: Evaluation of concrete components (after ACI 365.1R-17)

2.7.1 Typical defects in shallow foundations

There are two types of defects in reinforced concrete: internal and external defects. External defects include shrinkage cracking, surface air voids, spalling, pop outs, and scaling. Defects like honeycombing, voids, inclusions, and distress are internal flaws. Following are the definitions of flaws according to the ACI Concrete Terminology (ACI CT-13):

- **Shrinkage cracking**: these kinds of cracks occur when the shrinkage is restrained and leads to a decrease either in length or in volume because of variations in the moisture content or chemical damages. Cracks exist in different shapes such as random, parallel pattern or polygonal (Figure 2-3). This kind of cracking can be spaced a few millimeters to meters individually and can have a width of up to 3 mm. These can be shallow cracks and, in some cases, developed to be full depth cracks during the service life (ACI 224.1R-07).

- **Surface air voids**: represents cavities with a diameter not more than 15 mm, generally produced when air bubbles are entrapped in the surface of formed concrete during casting and consolidation (Figure 2-4).
- **Spalling**: this occur after forming of spalls in which portions from the concrete are detached because of weather action, expansion, or a blow (Figure 2-5).
- **Popouts:** refers to the results of the localized internal pressure that cause small portions of a concrete to break away, which produces a shallow, typically conical, depression (Figure 2-6).
- **Scaling**: happens when the near-surface zone of hardened concrete or mortar begins to peel away or produce local flaking (Figure (2-7).
- **Honeycombs:** represent gaps that are not filled with mortar and exist between coarse aggregate (Figure 2-8). This type of defects can be a result of improper placing methods, a mixture with excess of coarse aggregate and crowded reinforcement (Kosmatka et al., 2002).
- **Distress**: when a concrete structure experience cracking and distortion because of stress, chemical action, or temperature variation.
- **Segregation**: refers to unequal distribution of the aggregate in the mixture and the separation that happens between coarse aggregates and mortar. This cause zones with less aggregate amount to experience a large cracking, shrinkage and with a low resistance to abrasion. While the other portions of the mixture with dense coarse aggregate would be hard to consolidate and finish, honeycombing will form as a result of the segregation process (Kosmatka et al., 2002).

From the listed defects, the special interest for the current research is the internal defects (honeycombing, distress, and segregation) because they could be present in the concrete element with no trace at the surface. Other types of defects can be easily recognized using visual inspection. The advantage of the proposed methodology to assess concrete of shallow foundations is depicted through its ability to detect internal defects and deterioration at earlier stages, which is hard to achieve with current conventional NDT methods.

2.7.2 Nondestructive testing (NDT) methods for concrete

When the characteristics of the element under investigation are not influenced by the testing, this testing procedure is known as a nondestructive method.

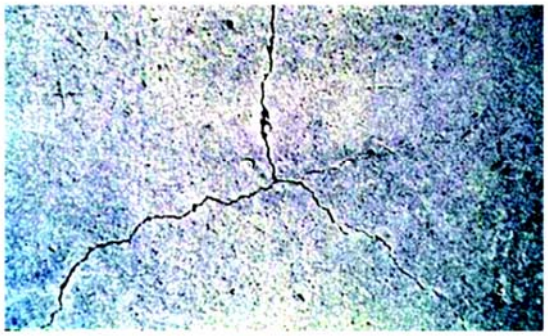

Figure 2-3: Shrinkage cracking (ACI 201.1R-08)

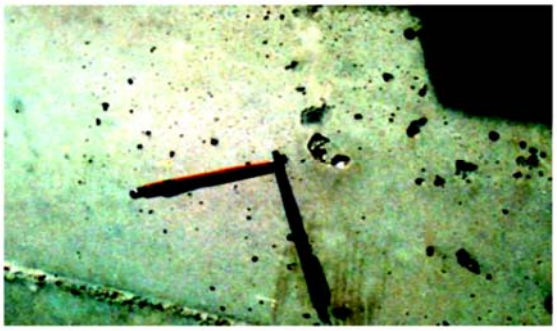

Figure 2-4: Surface air voids (also known bug holes, ACI 201.1R-08)

Figure 2-5: Concrete surface with medium spalling (ACI 201.1R-08)

Figure 2-6: Concrete surface with medium popout (ACI 201.1R-08)

Figure 2-7: Concrete surface with severe scaling (ACI 201.1R-08)

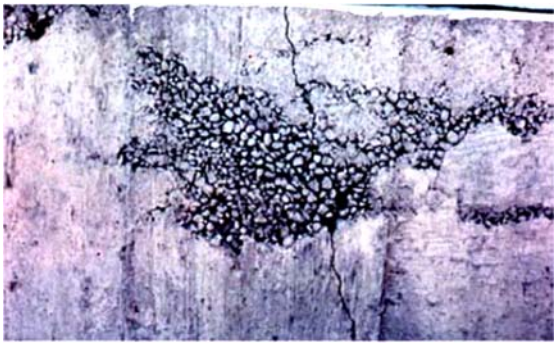

Figure 2-8: Concrete surface with honeycombing (ACI 201.1R-08)

During construction and operation stages, NDT methods can be used for different purposes: quality control of new structure, assessment of the condition of present structures, periodic maintenance and renovation applications, and quality control of restorations. They are divided into two groups based on the intended use: methods used in fresh concrete and methods used in hardened concrete.

Studying the new reinforced concrete elements is the interest of current research, in which the methods used for hardened concrete are highlighted. The NDT methods used

for hardened concrete include visual evaluation, acoustic methods (stress-wave methods), and non-acoustic methods which consist of nuclear, magnetic, electrical, infrared, and radar methods. The application of ultrasonic methods is the focus of this research; therefore, the stress-wave methods are considered in detail for structural members.

Stress-wave methods

The analysis of waves propagating through a concrete member under study is the basis of the Stress-wave methods. When a disturbance transmits in a medium, it is known as wave propagation. The source of the stress waves can be a transducer that converts energy of one kind to another or an impact force. A summary of the common stress-wave methods used to evaluate the condition of reinforced concrete members is given in Table 2-2, which highlights their main use, advantages and disadvantages. According to this table, the intended use of the standardized ultrasonic pulse velocity method is to estimate the velocity of propagation from the test results and to not identify defects. However, using the wave attenuation as a complementary procedure based on a consistent coupling would enhance application of the method to locate and examine internal defects in concrete members.

Table 2-2: Advantages and disadvantages of stress-wave methods for structures (after Rodríguez Roblero, 2017)

Method	Principle	Applications	Advantages	Limitations
Ultrasonic pulse velocity (ASTM C597)	The travel time of a pulse of ultrasonic waves over a path of known length is measure	To determine the relative condition or uniformity of concrete based on the measured pulse velocity.	- Portable equipment commercially available. - Relatively easy to use.	- Requires access to two sides of the members. - It does not provide information on the depth of the defect. - An experienced operator is required.
Ultrasonic echo	A transducer emits a short pulse of ultrasonic waves, which is reflected by the opposite side of the member or internal defects. The arrival time of the reflected pulse is recorded by an adjacent receiver and the round-trip travel time is determined.	To locate defects such as delaminations, voids, and honeycombing within the elements, or to measure an element thickness.	- It needs access to only one face of the element. - It provides information on the depth of the defect. - The method based on S-wave point transducers and SAFT (Synthetic Aperture Focusing Technique) permit construction of 3-D tomographic images.	- Applicable to limited member thickness. - An experienced operator is required.
Impact-echo (ASTM C1383)	A receiver adjacent to the impact point monitors the arrival of the stress wave, as it undergoes multiple reflections between surface and the opposite side of plate-like member or from internal defects. From frequency analysis it is possible to determine the distance to the reflector if the wave speed is known.	To locate defects such as delaminations, voids, honeycombing, or to measure element thickness.	- Access to only one face is needed. - Equipment is commercially available. - Capable of locating a variety of defects. - Does not require coupling material.	- An experienced operator is required. - Current instrumentation limited to testing members of maximum thickness of 1 m.
Spectral analysis of surface waves	A surface wave is generated through impact and two receivers monitor the surface motion. Using signal analysis, the wave speed is determined as a function of wavelength. The elastic constants of the layers are determined through an inversion process.	- To determine the stiffness profile of a pavement system. - To assess the depth of deteriorated concrete.	Capable of determining the elastic properties of layered systems, such as pavements, interlayered good and poor-quality concrete.	- An experienced operator is required. - Involves complex signal processing.
Impulse response (ASTM C1740)	The surface of the element tested is struck with an instrumented hammer and adjacent transducers measures the dynamic response. Through signal analysis it is possible to determine the characteristics of the tested element.	To locate anomalous regions in plate-like structures; voids below slabs on ground; cracks, and constrictions in deep foundations. It may provide information on low-strain dynamic stiffness of shaft/soil systems.	- Access to only one face is needed. - Equipment is commercially available. - Does not require coupling materials. - Large areas tested in short time.	- An experienced operator is required. - Thickness limitation of 1 m.

2.8 Theoretical Background

In this section, a brief outline of wave propagation and the principles of nondestructive methods implemented in this research are presented.

2.8.1 Fundamentals of wave propagation

The non-destructive methods used in this research study depend on the stress waves that propagate in a material. Hence, the basic concepts of wave propagation in elastic media is introduced in this section.

Ultrasonic test methods are used in a variety of scientific fields. Ultrasonic testing is a branch of acoustics that deals with mechanical vibrations at a frequency above the average range of human hearing. Typically, ultrasounds are considered to be above 18 kHz (Blitz and Blitz 1996) or 16 kHz (Ensminger & Bond, 2012). Since ultrasonic testing is the implementation of a particular extension of sound waves, the principles of wave propagation form the core of any ultrasonic approach. Ultrasound is a form of mechanical wave, and therefore, it represents the transfer of energy through a medium. Since the energy transfer of mechanical waves relies on particle interaction, they cannot propagate in voids (which by definition is without particles). In a mechanical wave, particle oscillation does not move the particle far from its initial position, and it is the energy that is transferred without any transfer of mass. For this reason, sound waves are considered stress waves and transmitted by direct contact (Ensminger and Bond 2012). When the generated stresses in the material are within the elastic range and that material obeys Hooke's law, the waves are considered elastic waves.

The oscillation modes of waves are used to describe the physical definition of these waves. Three modes of propagating stress waves are created when the surface of a large solid elastic medium is perturbed by a dynamic or vibratory load: (1) compressional waves (also called longitudinal or P-waves), (2) shear waves (also called transverse or S-waves), and (3) surface waves (also called Rayleigh waves). In solids, two modes of mechanical waves are transmitted: compressional and shear. The compressional mechanical waves could be either tensile or compressive, and the particle motion direction is in or opposite to the direction of wave motion, while in shear mechanical waves the particle motion direction is perpendicular to the direction of wave propagation.

In solids, sound waves can propagate in four principal modes that are based on the way the particles oscillate. Sound can propagate as longitudinal waves (P-waves), shear waves (S-waves), Rayleigh waves (R-waves), and in thin materials, as plate waves. Longitudinal and shear waves are the two modes of propagation most commonly employed in ultrasonic testing. Since the P-waves and S-wave have the ability to propagate through the entire volume of the elastic media, they are called body waves or bulk waves. The other types of waves are surface waves because the propagation takes place along the surface of the elastic medium. Figure (2-9) shows the basics modes of waves in solids. The following are the main characteristics of each wave type;

1- **P-wave:** are the waves associated with particles movement in parallel direction to the motion of the energy and are compressional or dilatational waves. They are also known as longitudinal waves or primary waves. In solids they propagate faster than other types of waves.

2- **S-wave:** are the waves corresponding to particle motion perpendicular to the motion of the energy without volumetric deformation. The S-waves propagate slower than P-waves, they are also called secondary waves or shear waves.

3- **R-wave:** or Rayleigh waves are known as surface waves because the surface of the medium that they propagate in limits their particle motion to approximately one wavelength below the surface and the particle motion is elliptical.

4- **L-waves:** which are known Love waves, propagate in a horizontal plane, where the particle motion is normal to the propagation direction.

5- **Lamb waves:** These types of waves are also known as plate waves. They exist in a medium with two free surfaces with a thickness of roughly one wavelength. The frequency of Lamb waves governs their velocity of propagation. The generation of these waves is associated with specific values of frequency, angle of incidence and material thickness. Furthermore, the wave velocity is restricted to the type of propagation and the product of the material thickness and the excitation frequency (Hellier 2001).

The medium characteristics (modulus of elasticity, Poisson's ratio, density) are the main parameters that affect the velocity of wave propagation; in turn, the mechanical wave propagation

behavior may be employed to infer properties of a material. For instance, velocity of a P-wave is determined by the relationship of the Young's modulus (E), Poisson's ratio (ν) and the density as below:

$$V_l = \sqrt{\frac{E(1-\nu)}{\rho(1+\upsilon)(1-2\upsilon)}}$$

(2.1)

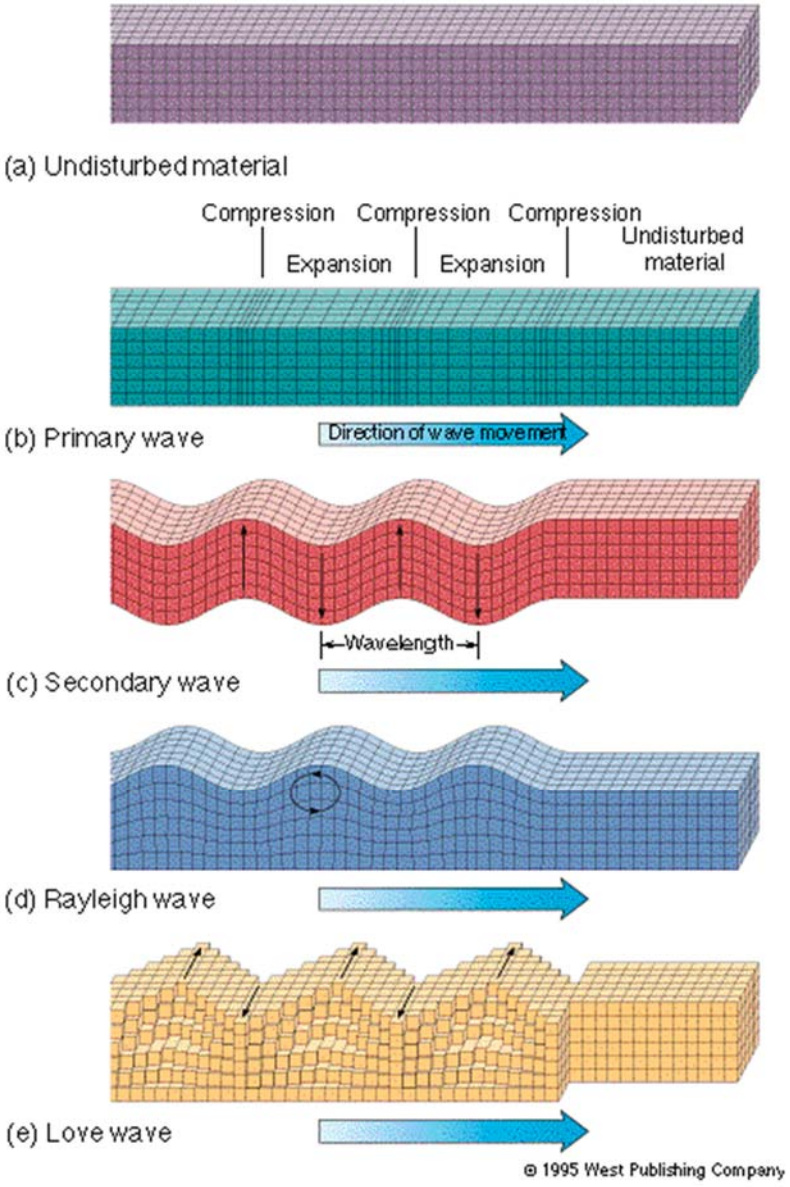

Figure 2-9: Type of waves in solids.

(http://www.geo.utep.edu/kidd/eqwave.html)

Similarly, the following equation illustrates the dependence of S-wave velocity on the density and shear modulus (G):

$$V_s = \sqrt{\frac{G}{\rho}} \tag{2.2}$$

The other two wave characteristics beside the wave velocity (V_l or V_s) which has a great impact on the testing results are the wavelength (λ) and the frequency (f). Both characteristics are associated with the wave speed V by the following mathematical expression:

$$V = f.\lambda \tag{2.3}$$

where: f is the number of oscillations per second of a wave (Krautkrämer and Krautkrämer, 1990) and the unit is generally hertz (Hz). The value of wave frequency can be determined from the inverse of the time period (T) and it depends on the angular frequency (ω) as:

$$f = \frac{1}{T} = \frac{\omega}{2\pi} \tag{2.4}$$

The wavelength (λ) is the distance between two planes in which the particles are in the same state of motion, for example two compression zones (Krautkrämer and Krautkrämer 1990). It is the distance that the sound will move in the direction of propagation in a given material at a specific frequency.

A wave can also be featured by the wave number (k) which is defined as:

$$k = \frac{2\pi}{\lambda} \tag{2.5}$$

The interaction between the wave during the propagation inside a medium and the discontinuities and the element boundaries results in the acoustic energy being partitioned. When a wave makes a perpendicular incidence at a boundary with another medium a part of the incident wave is reflected, and the remaining part is transmitted. The partitioning depends on the type of incident

wave and the acoustic characteristics of the media. For a normal incident wave, the **reflection** (*Rc*) and **transmission** (*Tc*) **coefficients** are determined by:

$$R_c = \left(\frac{(Z_2 - Z_1)}{(Z_1 + Z_2)} \right)^2 \tag{2.6}$$

$$T_c = \frac{4Z_1Z_2}{(Z_1 + Z_2)^2} \tag{2.7}$$

where Z_1 and Z_2 are the acoustic impedances of material 1 and material 2, respectively. The acoustic impedance Z of a material is the product of the material density and wave velocity:

$$Z = \rho V_l \tag{2.8}$$

For reinforced concrete members, the typical values of acoustic impedances of the mix components are shown in Table 2-3 which indicates that the acoustic impedance of air is relatively low. When a wave propagates in a material such as concrete or steel and encounters a discontinuity (air interface), the reflection coefficient is expected to be 1.0, which means that almost all the energy reflected. Therefore, it is reasonable to use NDT mechanical-wave methods to determine discontinuities or other defects within the concrete.

Table 2-3: Typical values for the acoustic impedance (ACI 228.2R-13)

Material	**Acoustic impedance (kg/m^{2}s)**
Air	0.4
Water	1.5 x 10^6
Concrete	7-0 x 10^6
Steel	47 x 10^6

When waves interact, they superimpose on each other, and the amplitude of the sound pressure or particle displacement at any point of interaction is the sum of the amplitudes of the two individual waves. The process is known as superposition or interference of multiple waves.

2.9 Wave velocities and material parameter calculations

In immersion UPV test, longitudinal velocity can be estimated based on the travel time of the signal in water as a reference. The travel time is identified either from a peak of the second cycle of the signal water or from the first arrival time (Figure 5-2). This is compared with the arrival time of the specimen signal that is obtained from inserting the specimen in the water path. The bulk longitudinal velocity (V_l) can be calculated from (Ginzel and Turnbull, 2016):

$$V_l = \frac{V_w}{\frac{1+(t_s - t_w)V_w}{d}} \tag{2.9}$$

where V_w is the wave speed in water at the measured temperature, t_w is the reference time in water, t_s is the reference time in the specimen, and d is the thickness of the specimen.

Based on a specified temperature of water, the sound velocity in water is calculated using the Bilaniuk and Wong (1993) equation:

$$V_w = 1402.39 + 5.04T_w - 0.058T_w^{\,2} + 3.287 - 4T_w^{\,3} - 0.56T_w^{\,4} + 0.027T_w^{\,5} \tag{2.10}$$

where T_w is water temperature (C^o).

The bulk shear velocity is also determined by using the reference arrival times in water and concrete specimen. In this case, the shear wave velocity can be calculated from (Ginzel and Turnbull, 2016):

$$V_s = \frac{V_w}{\sqrt{\sin^2(\theta_t) + \left[\frac{(t_s + t_w)V_w}{d} + \cos^2(\theta_t)\right]^2}} \tag{2.11}$$

where V_w is the wave velocity in water at the measured temperature, t_w is the reference arrival time of water signal, t_s is the reference arrival time of specimen signal, θ_t is the incident angle determined by the goniometer rotation, and d is the thickness of the specimen.

The calculated P-wave velocity (V_l) and specimen density (ρ) are used to determine the acoustic impedance (Z) of the specimen being tested using equation 2.8. The determination of acoustic impedances of water and specimens allows calculation of the coefficients of transmission (T_c) and reflection (R_c) at the interface of water and specimen. The following equation can be used to determine the transmitted part of the wave. While the reflected wave can be evaluated by subtracting the transmitted wave from the total wave or using equation 2.6.

$$R_c = 1 - T_c \tag{2.12}$$

Many useful parameters, specifically elastic constants, can be estimated once the acoustic velocities are calculated and the material density is assumed known. To do so, the following equations are used to calculate the elastic moduli (Ginzel and Turnbull, 2016):

Poisson's ratio (ν),

$$\upsilon = \frac{1 - 2\left(\frac{V_s}{V_l}\right)^2}{2 - 2\left(\frac{V_s}{V_l}\right)^2} \tag{2.13}$$

Young's modulus (E),

$$E = \frac{V_l^2 \rho (1+\upsilon)(1-2\upsilon)}{(1-\upsilon)} \tag{2.14}$$

Shear modulus (G),

$$G = V_s \rho \tag{2.15}$$

2.10 Ultrasonic wave attenuation

The reduction in ultrasound intensity or wave pressure during the propagation through a medium is called the wave attenuation. In through-transmission techniques, acoustic impedance mismatch due to a thin crack can cause the wave amplitude to reduce significantly; however, a measurable change in the wave velocity may not be produced (Berubé 2008). The attenuation can be expressed in many ways, but often expressed in decibels per unit length (Hellier 2001; ASTM E1316-11b 2011). The attenuation can also be defined in nepers (Np) per unit length. The reduction of one neper of the wave amplitude means its initial value has been reduced by 1/e, where e is the base of the natural logarithm.

When a plane stress wave propagates through a medium, attenuation would occur following (Punurai, 2006):

$$A(z,t) = A_o e^{i(\omega t - kz)} \tag{2.16}$$

where *A(z,t)* and A_o are the original wave amplitude and attenuated wave amplitude at distance z, ω is the angular frequency and *k* is the wave number (also known propagation factor). Assuming the wave number *k* or the wave velocity to be complex, the attenuated wave expression can be obtained. Considering the wave number as a complex, a plane attenuated wave can be expressed as:

$$A(z,t) = A_o e^{-\alpha z} e^{i(\omega t - k1z)} \tag{2.17}$$

Thus, the imaginary part of the complex wave number and the phase velocity ($c = \frac{\omega}{k}$) is the attenuation coefficient α. Therefore, knowing the exponential decay in amplitude caused by α, one can use the following expression

$$A(z) = A_o . e^{-\alpha z} \tag{2.18}$$

to determine the attenuation coefficient α. This equation can also can be written in a different way

$$\log_e A(z) = \log_e A_o - \alpha z \tag{2.19}$$

Thus, for two different points z_1 and z_2 where $z_1 < z_2$, the mathematical form of the difference at the two points is

$$\alpha = \frac{1}{z_2 - z_1} \log_e \frac{A(z_1)}{A(z_2)} \tag{2.20}$$

and, this expression can be in decibels (dB) or in nepers. It is known that any ratio of two pressure amplitudes can be written as

$$20 \log_{10} \frac{A(z_1)}{A(z_2)} \text{ dB} \quad \text{or} \quad \log_e \frac{A(z_1)}{A(z_2)} \text{ Np} \tag{2.21}$$

Therefore,

$$\alpha = \frac{1}{(z_2 - z_1)} 20 \log_{10} \frac{A(z_1)}{A(z_2)} \quad \text{dB/unit length} \tag{2.22}$$

$$\alpha = \frac{1}{(z_2 - z_1)} \log_e \frac{A(z_1)}{A(z_2)} \quad \text{Np/unit length} \tag{2.23}$$

For a given distance or time, one decibel is 8.68 times the value in nepers. Equations 2.22 and 2.23 are used to determine the attenuation coefficient α of the ultrasonic wave propagated in an elastic medium.

Many approaches are proposed to estimate the coefficient of attenuation α and some of those are used in this research project — for example, using the peak to peak amplitude or ratios between amplitudes in time domain is one of these methods so the expression can be written as:

$$\alpha = \frac{1}{d_s} 20 \log_{10} \frac{Pk_o(t)}{Pk_z(t)} \tag{2.24}$$

where Pk_o and Pk_z are the peak to peak wave amplitudes or amplitude ratios before and after the disturbance as a function of time t propagating a distance d_s in the medium. Equation 2.24 can also be used to calculate attenuation in frequency domain by either selecting maximum magnitudes or the spectrum areas (*SA*) (Kirlangic, 2013). To calculate the coefficient of attenuation of material tested in water, there is another method that considers the transmission losses from both interfaces of specimen with water (Pederson, 2014) which added to equation 2.24 to obtain:

$$\alpha = \frac{1}{d_s} 10 \log_{10} \frac{SA_o(t)}{SA_z(t)} - 20 \log\left(\frac{4 z_1 z_2}{z_1 + z_2}\right) \quad (2.25)$$

The second term is used as a correction factor which can be avoided in case of using different thicknesses from the same material being tested.

Moreover, the area that computed from Fourier spectrum is used also in this work to determine the material attenuation by comparing the area under the frequency spectra obtained from the ultrasonic measurements. The notion of this approach is to select regions (bandwidths) under the frequency spectra of the baseline specimen and the specimen with damage that caused by freeze-thaw cycles or compressive loading which are more sensitive to damage.

2.10.1 The cause of wave attenuation

There are many causes behind the total attenuation of ultrasonic wave in a material, which can be divided into two classes: intrinsic attenuations related to the physical properties of the material, and apparent or "extrinsic" attenuations that are a result of the method used to make the attenuation measurements.

Intrinsic attenuation

The intrinsic attenuation losses that occur because of the material physical properties are of two types: material loss (absorption) and scattering. The propagated stress wave energy is dissipated because of the material absorption. For a complete cycle of oscillatory stress, this happens when the stress and strain of the material is not single-values functions of one another. This type of behavior arises when the time derivatives of stress or strain exist in the stress-strain equation. When the strain cannot stand up with the stress alteration, this produces the hysteresis effect. Therefore, in case the strain is spatially inhomogeneous, as in the propagation of primary ultrasonic wave in metals (Ensminger & Bond, 2011), temperature gradients will be generated at the zones of compression and rarefaction. Thus, a heat flow arises with a production of entropy causing the ultrasonic wave to lose energy irreversibly and this results in the pressure wave amplitude being attenuated.

Scattering, which is the other aspect of intrinsic attenuation, appears at grain boundaries, or regions with different elastic properties. Many factors such as multiple phases, grain structures, and crystal

defects caused by dislocation are associated with these differences. A scatterer can be any heterogeneity object inside the medium such as aggregates, voids, and cracks. The main problem to describe the attenuation caused by scattering results from scatterers present in a material with given geometric properties and density. The loss produced by a single scatterer with low density may not be accompanied with any affect even with the presence of other scatterers. In this case, the so-called single scattering theory is used to calculate the total loss. Furthermore, the combined scattering attenuation effect is basically determined by adding the individual contributions of the scatterers that were treated independently (Ishimaru, 1978).

There are different scattering regimes which are distinguished based on the feature size and the wavelength of the radiation: Rayleigh scattering, mid-frequency scattering and long wavelength scattering (Ensminger and Bond 2012):

- Rayleigh scattering: occurs at small reflectors, where wavelength is large compared to the scatterer dimensions.
- Mid-frequency scattering or stochastic scattering: occurs when the dimensions of the scatterers are near that of the wavelength.
- Long wavelength scattering or diffusive scattering: occurs when the scatterer dimensions are several wavelengths.

Table (2-4) shows different relationships for the attenuation governed by the scattering regime.

Table 2-4: Attenuation relationship governs by different scattering regimes (after Ensminger and Bond 2012)

Scattering of ultrasonic waves	Relation between the wavelength and the target dimension	Attenuation
Rayleigh	$\lambda \gg D$	$\propto = A_1 D^3 f^4$
Stochastic	$\lambda \approx D$	$\propto = A_2 D f^2$
Diffusive	$\lambda \ll D$	$\propto = A_3 D$

- D is the average grain diameter,
- A1, A2, and A3 are the coefficients govern by the elastic moduli of the material.

Extrinsic attenuation

Extrinsic attenuation is a consequence of beam spreading which is emitted from the transducer into the material. When a real vibrating transducer is excited, the emitted pressure wave field diverges from a plane wave pattern. This is governed by the ratio of the transducer diameter *d* to the wave length which affects the radiation behavior (Hutchins et al., 1990). To illustrate that, Figure 2-10 shows the directivity function at three different ratios of transducer diameter to wavelength in a polar coordinate system. As the transducer diameter increases, this reduces the divergence of the wave field which, in turn, drops the wave energy.

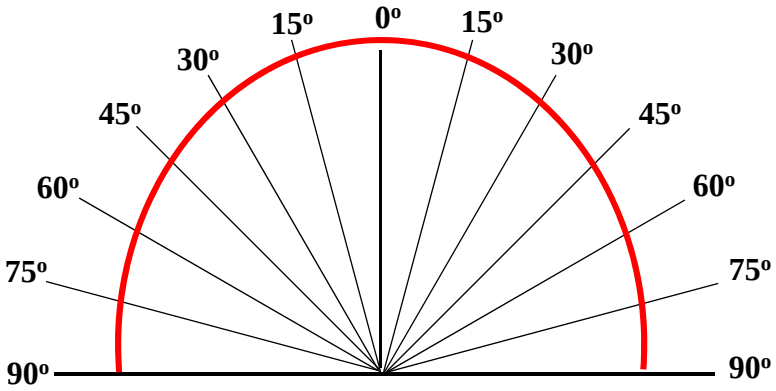

$d / \lambda = 0.5$

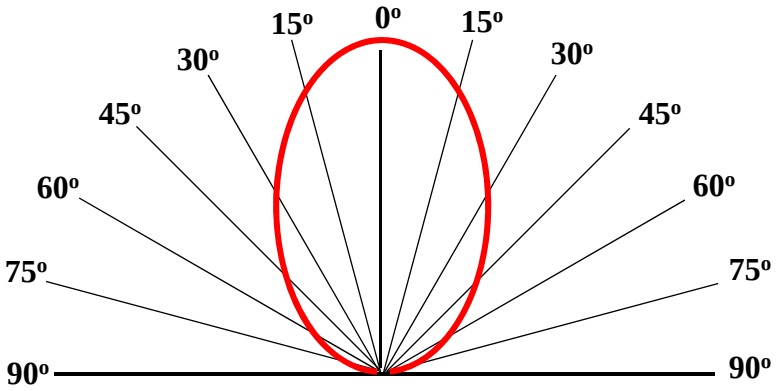

$d / \lambda = 1.2$

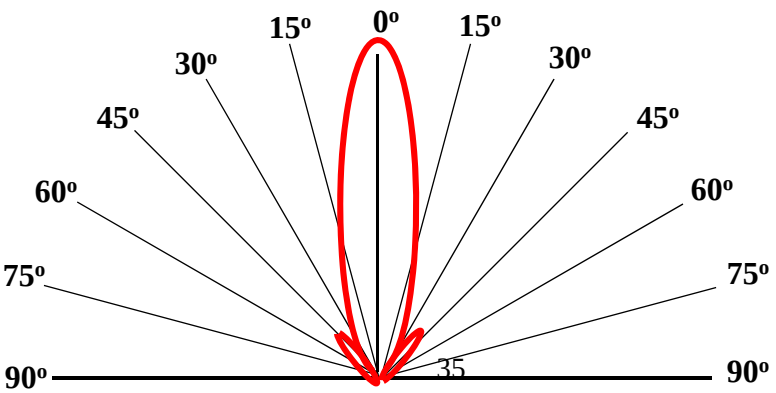

$d / \lambda = 3$

Figure 2-10: Influence of different ratios between transducer diameter *d* and wavelength λ on wave pressure at different angles (after Krautkrämer and Krautkrämer, 1990).

The reduction in pressure wave caused by beamspreading of a piston transducer at point z along the axis of the transducer can be expressed as (Punurai, 2006):

$$p(z) = 2p_0.\sin[\pi\frac{d}{\lambda}(\sqrt{(\frac{1}{2})^2 + (\frac{z}{d})^2}) - \frac{z}{d}] \qquad 2\text{-}26$$

The zone nearest the transducer surface is known as the near-field. In this zone the pressure wave shows large variations (see Figure 2-12, d/λ=3). As the wave moves away from the transducer surface to the point where the pressure variations change to a steady decay, the zone is called the far-field. In the far-field, the relationship between the pressure wave reduction and distance becomes inversely proportional and follows a decay approximation. The actual pressure is a function of the transducer area and the approximation of pressure wave in the far field is given by

$$p(z) = p_0 \cdot \frac{\pi}{(z/d)} \cdot \frac{d}{\lambda} \cdot \frac{1}{4} \qquad 2\text{-}27$$

Therefore, the beam spreading is influenced by increasing d/λ which causes the angle of divergence to decrease. This means less divergent beam can be obtained by using larger transducer sizes with higher frequencies. Figure 2-11 shows, at different ratios between transducer diameter and wavelength, the absolute values of distance to transducer diameter ratio.

2.11 Ultrasonic pulse velocity method

One of the most popular nondestructive testing (NDT) methods used to evaluate the condition of structural concrete members is the ultrasonic pulse velocity (UPV). UPV is employed widely in several applications such as assessing the relative quality and the uniformity of concrete mix,

detection of voids and cracks, and assessing the effectiveness of the crack repairs (ACI 228.2R-13). Evaluation of freeze-thaw damage in concrete is another usage of this technique.

This method has been standardized for concrete (ASTM C597-16) to determine the propagation velocity of the primary wave (P-w). The calculation of the pulse velocity of the primary stress waves is significant because of the dependence of the velocity on the elastic properties and density of the material. Therefore, the characteristics of a material may be inferred based on the behavior of the propagated stress wave.

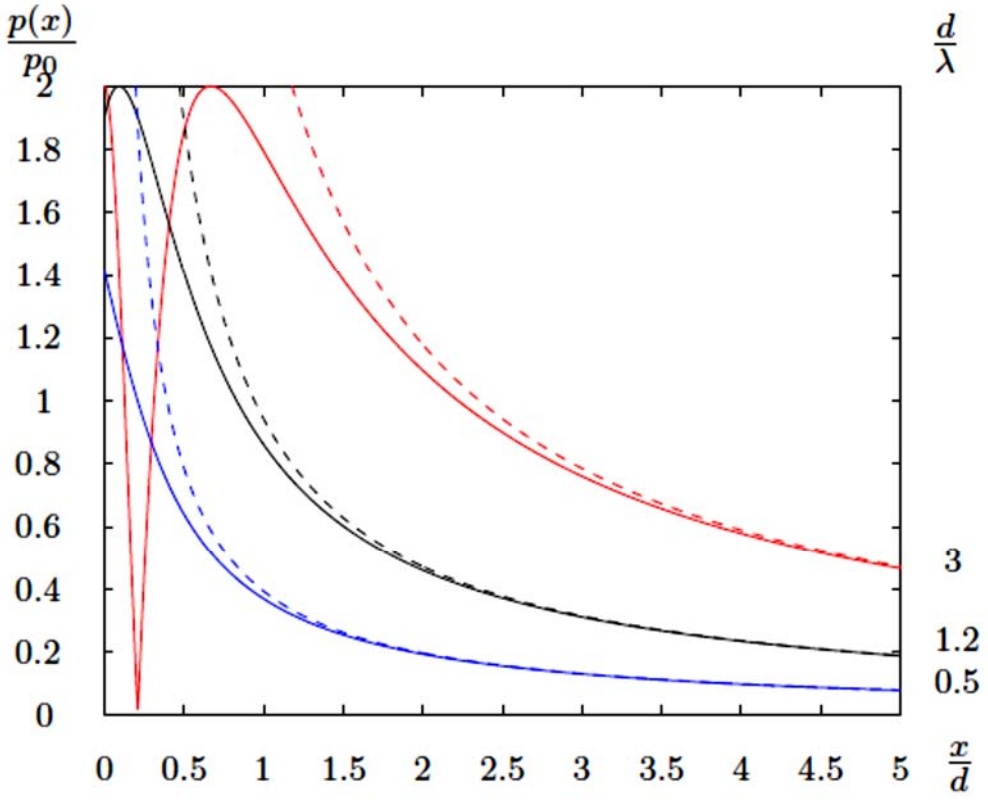

Figure 2-11: The relationship between the relative pressure wave $\frac{p(x)}{p_0}$ and the distance related to transducer diameter $\frac{x}{d}$ at different diameter to wavelength $\frac{d}{\lambda}$. The dotted lines are the approximated relative pressure (after Punurai, 2006).

To calculate the pulse velocity (V_p), the distance between centers of the transducer faces is divided by the arrival time. This transit time corresponds to the time taken by a pulse to propagate from the transmitter to the receiver inside the concrete specimen. As an example, Figure 2-12 shows the

schematic configuration employed to conduct the pulse velocity measurement for concrete specimen.

The arrival time is determined from the moment the transmitter triggers to emit the electrical pulse to the time of detection of the first arrival of the P-waves. To evaluate the correct time, the arrival time measured from the test must be corrected by subtracting the delay time caused by the electronic equipment and the transducers. The delay is determined either by placing the transducers face to face or using reference block to measure the transit time.

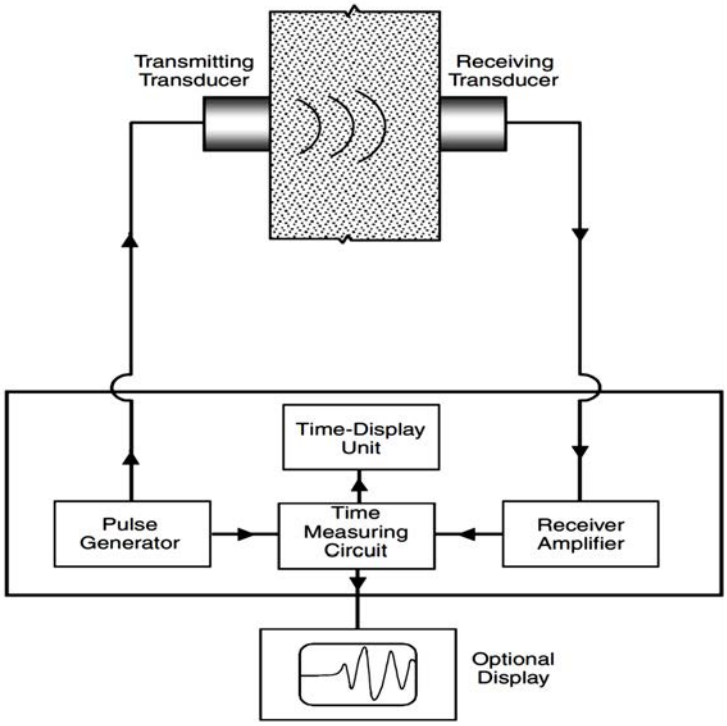

Figure 2-12: Schematic diagram of pulse velocity test circuit (after Malhotra, 2004).

According to the standard (ASTM C597-16), it is not recommended to use the pulse velocity to evaluate the compressive strength of the concrete, because there are many factors that influence the pulse velocity such as type and volume of aggregate, content of moisture, and the volume and distribution of the reinforcement. These factors can overshadow the values calculated from the UPV assessment (ACI 228.1R-03 2003). Furthermore, during the development of the concrete maturity, large variations in compressive strength may produce only subtle changes in pulse

velocity which is supported by the fact that the elastic modulus is proportional to the pulse velocity and the elastic modulus is related to the square root of the compressive strength (ACI 437R-03; ACI 228.1R-03). The detection of regions with different quality or internal defects can be suitable for evaluation purposes; however, the measured velocity is not sufficient to identify the nature of those defects (ACI 437R-03). Therefore, the ASTM standard for the UPV emphasizes that "The results obtained by the use of this test method are not to be considered as a means of measuring strength nor as an adequate test for establishing compliance of the modulus of elasticity of field concrete with that assumed in the design" (ASTM C597-16).

For the aforementioned reasons, the intended use of the pulse velocity method in this research is to identify the defects, such as voids or cracking, and it is not used to evaluate the strength of the concrete elements.

2.13 Basic principles of laser Doppler Vibrometer

Laser Doppler vibrometer (LDV) provides a non-contact method to inspect a broad range of structures from a distance where accessibility is not possible. This technique can be used to acquire data from elements under investigation through waves that propagate either electromagnetically or acoustically. To measure the displacement or velocity of a moving surface, laser vibrometry employs a Doppler shift generated on a conveyor frequency of the laser (Lutzmann et al., 2011). Therefore, this technique offers surface measurements, which obtain with a correct testing setup highly accurate information for assessing the mechanical properties of the elements under inspection.

The commercially available LDV systems consist of two main components: the optical portion (sensor and controller processor) and the scan portion (control and data acquisition system) (Hasanian, 2017). In the first component, the optical sensor includes the actual laser, the optical parts, and electrical elements, which are required to guide the laser beam spatially. The electronic components used to process the displacement information fed by the optical sensor represent the controller processor. This comprises the interface between interferometer and the second component of the laser system (optical sensor and controller). The scan control and data acquisition system consist of the instruments and software required to process the scan mirrors and to record the displacement data. In this study, the laser system, manufactured by Polytec, is used for

characterization and condition assessment experiments. The Polytec configuration is originally developed from the Mach-Zehnder interferometer. In this system, the laser beam is emitted from the inner interferometer cell and targets the object surface being tested (Figure 2-13).

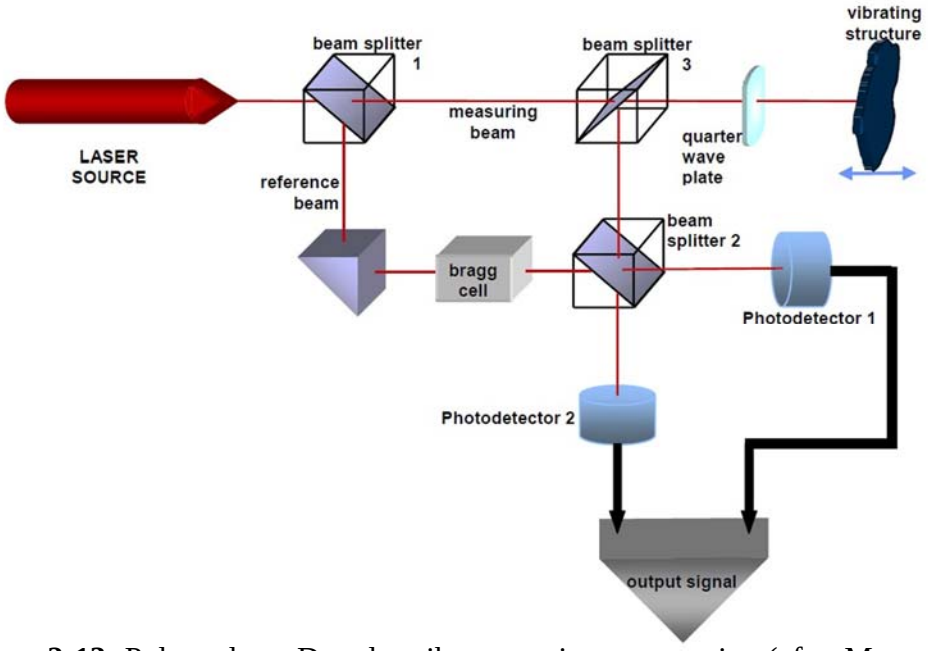

Figure 2-13: Polytec laser Doppler vibrometer instrumentation (after Martarelli, 2001).

2.14 Summary

The main findings of the literature review and a brief theoretical background are presented in this chapter that are considered necessary to illustrate the methodology and the results of the research work. This includes characterization of ultrasonic transducers, the wave propagation fundamentals, fracture characterization in homogenous materials, the description of the different stress-wave non-destructive evaluation approaches used to evaluate the hardened concrete condition, and a short explanation of the deterioration mechanisms in concrete. Also, the principles of the laser Doppler vibrometer have been outlined.

Chapter 3: Characterization of ultrasonic transducers

This chapter introduces the methodology and configuration used to characterize several ultrasonic transducers using conventional and laser vibrometer methods. A description of the material and instrumentation used in the characterization tests are also presented.

3.1 Introduction

In any testing procedure, the instruments require characterization to produce reliable results which can be achieved by comparing with or adjusted to a known reference (ASTM E1316-11b). The characterization process relies primarily on the equipment type used. For example, the common characterization in the pulse velocity test, which uses ultrasonic transducers, depends on the arrival time measured using a reference bar. This procedure allows to compute the adjustment in the time, where the transit time indicates the velocity of the transmitted wave in the specimen. This is performed manually determining zero-time to adjust for systems' electronic delays (ASTM C597-17). Nevertheless, this characterization procedure did not provide enough information about the characteristics of the transducers that are the main components of the ultrasonic testing setup (Schmer and Song, 2007).

When piezoelectric transducers are excited under a known input, it generates a signal with a combination of responses that includes the transducer, couplant and the specimen. To obtain the sample response from this combination, it is required to normalize the response by the frequency response of the transducers (Kirlangic, 2013). Commercially, it is known that the manufacturer provides the nominal frequency of the transducer which is assumed to be the frequency response of the transducers. Adding to that, the ageing and use can alter the technical characteristics of the transducers (Chevalier and Vinh, 2010). In this study, different types of transducers are characterized using conventional and laser vibrometer methods.

Another significant aspect affecting the repeatability of the tests is the coupling between the transducer and object surface. It is essential to study the coupling material as it can be difficult to maintain its consistency in the field and it affects the attenuation measurements. This represents one of the main limitations to use wave attenuation in ultrasonic measurements. Using coupling agent allows sound waves to transfer from the transducers to the specimen. There are different types of couplings that can be used with ultrasonic transducers, such as oil, petroleum jelly,

moldable rubber or grease (ASTM C57-17). In this study, two types of coupling that provide good coupling are used: vacuum grease with PMMA specimens and Sonotech Ultragel II® with concrete specimens.

The main objectives of the characterization experiments are to characterize ultrasonic transducers for non-destructive applications using laser vibrometer and to understand the mode vibrations of ultrasonic transducers excited under a square-wave pulse input voltage. This helps to enhance the efficiency of attenuation measurements in ultrasonic testing by exciting them using the actual resonance frequencies.

3.2 Experimental program

3.2.1 Ultrasonic transducers

Different ultrasonic transducers with a frequency range of 54 kHz to 1 MHz are used to perform characterization measurements which are divided into two groups: old transducers (more than 10 years old) and new transducers. Table 3-1 illustrates the main characteristics of the characterized transducers. All ultrasonic transducers, except 500MN which is used for immersion testing in water, are contact transducers.

Table 3-1: Details of characterized ultrasonic transducers

Designated symbol	Nominal frequency (kHz)	Wave type	Manufacturer	Diameter (mm)	Status
54O	54	P-wave	Proceq	50	Contact-Old
54N	54	P-wave	Proceq	50	Contact-New
150N	150	P-wave	Proceq	19	Contact-New
250N	250	P-wave	Proceq	19	Contact-New
500Oy	500	P-wave	Olympus	38	Contact-New
500Ut	500	P-wave	UTX	25	Contact-New
500MN	500	P-wave	UTX	19	Immersion-New
1MPO	1000	P-wave	Panametrics	28	Contact-Old
1MSO	1000	S-wave	Panametrics	28	Contact-Old
1MSN	1000	S-wave	Olympus	29	Contact-New

In this research, the set of transducers 54N,150N, 250N, and 500Oy in Table 3-1 are selected to implement ultrasonic pulse velocity and laser measurements of the materials under investigation in other sections of this project, while the others are used to study their characteristics and for comparison purposes (Figure 3-1).

Figure 3-1: Types of the characterized ultrasonic transducers.

3.2.2 Instrumentation setup

Conventional methods. It is usual in UPV testing to characterize transducers using conventional procedures, which include face to face and reference bar methods, to determine the time delay from electronics. The testing techniques follow the same principles used in the UPV method with the exception that the transducers are tested by placing them face to face or using a reference block between them. Figure 3-2 shows the employed configurations of the characterization instrumentation. In the face to face procedure, each transducer is excited with a square-wave pulse voltage input at the corresponding resonance frequency provided by the manufacturer. The input-output signals are recorded by a computer using software Keysight BenchVue ® to process them later to determine the delay time for each transducer.

The reference bar procedure uses 10 calibration rods; 5 steel rods and 5 aluminum rods. Table 3-2 illustrates the rods employed. For this characterization, a gel agent is used as a couplant because it provides better correlation on the curves of the arrival times versus heights. The sum of the electronic effects which represents human bias and coupling materials can be computed accurately using rods of varying sizes. All rods are made from same material which ensures they have a similar wave velocity.

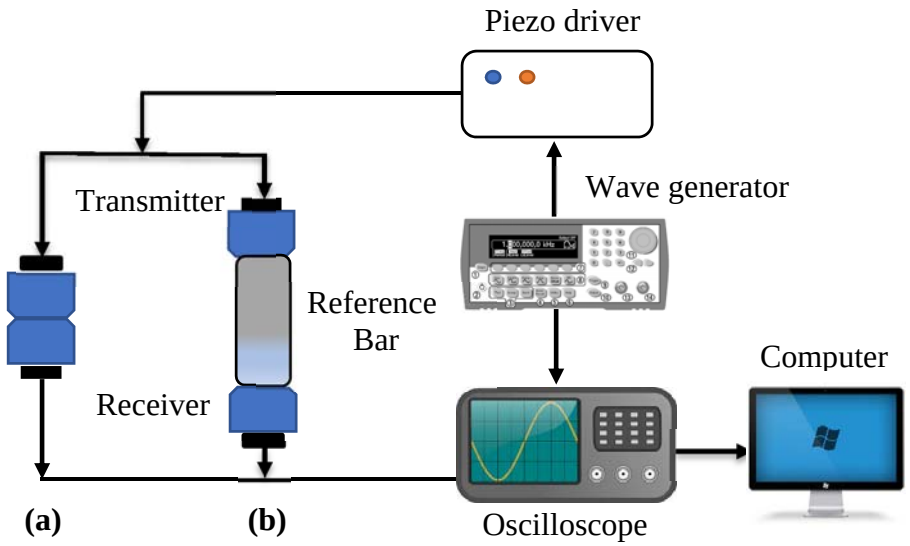

Figure 3-2: Characterization testing setup, for (a) face to face technique and (b) reference bar technique.

Plotting the arrival time measurements of each material rods against their heights achieves the characterization of each transducer. Therefore, the curve slope represents the value of the velocity and the intercept gives the delay time of the system as illustrated in Figure 3-5.

Table 3-2: Sizes of characterization standard rods employed.

Aluminum		Steel	
Height (mm)	**Diam. (mm)**	**Height (mm)**	**Diam. (mm)**
49.75	50.75	49.18	49.75
74.26	50.75	73.62	49.75
98.28	50.75	98.9	49.75
123.22	50.75	123.9	49.75
149.01	50.75	157.98	49.75

Laser Doppler vibrometer method. The laser experiment setup used to characterize the transducers utilized laser vibrometer interferometry which includes; laser head (Ploytec OFV-534), vibrometer controller (Ploytec OFV-2570), data management system, vibration isolated workstation, high-resolution positioning controller, wave generator (Keysight), amplifier (Krohn-Hite), piezo driver and set of transducers. Figure 3-3 shows the configuration testing setup of the laser vibrometer. The characterization is performed by exciting the ultrasonic transducer as a transmitter and measuring the response using the laser vibrometer (non-contact transducer) as a receiver. To do so, a one-cycle square-wave pulse at a frequency corresponding to the nominal frequency of the transducer with a known voltage is used as the electrical excitation for the transmitter.

The wear plate of each transducer is covered with a layer of retroreflective tape which is used to ensure effective measurements using the laser beam. It is worth mentioning that the placing of this tape should be achieved with great caution because tiny air bubbles underneath the tape can reduce the quality of the laser measurements and produce noisy signals. Depending on the transducer diameter, displacement-time histories at predefined points are measured using the laser vibrometer. The points are distributed based on a polar coordinate system, which is developed in this study (see appendix A), about the centre of the transducer. Table 3-3 illustrates the number of points scanned with laser for each transducer.

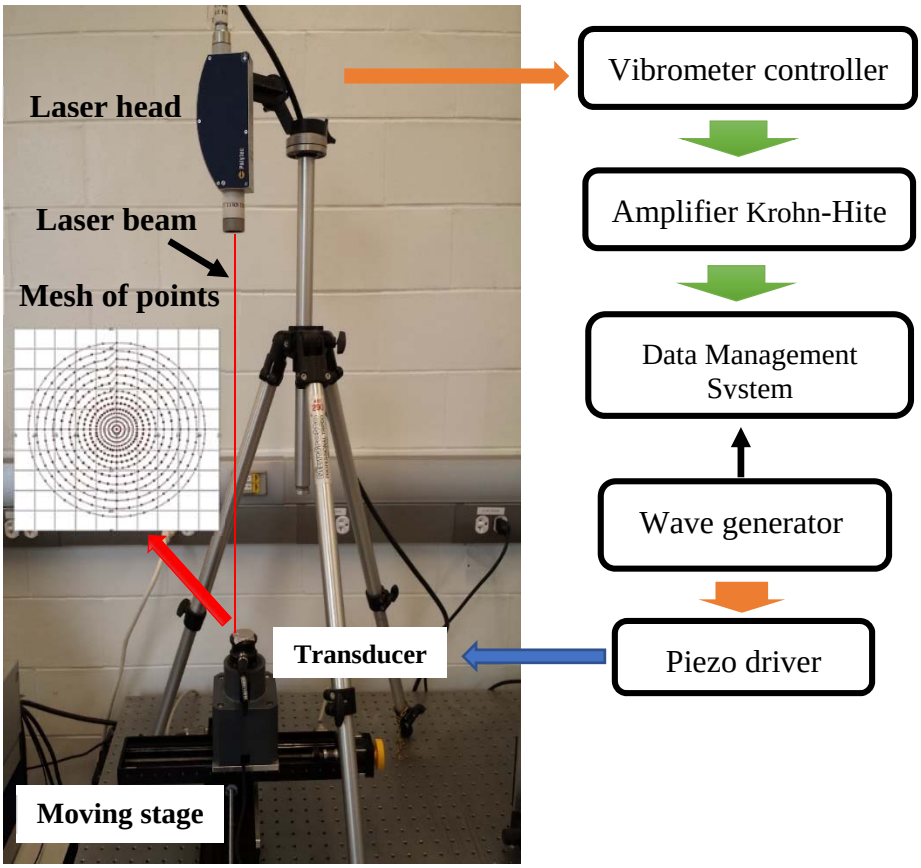

Figure 3-3: Instrumentation of Laser characterization technique.

3. Results and discussion

3.1 Effect of Coupling agent

Different coupling agents are used in ultrasonic testing depending on the condition of the specimen surface. Figure 3-4 illustrates the time signals obtained from testing aluminum and mortar cylinder specimens (10 cm diam.) using four common coupling materials, gel (Ultragel II), water, glycerin, and vacuum grease. In this figure, the gel provides better coupling results compared to other couplant materials. Therefore, the gel is selected for ultrasonic testing of concrete specimens in this project.

Table 3-3: Details of laser characterization parameters.

Transducer type	Nominal frequency (kHz)	Diam. (mm)	Points number	Excitation voltage (V)	Excitation frequency (kHz)	Average numbers
54O	54	50	521	5 10 100 150	60	100
54N	54	50	521	5 10 100 150	60	100
150N	150	28	329	10 100 150	150	150
250N	250	28	329	10 100 150	250	150
500Oy	500	38	441	100 200	500	250
500Ut	500	25	370	100 200	500	250
500MN	500	19	370	100 200	500	250
1MPO	1000	28	370	100 200	1000	250
1MSO	1000	28	370	100 200	1000	250
1MSN	1000	29	401	100 200	1000	250

The gel has many advantages. It can be applied easily on any surface regardless of the surface condition, it provides a thin coupling layer and it can be removed easily with water. Water is another good couplant, but its main drawback is rapid drying. This causes the waveforms to be altered quickly during the averaging. On the other hand, glycerin has similar characteristics to water with the advantage that it does not dry out during testing and it is nontoxic. The main disadvantages of the glycerin are that it aids fungal and bacterial growth and its high viscosity makes it difficult to clean from the test surface. Finally, the vacuum grease which is also called silicon gel, is preferable to utilize with very rough surfaces such as concrete that is not sanded. It

has also a drawback related to its high viscosity results in a relatively thick layer compared to other couplant agents. This makes it unattractive for measurements that needs high precision.

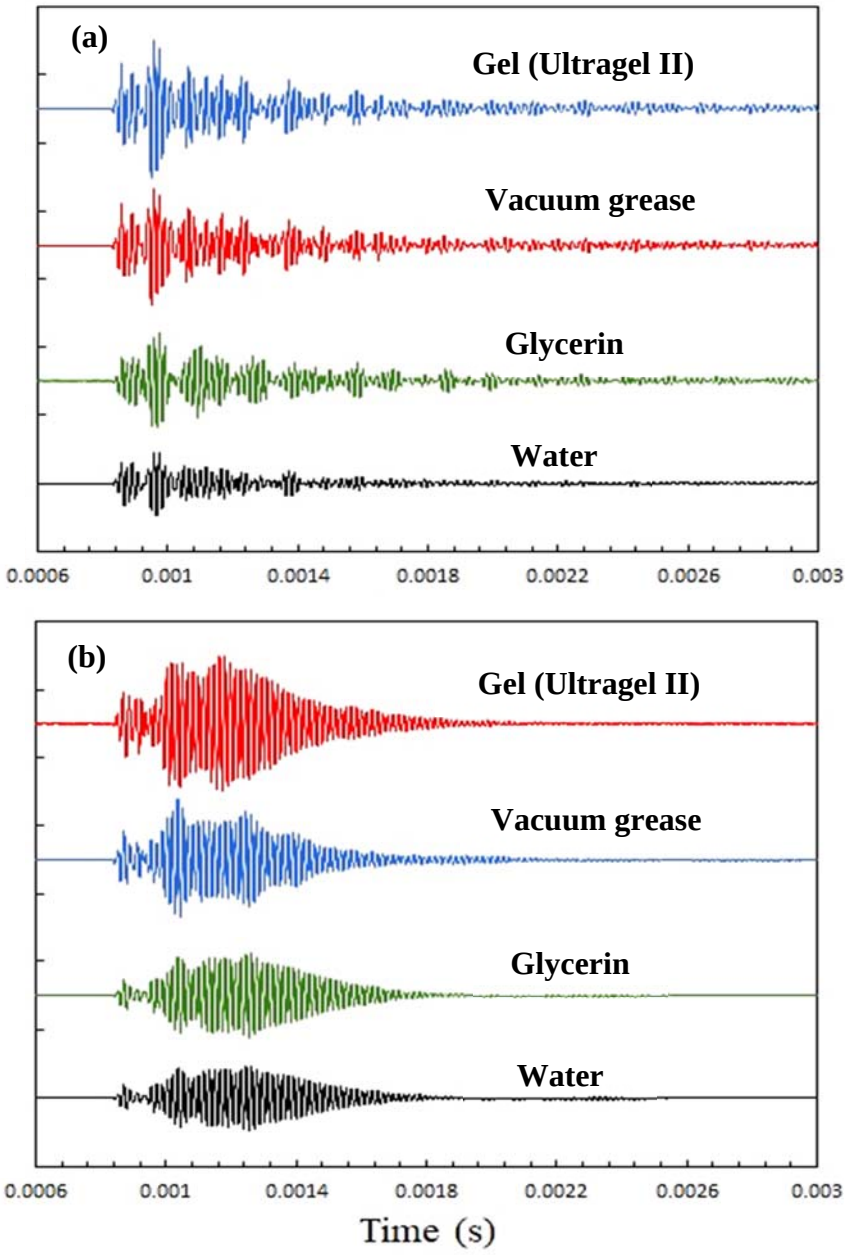

Figure 3-4. Influence of coupling on signal strength using a low frequency transducer (54 kHz). (a) signals of aluminum cylinder. (b) signals of mortar cylinder. Signal amplitudes are normalized to highest peak of gel coupling.

3.2 Determination of the time delay

As mentioned earlier, the plotting of arrival time results for each reference bar versus its height can be used to characterize the transducers. Figure 3-5 represents sample results of calibrating the 54 kHz transducer (L54-N) using aluminum and steel rods. Appendix A includes all figures of the characterized transducers used in this research. Each characterization was achieved using gel coupling agent. Table 3-4 shows the final results of the velocities and time delays obtained from characterization curves of the transducers.

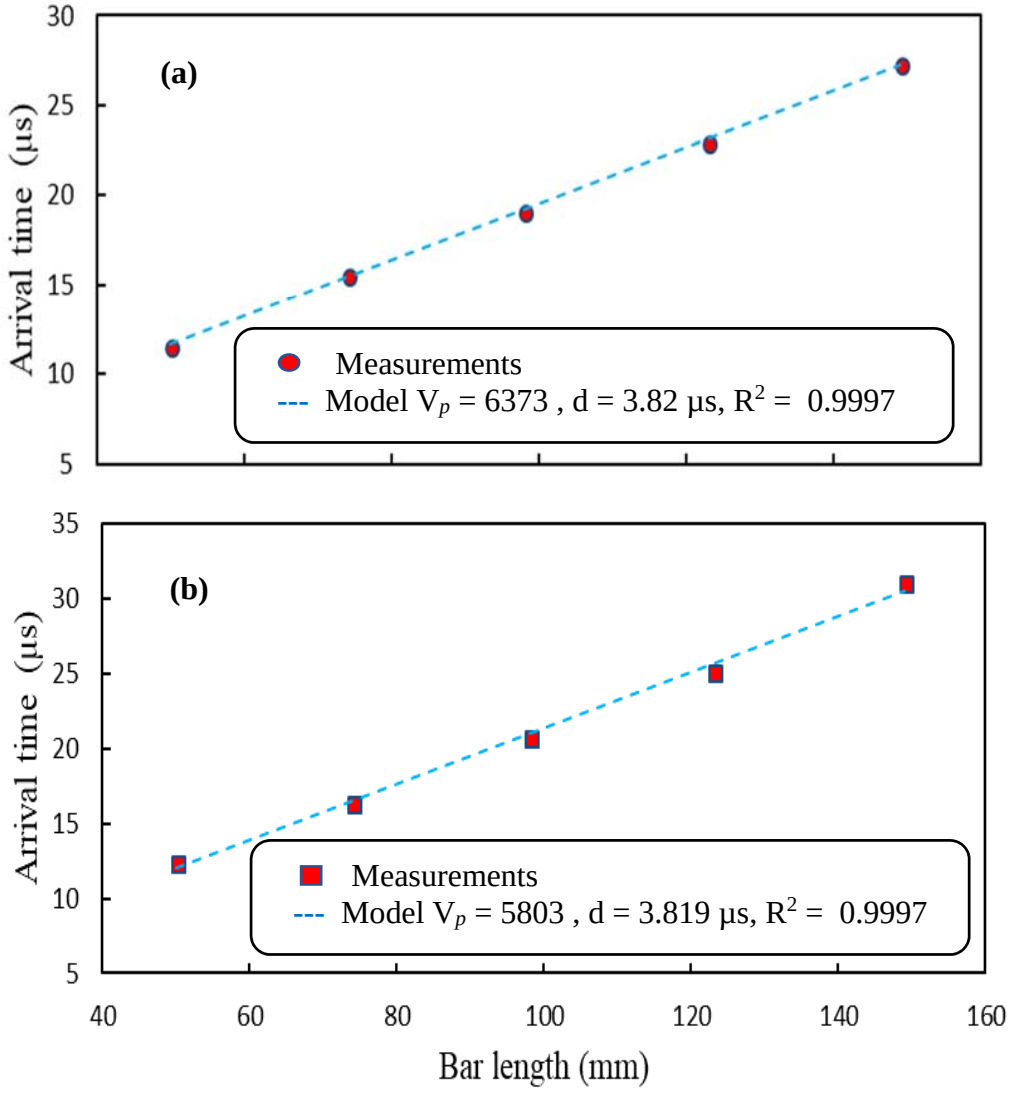

Figure 3-5. Characterization results of 54 kHz transducer (L54-N). (a) using aluminum rods, (b) using steel rods. where V_p is wave velocity (m/s), d is delay time, and R^2 is correction factor.

The delay time is also determined for the characterized transducers using the laser technique for comparison purposes. Table 3-4 shows the delay times calculated using different methods. The figure shows a good match between the two UPV methods results, while the laser technique produces higher values which may be a result of the laser electronics that convert pulse voltage into displacement history. However, for testing purposes and to ensure the consistency of ultrasonic measurements, the delay times of characterized transducers are utilized according to the testing program.

Table 3-4: Comparison of the delay times of the characterized transducers.

	Delay time (us)		
Transducer	UPV face to face	UPV bar reference	Laser
54O	1.87	1.98	2.05
54N	3.8	3.82	3.9
150N	1.63	1.65	1.75
250N	1.66	1.69	1.82
500Oy	0.74	0.764	0.85
500Ut	0.34	0.354	0.42
500MN	1.38	1.4	1.44
1MPO	0.42	0.413	0.44
1MSO	0.43	0.444	0.47
1MSN	0.14	0.14	0.15

3.3 Characterization using laser Doppler vibrometer

In any ultrasonic NDT of a component, the selection of ultrasonic transducer is a compromise based on the material properties and the parameters of interest. These features are necessary to identify the practical range of usable frequencies. For testing concrete in the field, the standard ASTM C597-16 recommends that the resonant frequency of piezoelectric transducers be in the range of 20 kHz to 100 kHz. This is due to the dispersive nature of concrete mixtures that attenuate the frequencies higher than this range.

Usually, the manufacturer of piezoelectric transducers provides the nominal frequencies which may not be necessarily indicate the centre or peak frequency that can be seen in the Fourier spectrum. Therefore, it is essential for NDT measurements to characterize the frequency response

of the piezoelectric transducer by measuring its response to a known applied voltage. For this purpose, the laser Doppler technique is selected in the current research to measure the response of the set of transducers based on direct measurement of transducer surface displacement histories under 50 volt excitation. Figure 3-6 illustrates the typical average frequency responses of all displacement histories measured on the wear plate of the 54 kHz transducers (54O & 54N) which are made by the same manufacturer (Proceq Inc.). The peaks of the corresponding Fourier spectra reveal that the resonance frequencies of these transducers are closer to 62 kHz and 51 kHz than 54 kHz which is the nominal frequency of these transducers.

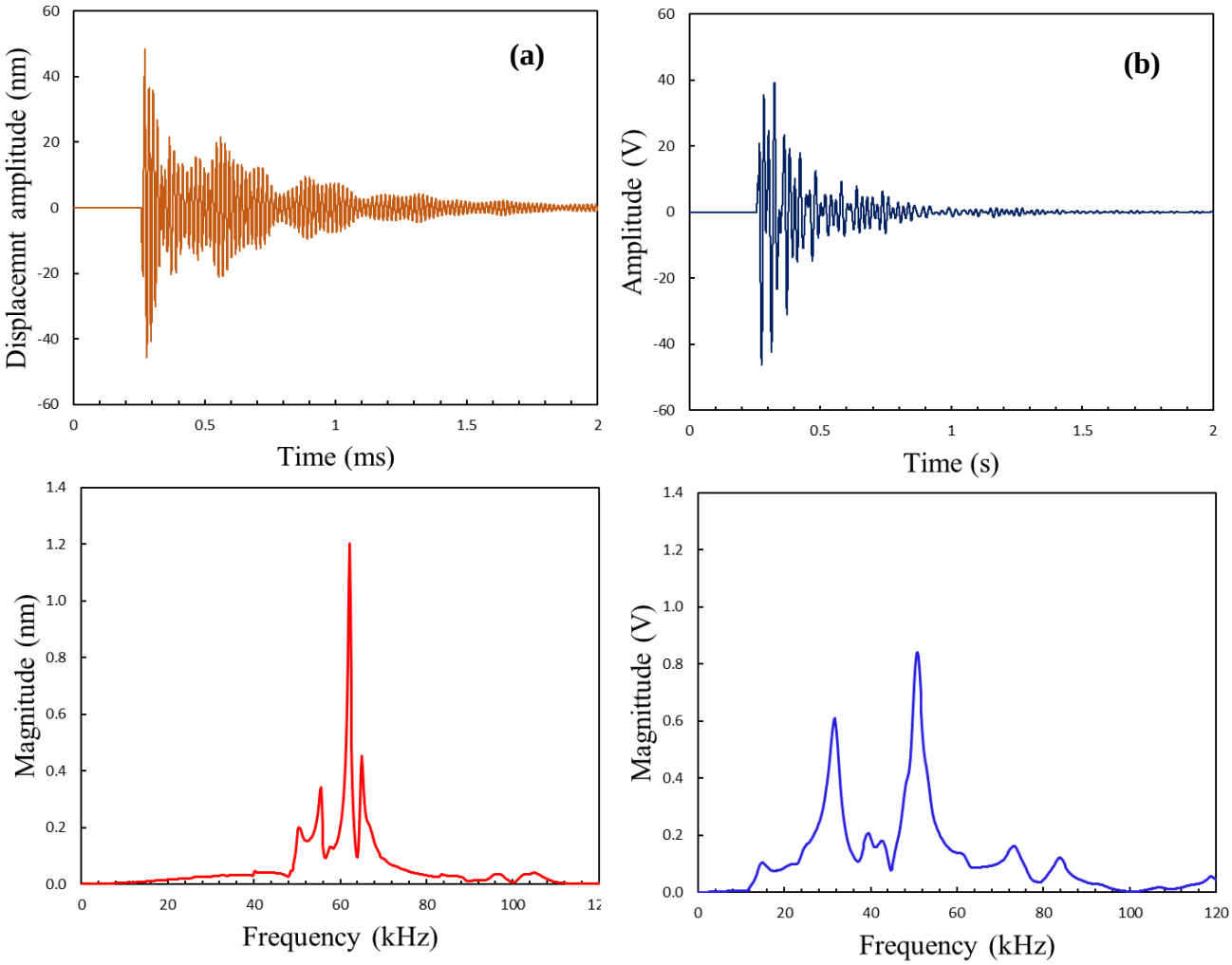

Figure 3-6. Typical characterization results of 54N and 54O transducers. (a) time displacement history of 54N and corresponding Fourier spectrum, (b) time displacement history of 54O and corresponding Fourier spectrum.

Even though, they are excited by the same input voltage, it is obvious that the new transducer (54N) shows more energy than the old one (54O). This can be attributed to the aging and use factors which has been recognized to influence the piezoelectric transducer response in NDT applications (Silk, 1984). Its is also known that newer transducers use improved piezo composite materials which are more efficient than the old materials. Similar findings are observed when these transducers are excited under different voltage inputs (5,10, 50, 100, and 150 V). Furthermore, the average displacement time histories of 150 kHz and 250 kHz transducers show resonance frequencies lower than nominal values and close to 144 kHz and 244.6 kHz, respectively (Figure 3-7).

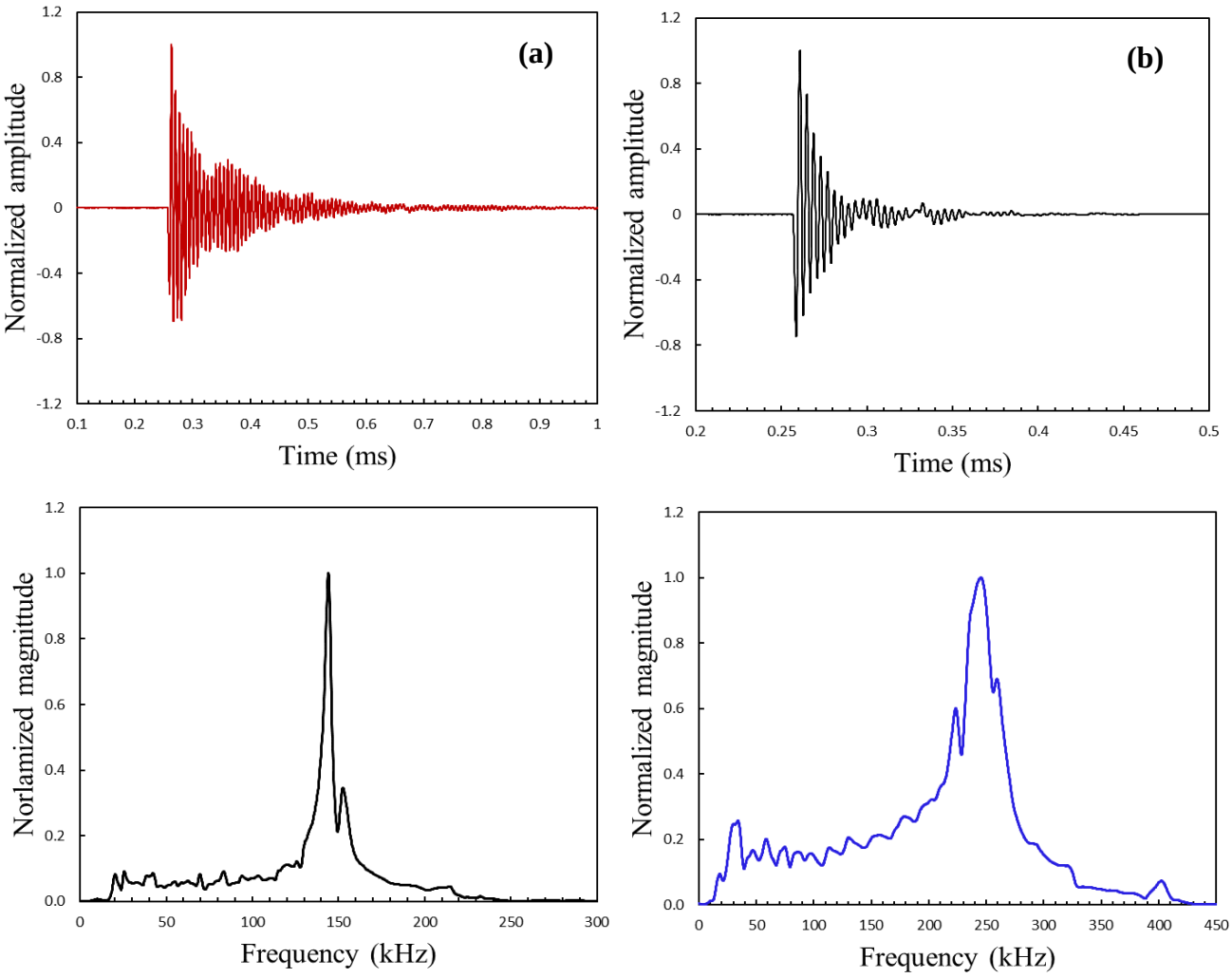

Figure 3-7. Typical characterization results of 150N and 250N transducers. (a) displacement time history of 150N and corresponding Fourier spectrum, (b) displacement time history of 250N and corresponding Fourier spectrum. Pulsed with 100 volts.

Figure (3-8) shown typical displacement time history and corresponding Fourier spectra of high frequency transducers 500Oy and 1MSN excited with 100 input voltage. From this figure, the resonance frequency identified for 500 kHz is higher by 4% that the value provided by the manufacturer, while the 1MHz shear transducer reveals less resonance frequency by 4%. These findings highlight the importance of using laser characterization to characterize the response of high frequency transducers for ultrasonic measurements.

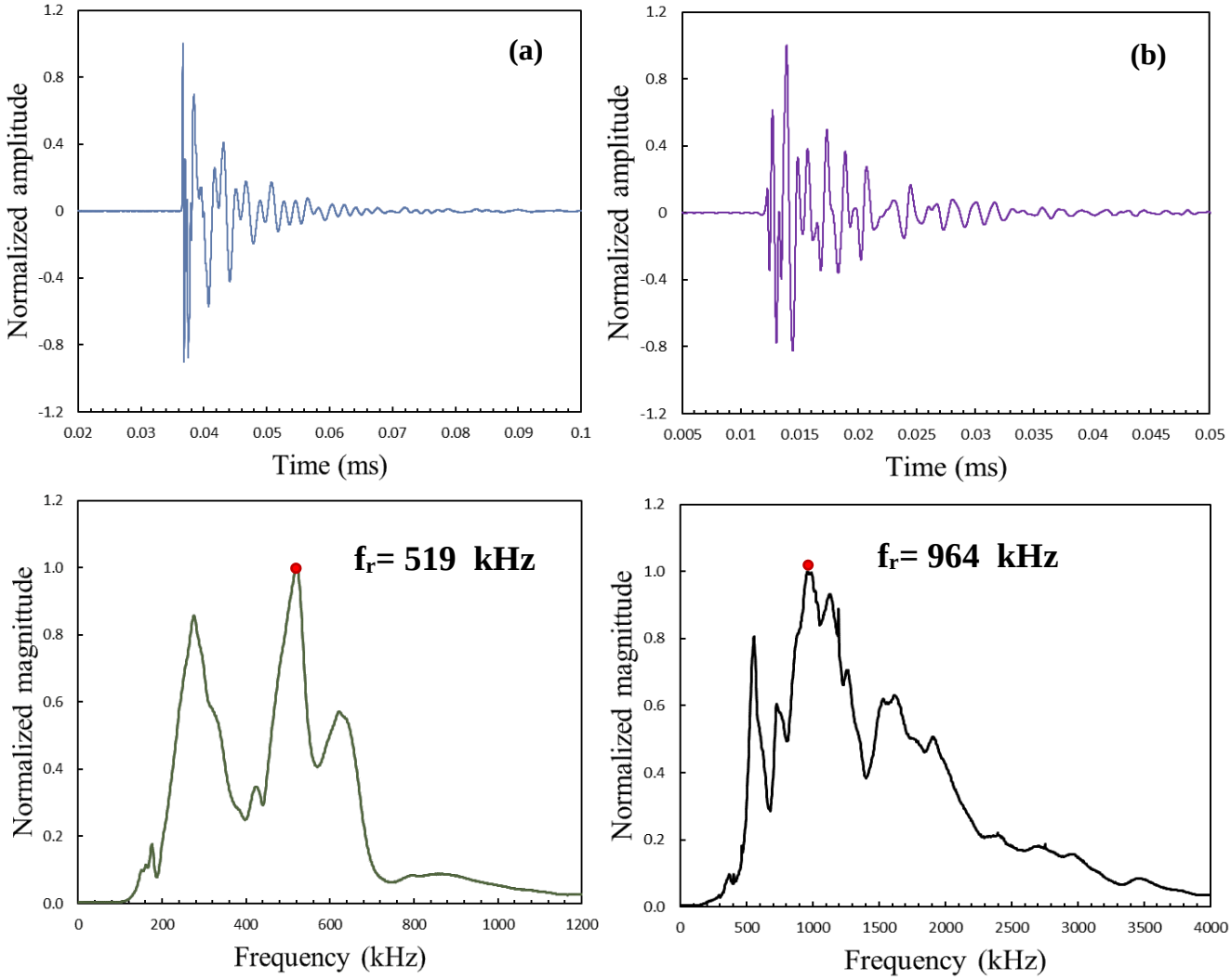

Figure 3-8. Typical characterization results of 500Oy and 1MSN transducers. (a) displacement time history of 500Oy and corresponding Fourier spectrum, (b) displacement time history of 1MSN and corresponding Fourier spectrum. Pulsed with 100 volts. f_r is resonance frequency.

Table 3-5 summarizes the comparison between resonance frequencies observed for all transducers characterized in this study with nominal data provided by the manufacturer. To identify the frequency range corresponding to the maximum vibration energy, its necessary to characterize the frequency response and later utilize these frequencies for testing specimens. Accordingly, the resonance frequencies of characterized transducers that were obtained using laser Doppler vibrometer measurements are employed in the subsequent tests of this research.

Table 3-5: Comparison of delay times of characterized transducers.

	Frequency (kHz)	
Transducer	Nominal	Resonance
54O	54	51
54N	54	62
150N	150	144
250N	250	244.6
500Oy	500	483.4
500Ut	500	519
500MN	500	513.6
1MPO	1000	1017
1MSO	1000	973
1MSN	1000	964

On the other hand, scanning the surface of the transducer with the laser allows us to obtain the displacement time histories which are necessary to observe the vibration modes under input excitation. For example, Figure 3-9 shows vibration modes of the 54 kHz transducers excited with 100 V input. By examining the vibration modes of both transducers, it is clear no flat response can be identified as its usually assumed with this kind of transducer which is used widely in concrete testing. The energy is concentrated primarily around the centres of transducers. An interesting result of the laser characterization is that it provides a novel procedure to analyse the vibration pattern of the transducer to examine the linearity between input voltage and observed displacement.

Figure 3-10 demonstrates the vibration modes of two types of high frequency transducers; 1MHz primary wave (1MPO) and 1MHz shear wave (1MSN). The behaviour of both transducers is clearly different in which a flat pressure mode is identified in the vibration response of the 1MPO

transducer, while mix of vibration modes is noticed with the 1MSN. The vibration mode results of other transducers obtained from laser measurements can be seen in appendix A.

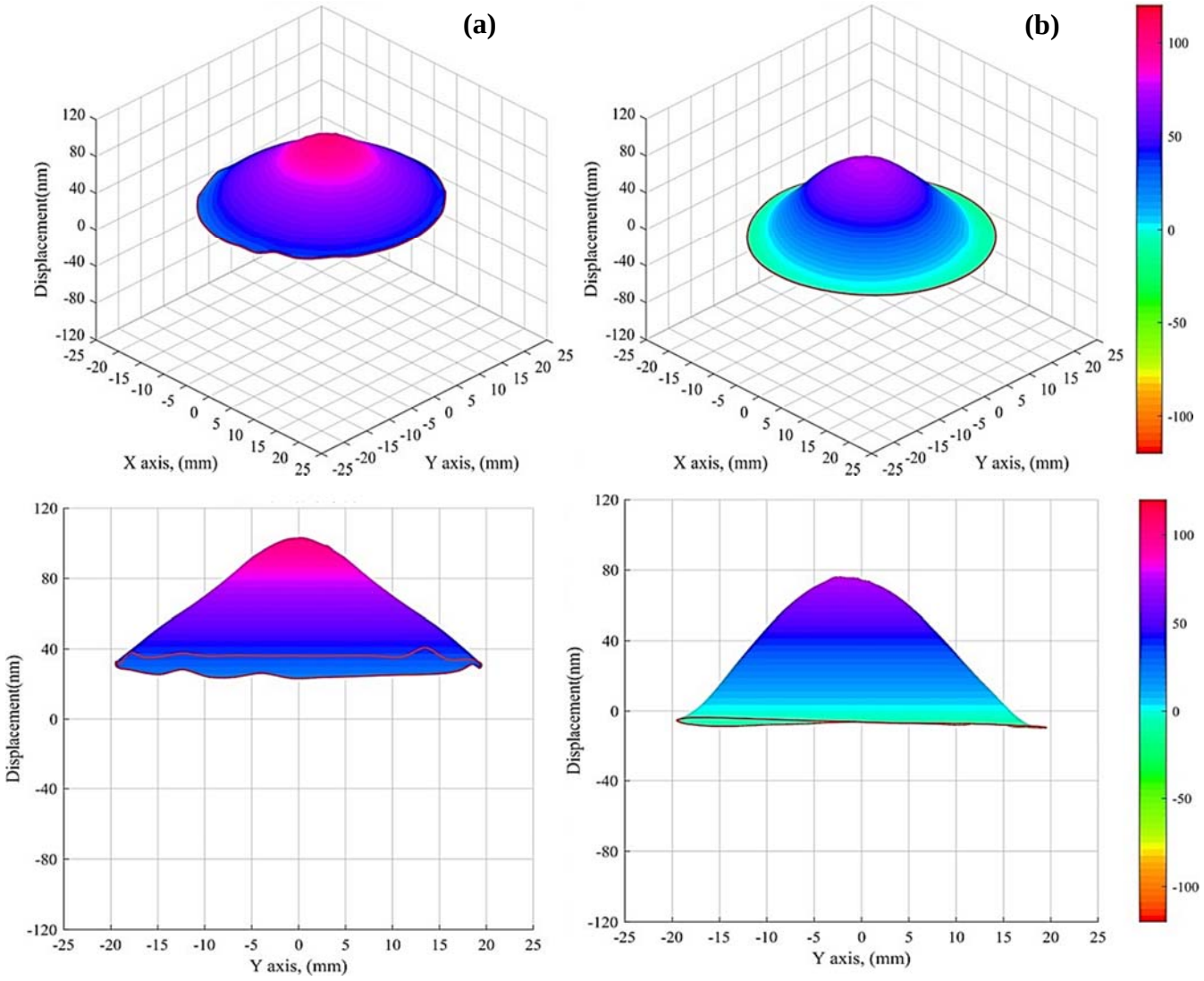

Figure 3-9. Typical vibration P-modes of 54N and 54O transducers. (a) perspective and side views of 54N, (b) perspective and side views of 54O.

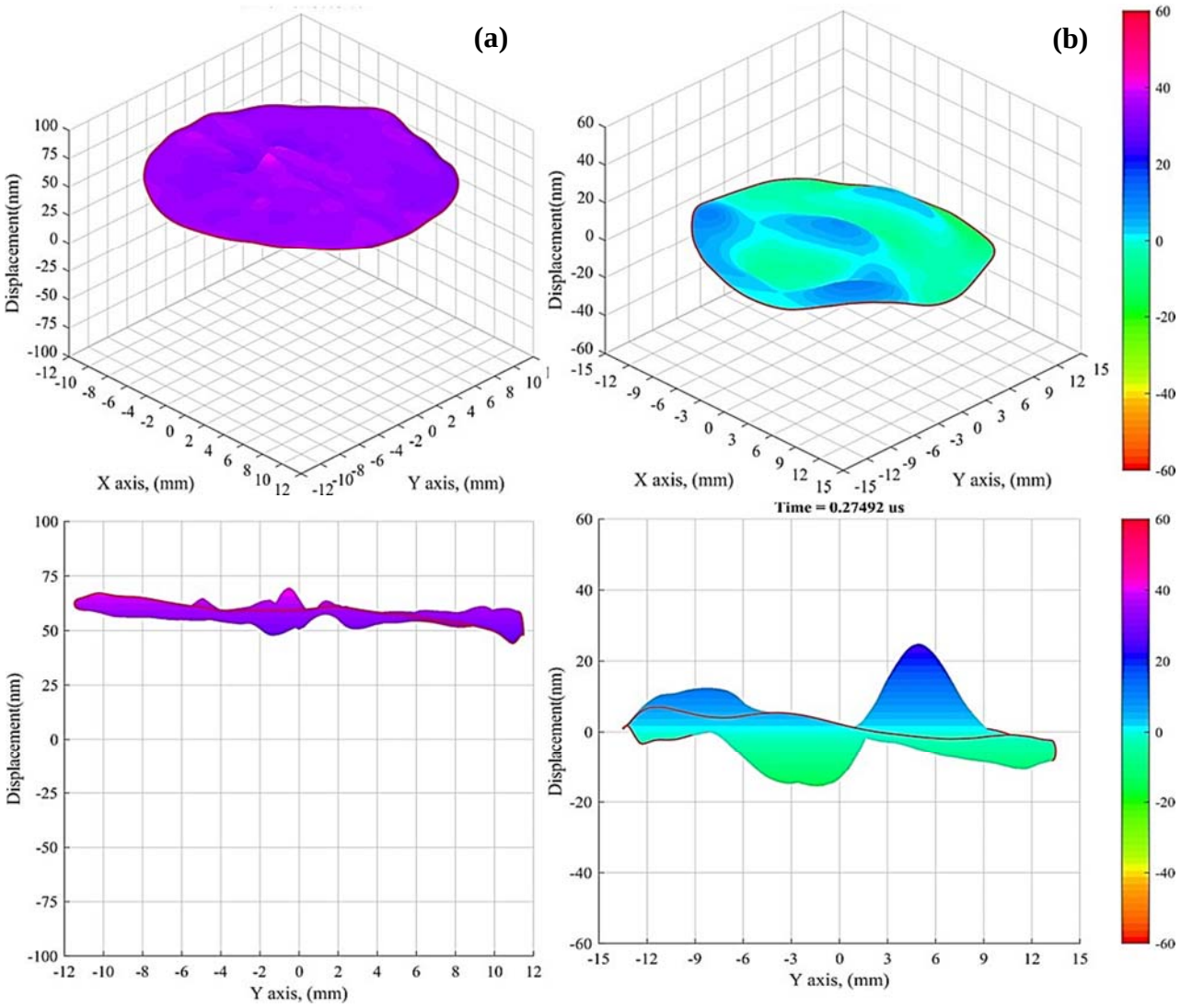

Figure 3-10. Typical vibration modes of 1MPO and 1MSN transducers. (a) perspective and side views of 1MPO vibration, (b) perspective and side views of 1MSN vibration.

3.4 Summary

In this chapter, the characterization measurements were described for different types of piezoelectric transducers using conventional methods (face-face and reference bar) to determine the delay time and laser Doppler vibrometer method to identify the frequency response of the transducers. In addition, the selection of the couplant for laboratory testing was described. These procedures are necessary to ensure reliable measurements from the ultrasonic testing.

The laser characterization of low frequency transducers did not confirm the flat response of the transducer surface, hence, the nominal frequency given by the manufacturer can not be adequate for the characterization of transducers response. Also, the results of low frequency transducers exposed that resonance frequencies of these two types of transducers deviate from the nominal values reported by the manufacturer by around (4%-15%). The resonance frequencies of the characterized transducers obtained from laser measurements are identified to be used in subsequent ultrasonic testing in this research project.

Chapter 4: Fracture evaluation in homogenous medium[1]

This chapter introduces the methodology configuration that used to evaluate fracture propagation in a homogenous (PMMA) specimens. Description of the material and instrumentation that used in the experiments tests are also presented.

4.1 Introduction

Fracture propagation is typically studied to better understand material failure from crack nucleation, growth, and coalescence. Macroscale physical tests have been carried out in various homogenous and heterogeneous materials, such as concrete, metals, ceramics, and, to a lesser extent, plastics to study fracture propagation (Ayatollahi et al. 2015; Haeri *et al*. 2013; Jiefan *et al*. 1990; Yang 2011). Standard procedures, such as the three-point test and four-point tests, are used to characterize fracture toughness of materials like concrete (Gerstle 2010; Tattersall and Tappin 1966; ASTM 2010). In metals, the tear test is a standard procedure to measure fracture toughness , and the Charpy test is also widely used (Tattersall and Tappin 1966). However, unstable fracture growth remains a major limitation of these test procedures; fracture propagation is unstable and only peak-load measurements become meaningful. On the other hand, in rock mechanics, the generation of tensile stresses during compressive loading has been used for many years to evaluate fracture toughness (Ulusay, 2015). Yang (2011), and Haeri *et al*. (2013) tested sandstone and rock-like specimens in a cylindrical mold containing two artificially created flaws to study fracture coalescence under uniaxial compressive load. Ayatollahi *et al*. (2015) used polymethylmethacrylate (PMMA) specimens to study fracture development in brittle material with a V-notch as a stress concentrator within a specimen under compression; a fracture developed from the tip of the notch and eventually reached the other end of the specimen. All these were attempts to quantitatively observe fracture propagation under quasi-static conditions. In the present study, a new more stable and controllable fracture propagation test method (Gomez Rodriguez *et al*. 2016) is used to evaluate the impact of a fracture growing along a weak, planar fused interface between PMMA specimens on the propagation of an ultrasonic wave front. In this configuration, the effect of a fracture on the propagation on an ultrasonic wave front (velocity and attenuation)

[1] The contents of this chapter incorporate with a paper that has been submitted for publication: Fartosy, Gomez Roderiguez, Cascante, Basu, & Dusseault. "Effects of a Fracture on Ultrasonic Wave Velocity and Attenuation in a Homogeneous Medium" . Submitted to the ASTM Journal of Geotechnical Testing. Submission date: July 3rd,2018.

can be readily studied. This simple model can represent any material that exhibits Mode I fracture propagation, such as polycrystalline rocks, ceramic materials, concrete, and mortar.

Wave propagation methods are commonly used in nondestructive testing (NDT) of materials such as rock, soil, and concrete. At low strains, wave propagation characteristics depend on the elastic material properties (Santamarina *et al*., 2001; Breysse, 2012; Slawinski, 2010), the structural details, and spatial distributions of the different materials composing the medium as well as the characteristic frequency of the wave. Among the NDT methods, the ultrasonic pulse velocity (UPV) method is most commonly used in practice (ACI 228.2R-13, 2013; Bungey *et al*., 2006), in medicine, chemistry, physics, biology, and engineering. The UPV technique is generally used in accordance with the ASTM C 597-16 and American Concrete Institute standard ACI 228.2R-13 to assess the quality of natural rocks and concrete elements (Hertlein, 2013; Malek and Kaouther, 2014), to quantify environmental impacts on geomaterials and concrete (Chen *et al*., 2015; Duan *et al*., 2011), and to determine material elastic properties (Ensminger and Bond, 2011).

Although wave velocity can be reliably used under certain conditions, it is not well-suited to identify material damage generated from loading or environmental conditions (Kirlangic, 2013; Rodriguez Roblero, 2017). In the case of small-scale internal damage (e.g. micro-fractures), wave attenuation is a more reliable parameter (Basu and Aydin, 2005; Chai *et al*., 2011; Kirlangic, 2013). Wave attenuation is sensitive to heterogeneities at many scales; it has been used to characterize defects and heterogeneities in different materials (Aggelis *et al*. 2009; Chai *et al*. 2011; Yim *et al*. 2012; Fereidooni and Khajevand, 2018). As a further development, Gaydecki *et al*. (1992) proposed frequency-dependent attenuation studies to determine aggregate particle size distribution in a concrete specimen; therefore, wave attenuation as function of frequency might be used to assess inhomogeneities in rocks. The relationship between wave amplitude and mechanical damage is studied by Nogueria and Willam (2001) to estimate the evolution of micro-cracks in concrete. Philippidis and Aggelis (2005) reported that wave velocity is significantly affected by aggregate quantity, while the attenuation is more influenced by aggregate geometry. Chaix et al. (2003) evaluated thermal damage (micro-cracking) in concrete from wave attenuation data. Cerrillo *et al*. (2014) used both ultrasonic P- and S-waves on granite specimens to investigate the feasibility of wave attenuation in quantifying the physical-mechanical properties of the medium.

They pointed out the reliability of wave attenuation in assessing properties such as apparent density, compressive strength, and dynamic elastic parameters.

The evolution of wave velocity and attenuation during UPV tests is used in this study to monitor a thin fracture growth in PMMA under controlled laboratory conditions, envisioning future applications to monitor fracture growth in geotechnical, geological, petroleum, and mining engineering. In ultrasonic testing, transducer characteristics play an important role in evaluating the internal conditions of the medium being tested (ASTM-E1316). For this purpose, a laser vibrometer is used to characterize the ultrasonic transducer used in this study.

Typically, in UPV testing the detection of damage depends primarily on the determination of the travel time (e.g. wave velocity), which it is not always a straightforward and practical measurement. Because, wave attenuation can cause the first arrival to be missed during the analysis. For example, the amplification of a typical time signal from this study (results section) can lead to a different determination of travel times and thus wave velocities (Fig. 1). In the original signal (e.g. no amplification), the arrival time is erroneously selected because of wave attenuation; whereas in the amplified signal the real arrival time can be readily determine. This effect is more significant if an automatic procedure is used (Finas *et al*., 2016). Despite the use of UPV testing over several decades (Hertlein, 2013), there is no data available on the use of wave attenuation analysis to monitor fracture growth in a brittle material such as rocks, ceramics, concrete, and mortar. A new methodology is used in this study to fabricate PMMA specimens to develop a stable and controllable fracture as a function of the compressive load. The results demonstrate that fracture growth in brittle materials can be monitored effectively by simultaneously measuring changes in wave velocity and wave attenuation for specific frequency bandwidths.

4.2 UPV Test Background

Ultrasonic waves can be generated by different sources like piezoelectric, laser, electromagnetic, and mechanical transducers (Ensminger and Bond 2011). In a homogenous specimen, the pulse velocity V_p is calculated as (ASTM C 597-16):

$$V_p = \frac{L}{T} \tag{4-1}$$

where L is the distance between the centers of the transducers and T is the pulse travel time.

The wavelength λ and frequency f are related to the pulse velocity as

$$V_p = f\lambda \tag{4-2}$$

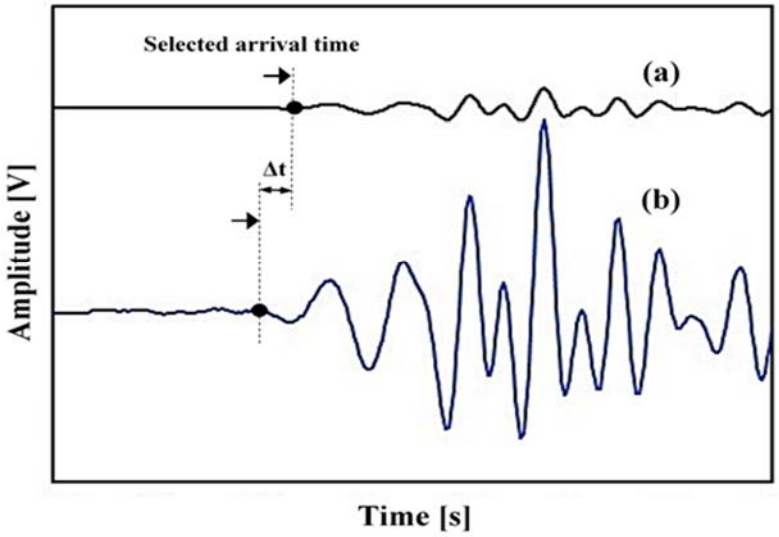

Figure 4-1. Effect of amplification in the determination of travel times. (a) original time signal, (b) amplified signal by a factor of 10. Δt represents the error in the arrival time due to wave attenuation.

The selection of the transducer frequency range can significantly influence the results. The defect size should be at least in the order of one wavelength to be detected by the propagating wave front (Krautkrämer and Krautkrämer, 1990). Wave attenuation arises from different mechanisms such as wave spreading (increase in the size of the wave front), scattering (wave reflection, refraction, and diffraction due to changes in the mechanical impedance of the medium), absorption (material energy dissipation e.g. heat, inelastic deformations) and mode conversion (e.g. energy split between compressional and shear waves) (Aki and Richards, 1980). Attenuation, manifested as a change in wave amplitude, is commonly represented by an exponential decay (Ensminger and Bond, 2011). In this study, the absolute attenuation is not measured, instead the relative change in wave amplitude as a function of frequency is used to represent the relative wave attenuation; which includes changes in amplitude because of geometrical and material effects. The normalized change in spectral area (SA_d) with respect to the spectral area in the intact condition (SAo) is used to evaluate the relative wave attenuation in a given frequency bandwidth (A_z);

$$A_z = \frac{(SA_o - SA_d)}{SA_o} \tag{4-3a}$$

where SA_o and SA_d represent the areas of the Fourier spectra in the selected frequency bandwidth for the intact and fractured conditions, respectively, and it is computed as

$$SA = \int_{f1}^{f2} FFT(f)df \tag{4-3b}$$

where FFT(f) is the Fourier spectrum of the corresponding time signal. The minimum frequency (f1) and the maximum frequency (f2) for the integration are selected based on the frequency range that shows more sensitivity to the presence of the fracture. This frequency range is selected after the completion of the tests. There are several mechanisms of wave attenuation. Wave spreading is simply geometrical attenuation as a wave front increases out from the source, scattering is the reflection, refraction, and diffraction of waves at acoustic impedance changes, and absorption is the conversion of wave energy to other forms of energy such as heat. In addition, mode conversion also occurs at mechanical impedance changes where a part of the wave energy is split into different modes (e.g. p-wave, s-wave, surface waves) along different ray paths (e.g reflected and refracted converted modes). In the case of wave spreading, scattering, and mode conversion, the total wave energy is the same; however, the wave amplitude changes because of energy splitting. In wave scattering, waves are reflected-refracted (relative large wavelengths) and diffracted (relative small wavelengths) at changes in the mechanical impedance of the medium. On the other hand, in mode conversion wave amplitude changes because of the generation of additional propagation modes at interfaces (e.g. p-waves into shear waves). All these attenuation mechanisms are included in the results of this study; however, wave scattering is the predominant mechanisms because of the presence of the fracture as the specimens are relatively small to induce significant absorption and mode conversion.

4.3 Specimen Preparation

The material chosen for the study, PMMA, is a transparent (homogenous) material permitting visual fracture growth tracking in real time along the weakly bonded interface being tested. A homogenous material in the context of ultrasonic pulse velocity (UPV) testing refers to materials

in which any inhomogeneity is smaller than the main wavelength of the signal. PMMA exhibits elastic and plastic deformations in a brittle manner, is a widely used and well understood material for basic studies of fracture (Ayatollahi *et al*., 2015), and has been used previously as an analogue material to study rock (Rubin, 1983). Further, PMMA can anneal itself through thermal bonding when subjected to high pressure and temperatures over a given period of time (Yang, 2011), thereby providing the possibility of creating specimens under conditions or scenarios that produce a specific bond strength of an interface.

Specimens are prepared using two identical solid PMMA rectangular prisms, 152.4 mm long, 101.6 mm wide, and 25.4 or 12.7 mm thick (Figure 4-2a), fused along the long and narrow edges by heating under stress for a set time. A hole is drilled normal to the interface as a controlled stress concentrator. Figure 4-2b illustrates the growth of a fracture along the partially fused interface as the axial compressive load is increased. Seventeen PMMA specimens with lightly fused interfaces and two intact PMMA specimens are prepared for this study. The seventeen specimens with interface are subjected to different pressure, temperature and time (**Error! Not a valid bookmark self-reference.** 4-1) to produce different levels of bonding. Out of the seventeen fused specimens, seven are 12.7 mm (1/2 in) thick and ten are 25.4 mm (1 in) thick.

In order to create a fused interface, the procedure described by Gomez Rodriguez *et al.*, (2016) is followed. Two flat-milled PMMA prisms are placed in a steel jig that restrains out-of-plane movement and allows normal compressive stresses to be applied. The jig is placed in an oven, a steel bar is used to distribute the load evenly, and a dead weight load is applied to the steel bar. This set up is heated using tow temperature sets 150^{o} C and 177^{o} C. After a prescribed set time required to attain the desired degree of interface bonding, the specimen is cooled down in the oven under the applied load. The specimens are then milled to final dimensions of 150 × 100 × 12.7 or 25.4 mm^{3}. A 6.3 mm stress concentrator hole is drilled symmetrically through the fused interface (Figure 4-2b). At this point, an ultrasonic test is also performed to assess the impact of the hole on the acoustic signals.

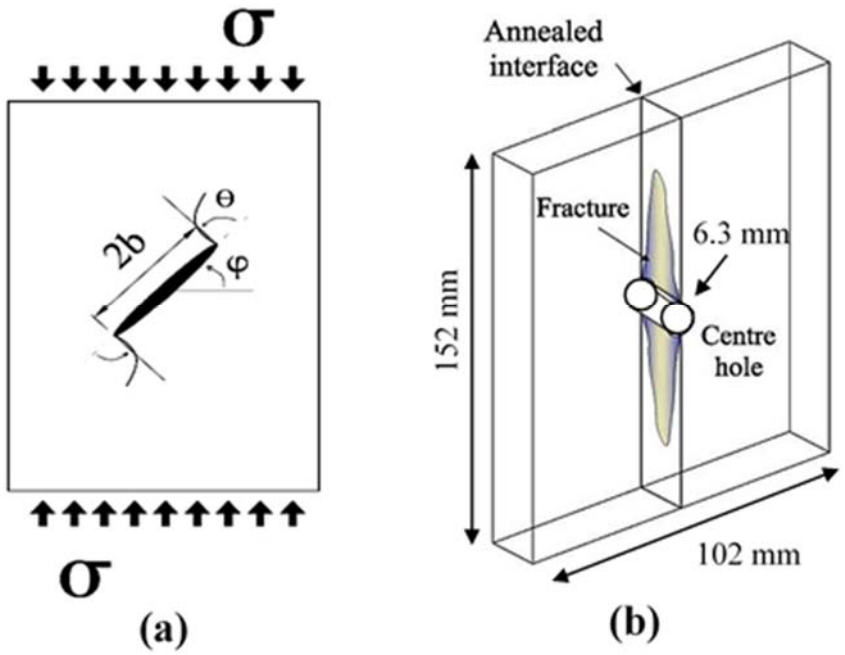

Figure 4-2. (a) Schematic of a general fracture during a compression test, (b) schematic of PMMA specimen, hole and fracture during a compression test.

TABLE 4-1. List of PMMA specimens tested and their corresponding bonding conditions

Specimen #	Type	Thickness (mm)	Numbers	Fabrication conditions of PMMA		
				Temperature (^oC)	Duration (hr)	Pressure (kPa)
PA-(1-4)	Fused	25.4	4	150	6	2
PA-(5-8)	Fused	25.4	4	150	6	12
PA-(9-10)	Fused	12.4	2	150	6	6
PA-(11-13)	Fused	12.7	3	150	6	12
PA-(14-15)	Fused	12.7	2	177	6	6
PA-(16-17)	Fused	12.7	2	177	6	12
PS-(1-2)	Solid	25.4	2	-	-	-

4.4 Test Setup

All PMMA specimens are tested under compression in an MTS (322) frame (displacement controlled at 0.01 mm/min (Figure 4-3), where the displacement and corresponding load are recorded continuously. The UPV setup consists of two piezoelectric transducers, a function generator, a digital oscilloscope, and a computer (Figure 4-4). Two piezoelectric transducers

(frequency bandwidth 20 to 100 kHz, nominal resonance frequency 54 kHz, 50 mm diameter) are used in this study. They are placed on opposite sides of PMMA specimens, using silicone grease and Loctite super glue for consistent coupling (Krautkrämer and Krautkrämer, 1990). An ultrasonic square pulse is emitted as electrical excitation; calculations in time and frequency domains are used to evaluate changes in wave velocity and wave attenuation (Krautkrämer and Krautkrämer, 1990). 3D printed transducer holders are built to maintain a constant contact pressure on both transducers. Vacuum grease is applied between the transducers and PMMA surfaces to improve the coupling and reduce signal losses. The electrical excitation consisted of a single cycle square pulse generated by the function generator, with a nominal resonance frequency of 54 kHz and amplitude of 10 volts.

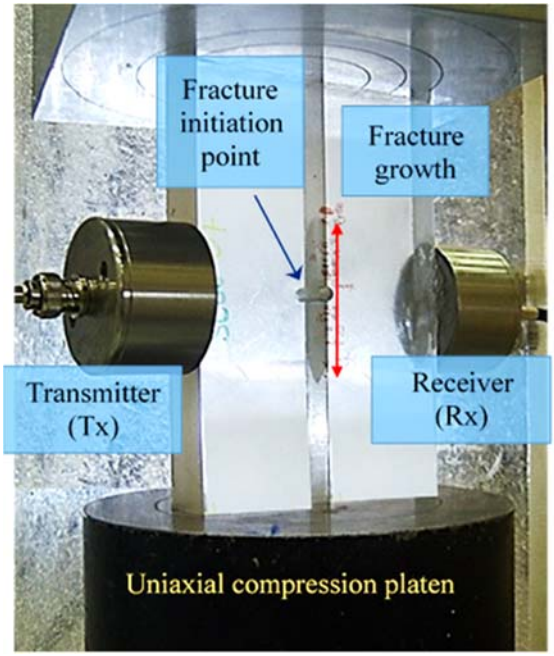

Figure 4-3. PMMA specimen (152 mm x 100) with a hole at the centre, fraction location, and transducers glued to the specimen in a uniaxial compressive test. Displacement rate 0.01mm/min.

To characterize the frequency response of the transducers, a state-of-the-art laser vibrometer (Polytec, 2013) is used to measure their actual response to an input square voltage pulse (Figure 5). The frequency of the square pulse is selected to match the nominal frequency of the transducer. To improve the laser reading, retroreflective tape is attached to the vibrating surface of the tape is placed carefully to avoid any trapped air bubbles underneath.

To minimize the effect of random noise and enhance signal quality, 16 readings are averaged for each UPV measurement. The time signal is then converted to a frequency spectrum for each signal using the fast Fourier transform (FFT). Figure 4-6 shows typical average plots in time and frequency domains, with standard deviations of 5.7×10^{-1} mV and 4.37×10^{-3} mV, respectively. The inherent time delay of the electronic system is determined using the face-to-face method with standard calibration specimens such as aluminum and steel bars of different lengths.

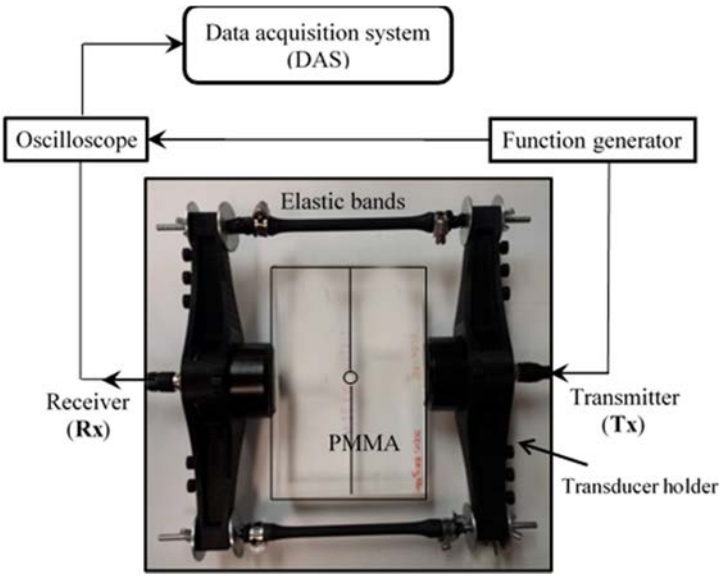

Figure 4-4. Ultrasonic pulse velocity instrumentation setup with 3D printed holders.

The measured time delay of the system (2 μs) is subtracted from the measured arrival times to calculate the wave velocity. Time windows are used to reduce the effect of wave reflections in the calculation of the Fourier spectra. Figure 6 shows typical results of applying two Tukey windows with different time falloffs (Alexander and Poularikas, 1998).

4.5 Testing Methodology

The seventeen fused PMMA specimens are tested under compression; and ultrasonic measurements are taken at the end of the fracture propagation and for selected specimens during the fracture propagation. Table 4-2 summarizes the testing programme for the different PMMA

specimens. At discrete load increments, the fracture length is recorded and UPV measurements are taken. Final UPV readings are taken once the maximum fracture length is reached. Time signals are sampled at 1 MS/s 1 (total of 4000 samples per signal). P-wave velocities are computed by manually selecting the first arrival times (equation 4-1).

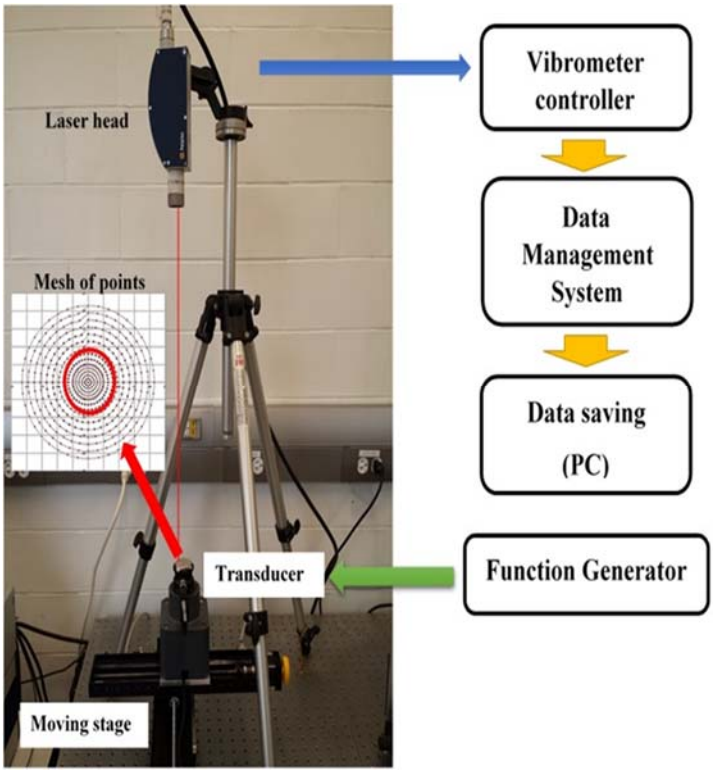

Figure 4-5. Laser vibrometer calibration setup.

Ultrasonic measurements are performed for three specimen conditions. First, specimens without fracture are tested (intact condition, case A). Then, specimens with a small hole to function as stress concentrator are tested (with hole condition, case B); and finally, the specimens are tested after loading when a fracture has been generated (fractured condition, case C). Four specimens (two fused and two made of a solid block) are also tested during the fracture growth, while subjected to uniaxial compression under strain-controlled conditions. All specimens showed fracture initiation at the stress concentrator hole, the fracture then propagated symmetrically with increased uniaxial displacement. Ultrasonic measurements are taken in four specimens during fracture propagation. The ultrasonic transducers are glued on the sides of the specimens after the centre hole was drilled but prior to application of load (Figure 4-3). These transducers remained

attached during loading and unloading stages until the maximum load was reached. The frequency spectra of the transducer's response are computed from the displacement time histories measured using the laser vibrometer in 121 points around the center of the transducer in an area of 50 mm^2.

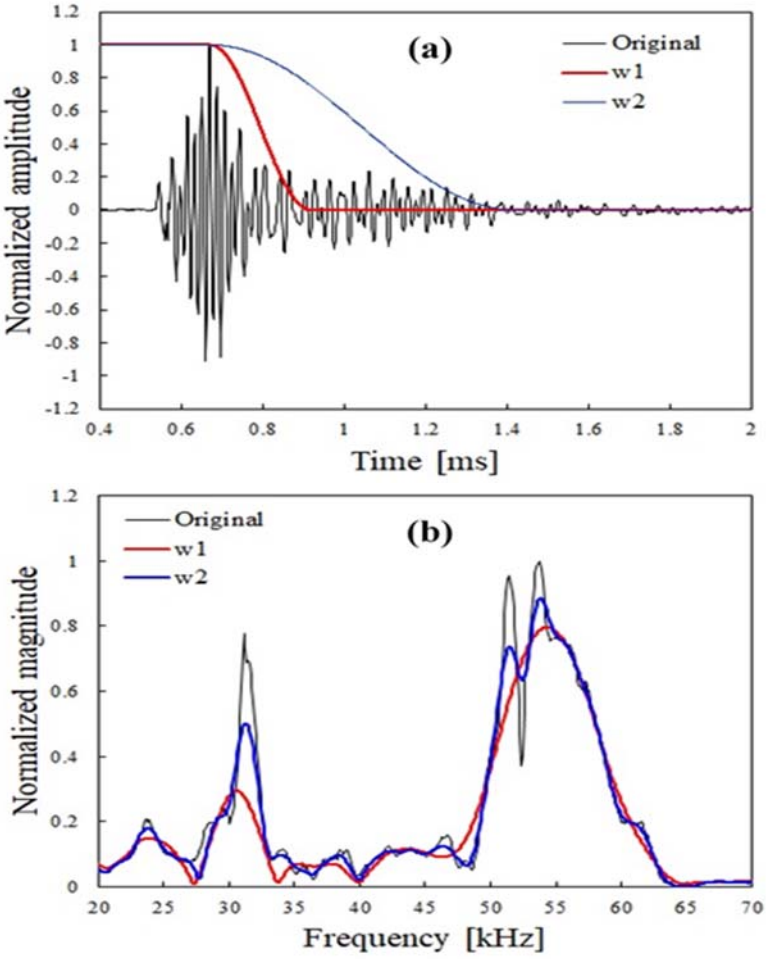

Figure 4-6. Typical time and Fourier spectra plots: (a) time signal with two selected time windows w1, and w2 (Tukey windows with time decay exponents **0.1** and **0.3** respectively, Alexander and Poularikas, 1998), (b) Fourier spectra of original and windowed signals.

4.6 Results and Discussion

4.6.1 Laser calibration of the transducer

Figure 4-7 illustrates the averaged time signal and corresponding Fourier spectrum for 121 point-measurements taken using the laser system (Figure 4-5). The displacement Fourier spectrum reveals that the resonance frequency of the transducer is 51 kHz; which is close to the 54 kHz

nominal frequency provided by the manufacturer (Proceq, 2017). On the other hand, the transducer shows another resonant peak at 30 kHz. This information is important for the analysis of the range of wavelengths present in the measurements (equation 4-2).

TABLE 4-2. Details of different tests performed on PMMA specimens.

Specimen #	Type	Testing configuration	Testing method
PA-(1-4)	Fused	A,B,C	UPV
PA-(5-8)	Fused	A,B,C	UPV
PA-(9-10)	Fused	A,B,C	UPV
PA-(11-13)	Fused	A,B,C	UPV
PA-(14-15)	Fused	A,B,C	UPV
PA-(16-17)	Fused	D	UPV
PS-(1-2)	Solid	D	UPV

A intact case, B with central hole, and C with fracture case , D strain controlled.

4.6.2 Stress-strain response of PMMA specimens

Although stresses and strains generated in the PMMA specimens during the compression tests are not uniformly distributed across the entire specimen; because of the presence of stress-hole concentrator and the induced fracture, the original dimensions of the specimens are used to calculate the stresses and strains shown in Fig. 8 and Fig. 9 (vertical strain = change in vertical length / original specimen length). The brittle behavior of the PMMA specimens is not shown in the figures because the compression tests were not performed up to failure. Two distinct zones (initial stiffness zone "za" and mid stiffness zone "zb") are identified (Figure 9); zone za shows a steeper slope, and zone zb displays a smaller slope. Two equivalent Young's moduli, E_{za} and E_{zb}, are calculated from the slopes of the plots in zones za and zb, respectively. E_b is considered to be the overall specimen stiffness once the fracture has propagated to some distance along the interface. E_{za} and E_{zb} for the four PMMA specimens tested under strain-controlled conditions are summarized in Table 3 ($E_{zb} \approx 0.55E_{za}$). The measured values of E_{za} and the observed non-linear behavior are in agreement with reported values in the literature (1.8-3.1 GPa; Parker, 1967). Thus, the effects of the small circular hole and the initial fracture propagation do not have a significant

impact on the load-displacement response. The similarity of the stress-strain behavior of the fused and solid specimens confirms the expected uniformity of the fusing methodology used. The dynamic (small-strain) Young's modulus (E) determined from the UPV measurements using the following expression;

$$E = V_p^2 \rho \tag{4-4}$$

where V_p is P-wav velocity, and ρ is material density.

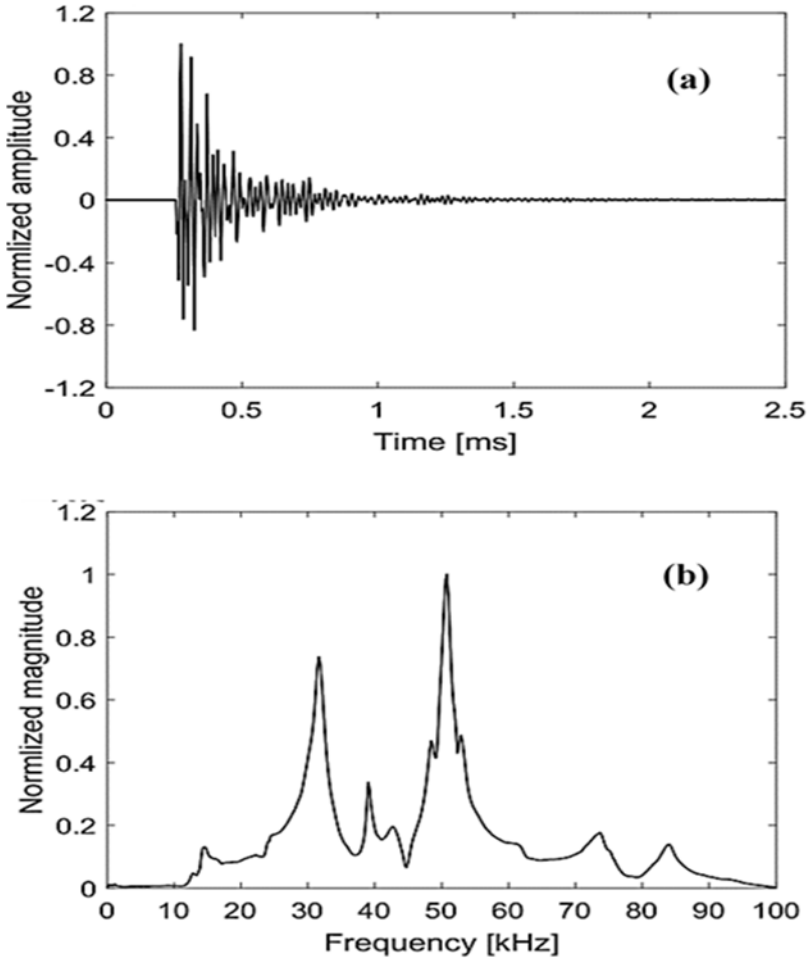

Figure 4-7. Laser calibration results: (a) normalized time signal (maximum displacement = 5.15 nm)**,** (b) corresponding Fourier spectrum.

The computed Young's modulus from UPV measurements is 4.96 GPa for the fused specimens and 4.66 GPa for the solid specimens; these values are in average three times greater than E_{zb}. The

difference between the small-strain stiffness and the large strain-stiffness is attributed to the micro-fractures generated in the PMMA specimens as evidenced by the non-linear behavior of the specimens. These results are in agreement with previous studies as the strain levels induced in ultrasonic tests ($\approx 10^{-9}$%) are orders of magnitude smaller than the strain levels used in the static tests ($\approx 10^{-6}$%) (e.g. Santamarina *et al.*, 2001).

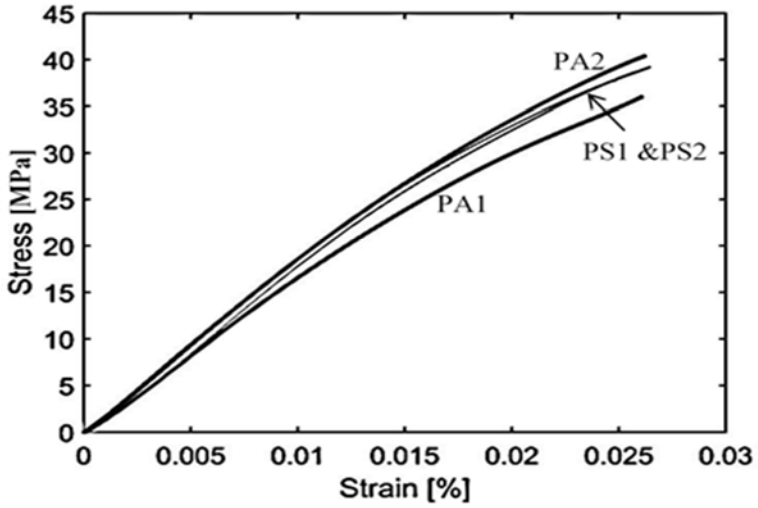

Figure 4-8. Typical stress-strain curves for fused (PA16, PA17) and solid (PS1, PS2) PMMA specimens.

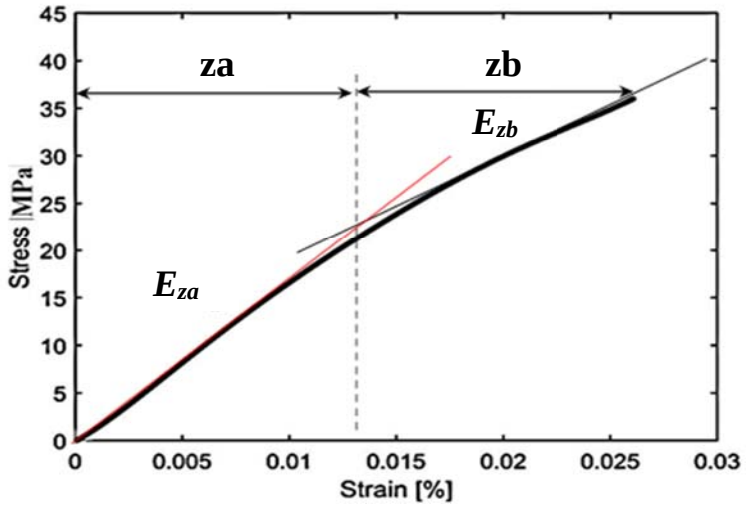

Figure 4-9. Stress-strain curve showing two distinct zones (za, zb) for the evaluation of the average elastic Young's modulus (E_{za} and E_{zb}).

The new specimen preparation technique used in this study allows a controlled fracture growth as a function of the compressive load applied to the specimen; which was not possible before. Figure 4-10 shows the variation fracture length as a function of the applied load for four specimens.

TABLE 4-3. Elastic moduli of specimens tested under strain-controlled load tests

	Static Young's modulus, *E* [GPa]			
Zone #	PA-1	PA-2	PS-1	PS-2
za	1.69	1.85	1.87	1.80
zb	0.86	1.07	1.05	0.93

This variation is approximately linear until a load of 90 kN for the fused specimens; thereafter, fracture length increases at a faster rate with increasing load. Conversely, macroscopic fractures develop in the solid specimens after threshold loads of 90 kN and 120 kN (specimens SP-1, SP-2, respectively). These macroscopic fractures form at a lower rate than in the fused specimens; because of the lower fracture toughness of the fused interface. Different specimens exhibited a similar fracture propagation growth rate.

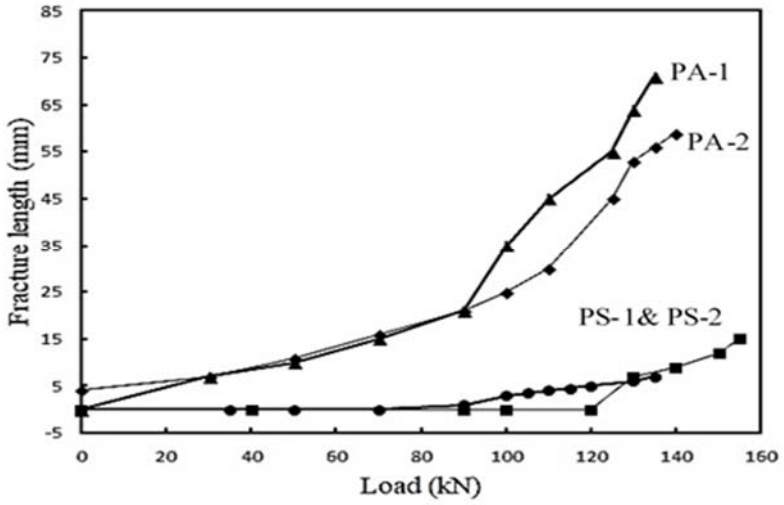

Figure 4-10. Fracture propagation in four specimens, two fused (PA) and two solid (PS) specimens during the strain-controlled load test**.**

The fracture lengths observed in fused specimens are greater than those of the solid specimens. The maximum fracture length observed in the fused specimens is 7.1 cm. In contrast, the maximum fracture length in solid specimens is 1.5 cm. The presence of a weak interface in the fused

specimens' results in lower loads required for producing fracture (i.e., lower fracture toughness). The fracture orientation in all PMMA specimens is normal to the loading direction. Thus, the new fabrication method used for the fused PMMA specimens is effective for monitoring fracture growth.

4.6.3 Fracture interaction with wave velocity

The UPV measurements of PMMA specimens tested under three different conditions (designated by case A for intact specimens, case B for specimens with a hole, and case C for specimens with fracture) are analyzed to determine changes in wave velocity and attenuation. Figure 4-11 shows the ultrasonic P-wave velocities of different PMMA specimens with two different thicknesses (12.7 mm and 25.4 mm).

The average velocities for the thin PMMA specimens (Figure 4-11a) are 2720 m/s ± 12 (case A), 2718 m/s ± 10 (case B), and 2630 m/s ± 10 (case C). The corresponding average velocity values for the thick PMMA specimens are 2803 m/s for cases A and B and 2709 m/s for case C. The small 3% increase in velocity observed in the thicker specimen is likely due to the larger contact area between the transducers and the specimen. The energy emitted from the transducer increases with contact area. The compressional wave velocities for cases A and B are practically the same, as expected because the diameter of the hole (6.3 mm) is only 12% of the main wavelength present in the signal (Vp= 2803 m/s, λ = 51 mm, f = 54 kHz). The wave velocities for cases B and C show only minor differences of 2% and 3.6%, respectively. Thus, the difference in wave velocities between the intact and damaged cases is not a strong indicator of the induced damage in the specimens reflected by 45% reduction in the static stiffness (Figure 4-9).

Figure 4-12 shows the UPV as a function of the applied compressive load for a fused and an intact specimen (PA1 and PS1). The wave velocity in fused specimen decreases slightly when the load exceeds 70 kN because of the induced fracture (Figure 4-12.a). However, after a load of P=125 kN, the wave velocity decreases quickly and linearly; likely because the wave travel path increases with the increase in fracture length; when the fracture length exceeds the main wavelength (λ = 51 mm) of the signal (Santamarina *et al*., 2001). Unlike the fused specimens, the wave velocities of

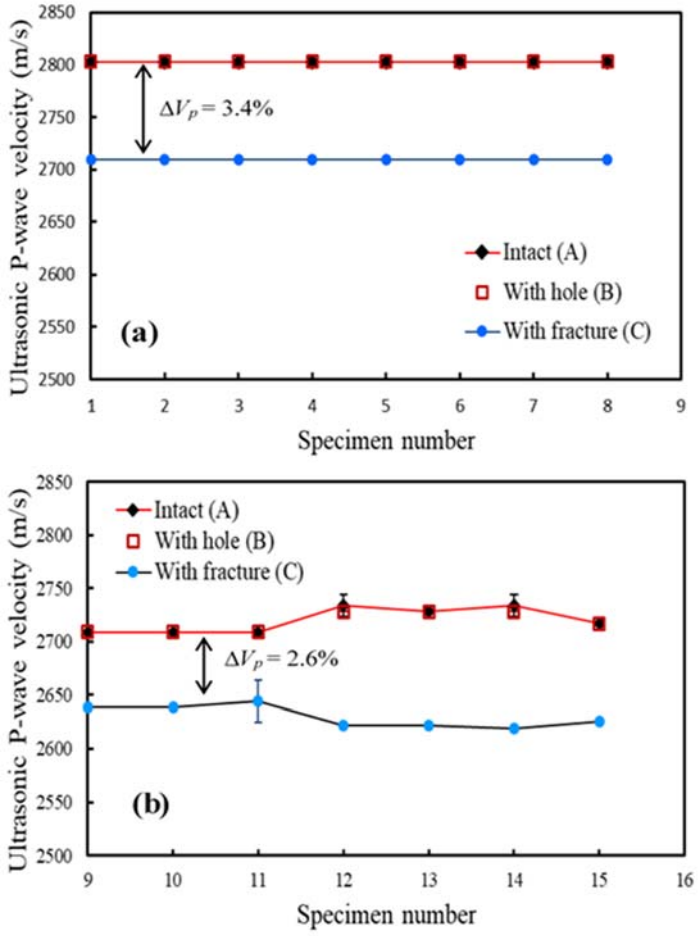

Figure 4-11. Average ultrasonic wave velocities for different specimens tested under three conditions (intact A, with hole B, with fracture C) : (a) 25.4 mm thick specimen, and (b) 12.7 mm thick specimen. Fractures measured for 25.4 mm and 12.7 mm are (42-82 mm) and (51-63 mm), respectively. The corresponding loads measured are (120-180 kN) and (48.3-55.8 kN).

solid specimens do not show any significant variation as the maximum fracture length is smaller than 1/3 of the main wavelength of the signal. The wave velocities results demonstrate that single velocity measurements are not sufficient to characterize the existence of a fracture in homogenous material as represented here by the PMMA material.

4.6.4 Fracture interaction with wave attenuation in time domain

Figure 4-13 shows typical time domain signals obtained for both 12.7 mm thick and 25.4 mm thick PMMA specimens. The presence of hole (case B) induces a slight reduction in the maximum amplitude (13% for both specimens) while the presence of fracture (case C) induces a noticeable

reduction (62% and 45% respectively). The reduction of signal amplitude can be related to absorption, mode conversion, and scattering mechanisms (Krautkrämer and Krautkrämer 1990) because of the presence of the fracture. These time domain outputs support the use of signal attenuation as a complementary tool to study the interaction between the ultrasonic waves and internal condition of a homogenous material.

UPV measurements are also obtained during fracture propagation within the loading frame to monitor the impact of fracture growth on wave velocity and attenuation. Figure 4-14 shows the waveforms corresponding to three selected loads: (i) zero load at the beginning of testing (no induced fracture), (ii) load corresponding to L=10 mm fracture, and (iii) load corresponding to

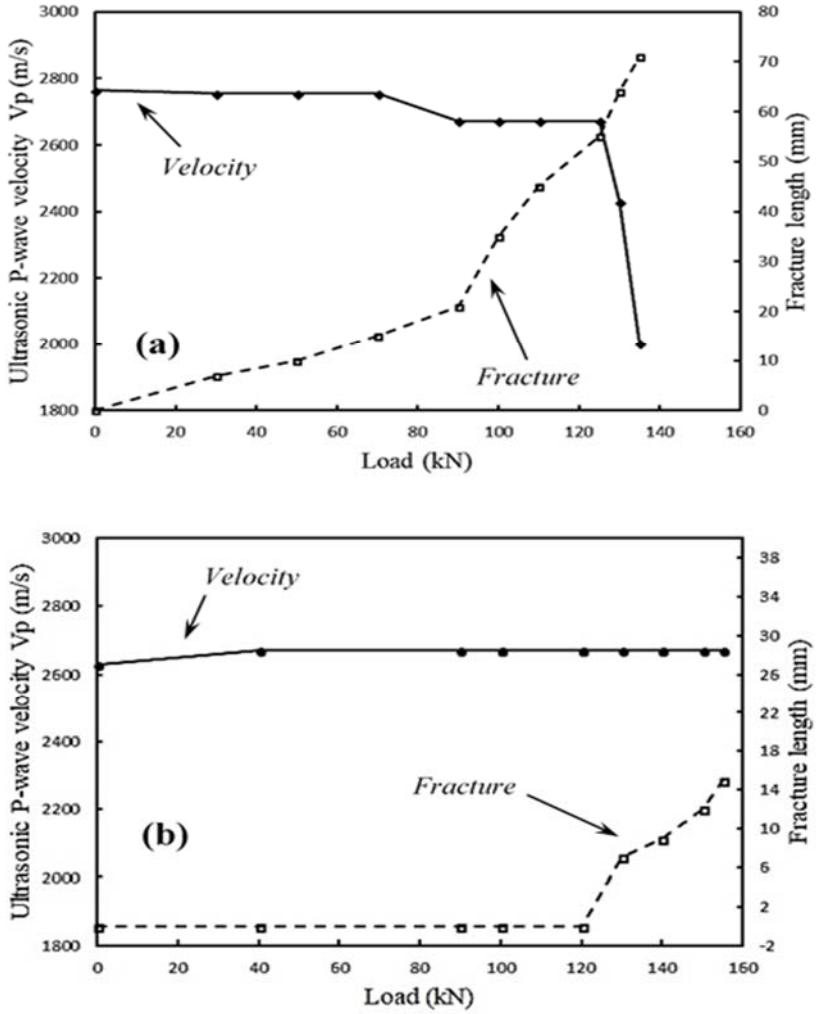

Figure 4-12. Effect of fracture propagation on ultrasonic P-wave velocity for (a) fused specimen (PA16), and (b) solid (intact) specimen (PS1).

maximum fracture length at the end of testing (Lmax). The observed reductions in maximum amplitudes between waveforms with respect to the initial condition are 36% (L= 10mm) and 68% (L=Lmax) for the fused PMMA specimens, and 50% and 76% for the solid PMMA specimens. The improved coupling, provided by gluing the transducers, shows greater consistency of attenuation measurements, even for small fracture lengths.

4.6.5 Fracture interaction with wave attenuation in frequency domain

Figure 4-15 shows the corresponding frequency spectra of the signals presented in Figure 4-13. To better quantify the attenuation of waveforms because of the presence of fracture, the areas under frequency spectra are calculated.

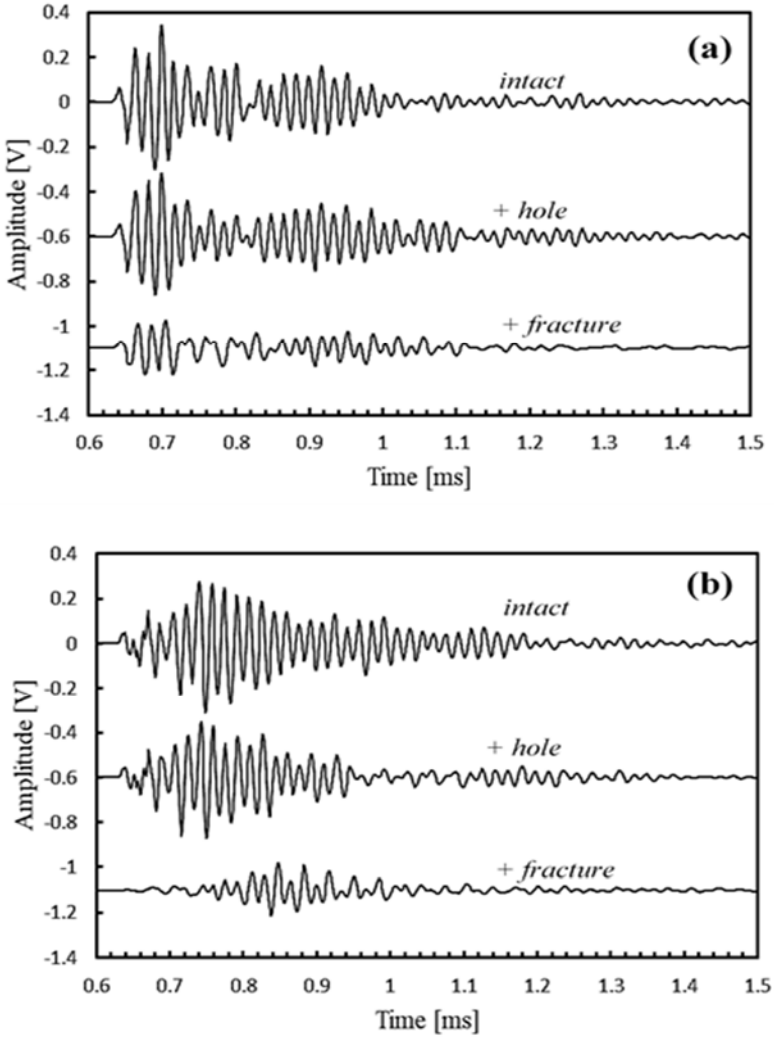

Figure 4-13. Typical time signals for three specimen conditions (intact, with a stress hole concentrator, and fractured) for two specimen thicknesses (a) 12.7 mm, and (b) 25.4 mm.

The presence of fracture existence is investigated by defining two distinct zones under the frequency spectrum: low band zone (LB) comprising of the frequency range 20-40 kHz (λ = 10.2 mm, $f \approx 27$ kHz), and high band zone (HB) comprising of the frequency range 40-70 kHz (λ = 51 mm, $f \approx 54$ kHz) (Figure 4-15). These frequency ranges represent wavelengths close to the transverse dimensions of the specimens and wavelengths related to the resonant frequency of the transmitter on air.

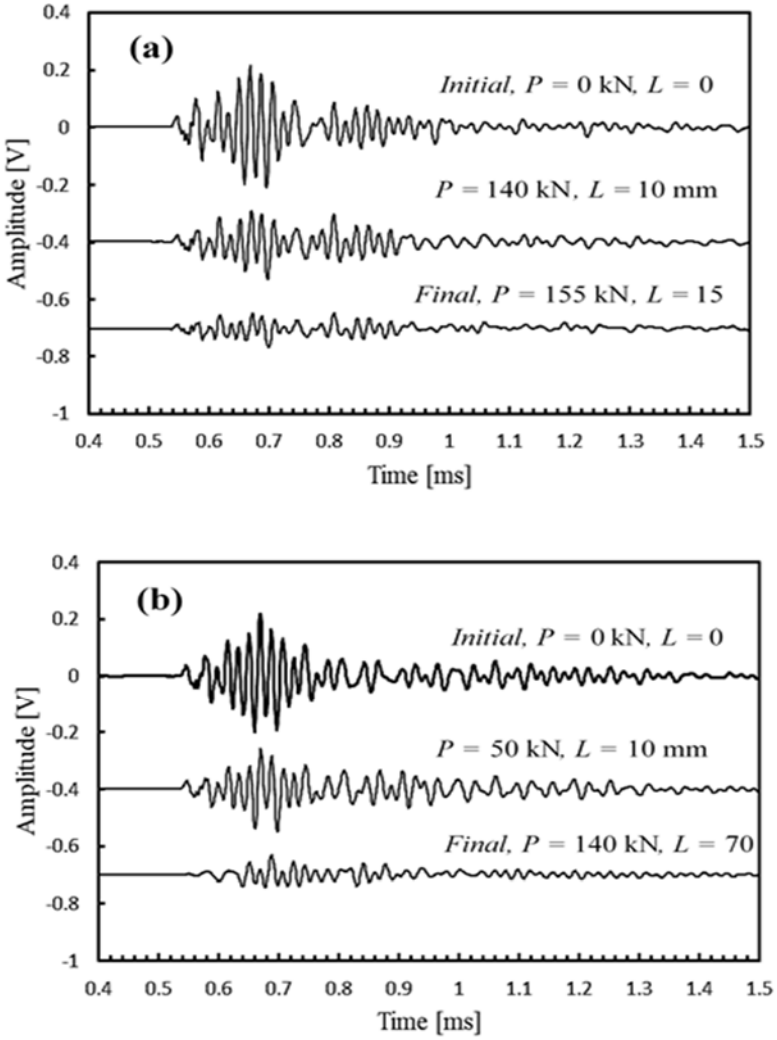

Figure 4-14. Typical time signals measured at three different compression loads, 25.4mm thick specimens, (a). solid specimen, (b). fused specimen. (P = load, L = fracture length).

The frequency spectra of Figure 4-15 confirm the attenuation results obtained in the time domain (Figure 4-13). There is a slight variation in the spectra between cases A and B confirming that the existence of the stress concentration hole is not enough to affect the time signals. In contrast, the

difference in frequency spectra between cases B and C reveals a noticeable influence of the fracture on the signal spectrum. The difference in the total spectral areas between cases A and B, and cases B and C are 15% and 52%, respectively. The low frequency bandwidth does not exhibit any significant variation, while reduction percentages for high bandwidths are 15% and 57%, respectively.

To enhance the frequency domain analysis of time signals during loading, a time window is used (Tukey window, time decay factor = 0.1, Alexander and Poularikas, 1998). Figure 4-16 shows the frequency spectra after applying the window.

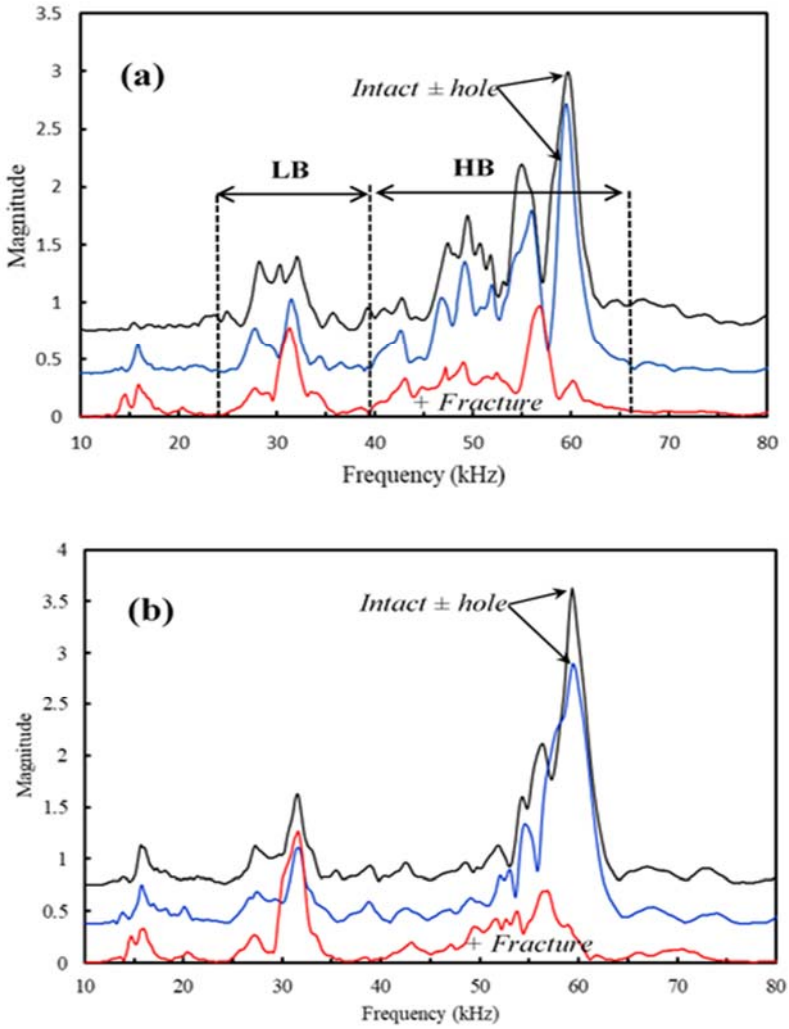

Figure 4-15. Typical Fourier spectra at three conditions (intact, with a stress hole concentrator, and fractured), (a) 12.7 mm thickness specimen, (b) 25.4 mm thickness specimen. Note, spectra of case A (black) and case B (blue) are shifted by 0.75 and 0.35, respectively.

The Fourier spectra reveal sensitivity to the fracture at earlier load steps (e.g. L = 10 mm). In the case of the fused specimens, wave velocity exhibits a slight variation until the test reaches a load of 130 kN (Figure 4-12). At the end of the tests (L_{max} = 15 mm, solid; L_{max} = 70 mm, fused), the reduction in signal attenuation is significant, 27% and

39%, for solid and fused specimens, respectively. A close examination of the spectrum for the no load condition reveals three main peaks (f_1 = 54 kHz, f_2 = 30 kHz, and f_3 = 16 kHz). When the load increased, the peaks in spectra experience a slight shifting because of the fracture.

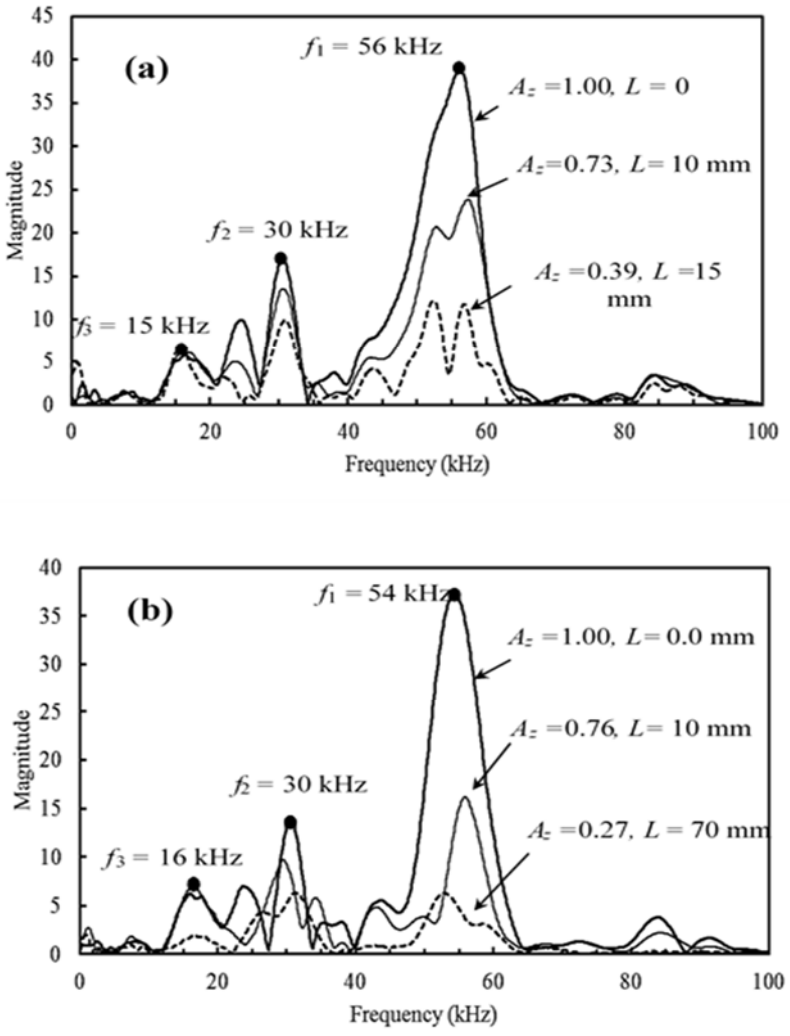

Figure 4-16. Typical Fourier spectra at three different compression loads for (a) solid specimen, and (b) fused specimen (A_z is the normalized spectral area with respect to the case of zero load, and L is the fracture length).

The peak at f_1 = 54 kHz is the more susceptible to the presence of a fracture than the other two peaks. The corresponding wavelengths for the main frequencies are λ_1 = 5 cm, λ_2 = 9 cm, and λ_3 = 16.7 cm (wave velocity of 2715 m/s). Thus, the first peak is most significantly affected because the fracture length is of the same order as that of the main wavelength. The results obtained for the solid specimens are similar to those observed for fused specimens with the exception that peaks exhibit slight variations. Even though, the maximum fracture length for the solid specimens is L_{max}=15 mm, which is smaller than the main wavelength. These results show the potential of attenuation measurements to identify the effect of multiple micro-cracks (Ranz *et al*., 2014). The attenuation of high frequency bandwidth in Figure 4-16 shows significant sensitivity to fracture length (up to 80% reduction). On the other hand, attenuation shows sensitivity to early damage as the attenuation increases up to 60% when the fracture length increases linearly with load up to 25 mm (half of the main wavelength). Then the attenuation increases at a slower rate with fracture length, likely because of the limited bandwidth of the transducer and the geometrical limitation of the specimen which does not allow the propagation of larger wavelengths.

To investigate the effect of fracture on wave attenuation, the same procedure was followed after testing 15 PMMA specimens for the three aforementioned cases. The relationship between fracture and wave energy was quantified by determining the total (A_{Tot}), low band (A_{Low}), and high band (A_{High}) areas of wave spectrum. In Figure 4-17, the relationship between fracture length, spectra areas, and applied load are shown. As expected, the high frequency bandwidth is more sensitive to fracture propagation because of the associated wavelengths, as discussed earlier.

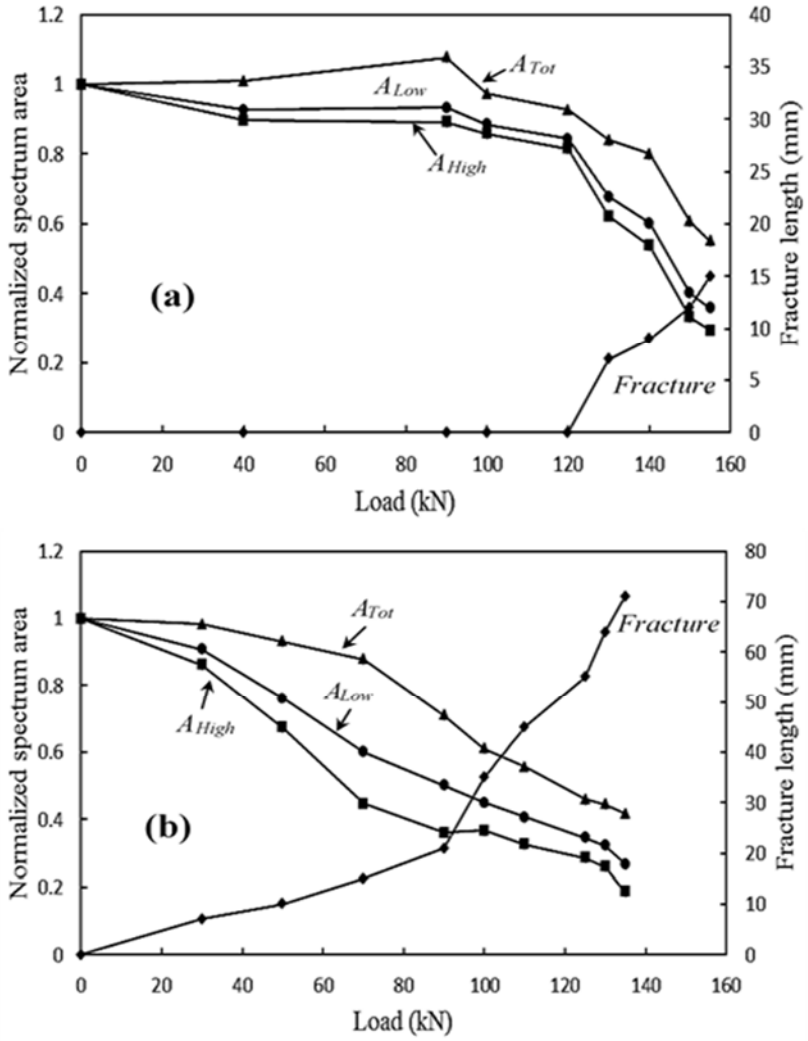

Figure 4-17. Effect of fracture propagation on spectral areas for (a) solid specimens and (b) fused specimens. A_{Tot} = total area of spectrum, A_{High} = area under high frequency bandwidth range, and A_{Low} = area under low frequency bandwidth range.

4.7 Summary

Ultrasonic pulse velocity (UPV) tests are performed on 19 PMMA specimens of two different thicknesses under three conditions (solid, with a stress-concentrator hole, and fractured). UPV measurements are also taken in two of the fused specimens and two solid specimens during strain-controlled compression tests. A new fabrication technique is used to generate a stable fracture growth at the fused PMMA specimens. Complementary ultrasonic pulse velocity and signal attenuation measurements are used to characterize the fracture growth in a homogenous media (PMMA specimens).

The UPV results show that wave velocity and fracture length are practically independent (compressional wave velocity decreased only by 4% for different fracture lengths). Nevertheless, time signal amplitudes and corresponding frequency spectra indicated that a significant amplitude change occurs with fracture growth in the selected frequency bandwidth (≈ 60% increase in attenuation). The readability of frequency spectrum peaks obtained from strain-controlled tests is improved by using a time window technique. The frequency spectra of damaged PMMA specimens show that spectral amplitudes at high frequencies (f > 50 kHz) are more susceptible to fracture propagation than lower frequencies (f < 40 kHz) because of the associated wavelengths. The dynamic Young's modulus of the PMMA specimens, obtained from UPV measurements, are about three times greater than static modulus because of the orders of magnitude difference in the strain levels used in each test.

The new fabrication method of fused PMMA specimens provides an effective procedure for monitoring fracture growth. The study reveals that the determination of arrival time requires a careful revision as there is a misleading use of wave velocity in the literature to identify material damage. The results presented here clearly indicate that changes in wave attenuation from material damage are significant. Thus, previous results indicating that wave velocity changed with material damaged are likely incorrect; the reported change in wave velocity is likely due to the incorrect selection of the arrival time as the real first arrival was removed by the effect of wave attenuation. An interesting finding of this study is the observed sensitivity of wave attenuation for the detection of fracture lengths even smaller than half the main wavelength of the propagating pulse; whereas, traditionally it has been accepted that the fracture length should be as minimum equal to one wavelength to significantly affect wave attenuation.

Chapter 5: Characterization of cement-based specimens using ultrasonic methods

Studying the possible combination of the wave velocity and wave attenuation to evaluate the integrity and condition of concrete elements was the main objective of this research work. In this chapter are illustrated the results of characterization of different cement-based specimens tested using ultrasonic pulse velocity and laser Doppler vibrometer methods.

5.1 Introduction

Methods based on stress wave propagation are used routinely in non-destructive testing of different materials such as metals and concrete. Several researchers (Kak and Dines, 1978; Evans et al. 1978; Kline, 1984; Lee et al., 1990; Zellouf et al., 1996) successfully employed ultrasonic wave characteristics (e.g. wave attenuation) in applications such as theoretical acoustics, ultrasound characterization of tissue, and non-destructive testing. Implementing experiments to determine attenuation in cement-based materials is not a straightforward task because the randomly distributed aggregate causes scattering of waves and the attenuation level is high. Efforts have been made (Malhotra and Carino, 2003; Wiggenhauser et al., 2003) to analyze the ultrasonic waveforms to correlate ultrasonic waves and concrete attributes such as strength, aggregates, porosity, and damage. The heterogeneous nature of concrete which consists of cement paste, fine and coarse aggregate, air bubbles and water allows only for qualitative conclusions. This excludes the possibility to correlate ultrasonic test results directly with structural integrity parameters. To establish any robust relation between wave characteristics and concrete properties, it is essential to investigate the interaction of ultrasonic waves with the different phases in concrete.

The most widely used ultrasonic testing technique to determine material characteristics is immersion test method. This technique can be used either with through-transmission configuration, in which, a pair of broadband transducers is immersed in water tank and properly aligned or with a pulse-echo setup that uses one transducer to transmit and receive signals. The consistency of coupling is the main advantage of this technique which allows to obtain basic parameters including; amplitude, time and frequency content. These are used to analyze the properties of materials such as polymers, metals, and tissues (Krautkrämer and Krautkrämer, 1990; Ensminger and Bond, 2011). Moreover, the test has been used effectively to estimate the mechanical properties based on the density of the material (O'Leary et al., 2005; Pedersen, 2014; Buiochi et al., 2014; Ginzel and Turnbull, 2016). Selfridge (1985) tested isotropic solids

in a relatively simple immersion technique using a pulse-echo setup to estimate wave velocity and wave attenuation. The study reports approximate properties of a wide range of isotropic materials determined using the pulse-echo test method. Several advantages were reported for using immersion through-transmission approach over the pulse-echo technique (Ginzel and Turnbull, 2016). In testing lossy materials such as coarse-grained materials using the second method, the two-way path produces more attenuation and scatter losses than the first technique which uses the one-way path from transmitter to receiver. Another disadvantage of using pulse-echo technique occurs when the material's acoustic impedance closely matches water. This produces signals smaller than would be if the through-transmission approach is used. Therefore, the only parameter required to be captured in through-transmission is the time shifted signal at the receiver.

In several other works (Kim et al., 1991; Gaydecki et al., 1992; Philippidis and Aggelis, 2005), attenuation measurements on cement-based specimens were reported using a simple through-transmission setup in air. The testing procedure used in their research was accomplished by comparing a face-to-face reference waveform to signals obtained from testing specimens placed between the transmitter and receiver transducers. The specimens used in these studies include paste (cement and water), mortar (cement, sand, and water), and concrete (cement, sand, coarse aggregates, and water) with different water-cement ratios. Broadband transducers with different central frequencies (up to 1MHz) were used to transmit a pulse through the specimens. This allowsto obtain attenuation measurements to study the effect of sand and aggregate content. The results highlight the significant influence of coarse aggregate content on the attenuation behavior. Despite the findings of these studies, concern still exists with regard the uncertainties of using this type of technique for attenuation measurement due to the variability of coupling between specimens and the transducer.

Becker et al. (2003) uses different sizes and distributions of glass beads in a cement-paste matrix as scatters to study the propagation of ultrasonic waves in cement-based materials using diffuse ultrasound. In this study, the specimens used were steel for reference measurements, cement-paste with two sizes of glass beads (1 mm and 3 mm) and three distributions (loose, medium, and dense), and cement-paste. All specimens had a circular geometry (diameter 76 mm, thickness from 14 to 16 mm. The study indicates the losses in the cement-paste matrix with glass beads was dominated the material attenuation in opposition to the losses at the interfacial zone between cement paste and glass beads. However, the coupling variability in this study can

be a major concern that leads to uncertainties about the attenuation measurements that need to be addressed carefully.

In present study, the main ultrasonic wave characteristics (wave velocity and attenuation) are used to characterize different cement-based specimens with/without glass beads (6 mm diameter) to obtain their approximate properties. Two different testing approaches are used in this study to take ultrasonic measurements; immersion through-transmission technique as developed by (Ginzel and Turnbull, 2016) and a laser vibrometer interferometry technique. The study also addresses the correlation between glass bead distribution and the wave characteristics. There appears to be no data reported in the literature about using immersion and laser vibrometer techniques to characterize cement-based materials.

5.2 Experimental procedure

5.2.1 Test methodology and equipment

Immersion through-transmission setup. The experimental setup for the immersion test was that developed by (Ginzel and Turnbull, 2016) and consists of a PCPR100 pulser-receiver made by Adaptronics used in conjunction with Winspect software that captures the signals during the test and an immersion tank made of acrylic with a plastic base filled with distilled water. Also, two 500 kHz immersion type transducers IX130 made by UTX are used to emit and receive the ultrasonic signals. The tank is equipped with a rotating specimen holder that can be used for obtaining shear wave signals (Figure 5-1). In addition, a PCPR100 system is used to generate a bi-polar ultrasonic pulse with frequency of 650 kHz at a voltage of 250 volts. The received signals are filtered using a built-in bandpass filter (0.1 MHz to 14 MHz).

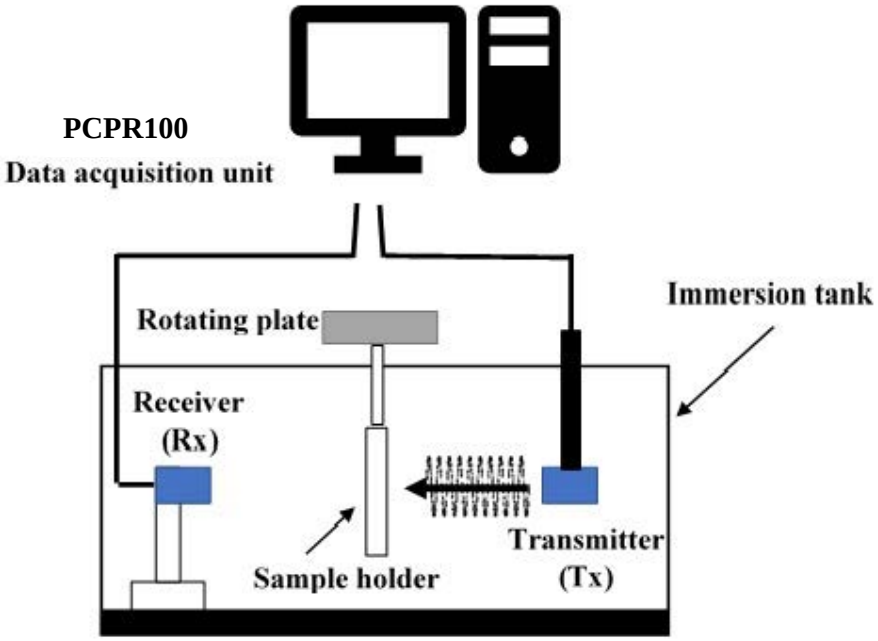

Figure 5-1. immersion through-transmission testing setup (adapted from Ginzel and Turnbull, 2016).

The attenuation is also adjusted to produce a non-saturating RF signal on the A-scan mode. Then, the signals were digitized using an STR8100 100MHz analogue to digital converter which is also a built-in unit in the ultrasonic test system. The first step in the immersion test was to acquire a water signal on the A-scan mode to use as a reference water path signal. Then, the temperature of the water is recorded to calculate the wave speed in water. Figure 5-2 shows the signal in water without any specimen. In this figure, two points are defined for comparison. The first point is selected based on the first arrival time of the response of signal, while the second is the maximum peak cycle as suggested by (Ginzel and Turnbull, 2016). The time point selected must be consistent for the signal with just water and the signal with the specimen in the sound path and these are used for the calculations of wave parameters. Without any adjustments made to the setup, the test specimen is then placed between the transmitter and receiver probes such that its surface is perpendicular to the ultrasonic beam. This configuration is monitored by observing the A-scan response.

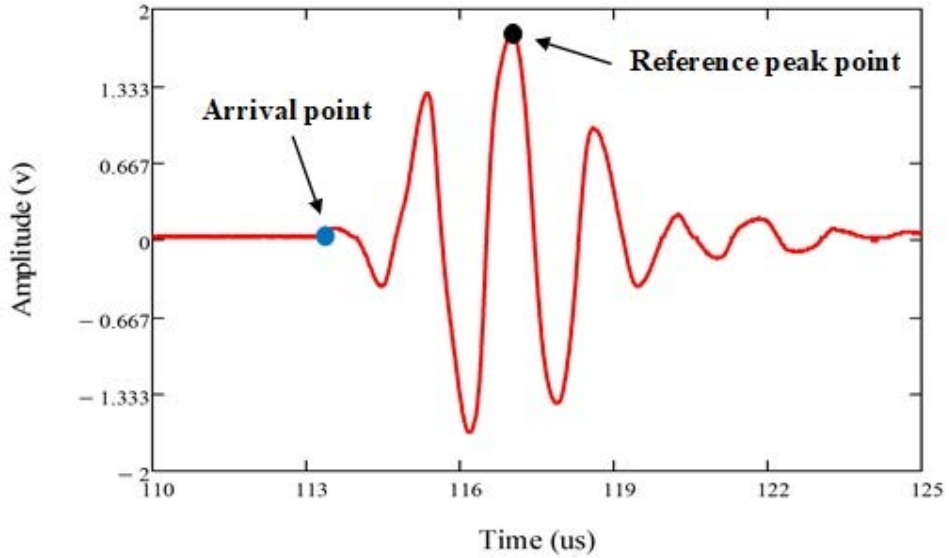

Figure 5-2. Determination of reference time points of immersion test signal.

One of the immersion setup advantages is the ability to generate a shear wave by rotating the goniometer (rotating base) until the first critical angle is reached. At the first critical angle the longitudinal mode is totally internally reflected in the specimen (in accordance with Snell's law) leaving only the shear mode in the material. Then, the shear mode exits the specimen from the far surface and coverts back to longitudinal mode in the water. The rotation angle is measured to allow shear wave velocity calculations. Figure 5-3 shows the effect of rotation on the propagated pulse.

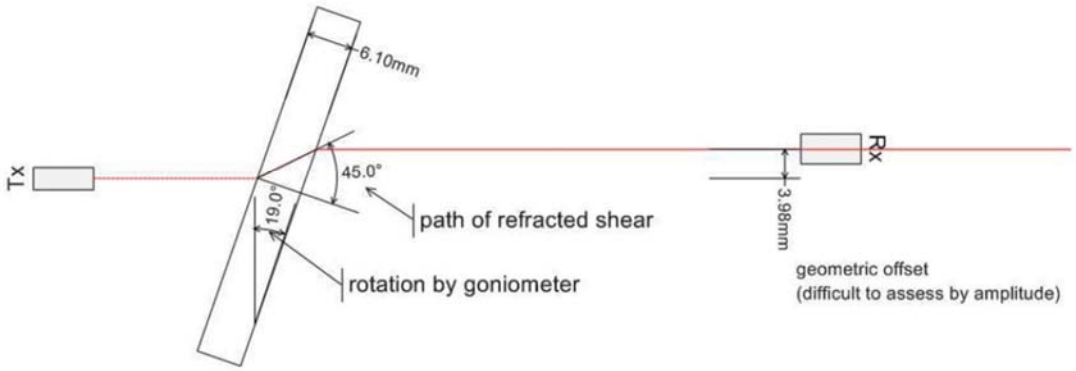

Figure 5-3. Rotating specimen to obtain shear mode in through-transmission immersion setup (after Ginzel and Turnbull, 2016).

***Laser vibrometer setup*.** The laser experiment setup utilized to test the cement-based specimens includes; laser head (Ploytec OFV-534), vibrometer controller (Ploytec OFV-2570), data management system, vibration isolated workstation, and high-resolution positioning controller, wave generator (Keysight), amplifier (Krohn-Hite), piezo driver. Also, a piezoelectric transducer with a nominal resonance frequency 500 kHz (CX484P) made by UTX is used in this study. The ultrasonic transducer was placed on one side of the specimen being tested, using gel for consistent coupling (Krautkrämer and Krautkrämer, 1990) and the laser received the displacement history in time from the opposed side. The testing setup of the laser vibrometer is shown in Figure 5-4. A square-wave voltage pulse is used as the electrical excitation of the transducer. Calculations in time and frequency domains are implemented to evaluate changes in wave velocity and wave attenuation. The electrical excitation consisted of a single cycle square-wave pulse generated by the function generator, with a nominal resonance frequency of 500 kHz and amplitude of 125 volts. The received signals are filtered using the amplifier with a high pass filter and a cutoff frequency of 1 kHz with a gain of 20 dB.

To minimize the effect of random noise and enhance signal quality, 100 readings are averaged for each laser measurement. The averaged time signal is then converted to a frequency spectrum for each sampling position using the fast Fourier transform (FFT).

5.2.2 Specimen preparations

Five hardened cement-based cylinder specimens (10 cm x 20 cm) are prepared with specified mixture proportions as shown in Table 5-1. These specimens are mortar cylinder (cement, sand, and water), concrete cylinder (cement, fine and coarse aggregates, and water), and three mortar cylinders mixed with three different borosilicate glass beads percentage; 15% (loose), 35% (medium), and 50% (dense) by total mass, respectively. The size of the glass beads, which is 6 mm, represents half of the nominal size of the coarse aggregates used in the mixture of the concrete specimens. Three discs (10 cm diameter) with different thicknesses (2 cm, 4 cm, and 8 cm) are obtained from each specimen using a saw machine. The matrix contains a Portland ASTM type I cement with a water/cement ratio of 0.47 by mass. All specimens include similar absolute content of cement-pastes matrix proportions and are stored in a humidity room for 28 days of curing. Also, the weight fraction of glass beads is determined by dividing the glass weight by the specimen weight. To avoid nearfield effects, the thicknesses of the discs are determined based on the approximate wavelength (λ=10 mm) of the Pulse generated by the transducer used in this study which are corresponding to 2λ, 4λ, and 8λ.

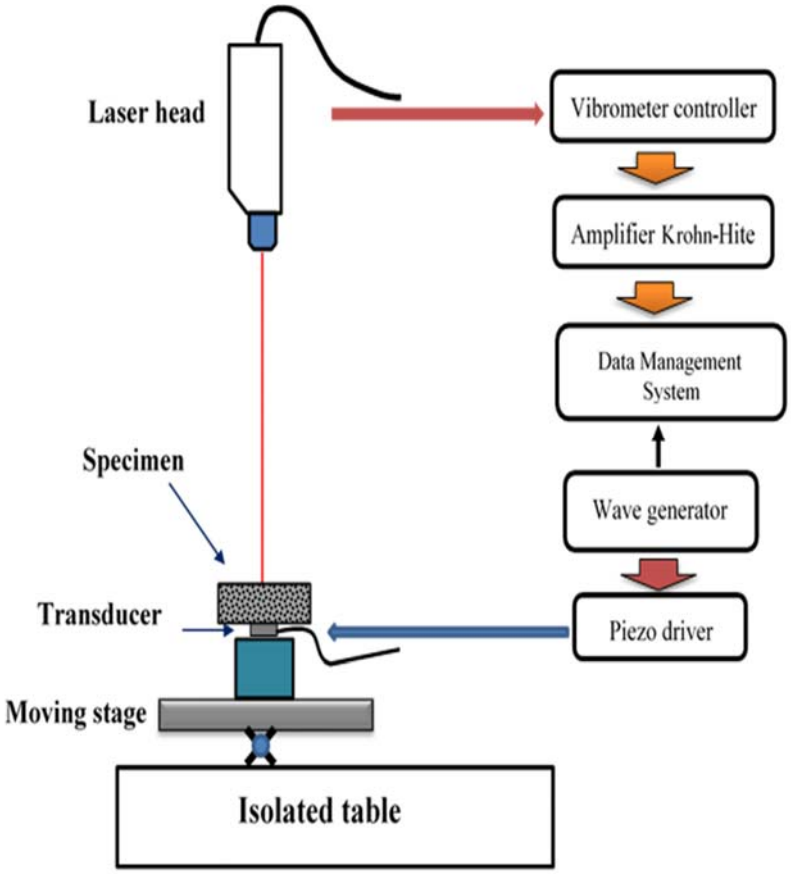

Figure 5-4. Laser Doppler vibrometer testing setup.

Table 5-1: Mix proportions of cement-based specimens.

Name	Cement (kg)	Sand (kg)	Coarse aggregate (kg)	Glass beads (kg)	Proportions
Mortar (Mr)	1.2	2.4	NA	NA	1:2:0:0
Concrete (Cr)	0.8	1.2	1.6	NA	1:1.5:2:0
Mortar+15%gb (Mra)	1.00	2.0	NA	0.6	1:2:0:0.5
Mortar+35%gb (Mrb)	1.00	1.2	NA	1.4	1:1:1.5
Mortar+50%gb (Mrc)	1.00	0.6	NA	2.00	1:0.5:0:2

Two different materials (disc shape), acrylic (11 cm x 2 cm) and nylon (11.5 cm x 2 cm) are employed for reference measurements as they are considered homogenous at the ultrasonic wavelength used in this study.

5.3 Experimental results

5.3.1 Immersion test results

Examination of the cementitious specimen waveforms that were obtained using the immersion test technique exposed considerable differences between these materials. For example, the presence of coarse aggregates and glass beads increases the degree of heterogeneity from mortar to concrete and mortar-glass beads groups. Therefore, it is a major interest to study the interaction of the material structure with the propagating wave. Comparison between water time signal and homogenous materials (acrylic and nylon) and cement-based specimens revealed that the latter are more attenuative. Figure 5-5 illustrates the typical time signals and their corresponding Fourier spectra in P-wave mode of mortar and concrete specimens.

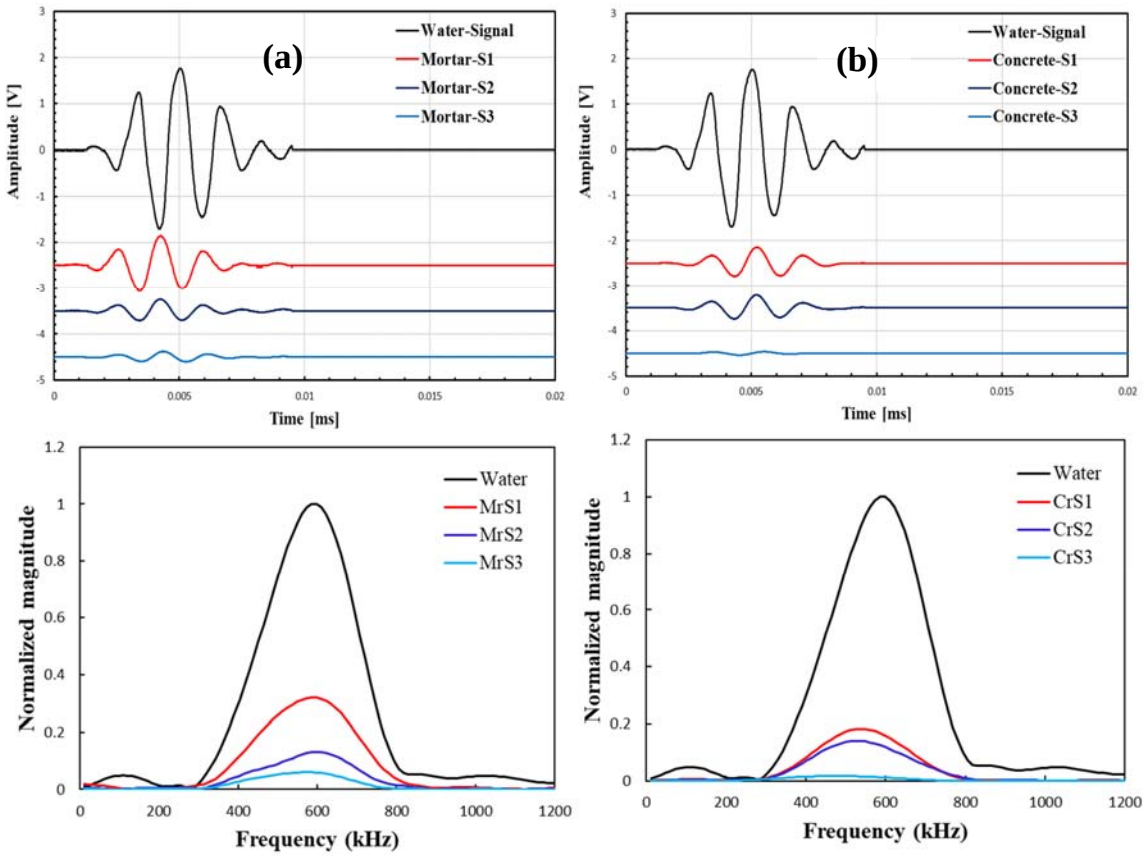

Figure 5-5. Typical waveforms of mortar and concrete specimens. (a) time signals and corresponding Fourier spectra of mortar, (b) time signals and corresponding Fourier spectra of concrete.

In Figure 5-5a, the thickness of mortar specimen influences the propagated wave and decreases its amplitude significantly. This behaviour becomes more attenuative with the presence of

coarse aggregates in concrete specimens as can be seen in Figure 5-5b. This difference in amplitude reduction can be attributed to the aggregate. The maximum gain size in mortar is 4.75 mm while the maximum size of aggregate in concrete is 12 mm. In addition, similar results can also be observed on the waveforms of mortars containing 15% and 50% glass beads as shown in Figure 5-7a & 5-7b. The other results can be found in Appendix B.

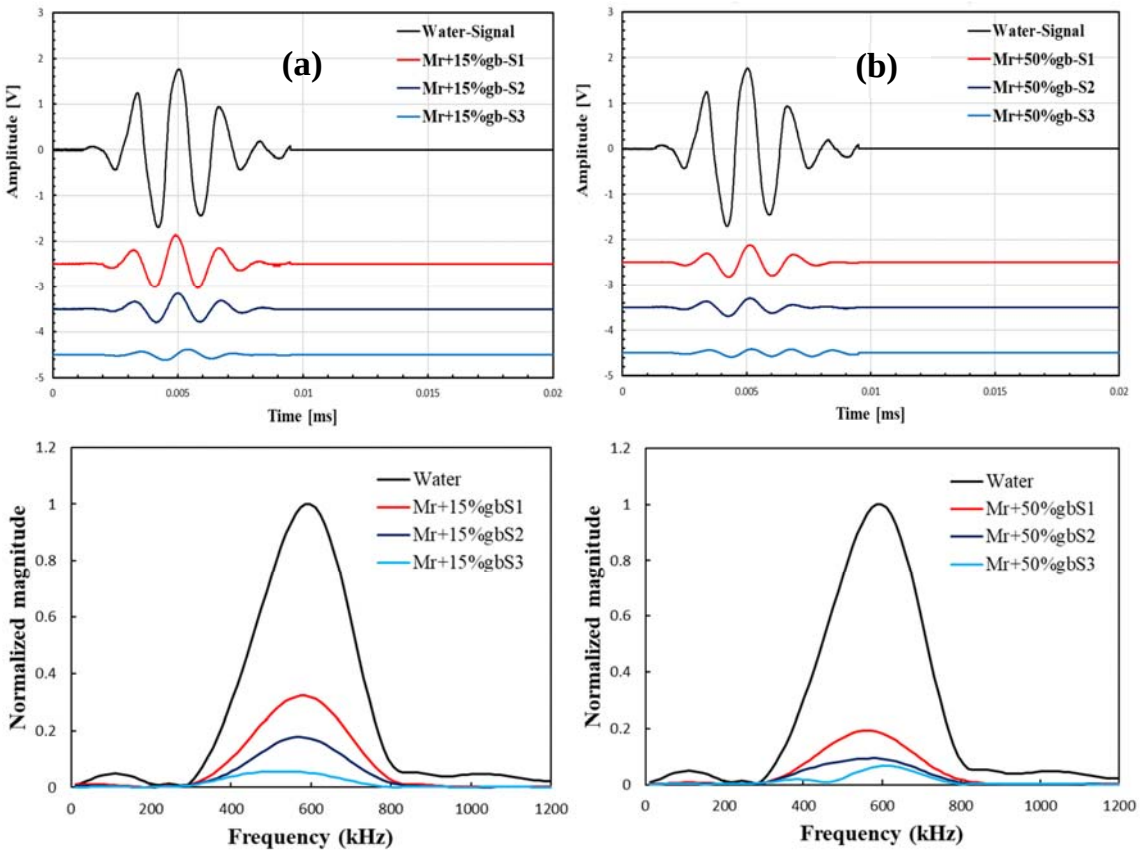

Figure 5-6. Typical waveforms of mortar containing 15% & 50% glass beads. (a) time signals and corresponding Fourier spectra of mortar with 15% glass beads, (b) time signals and corresponding Fourier spectra of mortar with 50% glass beads.

Table 5-2 summarizes the comparison between wavelength results obtained from immersion and Laser measurements.

Table 5-2: Wavelength results of immersion and laser measurements.

Material	Specimen	Immersion		Laser	
		Frequency (fr*/ kHz)	Wavelength (λ)	Frequency (fr*/ kHz)	Wavelength (λ)
Acrylic		598	4.5	454	6.3
Nylon		586	4.1	471	5
Mortar	S1-20 mm	586	7.4	547	8
	S2-40 mm	598	7.2	557	8.3
	S3-80 mm	574	7.5	471	9.4
Concrete	S1-20 mm	537	8.7	542	9.2
	S2-40 mm	525	8.8	486	9.8
	S3-80 mm	476	9.7	496	9.6
Mortar+15%gb	S1-20 mm	574	7.8	547	8.7
	S2-40 mm	574	7.7	576	8.4
	S3-80 mm	525	8.2	540	9.1
Mortar+35%gb	S1-20 mm	550	8.3	469	10.3
	S2-40 mm	562	8	564	8.2
	S3-80 mm	513	8.6	544	8.6
Mortar+50%gb	S1-20 mm	562	8.5	520	9.4
	S2-40 mm	574	8.2	559	8.1
	S3-80 mm	610	7.7	496	9.1

*fr = resonance frequency (maximum peak in the Fourier spectrum).

Pulse velocity of immersion test. Figure 5-7 depicts the P-wave and S-wave velocities that were obtained from immersion measurements of the specimens prepared for this research. The values of velocities are calculated using two different reference time points; first arrival point and peak point (Figure 5-2) and equations 2.9 & 2.11. Even though P-wave velocities of mortar specimens are show some discrepancy, all results are in good match which means both procedures can be used effectively in an immersion test technique to characterize concrete materials. On the other hand, cementitious specimens reveal average P-wave and S-wave velocities close to 4500 (m/s) and 2650 (m/s), respectively. The existence of aggregates and 50 % glass beads cause slightly higher P-wave and S-wave values by 100 (m/s) from its average. Also, the P-wave results illustrates there is a slight effect of thickness of specimen which can be related the fact that different wavelengths travel at different velocities and this generally relates to the stiffness and higher frequencies travel faster, while in S-wave, the effect is clear in concrete and mortar/glass beads specimen. This can be attributed to the heterogonies (aggregates or glass beads) present in these materials which has size in the order of the half

wavelength. In addition, this difference of velocities has been related to the interfacial transition zone between aggregates and cement paste characterized by increased porosity (Otsuki et al., 2000; Philippidis and Aggelis, 2005). Since the relationship between the surface of aggregate and the diameter is inversely proportional, it is reasonable to assume that in mortar, the material total volume present in this zone is higher, producing in general a lower values of wave velocity and elasticity.

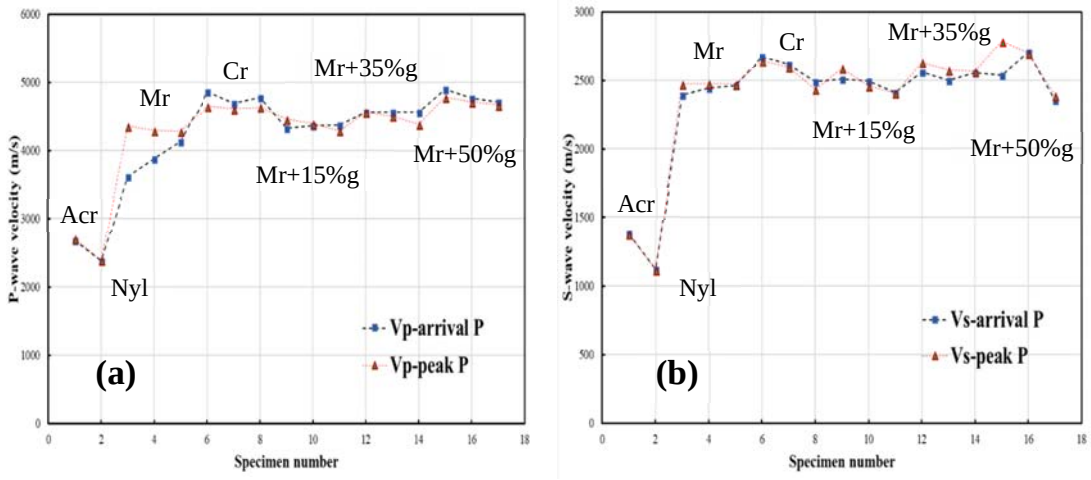

Figure 5-7. Wave velocities of specimens (a) P-wave velocities, (b) S-wave velocities. Acr & Nyl are acrylic and nylon abbreviations.

Another interesting remark, the percentage of glass beads also seems to influence the P-wave and S-wave velocities as it causes a linear rise in their values.

Material acoustic parameters. Characterization of cement-based specimens using through-transmission immersion technique provides a reliable procedure to estimate the acoustic properties such as acoustic impedance, transmission, and reflection coefficients of these type of materials. Acoustic impedance plays an important role in cement-based materials. It describes the relationship between propagated waves and heterogeneities. The mismatch in acoustic impedance between two materials such as concrete and air/water can help in detection of defect. This characteristic is important to be taken into consideration in NDT applications. The immersion test method can be a reliable procedure to determine the acoustic impedance of concrete materials. This is mainly because of the consistent coupling in this technique. Figure 5-8 illustrates the acoustic impedances of cement-based specimens calculated based on the P-wave velocity results.

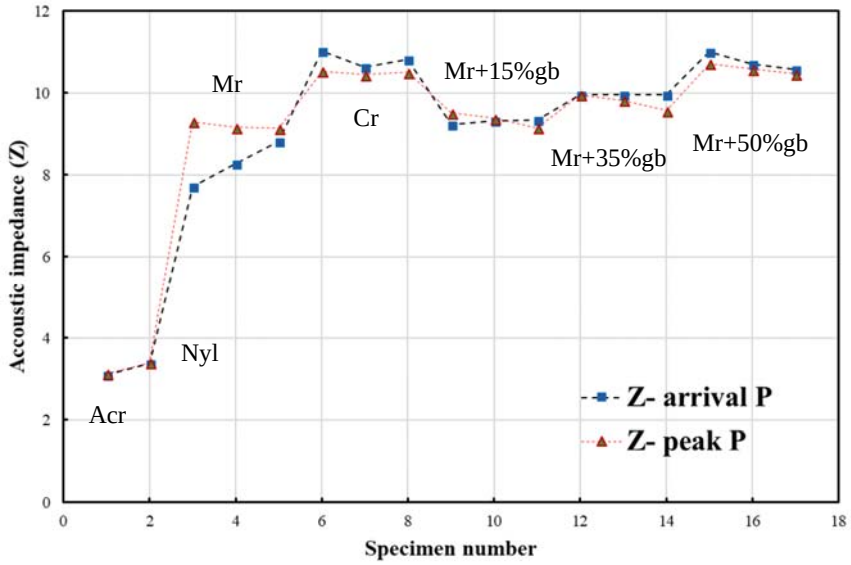

Figure 5-8. Results of acoustic impedances of cement-based specimens.

The determination of acoustic impedances of water and specimens allows calculation of the coefficients of transmission (T_c) and reflection (R_c) at the interface of water and specimen. Figure 5-9 illustrates the transmission and reflection coefficients calculated using velocities derived from arrival time and peak points from the immersion measurements of the specimens tested in this research.

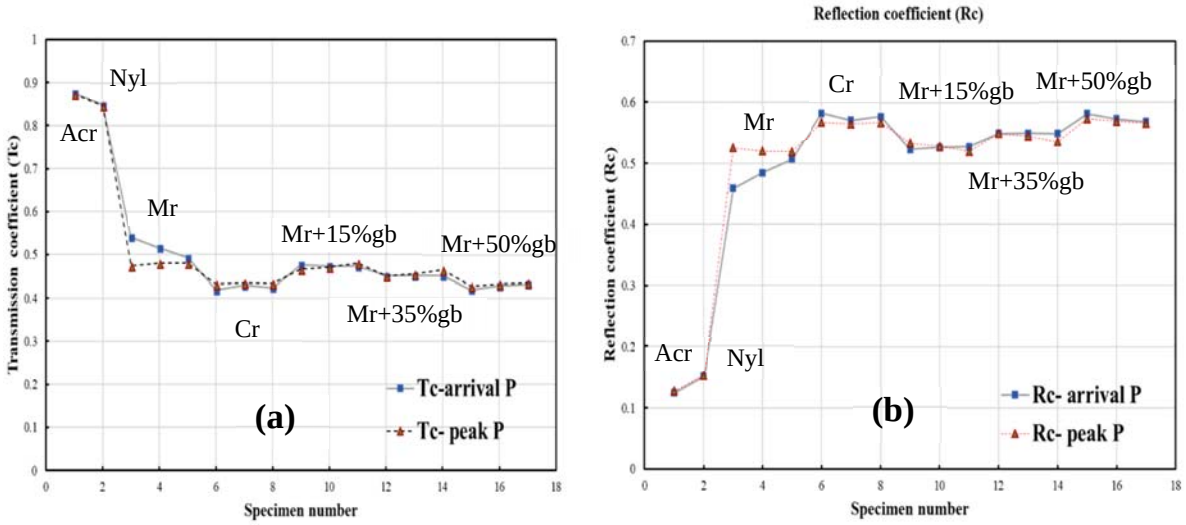

Figure 5-9. Transmission and reflection results of specimens (a) transmission coefficient, (b) reflection coefficient.

The change in grain size has a great influence over the percentage of wave transmitted and reflected at the specimen-water interface, the larger grain size causes less transmitted energy and higher reflected energy. Derivation of these coefficients is an advantage unique to the immersion test as it is difficult to obtain on other UPV methods.

Similarities to what was observed with wave velocities are noticed with transmission and reflection results. From the obtained results it can be inferred that grain size in concrete and mortar with 50% glass beads has a similar trend in transmission and reflection modes although there are two main differences between them; first the size of aggregate is twice the glass bead, second the uniformity of glass beads is greater than aggregates which means higher specific surface. This is also true in the case of mortar and mortar with 15% glass beads with the exception that the grain size in mortar is smaller than glass beads by 15%. The mortar with 35% glass beads shows intermediate behaviour between mortar and concrete materials.

Materials elastic moduli. The elastic moduli of materials can be also determined using an immersion through transmission setup. It is believed that immersion test produces more reliable results than others due to using (distilled) water as a testing medium which allows the waves to propagate without noticeable change in the wave amplitude. That means, the testing technique can be used effectively to determine the elastic constants which are useful in NDT and engineering applications. Figure 5-10 presents the results of the Poisson's ratio calculated based on the P-wave and S-wave velocities obtained from immersion measurements. In this figure, two velocity values are used to estimate the values of Poisson's ratio; the value from the first arrival and the value from the peak.

Figure 5-10 shows that values obtained using the first arrival time point have more variability than the peak point method and the latter is more consistent with regards to the results obtained. This can be attributed to the values of P-wave and S-wave velocities due to the inaccurate selection of the arrival point of the waves. The peak method relies on the maximum peak of the waveforms as shown in the immersion test results section. The maximum peak points are easier to identify than the first arrival signal.

Other elastic moduli, Young's modulus (E) and Shear modulus, can also be derived from the data obtained by the immersion measurements. Figure 5-11 illustrates their results which are also estimated using the determined values of P-wave and S-wave velocities.

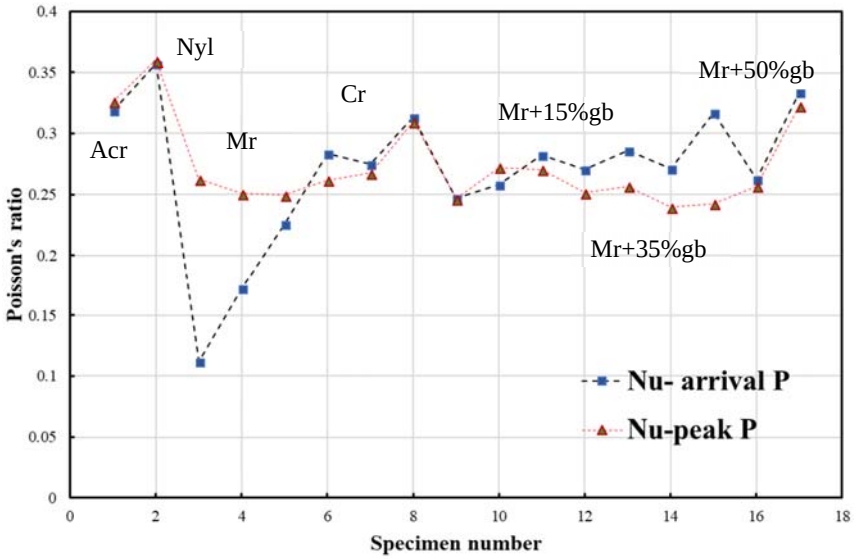

Figure 5-10. Results of Poisson's ratio of cement-based specimens.

Attenuation measurements of immersion test. In NDT testing it is important to investigate the attenuative behaviour of concrete to the propagated wave. This has received more attention with the time due to its significance in condition assessment of concrete elements. In this research, the examination of peak amplitude and spectrum area of the waveforms of the cement-based specimens obtained from immersion measurements provided interesting results with respect to the heterogeneity content and size.

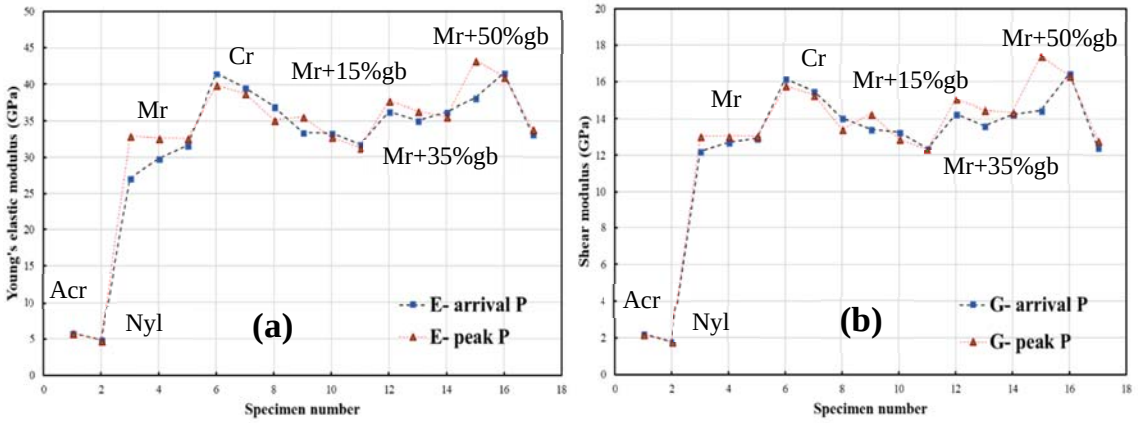

Figure 5-11. Elastic moduli of cement-based specimens (a) Young's modulus, (b) Shear modulus.

Coupling was assumed to be constant throughout the immersion experimental program and the same transducers are used; therefore, variations in the amplitude and spectrum can be related to the attenuative behaviour of the medium. This includes both absorption and scattering mechanisms which account for most of the total attenuation. Figure 5-12 represents the results of attenuation coefficients of cement-based specimens which are calculated using different procedures (amplitude method equation 2.24, Pedersen method equation 2.25).

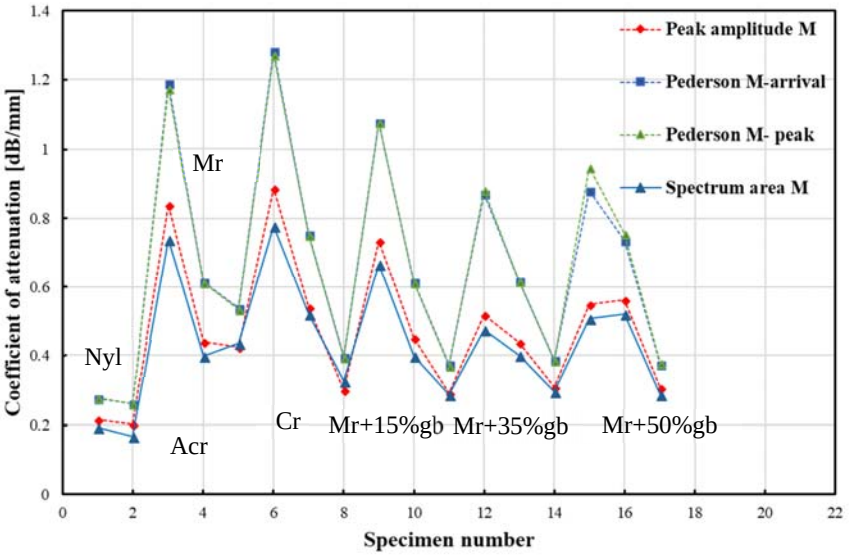

Figure 5-12. Results of attenuation coefficients of cement-based specimens.

From the results seen in this figure, the increase of grain size from reference specimens to cementitious specimens causes more attenuation to the propagated wave in the specimens. The trend is reversed when adding the glass beads to the mortar, which reduces the attenuative behaviour of mortar. This can be attributed to the higher acoustic impedance of the glass beads (around 14.5 MRayls) compared to the aggregate value thereby allowing more incident pressure to reflect at the surface of the glass beads and finally reach the opposite side of the specimens. The results show a linear reduction toward the mortar with 50% glass beads.

By a close examination of the results of attenuation methods, it can be noticed that Pedersen methods, which used both arrival time and peak points, lead to slightly higher values of attenuation coefficients than other methods which may be a result of the correction factor to account for the transmission loss effect. Moreover, the larger thickness of specimens influences the attenuation results that are obtained using the three procedures in which the Pedersen

method produces higher values in comparison to others. This effect can be related to the transmission loss term that is used in the Pedersen method.

5.3.2 Laser test results

Laser vibrometer (LV) provides a non-contact method to inspect a broad range of structures from a distance where accessibility is not possible. This technique can be used to acquire data from elements under investigation through waves that propagated either electromagnetically or acoustically. In the current research, LV is used to characterize the cementitious specimens by analysis of the waveforms and extract the parameters necessary to determine the P-wave velocity and attenuation parameters. Figure 5-13 shows the comparison between reference signal, obtained by testing the surface of the transducer, with the mortar and concrete signals.

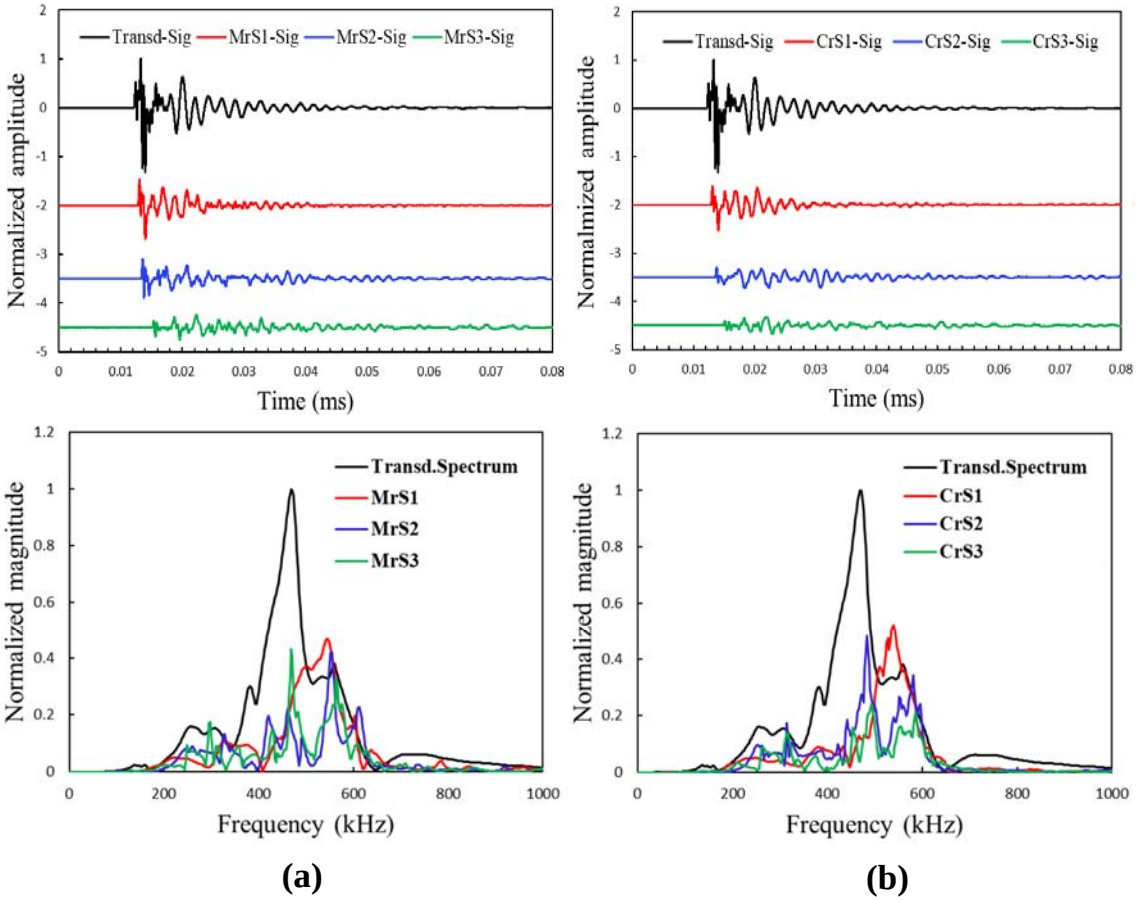

Figure 5-13. Typical laser waveforms of mortar and concrete specimens. (a) time signals and corresponding Fourier spectra of mortar, (b) time signals and corresponding Fourier spectra of concrete.

In Figure 5-13a, the thickness of mortar specimen influences the propagated wave and decreases its amplitude significantly as it was observed in immersion measurements. This behaviour

becomes more attenuative with the presence of coarse aggregates in concrete specimens as can be seen in Figure 5-13b. The spectra of waveforms here show different peaks in comparison to immersion spectra which have only one peak. This can be considered normal as the water in immersion allows only P-wave mode to propagate while the laser signal contains more wave modes. In addition, similar results can also be observed on the waveforms of mortars contain 15% and 50% glass beads as shown in Figure 5-14a & 14b.

Pulse velocity of Laser test. Figure 5-15 shows the P-wave velocities obtained from laser measurements of the cementitious specimens. The wave velocities are calculated by dividing the thickness of specimen over the travel time of the propagated wave. Cementitious specimens reveal average P-wave velocities close to 4650 (m/s).

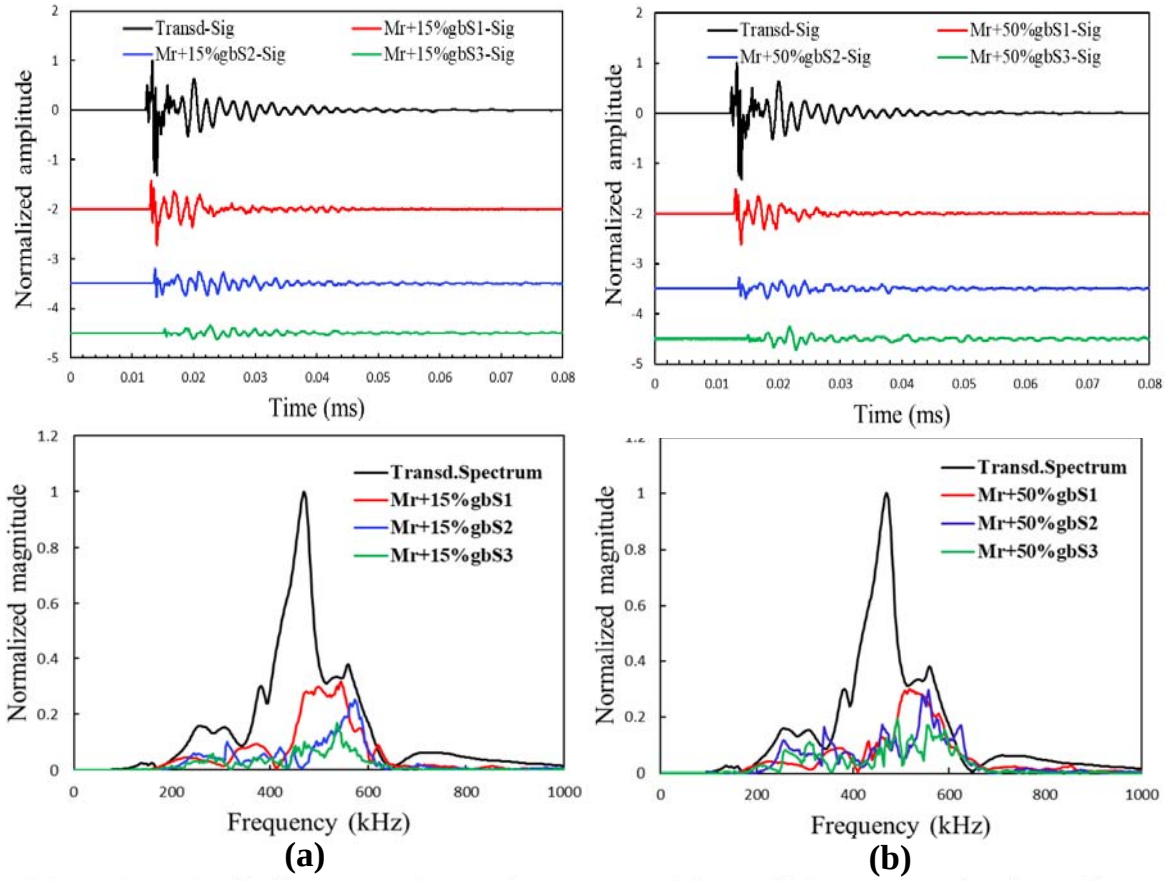

Figure 5-14. Typical laser waveforms of mortar containing 15% & 50% glass beads specimens. (a) time signals and corresponding Fourier spectra of mortar with 15% glass beads, (b) time signals and corresponding Fourier spectra of mortar with 50% glass beads.

Also, the presence of aggregates and glass beads produced slightly higher P-wave velocities by 150 (m/s) from its average. Also, the P-wave results illustrates there is a slight effect of thickness of specimen. This can be attributed to the heterogeneities (aggregates or glass beads)

that exist in these materials which has sizes on the order of the half wavelength of a 500 kHz pulse. By comparing the results of laser measurement with the dataset obtained from the immersion test, it can be noticed that laser calculate P-wave velocities slightly higher than immersion results.

Attenuation measurements of Laser test. In the present research, the LDV is also used to assess attenuation behaviour of cement-based specimens. The results are then compared with the values obtained in the immersion test. Figure 5-16 illustrates the results of attenuation coefficients of cement-based specimens which are calculated using only the amplitude method. From the results of this figure, the increase of grain size from reference specimens to cementitious specimens produces more attenuation to the propagated wave in the specimens. The trend is reversed when adding the glass beads to the mortar, which reduces the attenuative behaviour of mortar. This can be attributed to the higher acoustic impedance of the glass beads (around 14.5 MRayls) than aggregate value which allows more incident wave to reflect at the surface of the glass beads and finally reach the opposite side of the tested specimen.

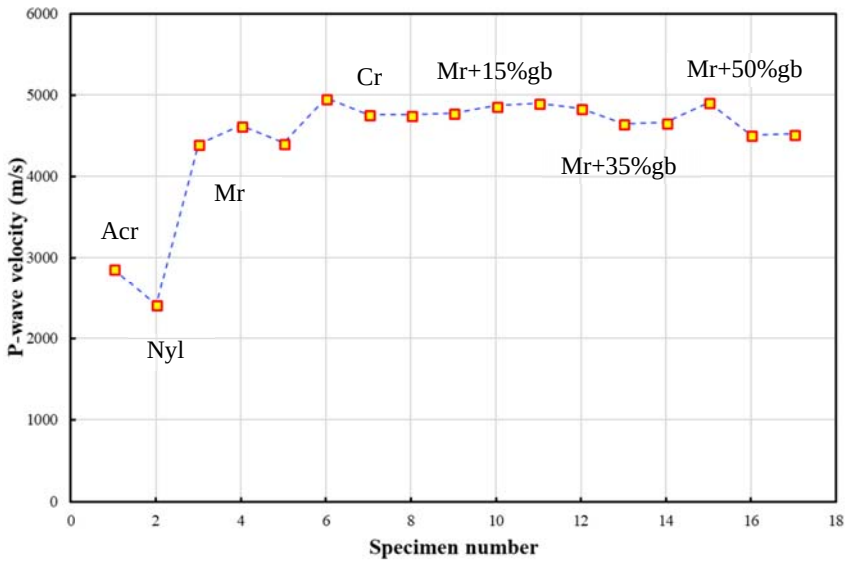

Figure 5-15. P-wave velocities of specimens obtained from laser measurements.

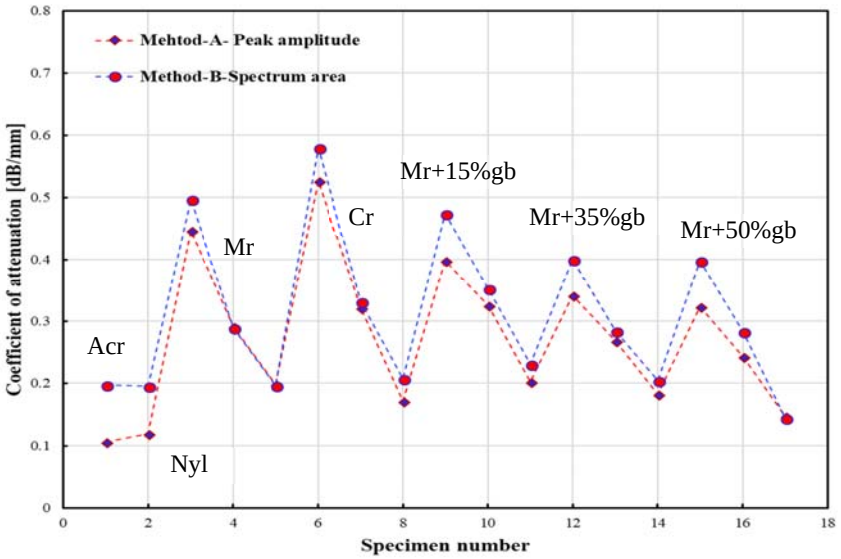

Figure 5-16. Laser results of attenuation coefficients of cement-based specimens.

Table 5-3 summarizes the results of attenuation coefficients obtained from immersion and laser measurements.

Table 5-3: Attenuation results of immersion and Laser measurements.

		Attenuation coefficient (dB/mm)			
Material	**Specimen**	Immersion (Peak M)	Immersion (Area S)	Laser (Peak M)	Laser (Area M)
Acrylic		0.43	0.19	0.2	0.1
Nylon		038	0.17	0.19	0.12
Mortar	S1-20 mm	1.58	0.74	0.5	0.44
	S2-40 mm	0.86	0.4	0.29	0.29
	S3-80 mm	0.88	0.44	0.2	0.2
Concrete	S1-20 mm	1.68	0.78	0.58	0.53
	S2-40 mm	1.1	0.52	0.33	0.32
	S3-80 mm	0.61	0.33	0.21	0.17
Mortar+15%gb	S1-20 mm	1.42	0.67	0.47	0.4
	S2-40 mm	0.84	0.4	0.35	0.33
	S3-80 mm	0.57	0.29	0.23	0.2
Mortar+35%gb	S1-20 mm	1.05	0.48	0.4	0.34
	S2-40 mm	0.86	0.4	0.28	0.27
	S3-80 mm	0.61	0.3	0.2	0.18
Mortar+50%gb	S1-20 mm	1.13	0.51	0.4	0.32
	S2-40 mm	1.11	0.52	0.28	0.24
	S3-80 mm	0.6	0.29	0.14	0.15

5.4 Summary

This chapter included the results of two procedures of tests, immersion through transmission and Laser vibrometer, intended to characterize cement-based materials. The characterization includes; materials' acoustic parameters, P-wave and S-wave velocities, materials' elastic moduli, and attenuation parameters. Two groups of specimens are tested; homogenous (acrylic, nylon, and mortar) and heterogeneous (concrete, and mortar with 15 %, 35%, 50% glass beads).

For testing with the immersion method, two different procedures (arrival time and peak points) were used to determine the acoustic parameters, wave velocities and attenuation parameters. The results obtained show that grain size plays an important role in the changing process of waveform amplitudes which causes a significance variability to the parameters calculated from this method. Also, the method proved to be a reliable technique to characterize cementitious materials, specifically in estimating the elastic moduli and attenuation coefficient of the cement-based materials being tested.

In the case of the Laser vibrometer testing, the observed results for P-wave velocities and attenuation measurements exposed different trends. For example, the grain size effect on the propagated wave has less influence than the ones noticed in the immersion test. While, the attenuation results reveal overestimated coefficients which can be attributed to many factors such as laser electronic effect and coupling concern between the transmitter and specimen under investigation. Nevertheless, the estimated P-wave velocities are in good match with the immersion measurements. On the other hand, the laser testing technique requires more careful study in characterization of cement-based materials to reduce any uncertainty.

Chapter 6: Study of ultrasonic techniques sensitivity to internal damage

In this chapter, the ultrasonic pulse velocity (UPV) and laser Doppler vibrometer (LDV) experiments performed on specimens of unreinforced concrete (cylindrical and prismatic) are described. The main goal of these experiments was to verify the adequacy of ultrasonic techniques to evaluate internal damage in concrete specimens. Two categories of damage were investigated: freeze-thaw and compression damage.

6.1 Introduction

In a multi-phase material like concrete, the cracking behavior is dependent primarily on the characteristics of its components. A variety of causes can form cracks in concrete specimens, these include; application of external load, temperature variations leading to volumetric changes, and internal chemical reactions because of aggressive chemicals entering concrete (Sih and Ditomasso, 1984; Li and Shah, 1994; Shields et al., 2018). In concrete it is well known that larger cracks can be developed due to the propagation of small cracks under unusual conditions (Puri and Weiss, 2006; Neville, 2011). Different nondestructive methods have been used to better understand cracking behavior within cementitious medium such as visual evaluation, ultrasonic pulse velocity (UPV), acoustic emission, resonant frequency, and microscopic analysis (Yang, 2004; Pour-Ghaz, 2011; Hwang et al., 2018). At low strains, wave propagation parameters depend on the elastic material properties (Santamarina *et al.*, 2001; Breysse, 2012; Slawinski, 2010). Among the NDT methods, the UPV method is most commonly used in practice (ACI 228.2R-13, 2013; Bungey *et al.*, 2006), in medicine, chemistry, physics, biology, and engineering. The UPV method is used in this study to monitor the damage in unreinforced concrete specimens under controlled laboratory conditions. The UPV technique is generally used in accordance with the ASTM C 597-16 and American Concrete Institute standard ACI 228.2R-13 to assess the quality of natural rocks and concrete elements (Hertlein, 2013; Malek and Kaouther, 2014), to quantify environmental impacts on geomaterials and concrete (Chen *et al.*, 2015; Duan *et al.*, 2011), and to determine material elastic properties (Ensminger and Bond, 2011). In this study, two types of damage are investigated: freeze-thaw and compression damage to study the sensitivity of UPV and LDV techniques to internal cracks in specimens of unreinforced concrete.

For decades, the freeze-thaw processes in concrete have been studied thoroughly to understand their effects on the mechanical properties of concrete, such as deformation capacity, strength,

and stiffness. Because concrete is a porous medium, this allows water and moisture to be absorbed by the intrinsic pores and shrinkage cracks that previously formed due to the hydration processes. Different approaches are used to mitigate the effect of freeze-thaw cycles on the mechanical properties of concrete, such as, air entrainment, decreasing water-cement ratio, and increasing curing time (Saboori, 2015). The most important procedure identified in the literature that shows significant impact on concrete durability is adding an air entraining agent. More air bubbles are produced in concrete when an air-entraining agent is added. This causes concrete to be more durable against the freeze-thaw cycle effects. The outcome of this procedure is to reduce the hydraulic pressure that accompanies the freeze-thaw process.

Several researchers (Hasan et al., 2004; Shang and Song 2006; Hasan et al., 2008; Duan et al., 2011; Liu and Wang, 2012) quantitatively studied the influence of freeze- thaw cycles on the mechanical properties of concrete. Shang and Song (2006) reported the impact of using freeze-thaw cycles (25, 50, and 75) on the strength, stiffness, and deformation performance of concrete specimens under biaxial compression. To make concrete more resistive to the freeze-thaw process, ACI E4-16 recommends adding an air-entraining agent to concrete within a range of 0.015% - 0.13% by cement mass. Many researchers (Shang and Song, 2008: Shang et al., 2009; Wong et al., 2011; Shang and Yi, 2013; Sonia et al., 2015) investigated the effect of adding different percentages (from 0.1 to 0.5) of air-entraining agent to concrete subjected to freeze-thaw cycles. The experimental data of these works demonstrate that durability of concrete enhanced significantly against freeze-thaw process when adding more air-entraining agent, while the strength of concrete is decreased. In this research project, three percentages (0.1%,0.15%,0.25% by cement mass) of air-entraining agent (Sika AERCA) are added to concrete specimens to evaluate the cracks induced under freeze-thaw cycles using ultrasonic pulse velocity and laser vibrometer methods.

Silica fume is another material that used widely as a supplementary cementitious material in concrete which strengthens the weak interfacial zone between cement paste and aggregate. Adding silica fume improves concrete properties by enhancing microstructure in the interfacial region, decreasing the permeability, and improving the durability (Lamond and Pielert, 2006; Siddique, 2011). Numerous studies have described the bond improvement effect of silica fume used in reinforced concrete (Aldred et al, 2006; Abadjiev et al., 1993; Sfikas and Trezos, 2013). Bentur et al. (1987) pointed out that the strength gain in concrete due to silica fume is greater than that of cement paste and attributed that to the modification of aggregate role in concrete. The influence of different silica fume contents (0, 6, 10, and 15%) on the compressive strength

of high performance concrete is also studied over a period of 400 days of aging (Mazloom et al., 2004). They reported that strength of silica fume concrete at early age (28 days) was stronger 21% than baseline concrete, while after the age of 90 days the strength development in silica fume concrete was negligible. Similar conclusions were observed by Hooton (1993) who used concrete specimens containing 0, 10, 15, and 20% silica fume. Based on a review of previous works, four silica fume contents (0, 5, 10, 20% by mass) are selected in this study to understand the cracking behaviour under compression load.

Several reasons can cause degradation or deterioration in concrete such as compression loading, fatigue cycling of low-level, and thermal loading. Compression loading is one of these causes that normally deteriorates concrete and produces distributed microscopic damage. This type of damage is often lead-up to large defects such as scaling, delamination, spalling, and cracks which can end up with the loss of concrete integrity (Selleck et al., 1998; Shah and Ribakov, 2009). The occurrence of cracks can be initiated near the end of material life. Once started, a catastrophic failure can occur due to the relatively fast growth of this crack. Therefore, it is recommended to investigate cracks in concrete at an earlier stage or even before the initiation of the crack that occurs in the microstructure level (Meyendorf et al., 2013).

Conventional acoustic non-destructive testing methods have been applied successfully to evaluate damage in concrete under compression load such as UPV, pulse-echo, and acoustic emission. The most common of these methods being used in concrete studies is the UPV technique (Malhotra and Carino, 2004). It is traditionally known that the ultrasonic pulse velocity is used as an indicator to quantify damage in concrete and this parameter is used extensively as a baseline for field studies using equipment to inspect concrete structures. Nevertheless, many researchers have pointed out that velocity alone cannot complete the picture of damage in concrete (Santhanam, 2010; Kirlangic, 2013; Maria, 2017). Therefore, using another ultrasonic parameter such as wave attenuation is essential for a reliable procedure to detect damage in concrete.

Knab et al., (1983) studied the capability of ultrasonic methods to detect cracks in concrete by performing laboratory experiments. They employed wave velocity and signal amplitude to evaluate concrete conditions in two orientations: parallel and normal to the plane of a crack. Both parameters provided useful information about the degree of damage. Other studies (Tharmaratnam and Tan, 1990; Popovics et al., 1990; Qasrawi and Marie, 2003; Sanathanam, 2010; Maria, 2017) reported that wave attenuation is more sensitive to damage than wave

velocity in concrete specimens subjected to uniaxial compression load. Though, the findings of previous studies have shown important information about using wave attributes to detect damage, these studies depended on using a pair of ultrasonic transducers which may not be enough to study the damage level in concrete because damage is estimated using a single wavelength value. It is essential to understand the behavior of cracking under compression load using an array of transducers with different nominal frequencies (different wavelengths) which is rarely reported in the literature.

In this present study, the main ultrasonic wave characteristics (wave velocity and attenuation) are employed to study the damage mechanism in unreinforced concrete specimens (cylindrical and prismatic) subjected to two different laboratory conditions: freeze-thaw cycles and uniaxial compression load. Ultrasonic pulse velocity and laser Doppler vibrometer measurements are taken in different approaches to better understand the interaction between ultrasonic wave and internal damage in concrete specimens. Furthermore, there is no data reported in the literature about using the laser vibrometer to evaluate damage in concrete specimens subjected to freeze-thaw cycles and uniaxial compression load.

6.2 Experimental procedure

6.2.1 Specimen preparations

Sixteen hardened concrete specimens (unreinforced) are made with designed mixture proportions that contain two different chemical admixtures: air-entrained (Sika AERCA) and silica fume (Sikacrete 950 DP) as shown in Table 6.1. Eight of these specimens are standard cylindrical (10 cm x 20 cm) and the remaining are prismatic (41 cm x 8 cm x 10 cm). For the freeze-thaw testing program, four cylinders and four prisms are prepared by adding four different air-entrained agent ratios 0, 0.1, 0.125, 0.25% by cement mass to the concrete mixture. Another set of specimens (four cylinders and four prisms) are also prepared for the compression testing program by mixing the concrete batch with four different silica fume agent ratios 0, 5, 10, and 20% by cement mass. All concrete mixtures, which are designed according to American concrete institute (ACI) code 211.1R-91, contain a Portland ASTM type I cement, fine and coarse aggregates with 12.5mm nominal aggregate size, and water/cement ratio of 0.40 by mass. Table 6.2 shows the physical properties of the aggregates used in the mixtures. The

designed mix parameters are 35 MPa compressive strength at age 28 days, slump rate ranging from 75 to 100 mm, and air content from 5% to 8%.

Table 6.1: Mix proportions of concrete specimens.

Name	Admix.- (%, g/m^3)	Cement (kg/m^3)	Fine agg. (kg/m^3)	Coarse agg. (kg/m^3)
C1-AR	AER*-(0, 0)	2.5	3.6	4.4
C2-AR	AER-(0.1, 3)	2.5	3.6	4.4
C3-AR	AER-(0.125, 4)	2.5	3.6	4.4
C4-AR	AER-(0.25, 6.5)	2.5	3.6	4.4
B1-AR	AER-(0, 0)	4.95	7.2	9
B2-AR	AER-(0.1, 5)	4.95	7.2	9
B3-AR	AER-(0.125, 7)	4.95	7.2	9
B4-AR	AER-(0.25, 12.5)	4.95	7.2	9
C1-SF	SF**-(0, 0)	2.3	4	4.4
C2-SF	SF-(5, 120)	2.18	4	4.4
C3-SF	SF-(10, 240)	2.06	4	4.4
C4-SF	SF-(20, 360)	1.94	4	4.4
B1-SF	SF-(0, 0)	4.6	8	9
B2-SF	SF-(5, 230)	4.37	8	9
B3-SF	SF-(10, 460)	4.14	8	9
B4-SF	SF-(20, 690)	39.1	8	9

*Air-entrained admixture.
**Silica fume admixture.

6.2.2 Equipment description

Freeze-thaw chamber. The concrete specimens prepared for this research were subjected to eight weeks of freeze-thaw cycles. Each accelerated freeze-thaw cycle is simulated over one day (24 hours) with a gradual temperature variation set to be increased gradually from -25 C to +25 C with ±2 C^o (Figure 6-1). For this purpose, a commerical small freezer were modified to use as a freeze- thaw chamber which includes adding an electric heater inside to make sure the temperature reached the level required during thaw process. Both freezer and heater are connected to electrical-switch timers that control the operation period which was set to 8 hours for freezeing and 14 hours for thawing. Figure 6-2 shows the commercial feerzer that was used as the freeze-thaw chamber.

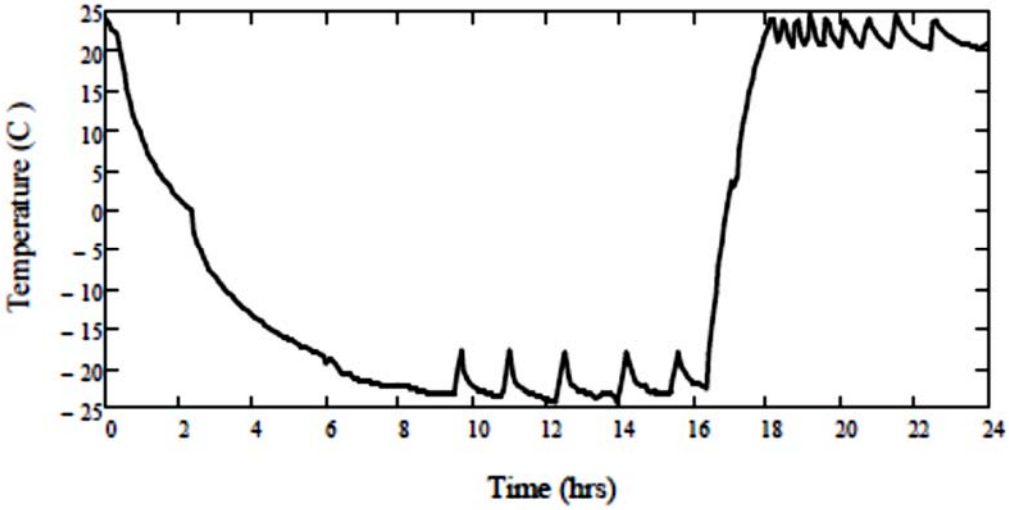

Figure 6-1. Temperature variation recorded during one freeze-thaw cycle (24 hours).

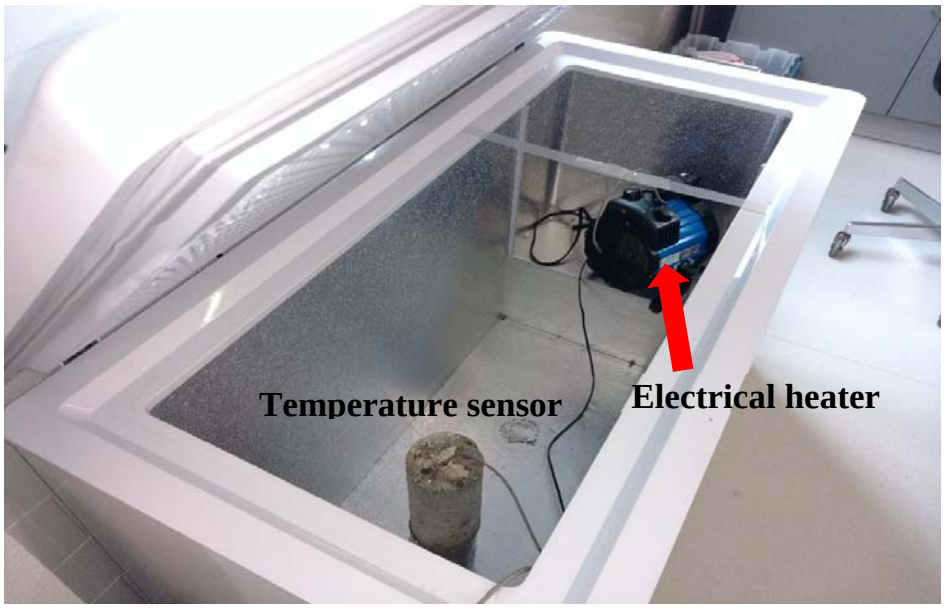

Figure 6-2. Modified commercial freezer used as freeze-thaw chamber.

Compression machine test. The silica fume concrete specimens were tested using a new compression machine MTS600kN (Figure 6-3). This machine can apply a static load up to 600 kN which is adequate to produce cracks inside the concrete specimens tested under this machine. Also, it can be programmed to perform different tasks according to the purpose of testing. For current research, the strain control test is utilized with a strain rate of 0.002 mm/min, where the displacement and corresponding load are recorded continuously.

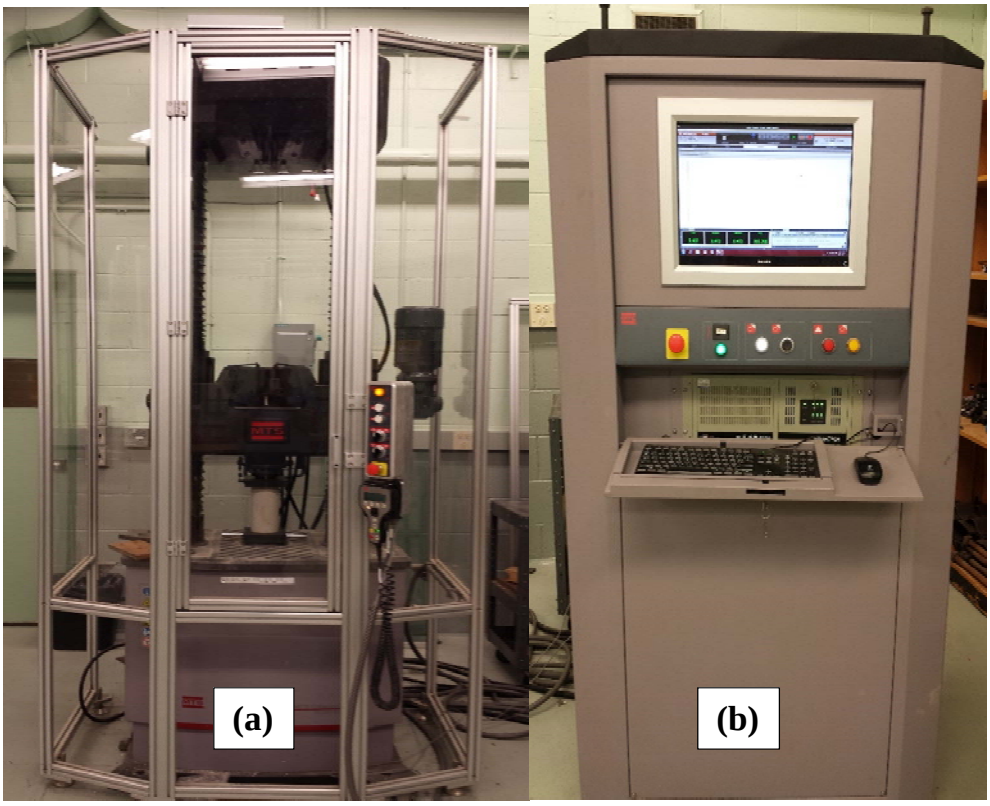

Figure 6-3. Compression machine MTS600KN. (a) the main frame of the machine, (b) the control station.

Laser vibrometer setup. The laser experiment setup that was used to test the concrete specimens consisted of: laser vibrometer interferometry which includes laser head (Ploytec OFV-534), vibrometer controller (Ploytec OFV-2570), data management system, vibration isolated workstation, and high-resolution positioning controller, wave generator (Keysight), amplifier (Krohn-Hite), and a piezo driver. Also used was a set of piezoelectric transducers with a nominal resonance frequency 54 kHz, 150 kHz, 250 kHz, and 500 kHz (CX484P) made by UTX. These transducers were glued to one side of the concrete specimen being tested, using super glue Loctite instant adhesive for consistent coupling (Krautkrämer and Krautkrämer, 1990) and the laser received the displacement history from the surface of a reflective tape placed on the opposite surface of the specimen. The testing setup of the laser vibrometer shown in Figure 6-4 is used to take laser ultrasonic measurements.

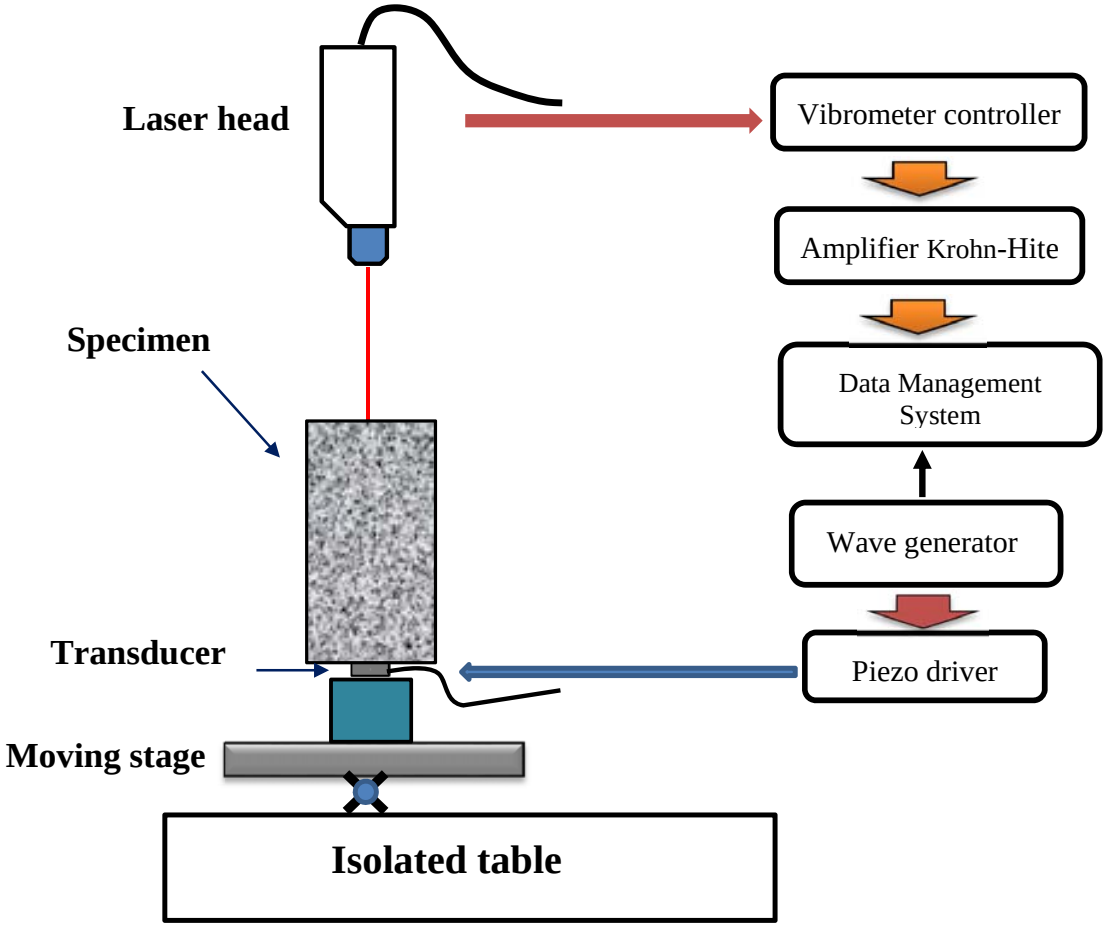

Figure 6-4. Laser Doppler vibrometer testing setup.

***Ultrasonic pulse velocity setup*.** The UPV setup used to take ultrasonic measurements includes two configurations; Single and multi-measurement setups. The first setup consists of a set of four piezoelectric transducers, a function generator, a piezo driver, a digital oscilloscope, and a computer (Figure 6-5). Four piezoelectric transducers (nominal resonance frequency 54 kHz, 150 kHz, 250 kHz, 500 kHz) are used in this study. They are placed on opposite sides of concrete specimens, using Sonotech Ultragel II® for consistent coupling (Krautkrämer and Krautkrämer, 1990). The second setup includes the same set of transducers used in first setup, with the addition of a high-speed data acquisition (Genesis, 24 channels), a function generator, a piezo driver and a computer (Figure 6-6). The setup is employed to take UPV measurements when the concrete specimens are subjected to uniaxial compression loading.

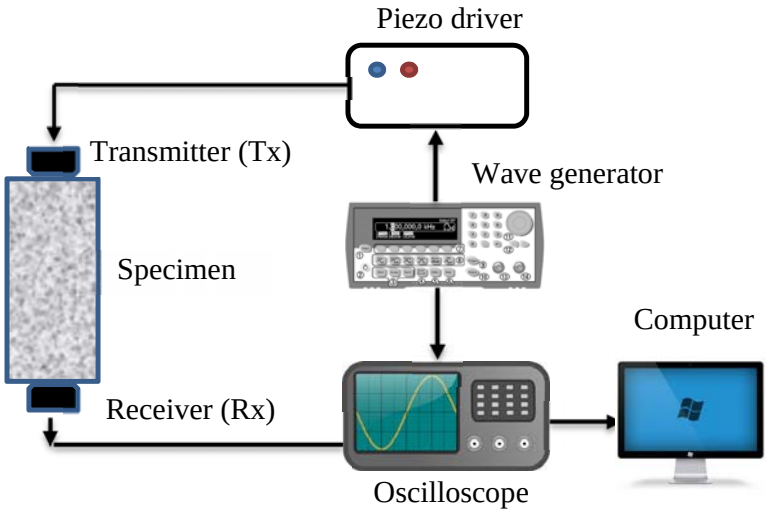

Figure 6-5. UPV instrumentation testing setup (single measurement setup).

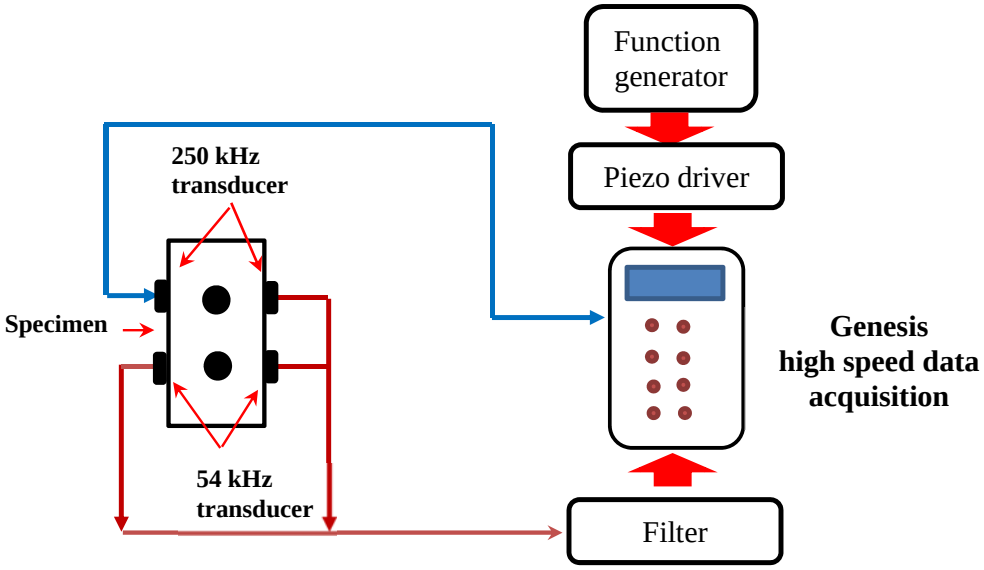

Figure 6-6. UPV instrumentation testing setup (Multi-measurement setup).

6.2.3 Testing Methodology

The testing procedure includes two phases; evaluation of microcracks induced by freeze-thaw cycles and evolution of macrocracks under compression load in cylindrical and prismatic unreinforced concrete specimens. The first phase consists of two testing procedures; UPV and laser Doppler vibrometer to monitor freeze-thaw effect on a weekly basis, and laser Doppler vibrometer to evaluate the condition of concrete specimens before and after the freeze-thaw

period. Eight unreinforced concrete specimens (four cylindrical and four prismatic) are tested. Both sides of each specimen are polished, and any void found is treated with a cement paste. Then, a thin aluminum disc (diam 8 cm and thick 2.5 mm) is glued to one side using concrete epoxy. The purpose of using the disc is for laser measurements to allow gluing of the transducers to the specimens to obtain consistent readings and to avoid causing any damage to the surface of specimen. Before exposing the specimens to the effect of freeze-thaw, all specimens are immersed in a water tank for four days to accelerate the impact of freeze-thaw cycles. Then they were removed from the tank to record the weights and perform the first UPV and laser measurements using four pair of transducers 54 kHz, 150 kHz, 250 kHz, and 500 kHz.

For laser testing, a layer of reflective tape, very sensitive to vibration, is placed on one side of specimen with caution to avoid any air bubble forming under the tape which can significantly affect the laser signals. The number of points scanned with the laser are 241 points for cylinder specimens distributed using polar coordinate system, while 143 points are utilized in prisms based on a rectangular coordinate system. After that, each concrete specimen is wrapped with a thin layer of nylon sheet to keep the moisture inside specimen stable and prevent any loss. Then specimens are placed inside the freezer for an exposure period of eight weeks. UPV measurements are taken on weekly basis. A square-wave voltage pulse is used as the electrical excitation of the piezo elements; calculations in time and frequency domains are used to evaluate changes in wave velocity and wave attenuation (Krautkrämer and Krautkrämer, 1990). 3D printed transducer holders are built to maintain a constant contact pressure on both transducers. Sonotech Ultragel II® is applied between the transducers and concrete specimen surfaces to improve the coupling and reduce signal losses. The electrical excitation consisted of a single cycle square pulse generated by the function generator, with a nominal resonance frequency and amplitude corresponding to the transducer being used. Table 6-1 summarizes the testing parameters of the UPV procedure. The electrical excitation used with laser vibrometer is similar to the one used in UPV testing. To minimize the effect of random noise and enhance signal quality, 16 readings are averaged for each UPV measurement and 100 for laser measurement. The time signal is then converted to a frequency spectrum for each signal using the fast Fourier transform (FFT).

Table 6-1. Excitation parameters of UPV procedure.

Transducer	Excitation frequency (kHz)	Pulse amplitude (V)
54	62	50
150	144	50
250	245	100
500	500	100

In Phase two, the concrete specimens with silica fume are tested under compression load. The damage is evaluated using two approaches; UPV and laser vibrometer measurements. In the UPV approach, two testing procedures are followed; first, specimens are tested before and after and second UPV measurements taken during the application of load using the same pairs of transducers that were used in freeze-thaw testing. The purpose of first UPV procedure is to evaluate the evolution of cracks parallel to the load application. Prior to testing, each specimen surface is polished from one side and any void found is treated with cement paste. On the opposite side, the same disc of aluminum that was used with freeze-thaw specimen group is also used here. In addition, eight aluminum discs (diam 1.5 cm and thick 2 mm) are glued around each specimen using concrete epoxy and distributed as shown in Figure 6-7.

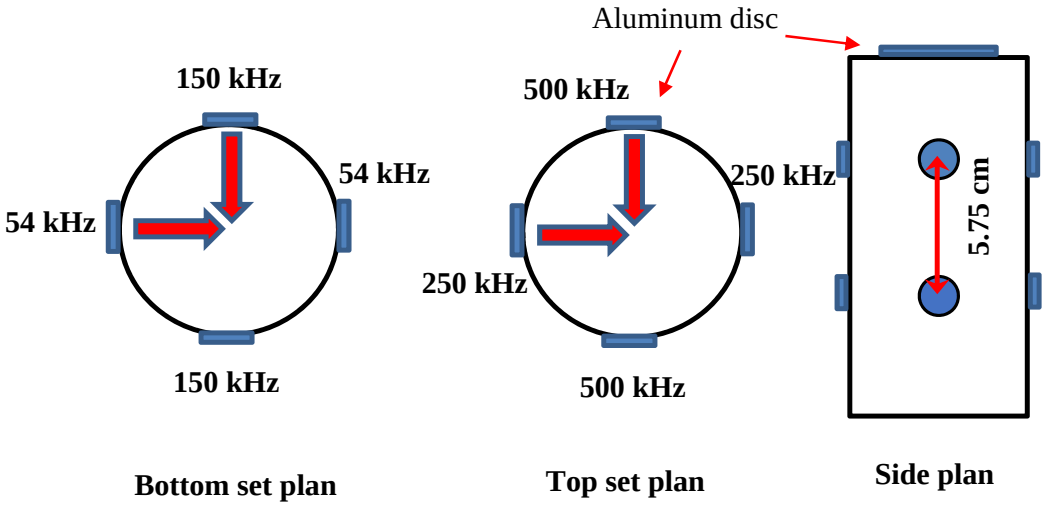

Figure 6-7. Typical outline of concrete specimen with distribution of aluminum discs and transducers. Red arrows are the triggering directions.

These discs are used to glue the transducers when taking UPV measurements under compression load.

In the second UPV procedure, the testing setup is different in that it uses a high-speed data acquisition system (Genesis) which contains 24 channels to take measurements instantly. For current research, only 9 channels are used to obtain UPV measurements. The procedure includes taking several UPV measurements in a mutual process at predefined load steps. For example, at each load step, first the system triggers by sending a one cycle square pulse through the 54 kHz which used as a transmitter and using the other transducers to receive waveforms. Then, the same steps are repeated with other transducers 150 kHz, 250, and 500 kHz in which different orientations are scanned to monitor the changes in wave velocity and wave attenuation corresponding to the evolution of cracks under the applied load. Finally, the laser approach is performed in the same manner that followed with the freeze-thaw process.

6.3 Experimental results

6.3.2 Freeze-thaw results

Pulse velocity results. Figure 6-8 represents the variation of the ultrasonic pulse velocities obtained from the UPV measurements using 54 kHz and 500 kHz of cylinder specimens during the testing period.

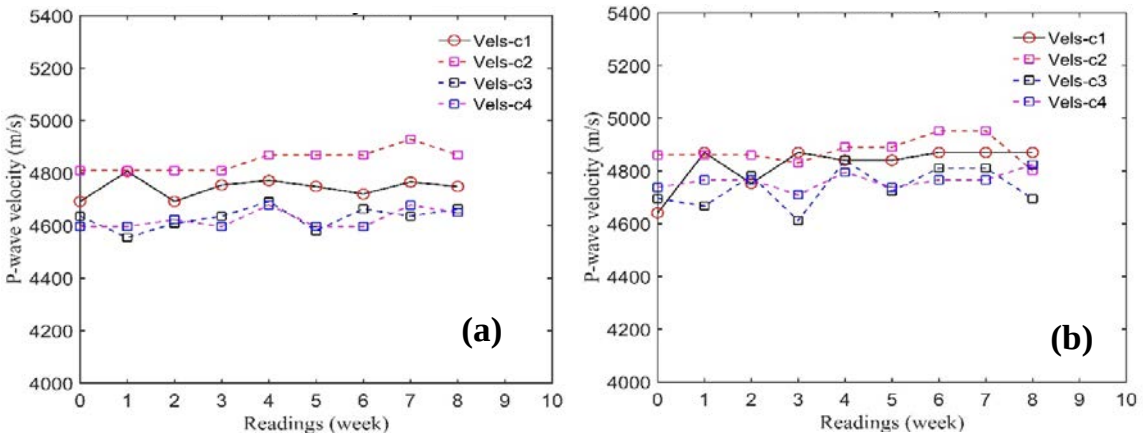

Figure 6-8. Typical variations of ultrasonic velocity for concrete specimens with and without air-entrained. (a) using 54 kHz probe, (b) using 500 kHz probe.

The figure illustrates the difficulty of using the change in wave velocity to monitor microcrack evolution in concrete specimens during the complete period of study. This trend was also observed with prism specimens and with other measurements that used 150 kHz and 250 kHz transducers even when the concrete mixture includes air-entrained agent. Therefore, the change in the velocities cannot be used as a reliable procedure to evaluate the damage related to the

freeze-thaw cycles. It is necessary to investigate another parameter such as wave attenuation that can be used effectively to evaluate the frost damage in concrete.

Attenuation measurements. The investigation of frost damage in concrete has received more attention with time because of its significance in condition assessment of concrete elements. In this research, the examination of peak amplitude and spectrum area of the waveforms obtained from testing concrete specimens treated with air-entrained agent using UPV method exposed interesting results. Figure 6-9 illustrates the typical time signals and their corresponding Fourier spectra of cylinder concrete specimens.

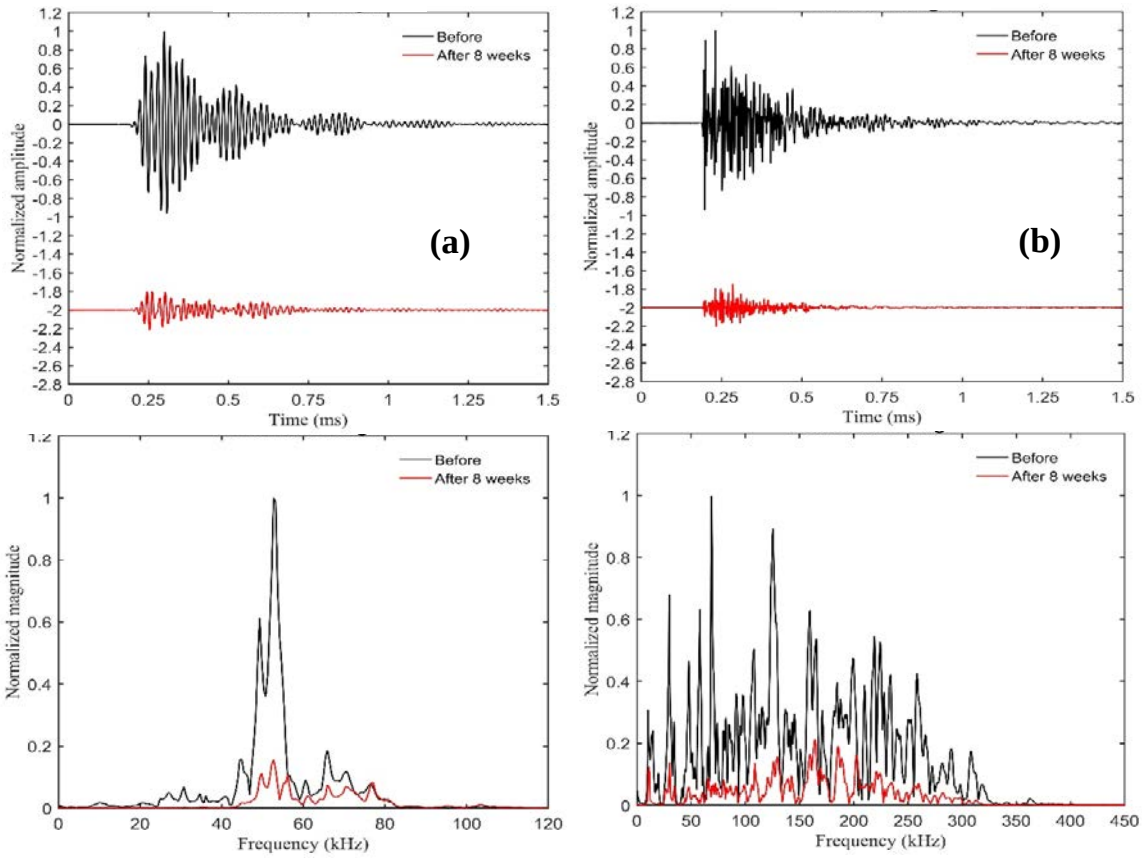

Figure 6-9. Typical waveforms of untreated cylinder concrete specimen before and at the end of the period of study. (a) time signals and corresponding Fourier spectra of 54 kHz transducer, (b) time signals and corresponding Fourier spectra of 250 kHz.

The figure reveals that even with different wavelengths (λ = 8 cm for 54 kHz, λ = 2 cm for 250 kHz), both results show similar indications of the damage induced by the freeze-thaw cycles by a reduction in magnitude (around 80% reduction in magnitude of the amplitude and Fourier spectrum). This trend is noticed in the same manner with other transducers at 150 kHz and 500 kHz for the same intact cylinder concrete specimen.

On the other hand, the results shown in Figure 6-10 which are related to treated specimen with 0.1% of air-entrained, the change in amplitude and spectrum are less pronounced than what was observed with the untreated specimen. This is an indication of the influence of the air-entrained agent which produces more air bulbs that reduce the hydrostatic pressure present in pores.

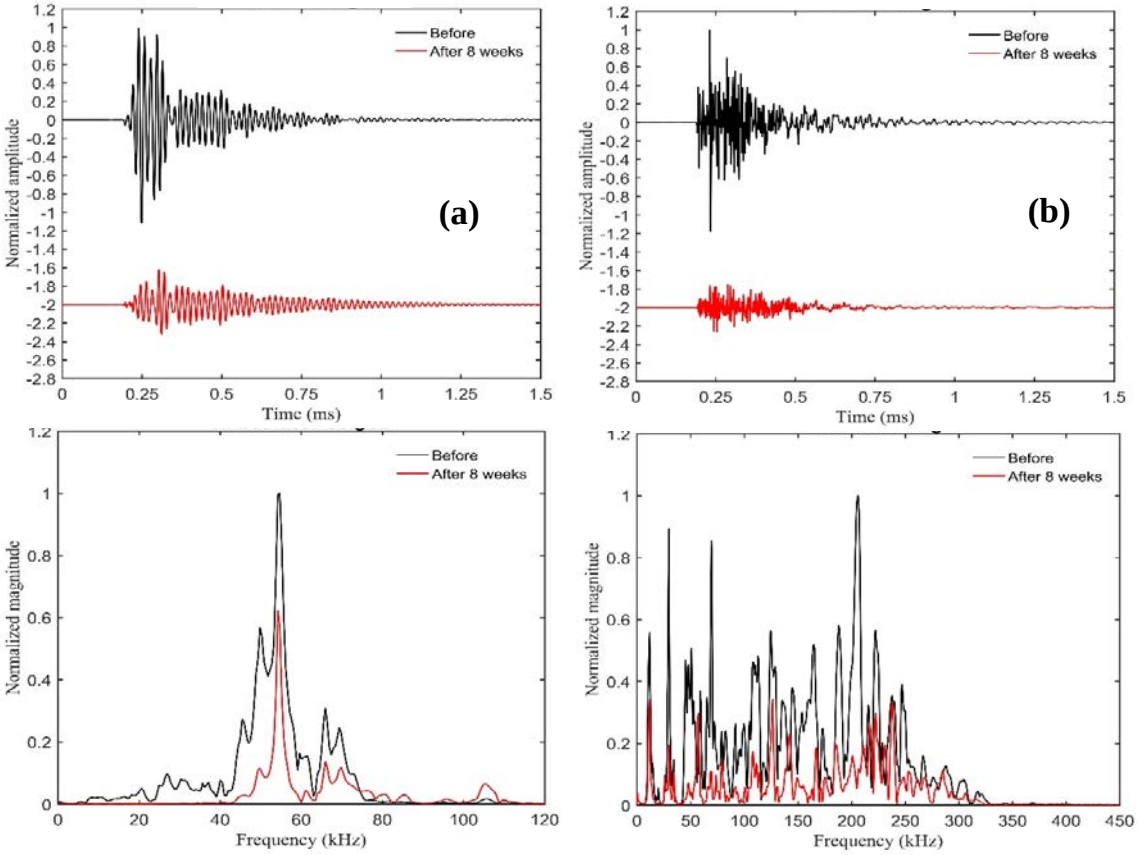

Figure 6-10. Typical waveforms of treated cylinder concrete specimen with 0.1% air-entrained before and at the end of the period study. (a) time signals and corresponding Fourier spectra of 54 kHz transducer, (b) time signals and corresponding Fourier spectra of 250 kHz.

Figure 6-11 shows the total attenuation measurements obtained from testing cylinder specimens (C1, C2, C3, C4) during the period of the study using 54 kHz transducer. The attenuation is computed using two procedures; amplitude method and spectrum area methods. In the first procedure, the maximum amplitude in time domain is used to investigate the frost damage, while in the spectrum procedure the area under Fourier spectrum is utilized to evaluate the freeze-thaw effect.

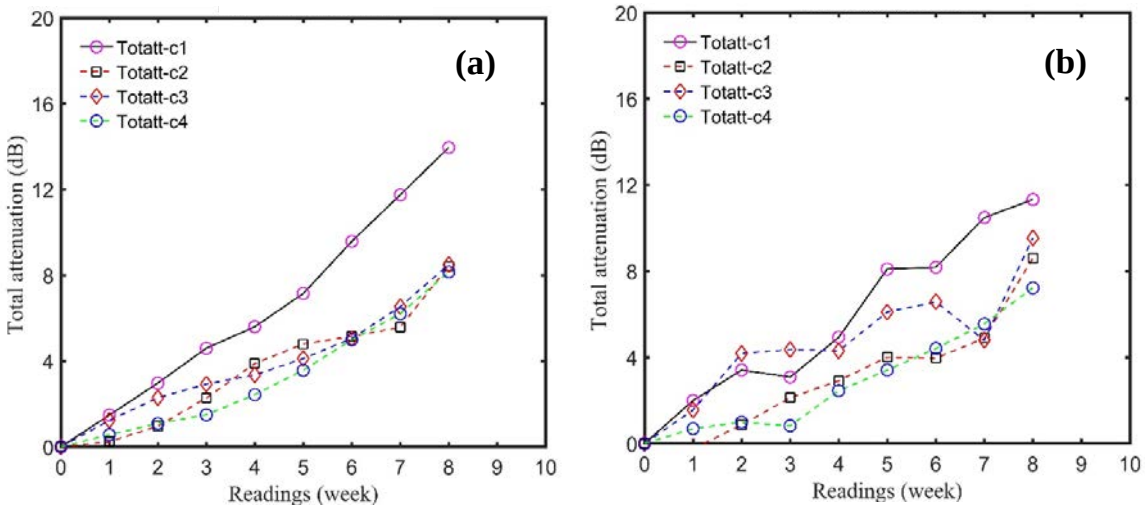

Figure 6-11. Typical total attenuation of cylinder concrete specimens using 54 kHz transducer. (a) amplitude method, (b) spectrum area method.

In Figure 6-11a, the amplitude method shows more sensitivity in comparison to the spectrum area to the accumulated freeze-thaw damage in the cylinder untreated with air-entrained (around 30%), while the trend is almost similar for both methods. In addition, the results in amplitude method are consistent and exposed a linear trend of deterioration due to the accumulated freeze-thaw damage. On the other hand, Figure 6-12 presents the results of testing cylinder specimens with 250 kHz. In contrast to the 54 kHz results, the finding indicates that all specimens experienced accumulated damages with different levels. The addition of air- entrained has less improvement to concrete resistivity to frost action than what was noticed with lower frequency (54 kHz). This can be attributed to the amount of air bubbles produced in concrete which attenuates the propagated waves with wavelength ($\lambda \approx 2$ cm). This observation is also identified with other high frequency transducers. The results highlight the importance of careful selection to the frequency range used to monitor the impact of freeze- thaw process.

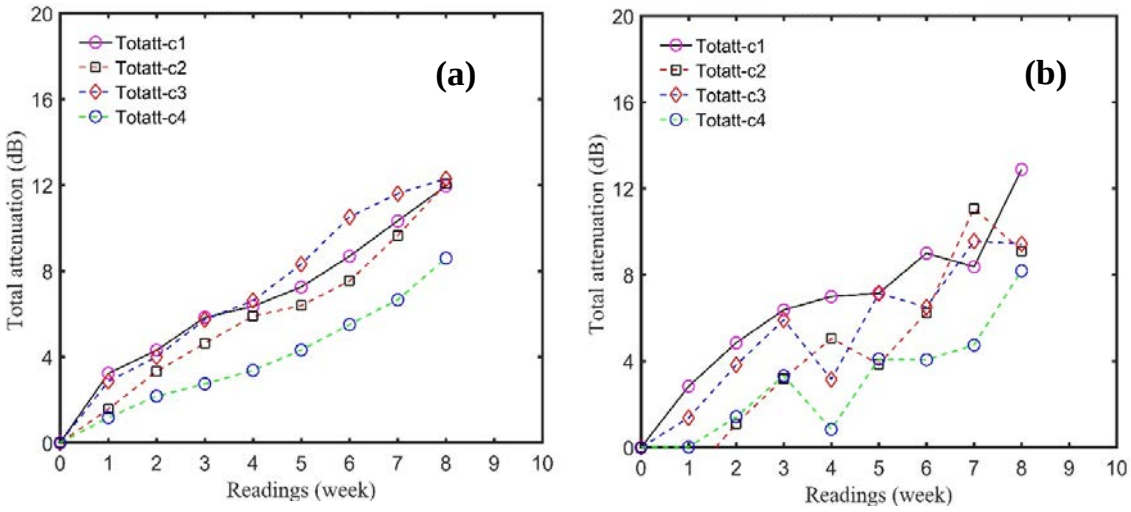

Figure 6-12. Typical total attenuation of cylinder concrete specimens using 250 kHz transducer. (a) amplitude method, (b) spectrum area method.

Laser vibrometer results. In the current research, the laser technique is selected to monitor the change in wave velocity and wave attenuation as it occurs due to the freeze-thaw cycles. Laser Doppler vibrometer (LDV) offers a non-contact procedure to measure the vibration in the out-of-plane surface based on the Doppler shift phenomenon which allows us to determine the velocity of the object surface under study.

Figure 6-13 illustrates the vibration mode obtained from laser measurement of untreated cylinder specimens using a 54 kHz transducer. The results of laser measurement reveal the level of attenuation that occurs to the propagated wave received by the laser to be around 75% of the initial displacement. The laser permits identification of which areas exhibit more signs of damage than others on the same surface. This is localization is difficult or not possible to obtain with UPV testing methods. Even with the attenuative behaviour of concrete, the vibration response of the intact case shows a mode shape like the mode of vibration observed when the transducer surface is scanned with laser. After the specimen was exposed to eight weeks of freeze-thaw, the vibration shape is noticeably lowered and implies more vibration modes.

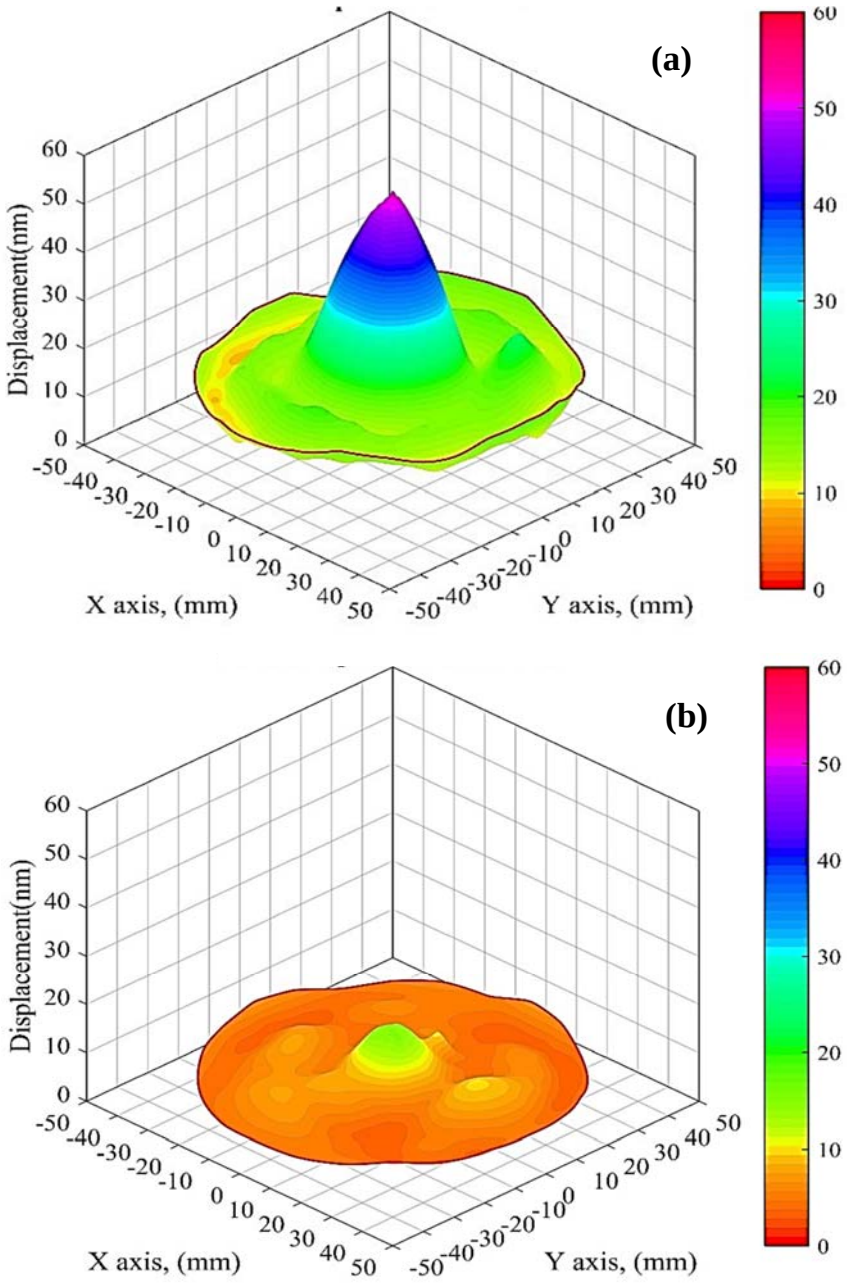

Figure 6-13. Typical vibration modes of untreated cylinder specimen using 54 kHz. (a) before freeze-thaw process, (b) after 56 freeze-thaw cycles.

Moreover, other procedures were implemented on the LDV results to investigate the damage of freeze-thaw effect. These involved computing the total attenuation using peak amplitudes and areas under Fourier spectra as shown in Figure 6-14. The figure is plotted using contour lines that clearly show the areas (marked with black circles) more influenced by the accumulated damage of the freeze-thaw process. In Figure 6-14a, the peak amplitudes show

better results than what are observed using the spectrum method. This is a significant advantage of the laser vibrometer to identify the damage caused by external factors.

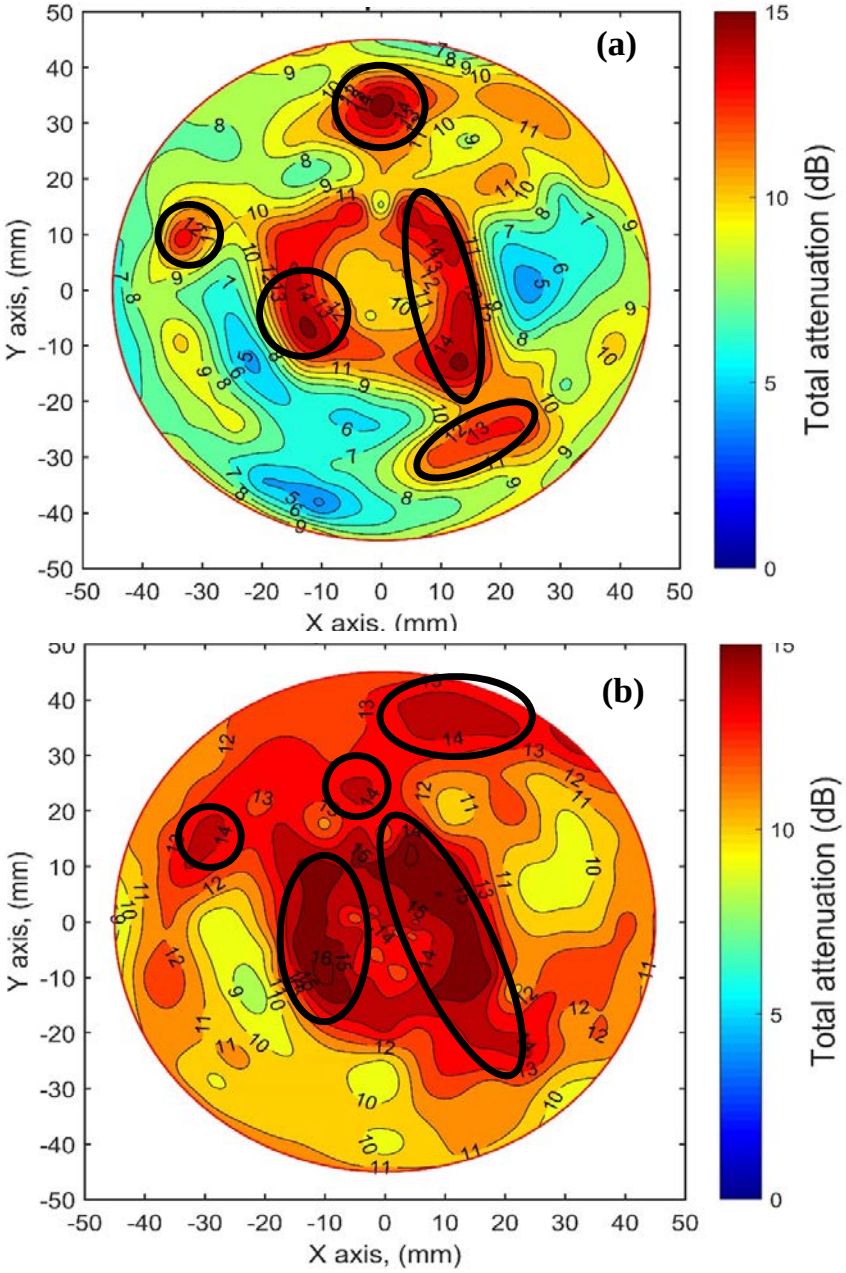

Figure 6-14. Typical contour lines of total attenuation results of untreated cylinder specimen scanned with laser using 54 kHz. (a) using peak amplitude, (b) using spectrum area.

Figure 6-15 presents the total attenuation results of cylinder specimen treated with 0.1% of air entrained. Examining the figure reveals the same conclusion reached with UPV velocity results about the effect of addition of air-entrained which attenuates high frequency waves.

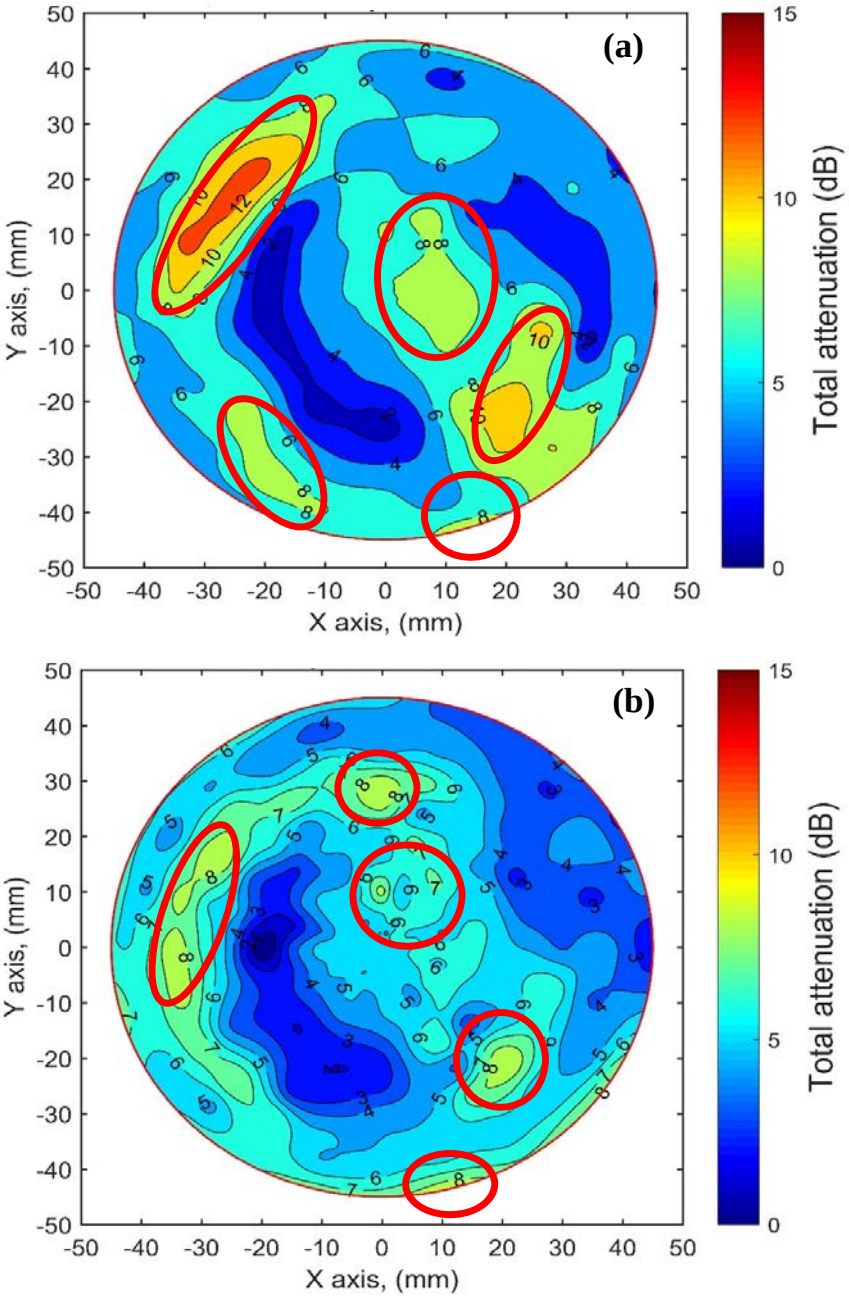

Figure 6-15. Typical contour lines of total attenuation results of treated cylinder specimen with 0.1% air-entrained scanned with laser using 54 kHz. (a) using peak amplitude, (b) using spectrum area.

A comparison between results of testing prism concrete specimens is also studied. Figure 6-16 illustrates the attenuation results of testing untreated prismatic specimen using 54 kHz as

contour lines before and after the freeze-thaw process. The attenuation also computed using two procedures; peak amplitude and spectrum area.

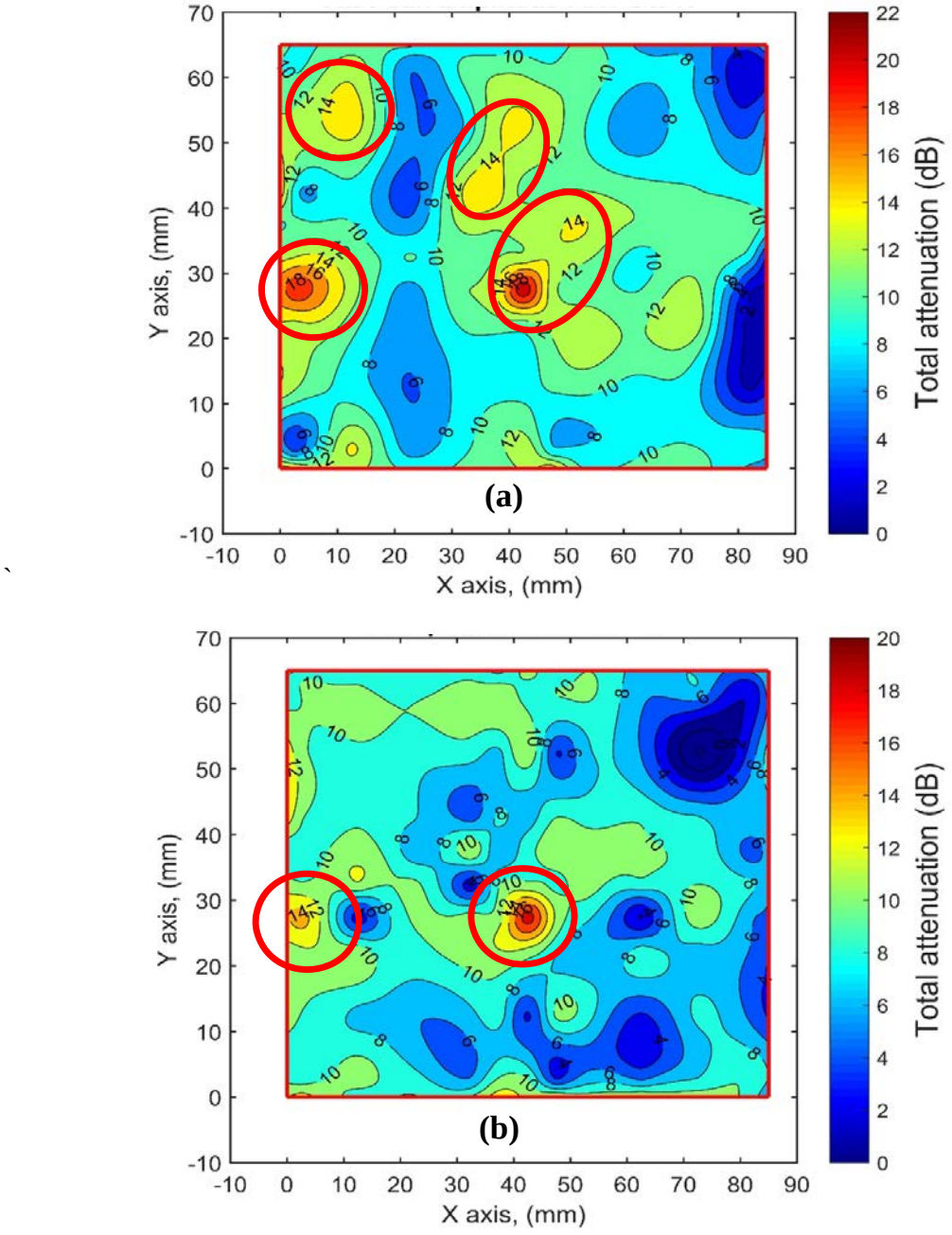

Figure 6-16. Typical contour lines of total attenuation results of untreated prismatic specimen scanned with laser using 54 kHz. (a) using peak amplitude, (b) using spectrum area.

The observed attenuation plots reveal several spots (red circles) that indicate higher attenuation values (14-18 dB) which in comparison to UPV has a more selectivity to the accumulated

deteriorations due to the freeze-thaw cycles. The trend is also observed in the results of other prisms that treated with different percentages of air-entrained agent. Some typical results can be found in appendix C.

6.3.3 Compression test results

Pulse velocity results. Figure 6-17 shows the variation of the ultrasonic pulse velocities obtained from the UPV measurements using 54 kHz and 250 kHz of cylinder specimens before and after the compression load.

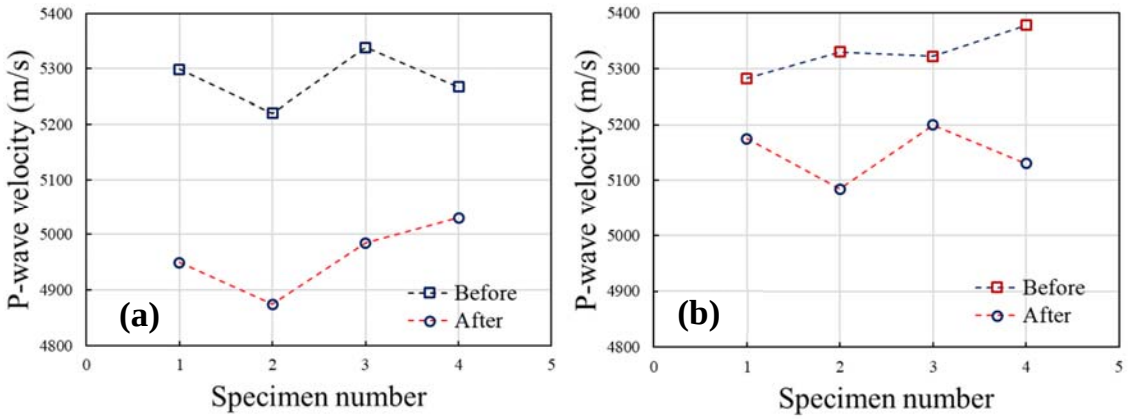

Figure 6-17. Typical variations of ultrasonic velocity for cylinder specimens. (a) using 54 kHz probe, (b) using 250 kHz probe.

UPV readings were taken in a direction parallel to the load application to evaluate the cracks induced in this orientation. Figure 6-17a shows that changes in wave velocities indicate the presence of damage inside the concrete specimen. The last specimens with 20% silica fume revealed the influence of adding high percentage of additive which causes less change in the wave velocity. The case is different in Figure 6-17b, where the untreated specimen and 10% treated specimen are exposed less variation in wave velocity. This pattern of variation in wave velocity is also observed with other transducers which indicates the potential to use variability of wave velocity as a sign of material conditions.

Figure 6-18 presents the relative velocity ratio (dV) which is computed using:

$$dV = \frac{(V_b - V_f)}{V_b} \tag{6.1}$$

where V_b and V_f are wave velocities before and after the application of load.

and obtained from the UPV measurements before and after the compression load. It can be observed that the low frequency transducers (54 kHz, 150 kHz, and 250 kHz) are shown similar variations in wave velocity (around 5%), while the 500 kHz indicates an increase in the wave velocity after the compression load (around 8%).

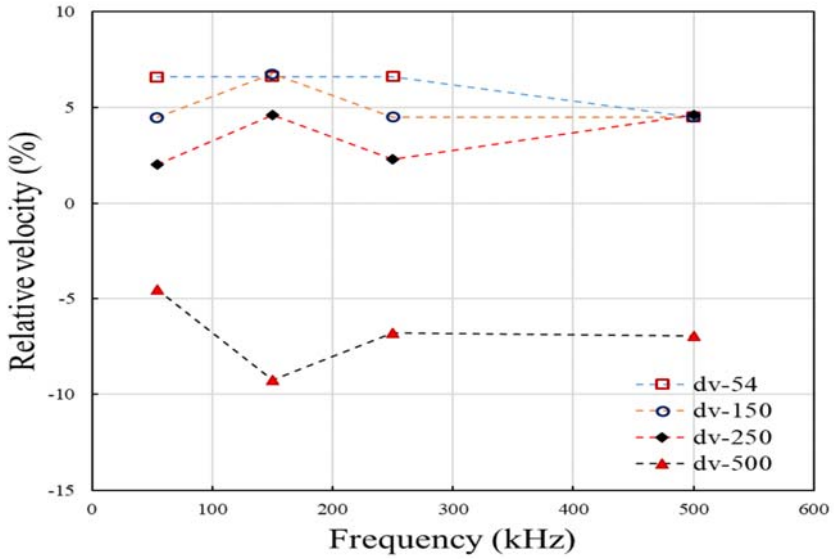

Figure 6-18. Typical variations of relative ratio of ultrasonic velocity for cylinder specimens using all transducers (54 kHz, 150 kHz, 250 kHz, and 500 kHz).

The figure illustrates the difficulty of using the change in wave velocity to monitor crack evolution in concrete specimens under compression load. This trend was also observed with prism specimens and with other measurements that used 150 kHz and 250 kHz. Therefore, the change in the velocities cannot be used as a reliable procedure to evaluate the damage related to the compression load. It is therefore necessary to investigate another parameter such as wave attenuation that can be used effectively to evaluate the load damage in concrete.

6.3.3.2 Attenuation measurements

Single testing measurements. The inspection of load damage in concrete is being paid more attention with time because of its significance in evaluation of the integrity of concrete elements. In this research, the examination of peak amplitude and spectrum area of the waveforms obtained from testing concrete specimens treated with silica fume agent using the UPV method has provided interesting results. Figure 6-19 illustrates the typical time signals and their corresponding Fourier spectra of cylinder concrete specimens.

The figure reveals that even with different wavelengths (λ = 8 cm for 54 kHz, λ = 2 cm for 250 kHz), both results show a detection of the damage induced by compression load (around 80% magnitude drop for 54 kHz and 55% for 250 kHz). This trend is also noticed with the 150 kHz and 500 kHz transducers for the same intact cylinder concrete specimen. Additionally, UPV measurements indicate a small change in the resistivity of the specimens under investigation which are supposed to be enhanced with this type of chemical additive used to improve the durability of concrete against harsh conditions.

Figure 6-20 shows the results of waveforms of a cylinder specimen treated with 20% silica fume and obtained from ultrasonic measurements under compression load. In this figure, it is noticed that amplitude and spectrum area of 250 kHz is more sensitive to load damage than the 54 kHz transducer.

Figure 6-21 illustrates the total attenuation measurements obtained from testing cylinder specimens (C1, C2, C3, C4) under compression load for all transducers.

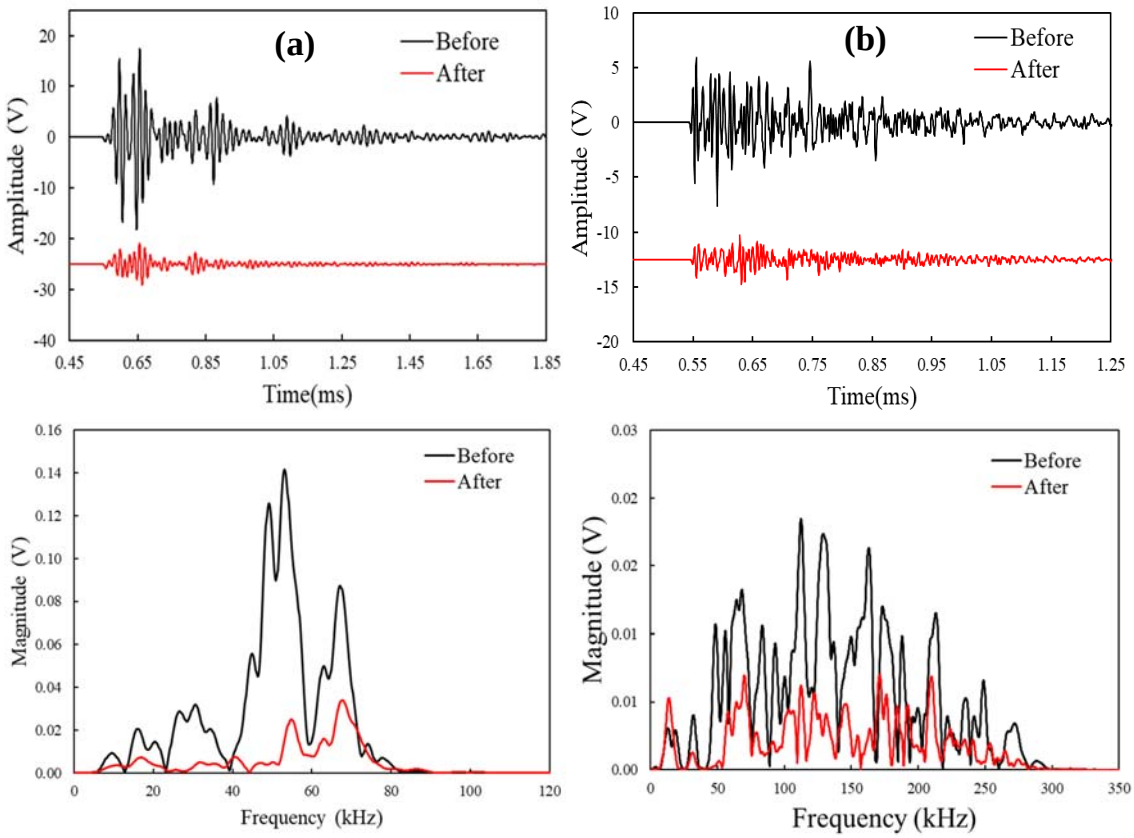

Figure 6-19. Typical waveforms of untreated cylinder specimen before and after compression load. (a) time signals and corresponding Fourier spectra of 54 kHz transducer, (b) time signals and corresponding Fourier spectra of 250 kHz transducer.

The attenuation is computed using two procedures; amplitude method and the spectrum area method as followed with the freeze-thaw process.

Figure 6-21a shows the peak amplitude indicates damage more than the spectrum area, even though both methods produce similar trend with regards to adding the silica fume. It can be seen also that specimen with 10% of silica fume has lower attenuation in both cases.

Multi-testing measurements. Evolution of load damage in different orientations is the motive of this section in which several transducers are distributed around the centre of the concrete specimen under investigation. Eight unreinforced concrete specimens are tested using this methodology, four cylindrical shape and four prismatic shape. Several procedures were followed to take UPV measurements under compression load. Sequenced transmitting was performed so that each type of the selected transducers is excited with a one cycle square-wave pulse and corresponding amplitude and frequency parameters.

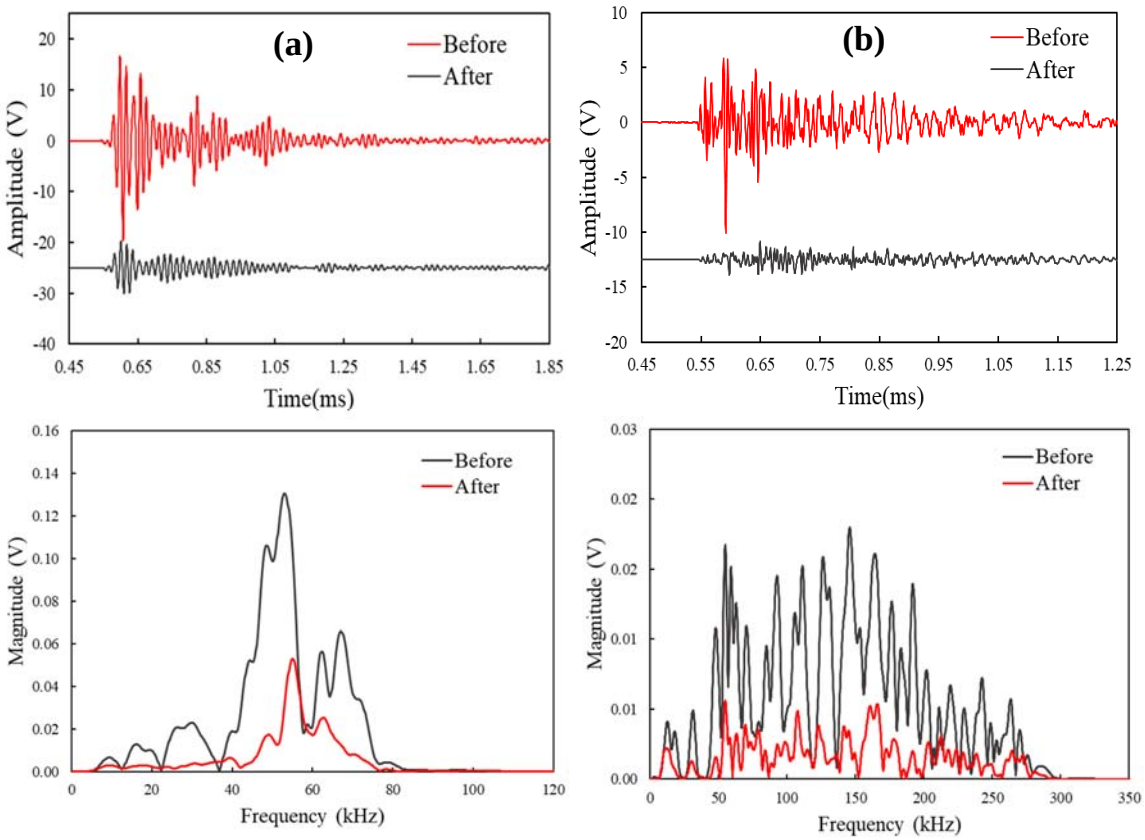

Figure 6-20. Typical results of treated cylinder specimen with 20% silica fume before and after compression load. (a) time signals and corresponding Fourier spectra of 54 kHz transducer, (b) time signals and corresponding Fourier spectra of 250 kHz.

Figure 6-22 represents a typical waveforms and corresponding Fourier spectra obtained by exciting the 54 kHz and received by 54 kHz in the opposite side for the untreated cylinder specimen subjected to compression load. These results were measured at different load steps. The figure indicates clearly that there is a change in the waveform amplitudes during the compression load which is related to the damage induced in the middle of the specimen.

On the other hand, Figure 16-23 illustrates the results of using 150 kHz transducers as a transmitter and receiver for the same specimen and under similar test conditions. In this figure, the amplitude of waveform reduced significantly beyond 150 kN load. Even though both 150 kHz transducers are aligned at the same plane where the 54 kHz transducers are placed, the sensitivity of 54 kHz at lower loads was better than the 150 kHz. Near the failure load, the 150 kHz transducer indicates a more significant reduction in amplitude than the 54 kHz ones.

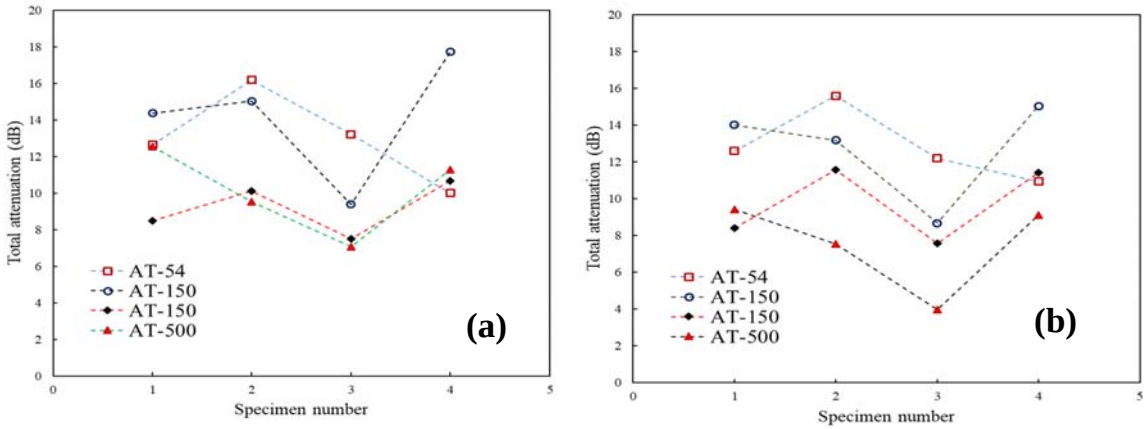

Figure 6-21. Typical total attenuation results of cylinder concrete specimens test parallel to the load direction. (a) amplitude method, (b) spectrum area method.

Figure 6-24 illustrates the total attenuation measurements obtained from testing the untreated cylinder specimen using 54 kHz and 150 kHz as transmitters. The measurements represent different transducer configurations. In Figure 6-22a, the 54 kHz results indicate better detection to the load damage for all transducer configurations expect 54-25 and 54-15 which exhibit

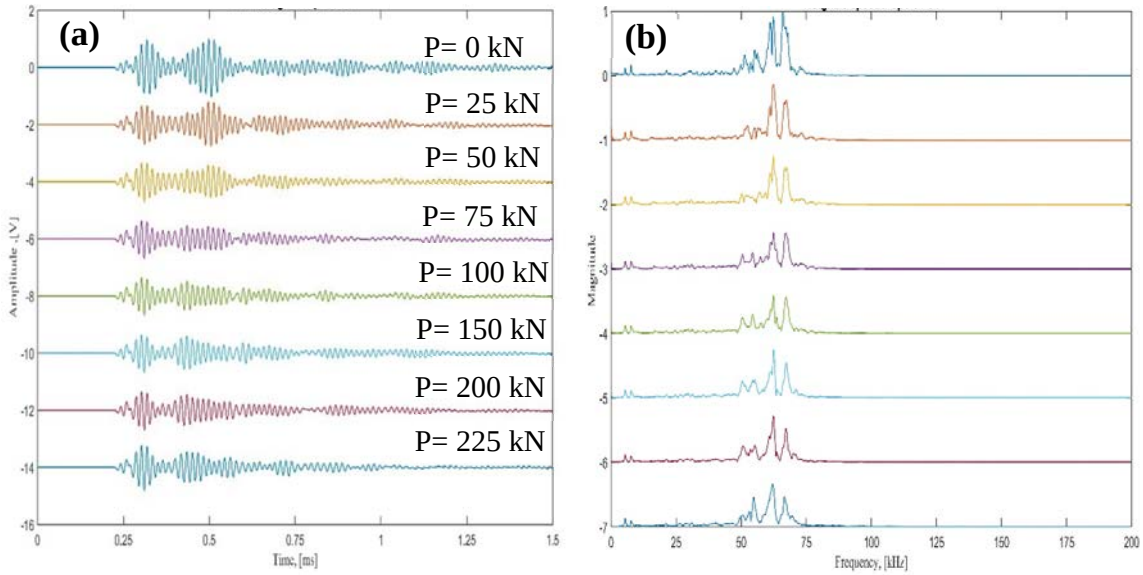

Figure 6-22. Typical waveform results of untreated cylinder specimen subjected to compression load and using 54 kHz transduces at different load steps. (a) in time domain, (b) in frequency domain. P is the applied load.

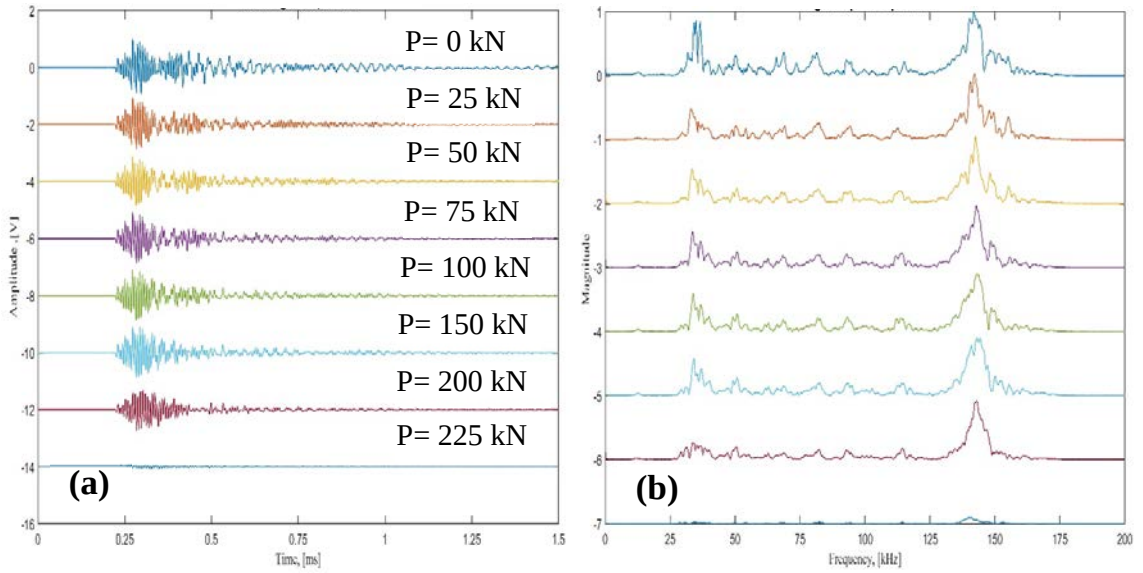

Figure 6-23. Typical waveform results of untreated cylinder specimen subjected to compression load and tested using 150 kHz transduces at different load steps. (a) in time domain, (b) in frequency domain.

results like the 150 kHz. In Figure 6-24b, the trend is for all configurations to exhibit a similar change. The proposed procedure proved to be helpful to detect the load damage effectively

which can be used for condition assessment of concrete specimens under experimental conditions. The results of other cases can be found in appendix C.

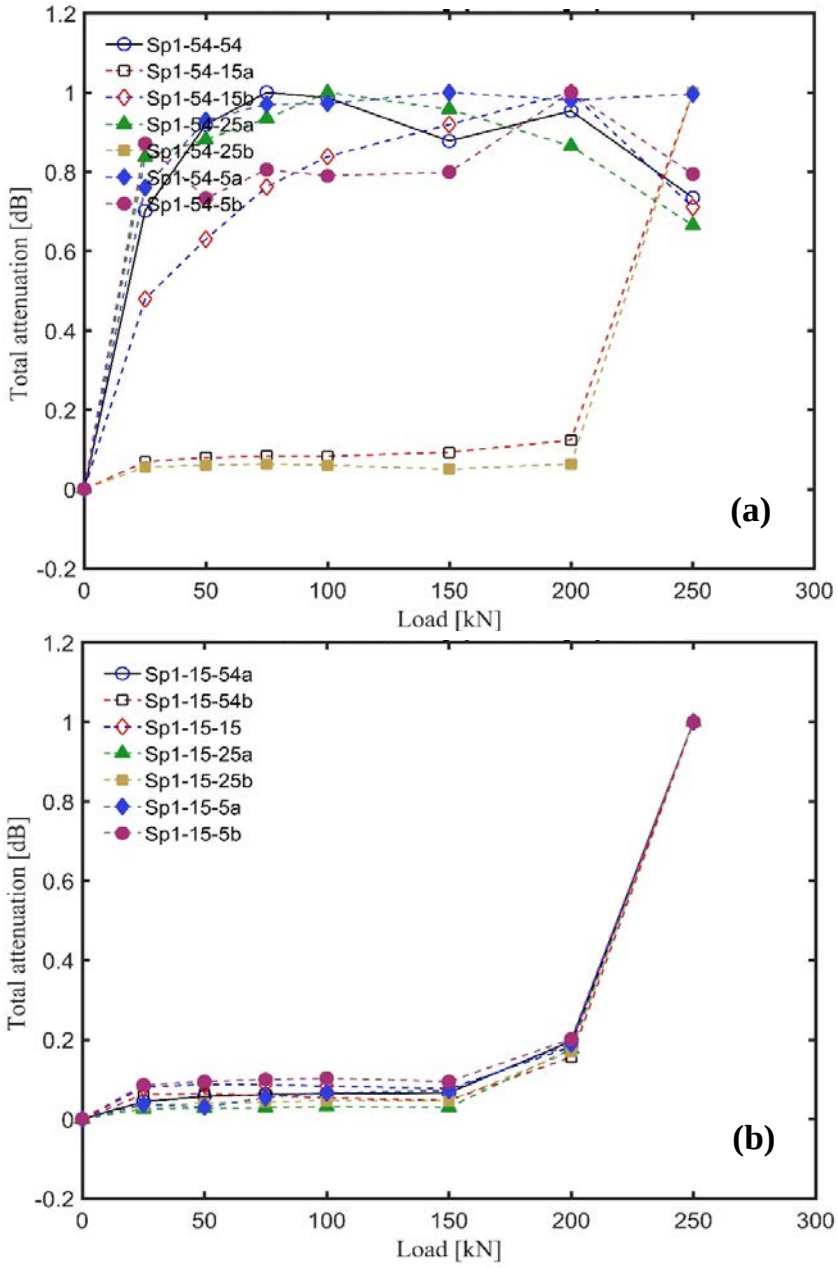

Figure 6-24. Typical total attenuation results of untreated cylinder specimen subjected to compression load and tested using different orientations. (a) using 54 kHz as transmitter, (b) using 150 kHz as transmitter.

Laser vibrometer results. The laser technique is selected to evaluate the change in wave velocity and wave attenuation occurring due to the compression load. Laser Doppler vibrometer (LDV) offers a non-contact procedure to measure the vibration in the out-of-plane surface based on the Doppler shift phenomenon which allows to determine the velocity of the object surface under study. It is designed and used widely in several engineering applications to measure vibrations in inaccessible areas and harsh environments. It can be used in the lab or in the field depends on the object under investigation.

Figure 6-25 presents the vibration mode obtained from Laser measurements of an untreated cylinder specimen using a 54 kHz transducer. The results of laser measurement reveal some interested findings, one of these findings is the level of attenuation that occurs to the propagated wave which is received by the laser is approximately 80%.

The laser permits us to identify which areas exhibit signs of damage compared to other areas on the same surface. This is difficult or not possible with UPV testing methods. Even with the attenuative behaviour of concrete, the vibration response of the intact case shows a mode shape like the mode shape of the vibration observed when just the transducer surface is scanned with the laser. After application of the compression load, the vibration shape is lowered, and multiple peaks implies more vibration modes.

Figure 6-26 illustrates the vibration response obtained from laser measurements of a treated cylinder specimen with 5% silica fume and using a 250 kHz transducer. The results of laser measurements indicate the level of attenuation that occurs to the propagated wave received by the laser (around 75%). The figure, both Figures 6-26(a) and 6-26 (b) shows the mode mixing occurring. This suggests that the vibration response can be related to the attenuative scatter behaviour of concrete with high frequency waves. Also, the load damage produces significant reduction in the vibration amplitude and the multiple peaks implies more vibration modes.

Additionally, total attenuation was computed using two procedures; peak amplitudes and areas under Fourier spectra as shown in Figure 6-27. The figure is plotted using contour lines, clearly shows the areas (marked with red circles) where there is more evidence for the accumulated damage of the compression loading process. In this figure, the peak amplitude and spectrum methods show similar trends and indicate better results than what was observed using the UPV method. This is a significant advantage of the laser vibrometer to identify the damage caused by external factors.

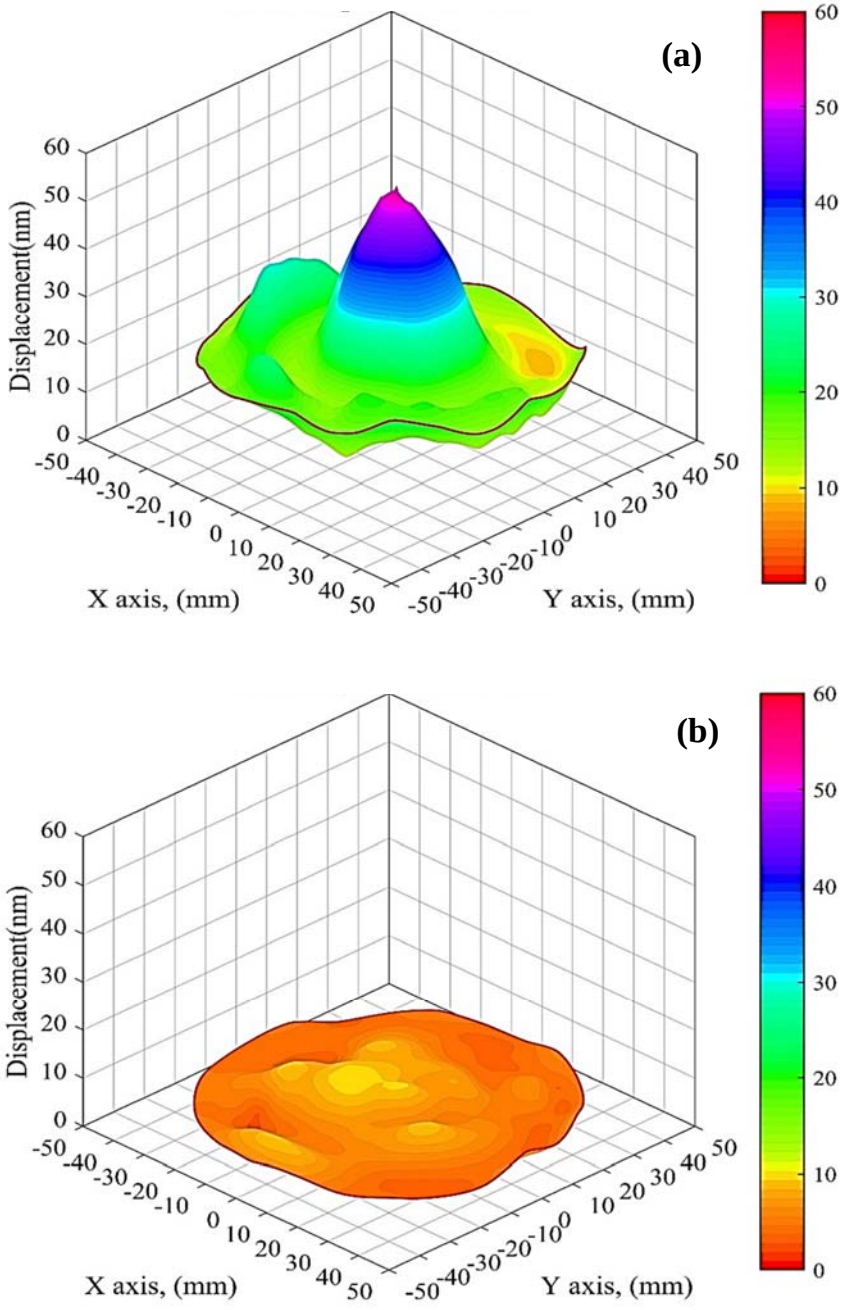

Figure 6-25. Typical vibration modes of untreated cylinder specimen using 54 kHz. (a) before applying the load, (b) after applying the load. Note that the displacement scale of the pre-load condition is nearly five times greater.

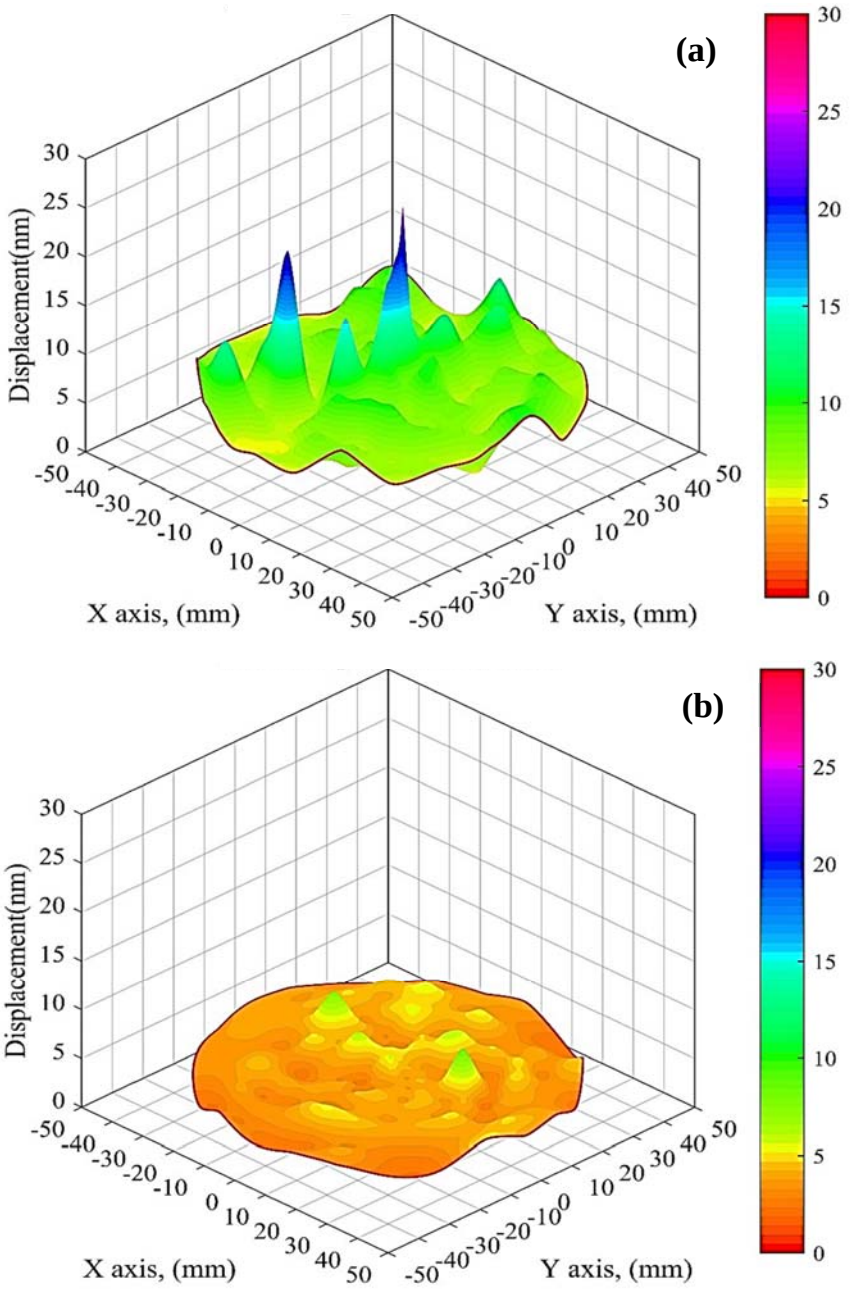

Figure 6-26. Typical vibration modes of treated cylinder specimen with 5% silica fume using 250 kHz. (a) before applying the load, (b) after applying the load.

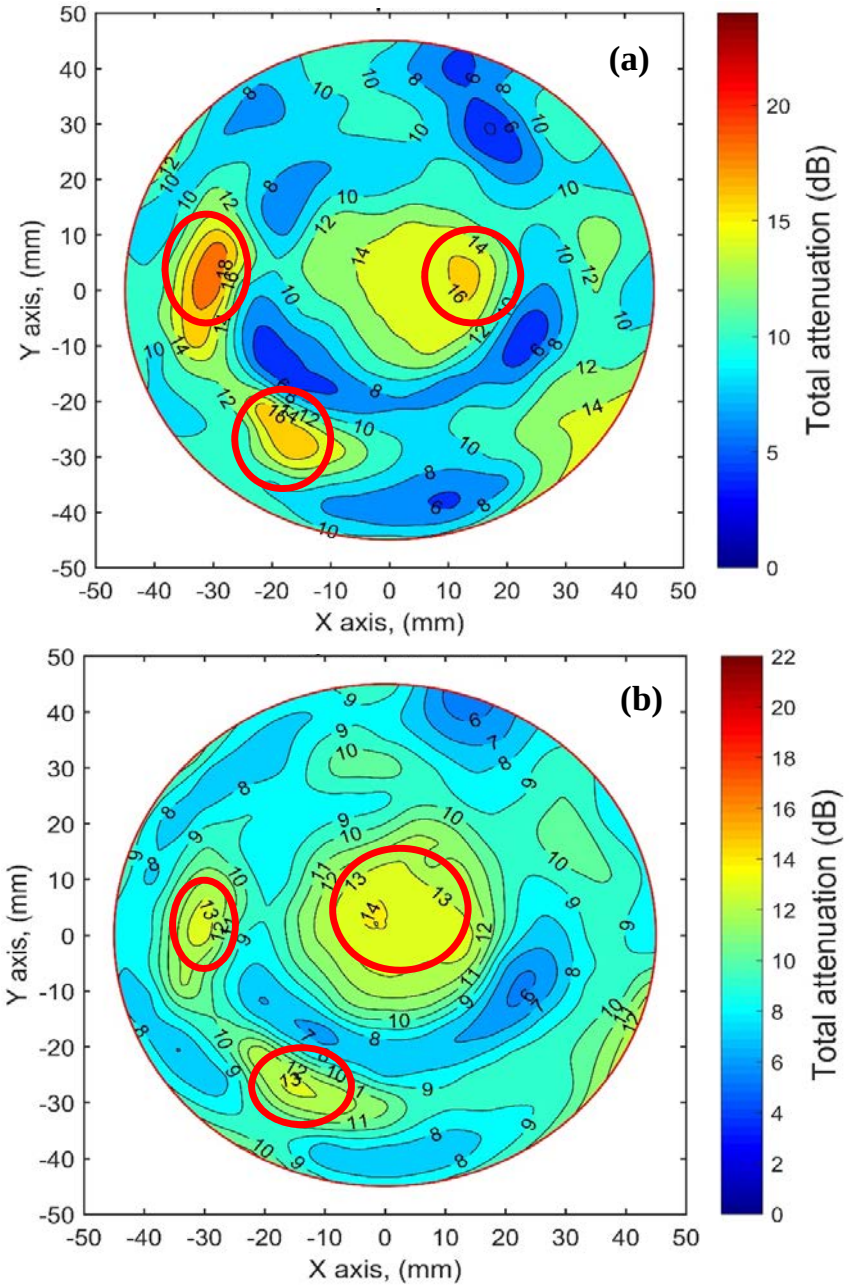

Figure 6-27. Typical contour lines of total attenuation results of untreated cylinder specimen scanned with laser using 54 kHz. (a) using peak amplitude, (b) using spectrum area.

Figure 6-28 presents the total attenuation results of the cylinder specimen treated with 10% silica fume and tested with 250 kHz. Examining the figure reveals the same conclusion that was reached with the untreated specimen tested using 54 kHz, except that amplitude method indicate more damage areas (areas surrounded by red circles).

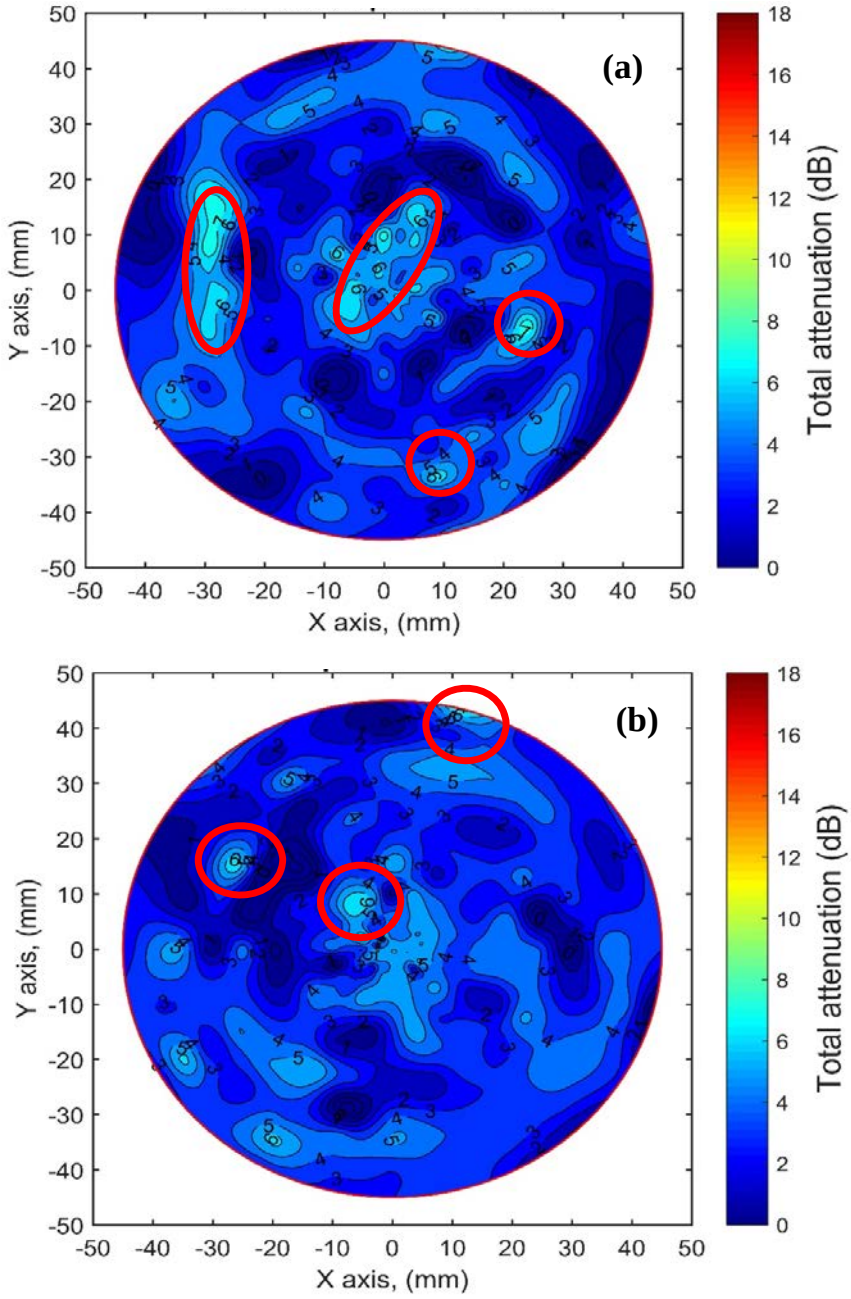

Figure 6-28. Typical contour lines of total attenuation results of treated cylinder specimen with 10% silica fume and scanned with laser using 250 kHz. (a) using peak amplitude, (b) using spectrum area.

On the other hand, the comparison between results of testing prism concrete specimens under compression test are also investigated. Figure 6-29 shows typical attenuation results of testing an untreated prismatic specimen using 54 kHz. In this figure, it is easily to identify zones (red circles) that exhibit higher attenuation values (6-8 dB) which can be attributed to the presence

of cracks that induced under the compression load. In general, this trend is similar to the one that observed with the results of freeze-thaw section.

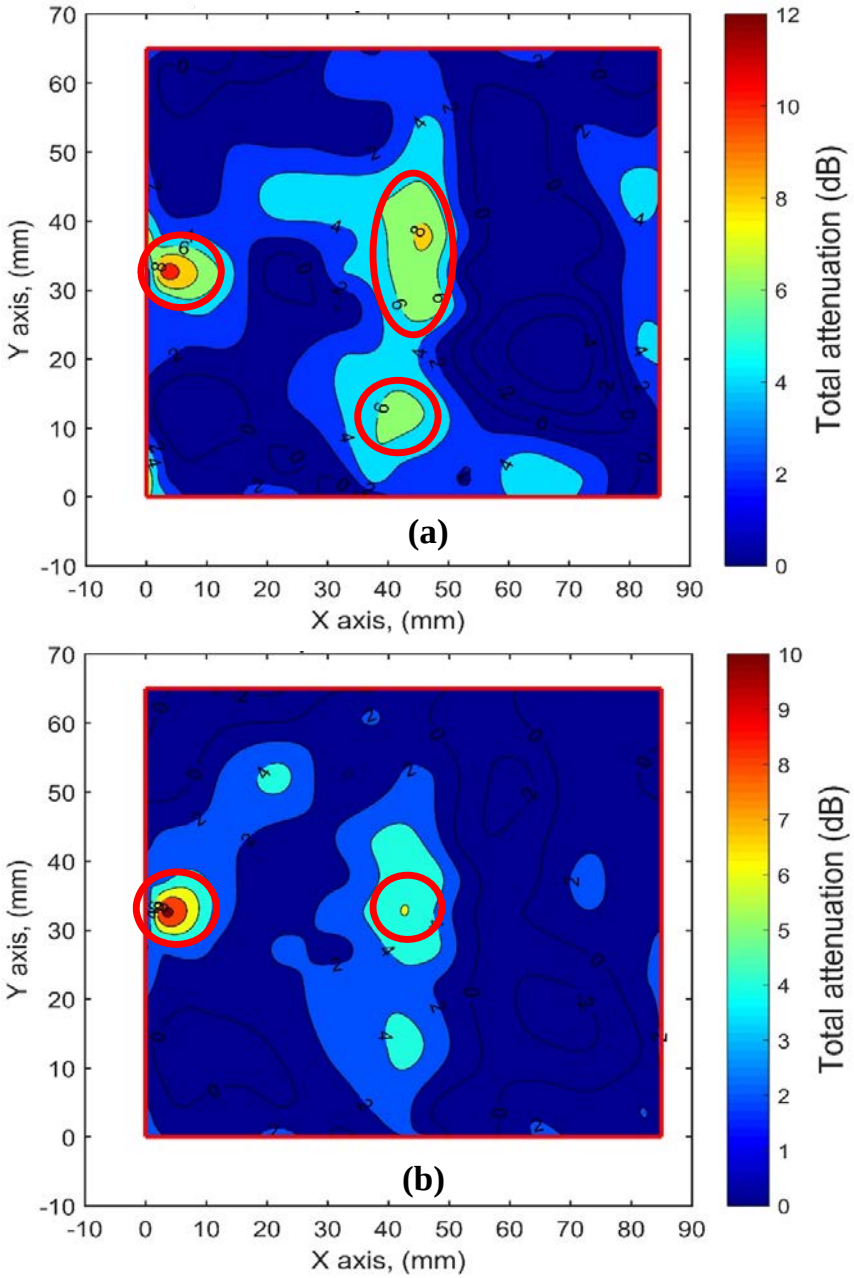

Figure 6-29. Typical contour lines of total attenuation results of untreated prismatic specimen scanned with laser using 54 kHz. (a) using peak amplitude, (b) using spectrum area.

Therefore, it is feasible to use the laser testing technique under lab conditions to locate the damaged areas inside concrete specimen exposed to uniaxial compression load. Interestingly, the inspection of the specimen surface visually did not show any indication of crack due to the application load. Some typical results can be found in appendix C.

6.4 Summary

This chapter included the finding of two procedures of tests, UPV through transmission and Laser Doppler vibrometer, intended to evaluate two types of damage induced using freeze-thaw cycles and compression load. The experimental program includes adding to concrete mixture two set of additives; air-entrained and silica fume. For this purpose, eight unreinforced concrete specimens (four cylinders and four prisms) are prepared with four percentages of air-entrained to evaluate frost damage. Similar number of specimens are prepared with four percentages of silica fume to investigate the damage induced under compression load.

The sensitivity of wave velocity and wave attenuation is studied using UPV measurements and the results indicate that wave velocity did not show any clear trend about the presence of frost damage. In contrast, wave attenuation shows better indication to frost damage. In the compression load process, the results obtained show that wave velocity also indicates less sensitivity to damage than wave amplitude. Also, the multi-measurements procedure proposed in this study presents a reliable technique to evaluate load damage in different orientations based on a preferable frequency range.

In the case of the Laser Doppler vibrometer testing for freeze-thaw and compression load, the observed results of attenuation measurements exposed very interested findings. For example, the damage areas were identified by computing the total attenuation using two procedures; peak amplitude and spectrum area methods in which the first has shown better results than the latter. The findings of laser vibrometer exhibited a significant indication of zones that were influenced by load damage and this can be a motive to establish a reliable testing program to evaluate internal condition of concrete specimens under lab conditions.

Chapter 7: Health monitoring of concrete shallow foundation lab-scale models

7.1 Introduction

Different methods are developed to assess the integrity of in-service concrete elements. The inspection scope and the resources available are essential to select appropriate methods. The techniques that are used to detect flaws, to determine the material properties or to evaluate the integrity of elements are known as nondestructive testing (NDT) methods which do not affect the component characteristics under inspection. One of the NDT techniques that is used commonly in concrete and depends primarily on the wave propagation is called stress-wave methods. Though many NDT approaches are designed to evaluate the integrity of concrete members structures, shallow foundations, which are concrete elements embedded in soil and used to transfer load to soil, received less attention due to several reasons. The most challenging one is the limited accessibility for in-service foundation inspections because of structural restrictions. Even when accessibility is possible, the NDT methods (UPV) used may produce measurements with high uncertainties because of inconsistent coupling.

Concrete shallow foundations are widely utilized in large-scale civil infrastructures. These structure elements are divided into different types; strip, spread or isolated, combined and raft foundations. Spread foundations are most commonly used to support sustainable concrete structures such as wind turbines (ACI ITG-9R-16). Under some critical circumstances such as natural disasters (e.g. earthquakes), it is highly expected that shallow foundations will undergo severe damage. Therefore, it is essential to quickly evaluate the severity of the damage and the health integrity in real time or even near real time after an earthquake to get significant safety data of the structure for decision makers. To perform structural health monitoring of shallow foundations, it is vital to develop an automated and distributed system to do health integrity observation for this type of infrastructure.

For many years, many studies reported various sensors and methods that were developed to detect damage and to monitor the integrity of concrete structures. Fiber optic sensors (FOS) is one of these methods which is used now for health monitoring of various concrete structures (Ghanderhari et al., 2018; Lu and Xie, 2006; Ren et al., 2006; Chen and Ansari, 1999). However, this type of sensor has some drawbacks; it is fragile, expensive, and provides only local measurements. On the other hand, piezoceramic materials represent an ideal option for

heath monitoring purposes with some advantages of quick response, low cost, solid-state actuation and high reliability.

Recently, there is a trend to install sensor networks in concrete to determine the dynamic signature of the concrete elements. Several attempts (Dumoulin et al., 2012, 2015, and 2016; Gu et al., 2010; Cheng et al., 2010; Fröjd and Ulriksen, 2016; Lu and Li, 2010; Zongjin et al., 2000; Xu et al., 2018; Dixit and Bahalla, 2018; When et al., 1998; Turner and Arif, 1991) were reported to embed low-cost piezoelectric transducers in concrete to estimate P- wave velocity in fresh concrete and to evaluate damage development. The existence of transducers inside concrete may have different purposes, such as to improve the interpretation of the test results, to obtain more reliable and consistent measurements, and to adjust the impact of a specific parameter in the measurements. All the proposed procedures that are described in the previous works are developed to inspect concrete condition of superstructures. For infrastructure concrete elements (e.g. shallow foundations), they are impractical to use for several reasons such as, the limited accessibility to send the excitation pulse and the transducers used are not compatible with concrete due to their metal shell and poor waterproof performance.

In present research project, a new NDT procedure is developed based on new fabricated transducers, which are waterproofed and cost-effective, embedded at the base of lab-scale concrete foundation models. These transducers consist of radial-mode piezoceramics which are efficient to detect waves from different orientations, they are cheap with a size smaller than the other piezoelectric transducers of similar centre-frequencies. The developed methodology also includes two procedures proposed to emit the pulse from different locations for comparison purposes; either using a transducer coupled to an aluminum plate glued to the concrete surface or using a tube filled with distilled water and partially embedded in concrete. The second option is a key factor of the proposed procedure to reach the concrete surface of foundations and produce reliable results. This notion is barrowed from the SONAR technique that used low frequency transducers to send pulse into the sea water to travel long distance without significant attenuation. Using water as a perfect coupling material allows to extend the length of tube according to the depth of the shallow foundation. Also, the new testing procedure can be used in different stages: during construction of foundations to monitor the uniformity and quality of the concrete, and in-service life to periodically assess the condition of foundations, specifically after any possible effect that can cause severe damage in concrete such as earthquakes and overloading.

7.2 Experimental procedure

7.2.1 Model preparations

Four hardened concrete shallow foundations of lab-scale models are fabricated with designed mixture proportions as shown in Table 7-1. Three of these models are reinforced with steel bar of diam. 10 mm and one model is plane used as a control model.

Table 7.1: Mix proportions of concrete models.

Material	Kg/m^3
Type I cement	910
Fine aggregates	1310
Coarse aggregates	1600
Water	400

Figure 7-1 illustrates the geometry of the cast concrete models. The cast models are square plain concrete (MA-SP), square light reinforced concrete (MB-SLR), square dense reinforced concrete (MC-SDR), and circular light reinforced concrete (MD-CLR) models. Two types of tubes are partially embedded (3 cm) in each model, acrylic (diam. 6.2cm X height 45 cm) and nylon (diam. 6.0cm X height 45 cm). Also, two aluminum discs (diam 25 cm X thick. 3 mm) are glued to the surface using concrete epoxy in each model (Figure 7-2). All concrete mixtures, which are designed according to American concrete institute (ACI) code 211.1R-91, contain a Portland ASTM type I cement, fine and coarse aggregates with 12.5 nominal aggregate size, and water/cement ratio of 0.45 by mass. The designed mix parameters are 35 MPa compressive strength at age 28 days, slump rate ranging from 75 to 100 mm, and air content from 5% to 8%.

7.2.2 Transducer fabrication

Thirty-six piezoelectric transducers are fabricated to embed in concrete models. Each constructed transducer consists of a radial piezoelectric disc (diam. 50 mm X thick. 2.5 mm) made by STEMiNC (Steiner & Martines Inc.), aluminum case, backing material (steel), and 3D printed plastic cover. The resonant frequency of the radial piezoelectric disc is 45 kHz ± 3 kHz. Then, two layers of plastic paint (Plasti Dip®, multi-purpose rubber coating) which is waterproof and resists chemical agents are used to coat each transducer before imbedding them in the models. Figure 7-3 illustrates a typical sample of fabricated transducer in this research.

To ensure functionality of the fabricated radial transducers, each transducer is tested using a steel bar (diam. 10 cm). The test includes sending a single cycle square wave pulse generated by the function generator, a piezoelectric transducer with a nominal resonance frequency of 54 kHz and amplitude of 10 volts.

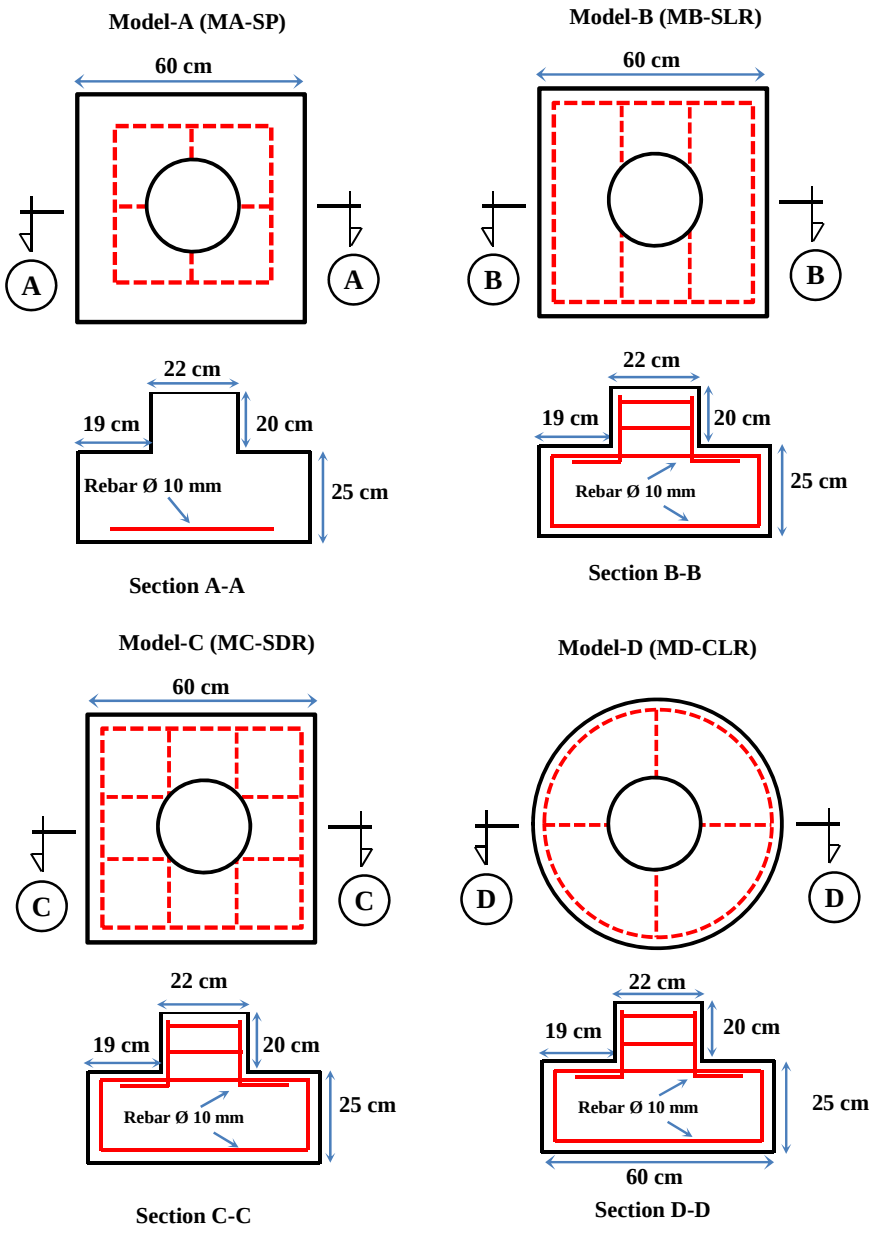

Figure 7-1: Sketches plan of the concrete models. (a) Square plain concrete model, (b) square light reinforced concrete model, (b) dense reinforced concrete model, (c) circular light reinforced concrete model. All dimensions are in cm.

Figure 7-4 presents a typical waveform signals and corresponding Fourier spectra obtained from testing the fabricated radial transducers using steel bar. In the other hand, the functionality of the same fabricated transducers is also examined as shown in Figure 7-5. To ensure better detection of the evolution of the damage inside the concrete models, the transducers are installed at the zones which are believed to exhibit more damage under compression load as shown in Figure (7-6).

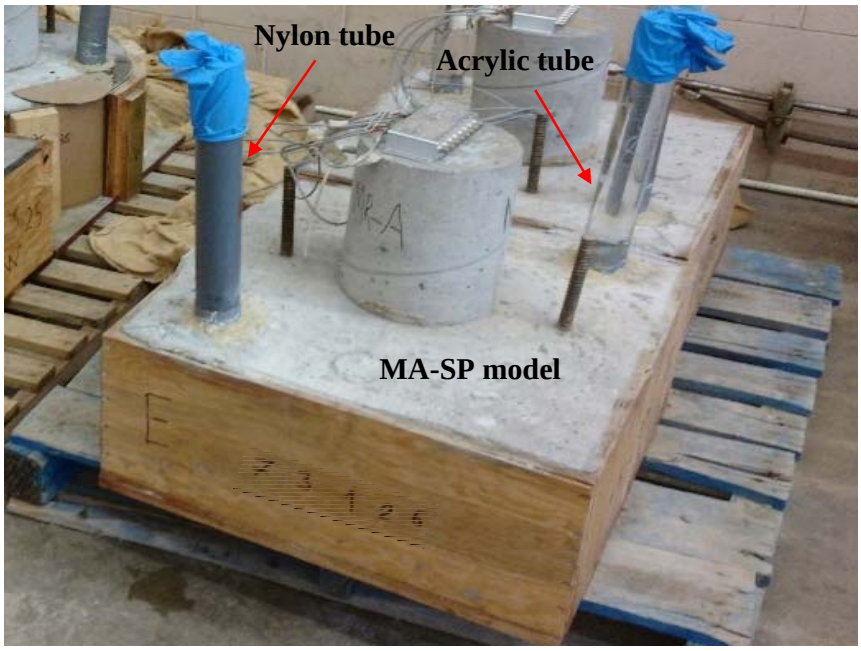

Figure 7-2: Locations of the tubes that used to send the excitation pulse.

7.2.3 Equipment description

Compression machine test. The concrete lab-scale models were tested using a compression machine MTS35000kN (Figure 7-6). This machine can apply a static load up to 35000 kN which is adequate to produce cracks inside the concrete models tested under this machine. Also, it can fit the size of the concrete models that were made for this research. For the current research, the strain control test is utilized with a strain rate of 0.02 mm/min, where the displacement and corresponding load are recorded continuously. Figure 7-7 illustrates a typical Load-displacement curves obtained from testing models MA-SP and MC-SDR under compression load.

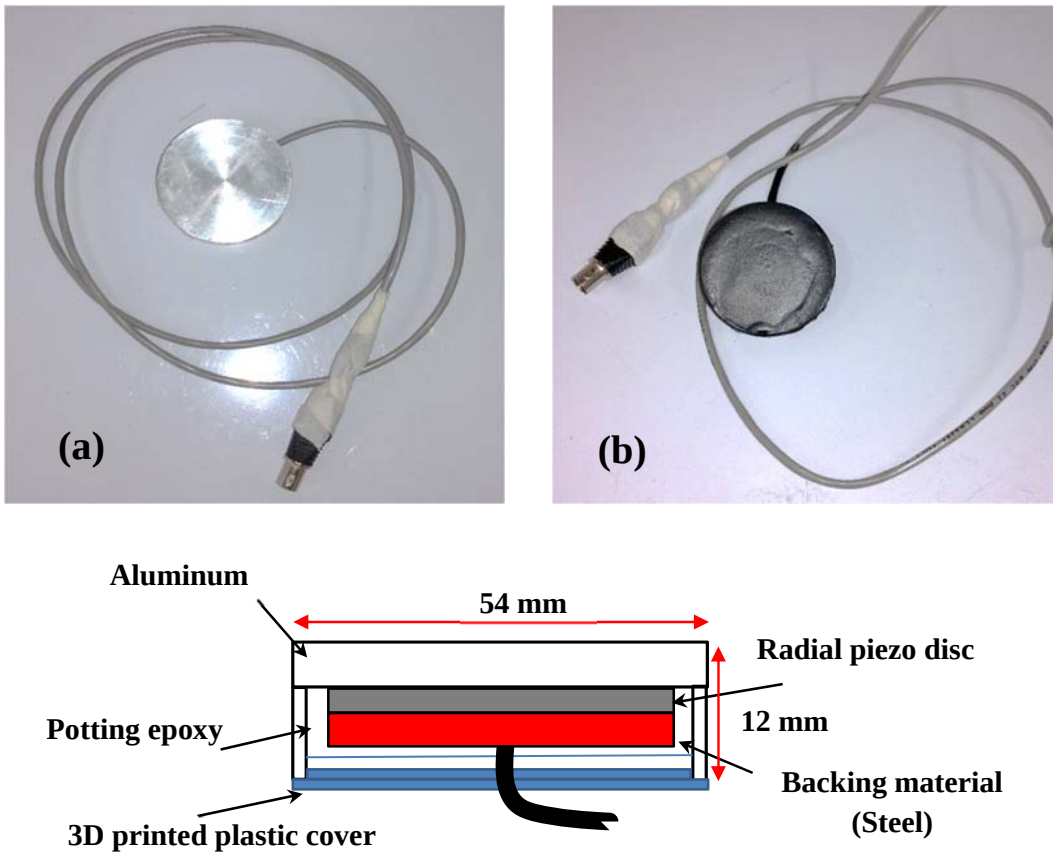

Figure 7-3: Typical fabricated radial transducers. (a) before coating, (b) after coating, (c) cross-section of the fabricated transducer.

Ultrasonic pulse velocity setup. For quality control testing, the ultrasonic testing consists of a piezoelectric transducer, high speed data acquisition (Genesis, 24 channels), a function generator, a piezo driver, three filters and a computer. Piezoelectric transducers (frequency bandwidth 20 to 100 kHz, nominal resonance frequency 54 kHz, and 50 mm diameter) are used in this study (Figure 7-8). The approximate distribution of the embedded transducers is illustrated in Figure 7-9.

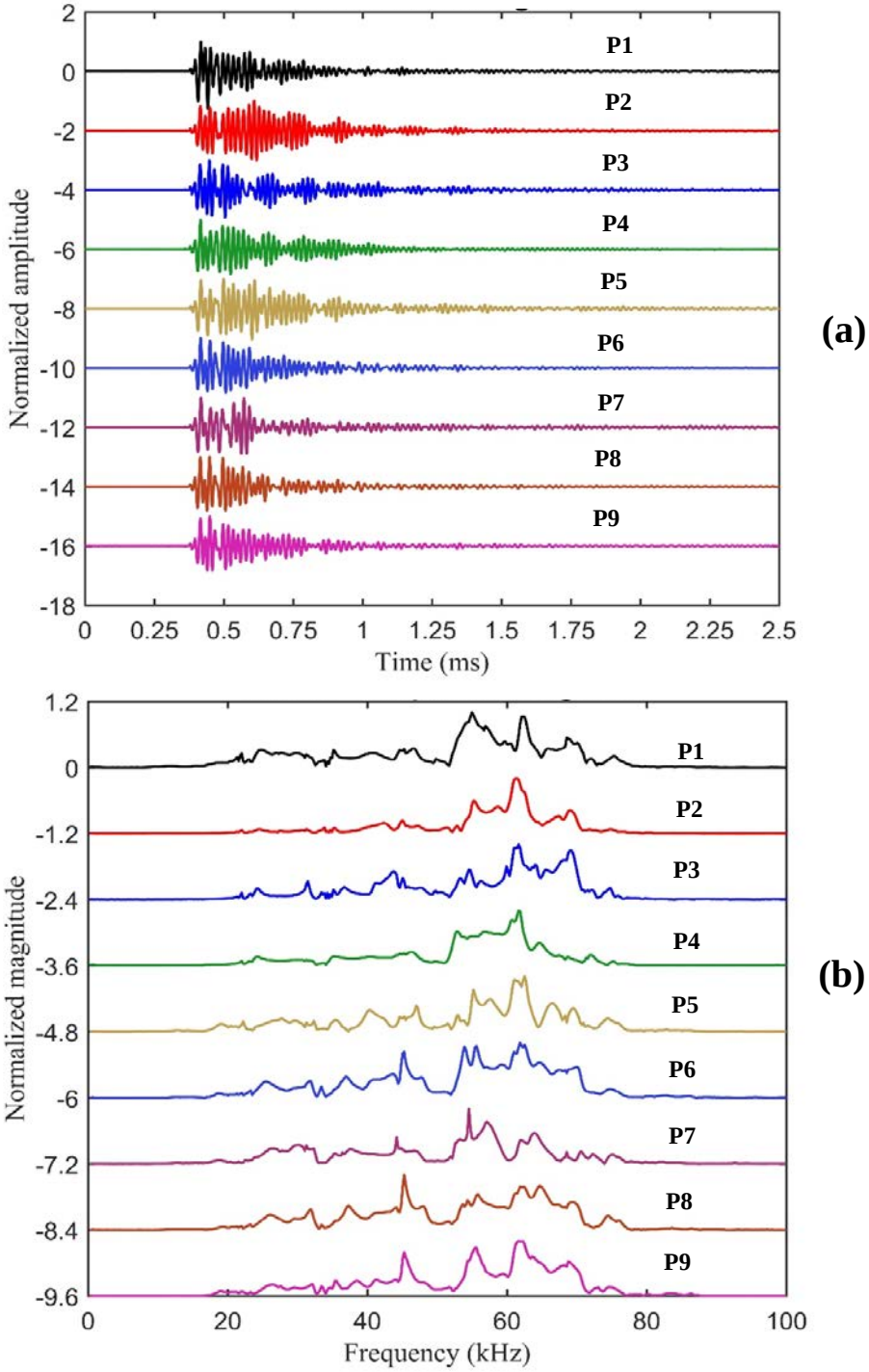

Figure 7-4: Typical waveform signals of the fabricated radial transducers (model MA-SP transdcuers). (a) in time domian, (b) in frequency domain. P1-P9 refer to nine fabircated transducers.

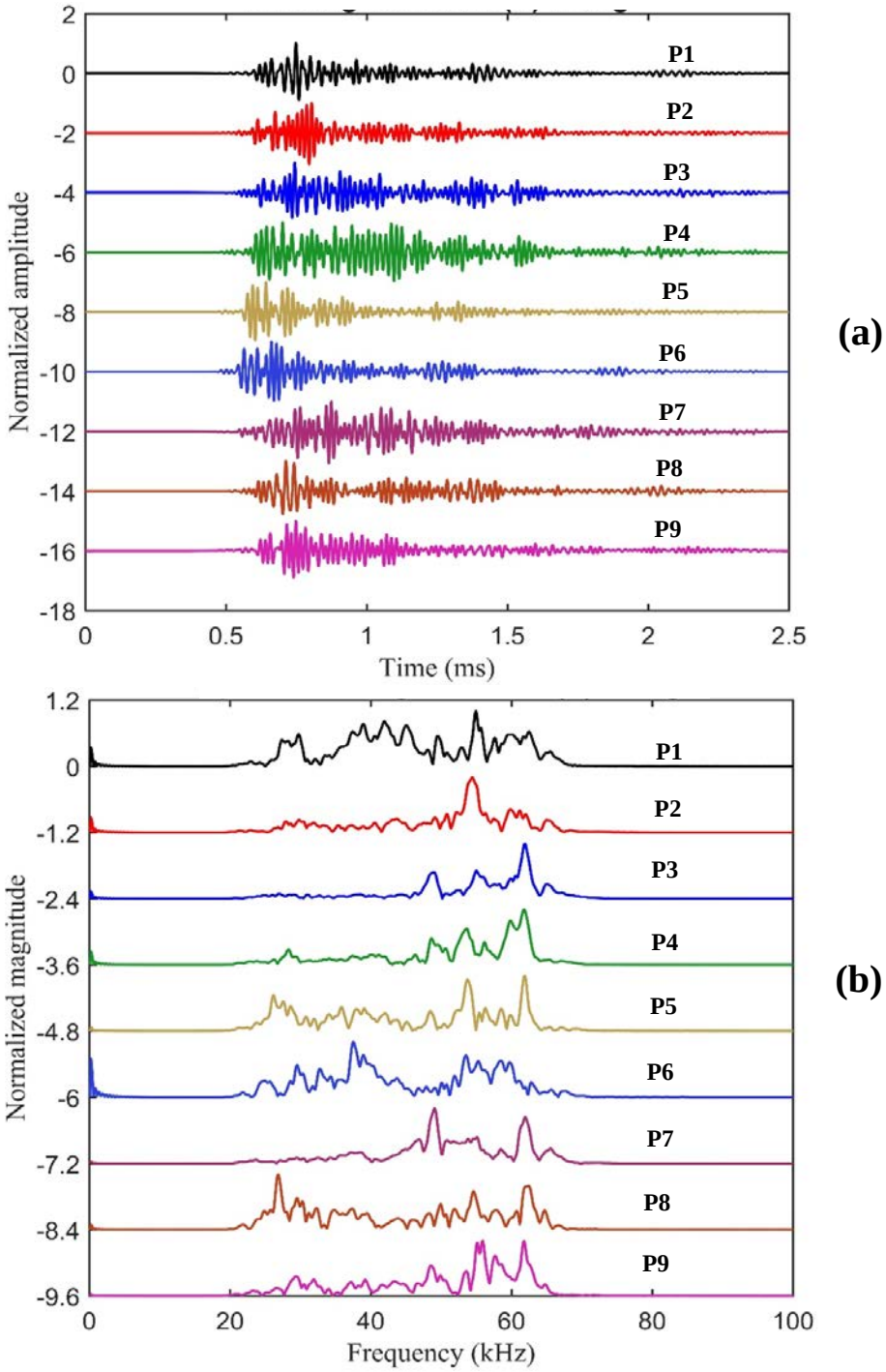

Figure 7-5: Typical waveform signals of the fabricated radial transducers embedded in concrete model MA-SP. (a) in time domian, (b) in frequency domain.

Figure 7-6. The main frame of the compression machine MT35000KN for testing concrete models.

These 50 mm diameter probes were then placed at the top of the water column formed by filling the plastic tubes with distilled water, for the water column ensured consistent coupling (Krautkrämer and Krautkrämer, 1990). An electric square-wave pulse is emitted as electrical excitation for the transmitter probe at the top of the water column. Calculations in time and frequency domains of the signals received by the embedded radial mode transducers are used to evaluate changes in waveform amplitude and Fourier spectrum area (Krautkrämer and Krautkrämer, 1990). Electrical excitation consisted of a single cycle square pulse generated by the function generator, with a nominal resonance frequency of 54 kHz and amplitude of 200 volts.

All concrete models are tested under compression using the machine MTS35000KN where the displacement and corresponding load are recorded continuously. The UPV is the same as the quality control testing setup except four transducers are used, two piezoelectric transducers

(resonance frequency 54 kHz), two bolt-clamped Langevin transducers (resonance frequencies 52 kHz and 40 kHz) made by STEMiNC (Steiner & Martines Inc.)

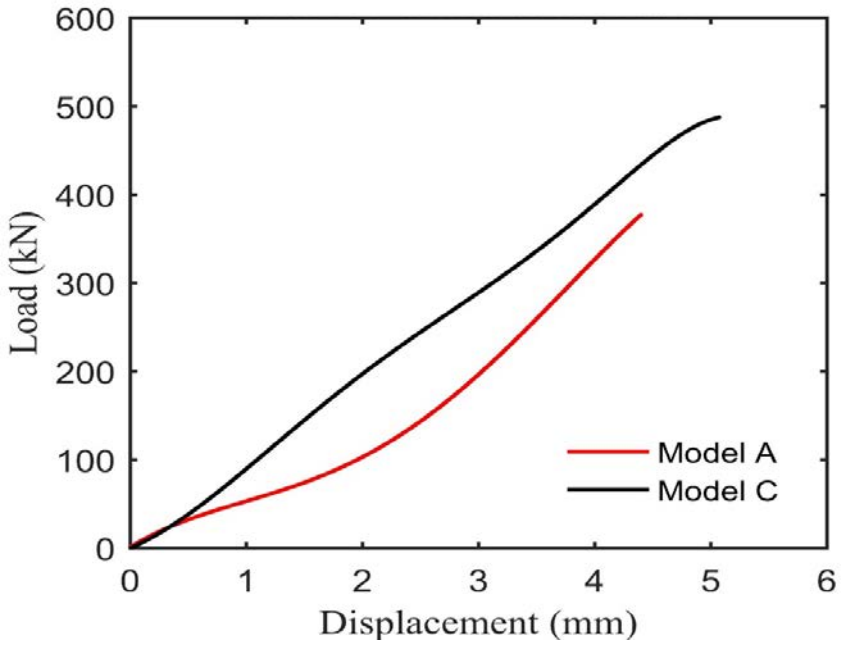

Figure 7-7: Typical load-displacement curves obtained from testing concrete models MA-SP and MC-SDR under compression load.

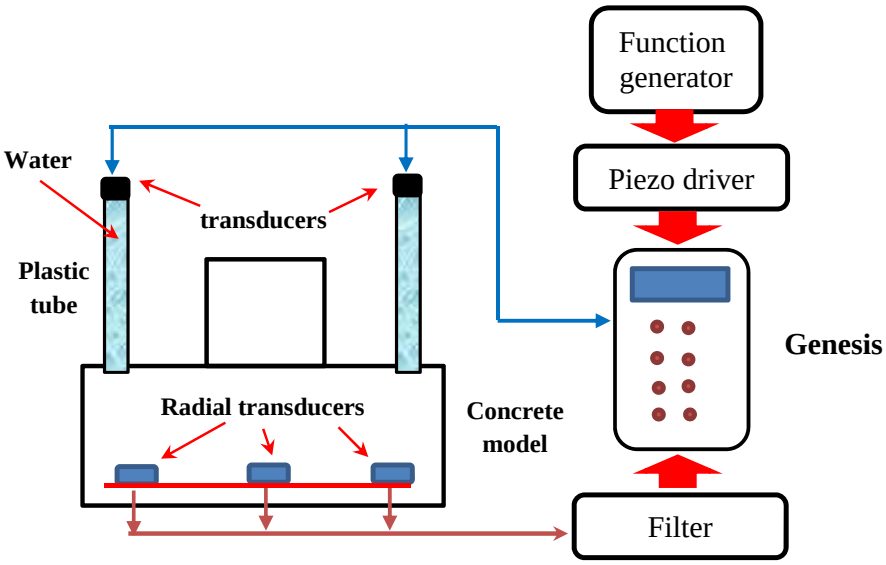

Figure 7-8. Ultrasonic testing setup.

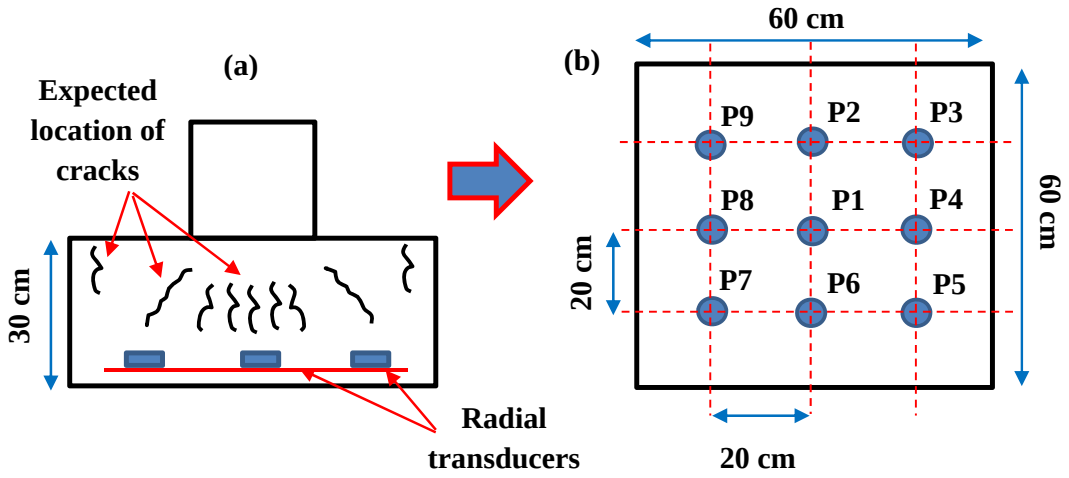

Figure 7-9: Typical distribution of transducers based on expected cracks location. (a) side section with expected crack locations, (b) Top view with transducer distribution outline.

The 54 kHz transducers are glued to aluminum discs, placed at two corners of each concrete model, using Loctite super glue for consistent coupling, while the Langevin transducers are placed on the top of the tubes and coupled to the water column. Also, the electrical excitation consisted of a single cycle square pulse generated by the function generator, with excitation frequency of 50 kHz and amplitude of 200 volts.

7.2.4 Testing Methodology

The testing procedure includes two phases; evaluation of quality control of concrete model during curing period (28 days) represents the phase one. In every model, the acrylic tube filled with distilled water, used to couple the pulse using the 54 kHz transducers, and the nine embedded radial transducers are used to receive the responses which are stored for further processing. The process is repeated with the nylon tube which is also filled with water using the same transducer. The measurements are performed weekly until the fourth week which is the end of curing period. The monitoring process is estimated using two procedures; computing peak amplitude in time domain and spectrum area in the frequency domain.

In the second phase, the concrete models are tested under uniaxial compression load. During the application of load, UPV measurements are obtained based on two procedures; using the tubes with the Langevin transducers (52 kHz and 40 kHz) and using aluminum discs glued to model surface with the 54 kHz transducers glued to the aluminum discs. Figure 7-10 shows the

locations of the tubes and aluminum discs which are located at each corner. This distribution allows to make sure that most of the model volume is inspected effectively. Also, a single cycle square-wave pulse with a 50 kHz (excitation frequency) and amplitude of 200 volts is employed to trigger the transducers of the two configurations. Then, the embedded transducers are employed to receive the responses from four different locations at each load step. In this way, several orientations can be inspected to detect the evolution of cracks induced during the progress of the compression load.

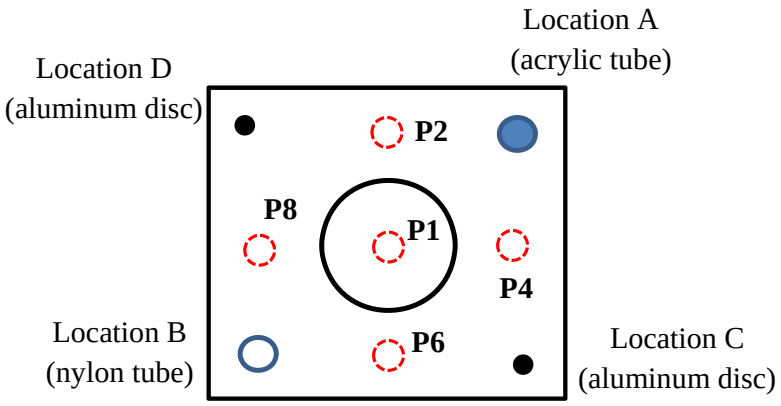

Figure 7-10. Typical outline of concrete model showing the locations of tubes and aluminum discs.

7.3 Experimental results

7.3.1 Quality control phase

P-wave velocity. Inspection to assess integrity and the safety of concrete infrastructures such as shallow foundations has become an urgent topic in civil engineering. To ensure the durability of concrete, it is important to develop a suitable testing procedure. For this purpose, a new NDT testing procedure is developed in the present research to monitor the concrete durability of lab-scale shallow foundation models. The concepts in this method are two-fold; first it based on a new design of fabricated radial transducer (waterproofed and omnidirectional reception of waves) prepared in the infrastructure NDT lab at Waterloo university and suitable to embed in concrete medium. Second, it uses a new technique that sends the excitation pulse via a water column with distilled water to ensure a consistent coupling and ease of access to the surface of the shallow foundation.

Figure 7-11 presents typical results of P-wave velocities computed from the ultrasonic measurements of concrete models MA-SP by sending pulse using 54 kHz transducer through acrylic and nylon tubes during the curing period. Figure 7-11(a) illustrates that the results obtained using acrylic tube are most consistent then the nylon tube. However, both procedures reveal the efficiency of the fabricated transducers to give a good indication of the increase in the P-wave velocity at selected locations which can be attributed to the development of the model concrete strength.

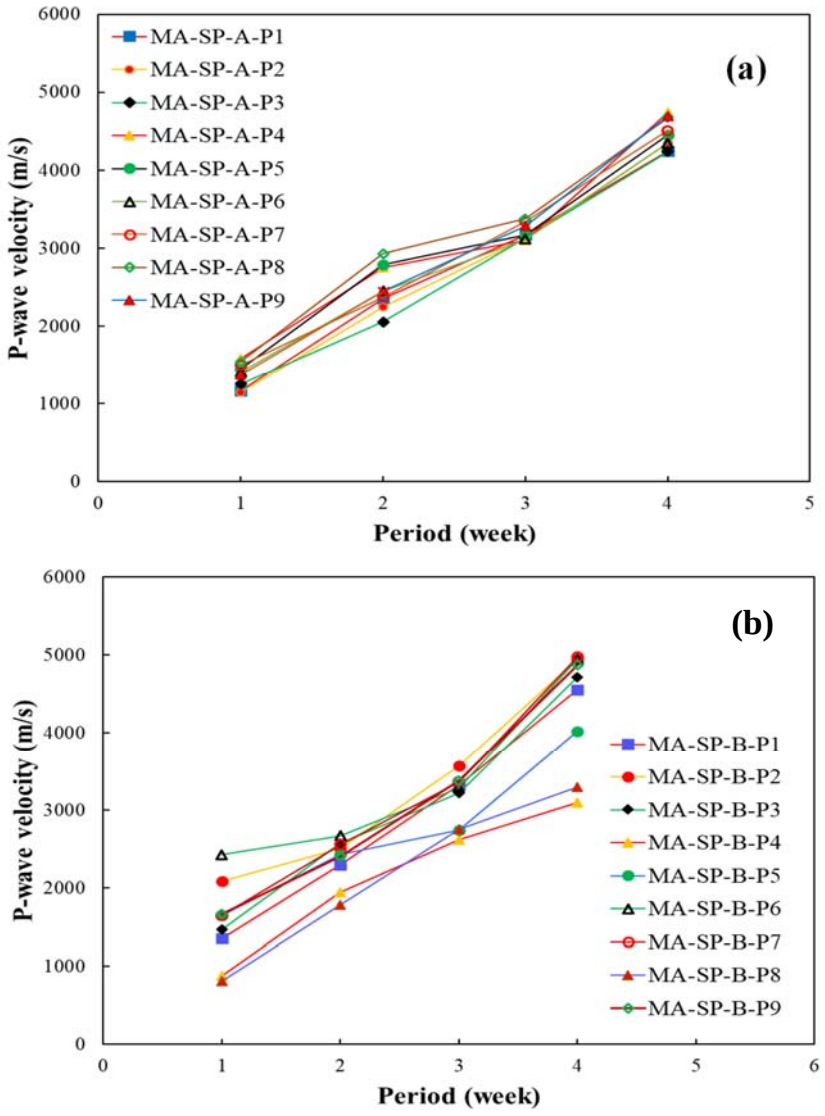

Figure 7-11. Typical P-wave velocities computed using the embedded transducers in concrete model MA-SP, (a) sending pulse using acrylic tube (A), (b) sending pulse using nylon tube (B).

Interestingly, a similar observation can be seen in Figure 7-12 which is the model reinforced with dense steel rebar. In NDT testing of concrete, wave velocity can be considered as a first

evaluation of concrete quality by comparing the measured value with a reference value (Lamond and Pielert, 2006; Krautkrämer and Krautkrämer, 1990; Ensminger and Bond, 2012). According to that, the computed wave velocity between 3600 m/s and 4600 m/s can be considered as good and very good when the value is above 4600 m/s. The minimum value computed from both models was 4242 m/s and 4251 m/s and the maximum values were 4850 m/s and 5000 m/s.

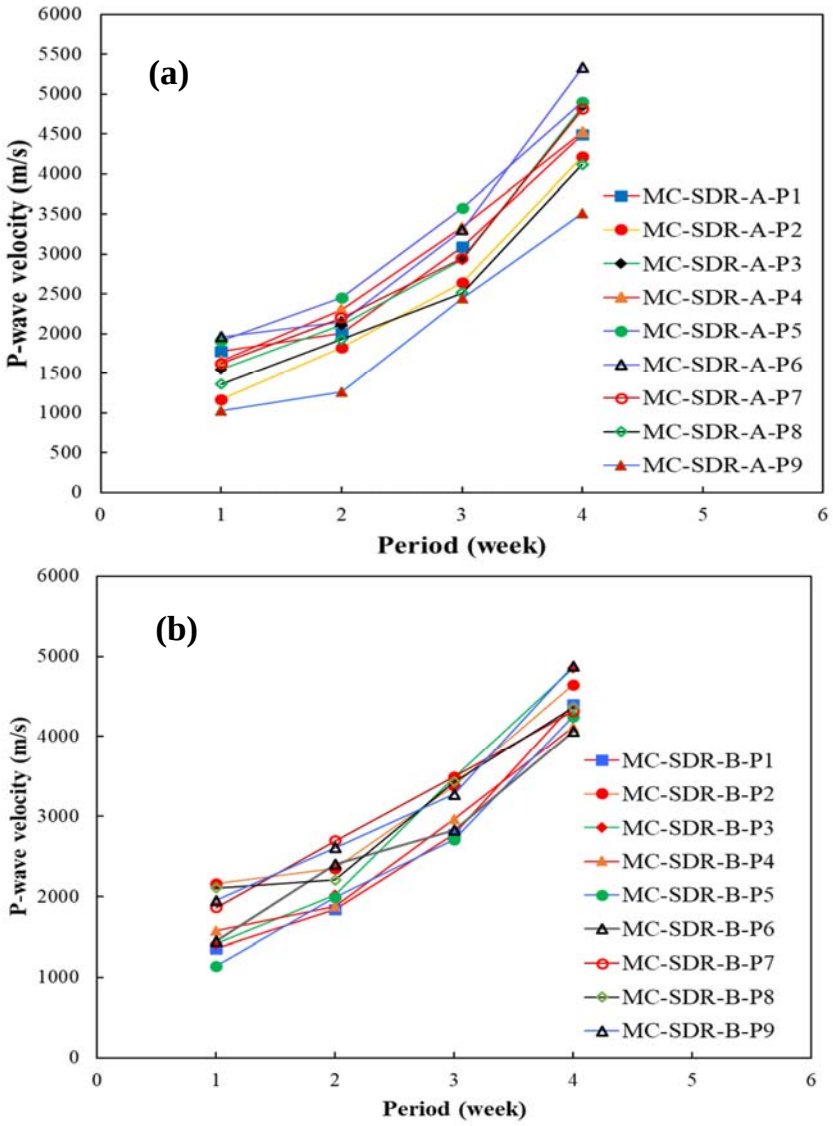

Figure 7-12. Typical P-wave velocities computed using the embedded transducers in concrete model MC-SDR, (a) sending pulse using acrylic tube (A), (b) sending pulse using nylon tube (B).

Therefore, according to the computed wave velocities of both models at the end of the curing period is 4242 m/s and the 4695 m/s and 4878 m/s, respectively and according to the reference values, the concrete of both models may be considered of good and very good quality. This trend is also observed with concrete models. More results can be found in appendix D.

Frequency content. The peak amplitude and spectrum area are other important indices which can be used to observe the concrete quality for the same concrete models. Figure 7-13 shows the waveform signals and corresponding Fourier spectra of model MA-SP received at the centre transducer during the curing process and using the acrylic tube to send the excitation pulse.

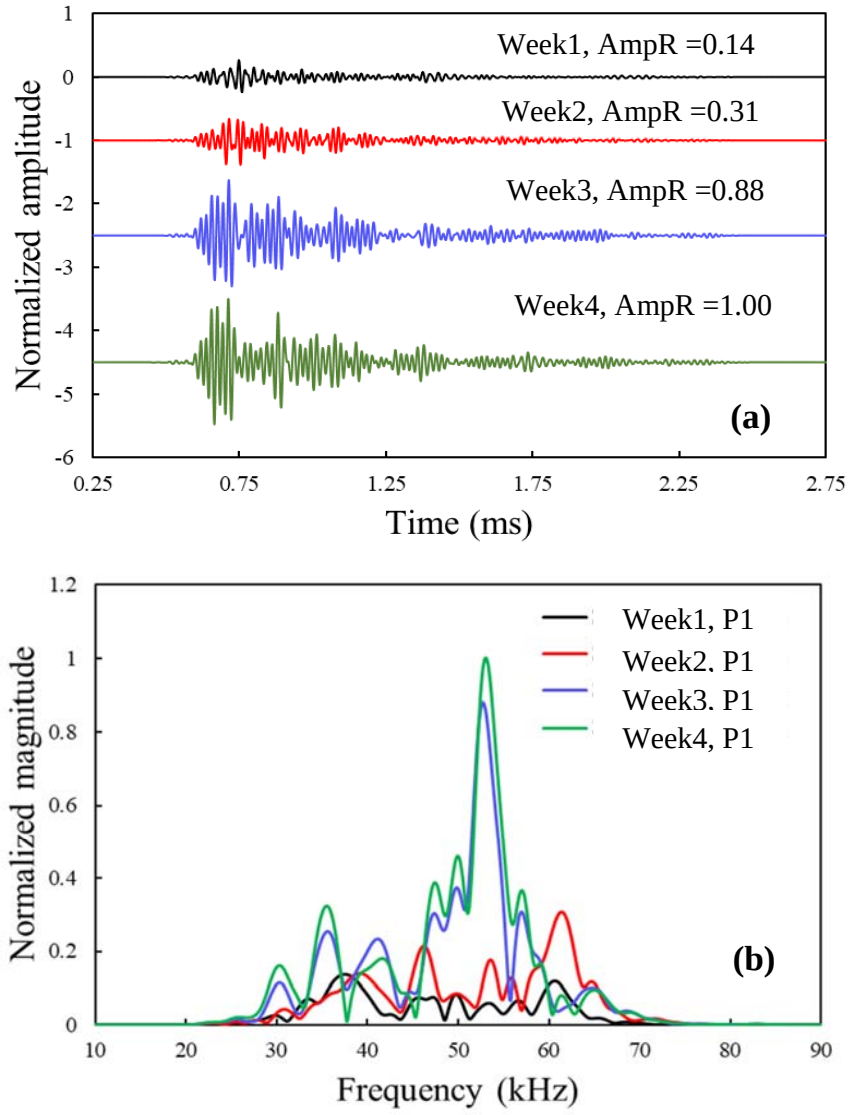

Figure 7-13. Typical waveform signals received at the centre transducer embedded in Model MA-SP during the curing period, (a) in time domain, (b) in frequency domain. AmpR is the maximum amplitude ratio with respect week 4.

The observed waveforms exhibit a good indication of the concrete durability of model MA-SP. By comparing the peak amplitudes and spectrum area of week1 and week4, the differences are around 75% and 86%, respectively. This significant increase demonstrates the reliability of the proposed testing technique to monitor the quality of concrete. Adding to that, similar results are observed with the measurements of other transducers that were embedded in the concrete model MA-SP. More results can be found in appendix D.

Investigation of the steel bar effect in concrete is one of the main interests of current research. The presence of rebar imposes a challenge to the monitoring process of concrete durability. This requires careful analysis of the possible influence of the rebar over the results obtained from health monitoring. In the present study, concrete models reinforced with light and dense steel bar were studied. For example, the observed amplitudes and spectrum areas obtained from the measurements of concrete model reinforced with dense rebar reveal a good indication of the strength development of the concrete as shown in Figure 7-14. Examining Figure 7-14 also shows significant increase in the amplitude and the spectrum area of the recorded waveform as an indication of the development of the concrete durability. It was also noted that the observed gain is less in comparison to the plain concrete model MA-SP which may attributed to the curing conditions.

Figure 7-15 shows the normalized gain in amplitude of the waveforms obtained from testing concrete model MA-SP during curing time. Figure 7-15(a) represents the results obtained using acrylic tube to send the pulse, while Figure 7-15(b) the result indicates the results of the nylon tube. Even the results shown different trends of amplitude gain, the main observation is the increase of the amplitude over the curing time which can be attributed to the progress occurs in concrete strength.

This interesting pattern is also observed with the results of concrete model that reinforced with dense rebar MC-SDR as shown in Figure 7-16. The observed results shown that nylon tube has better indication of strength development than acrylic tube.

7.3.2 Damage evaluation under compression load

Monitoring damage induced under compression load is another application of the NDT technique that developed in this study. Also, the measurements obtained using this technique are compared with the results of using transducers glued directly to the surface of the lab-scale models.

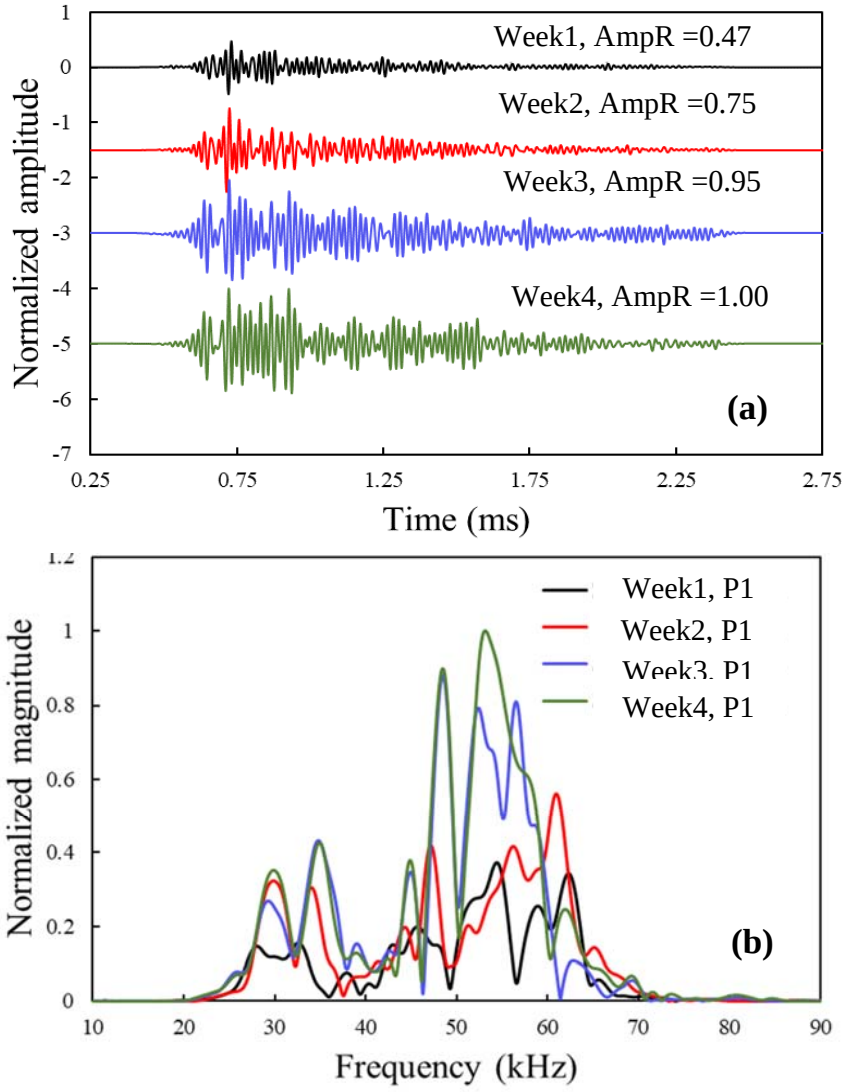

Figure 7-14. Typical waveform signals received at the centre transducer embedded in Model MA-SDR during the curing period, (a) in time domain, (b) in frequency domain.

The visual surface cracks that appear on the sides of concrete models are monitored to compare with their influences on the characteristics of the propagated waveforms. For example, Figure 7-17 shows the observed surface crack on one side of the concrete model MA-SP which is located underneath transducer P6. On the other hand, Figure 7-18 represents waveform signals and corresponding Fourier spectra obtained from ultrasonic measurements of model MA-SP at transducer (P6), in this case, the pulse sent through the nylon tube (location B) using Langevin 40 kHz.

Figure 7-18 illustrates that the magnitude reductions in both time domain and frequency domain (65% and 66%) indicate the damage seen by the propagated waveform which was received at

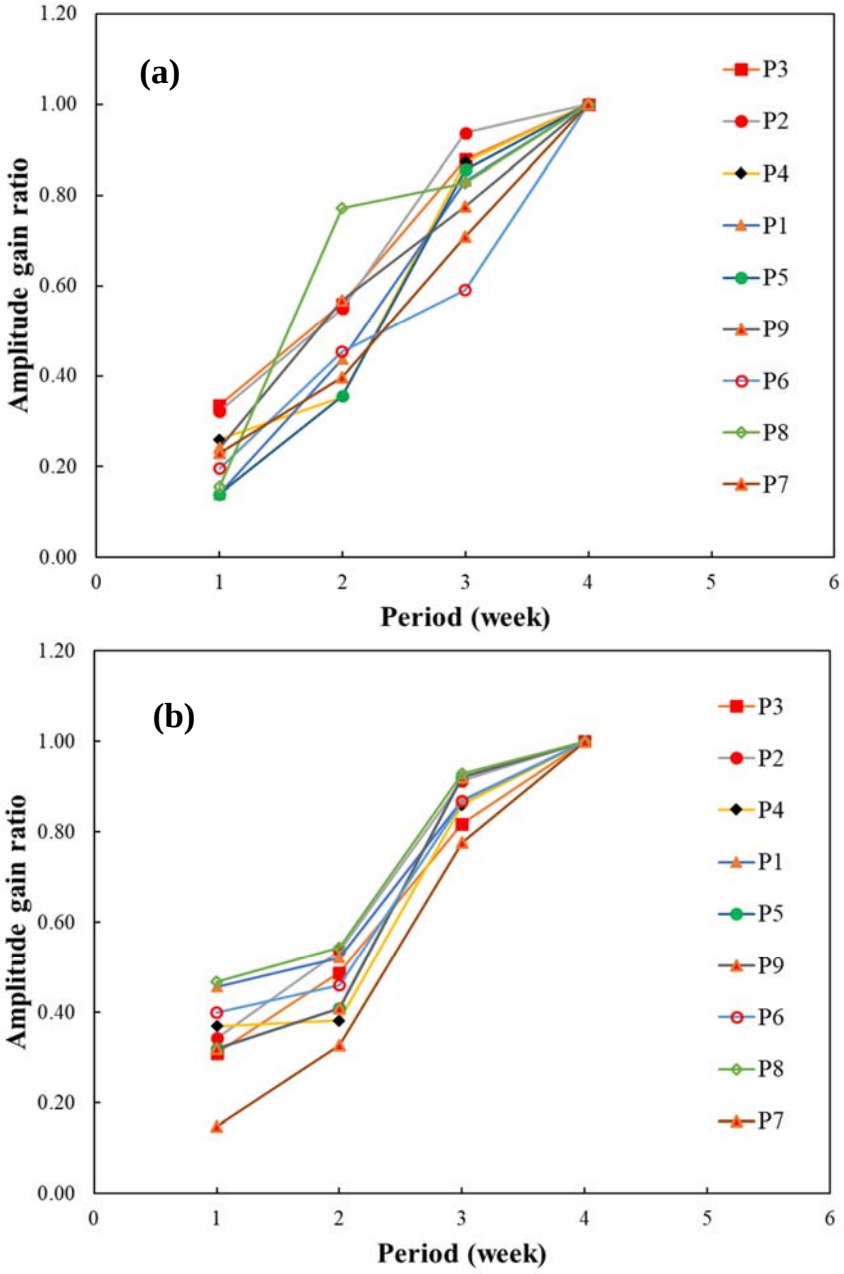

Figure 7-15. Typical amplitude gain ratio results of the waveforms received at the embedded transducers in concrete model MA-SP during curing period. (a) sending pulse through acrylic tube (A), (b) sending pulse through nylon tube (B). Transducers are arranged based on the distance from the excitation source.

transducer (P6). Comparing with the visual inspection of the crack that observed in model MA-SP as shown in Figure 7-17 which reveals a crack beside the location of the transducer (P4).

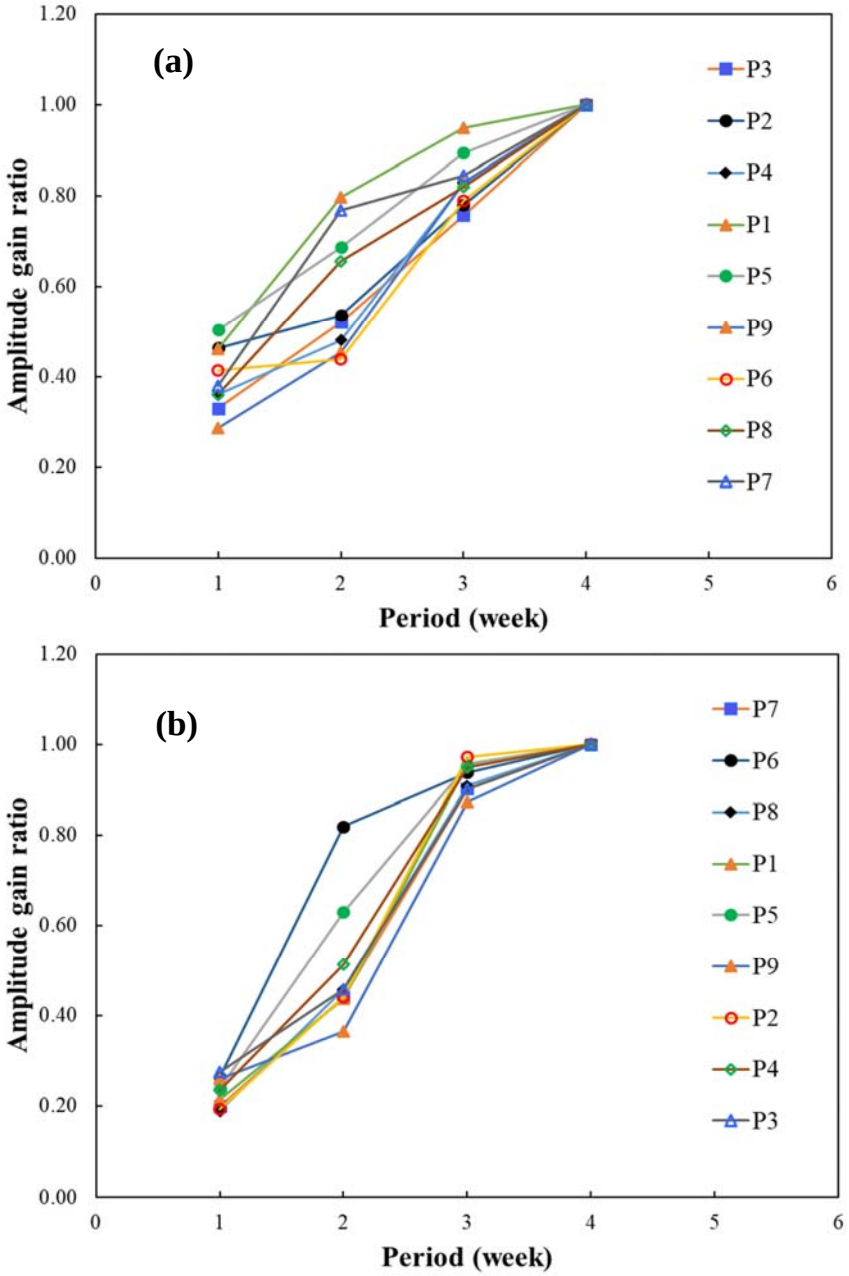

Figure 7-16. Typical amplitude gain ratio results of the waveforms received at the embedded transducers in concrete model MC-SDR during curing period. (a) sending pulse through acrylic tube (A), (b) sending pulse through nylon tube (B).

The developed testing technique shown a good indication of the crack growth under compression load. This observation is also noticed with other transducers.

On the other hand, the results obtained from using 54 kHz to send the pulse, location C in Figure 7-19, indicate waveform signals less attenuated because of the induced crack in comparison to the observed values with the 40 kHz as shown in Figure 7-18. The reductions in time domain

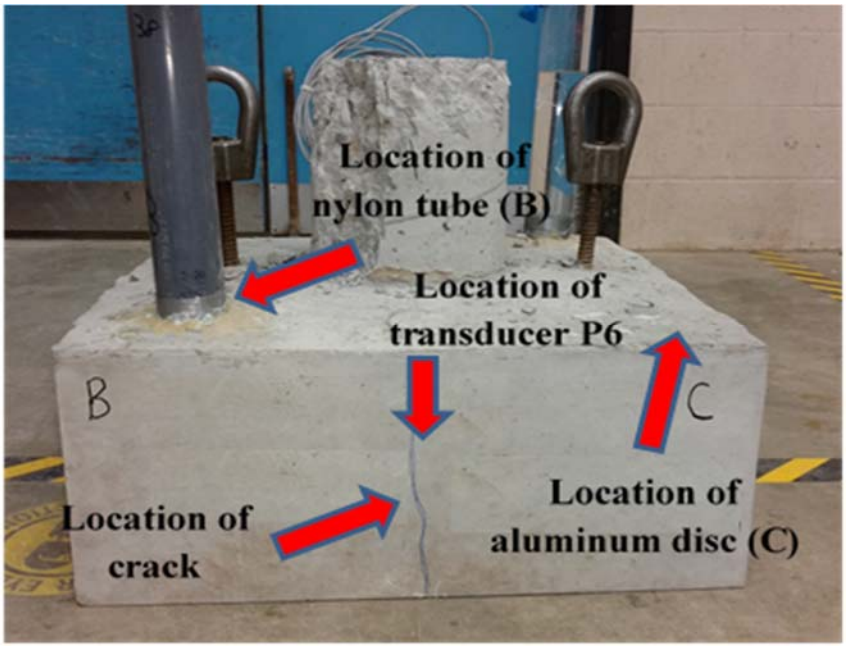

Figure 7-17. Picture of the model MA-SP shown a crack marked with blue color underneath the location of transducer (P6).

and frequency domain are 13% and 7%, respectively. The lower results of 54 kHz which is glued to the surface of the model highlight the reliability of using the tube technique to send the excitation pulse, even though both transducers are approximately located at the same distance from the crack location.

In the case of concrete model MC-SDR that reinforced with dense rebar, the results of waveform signals obtained from ultrasonic measurements using Langevin 52 kHz with acrylic tube and received at transducer (P2) reveal a similar trend of crack detection that was observed in model MA-SP. For example, Figure 7-20 shows a visual surface crack observed on the side located nearby transducer P2. This observation is essential to compare the detection of crack presence with the visual inspection and to examine the feasibility of the developed NDT procedure to monitor crack growth at early stage of loading.

Figure 7-21 presents typical waveform signals and corresponding Fourier spectra received at transducer P2 under compression load and using acrylic tube with 52 kHz to send the excitation pulse. In this figure, the reduction in amplitude and spectrum area are 50% and 43% respectively. In contrast to this result, the waveforms shown in Figure 7-22 received at the same

transducer (P2) and triggered by 54 kHz at location D show lower indication of damage even though the transducer (P2) was located between locations A and D (Figure 7-20) in which the reduction in amplitude and spectrum area are 7% and 8%, respectively.

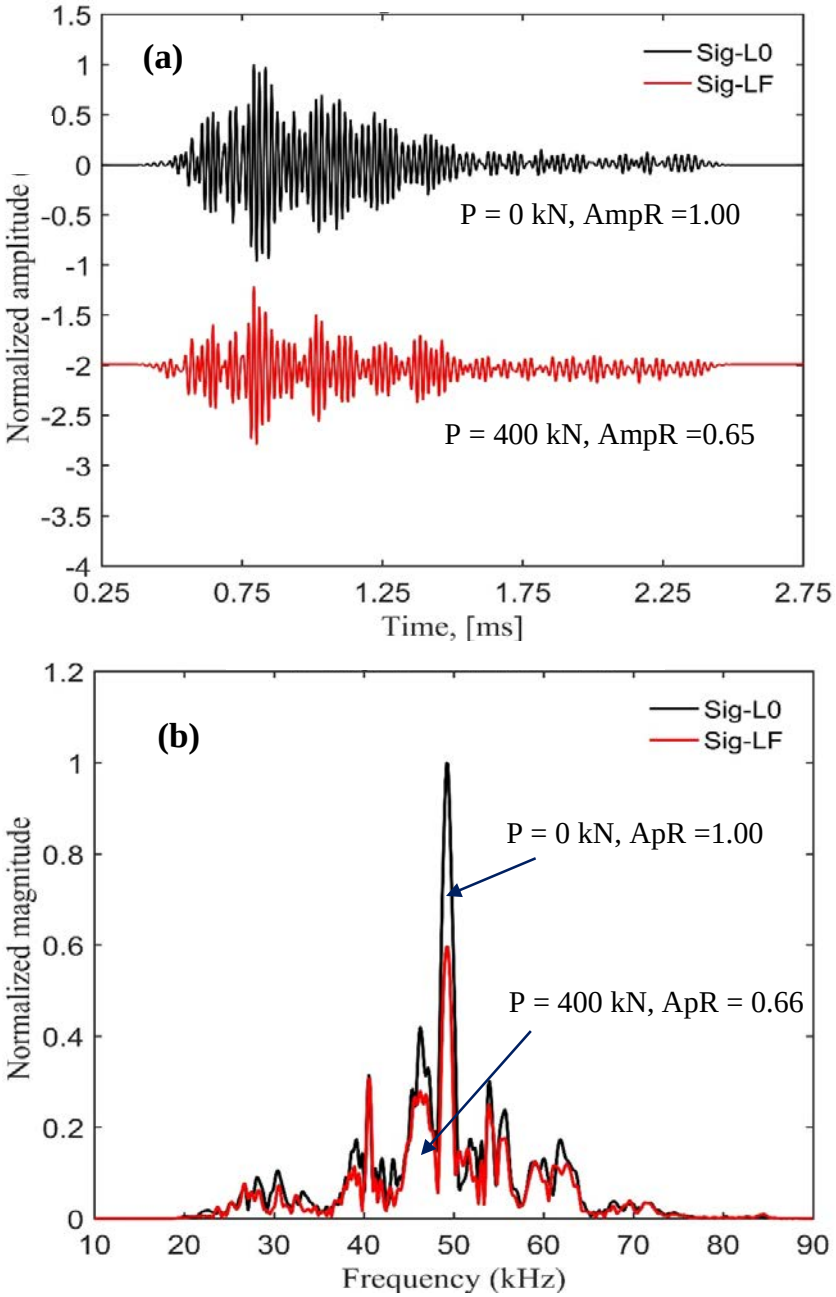

Figure 7-18. Typical waveform signals send using nylon tube (B) with 40 kHz and received at transducer (P6) embedded in Model MA-SP during compression load, (a) in time domain, (b) in frequency domain. P is applied load. ApR is the spectrum area ratio with respect week 4.

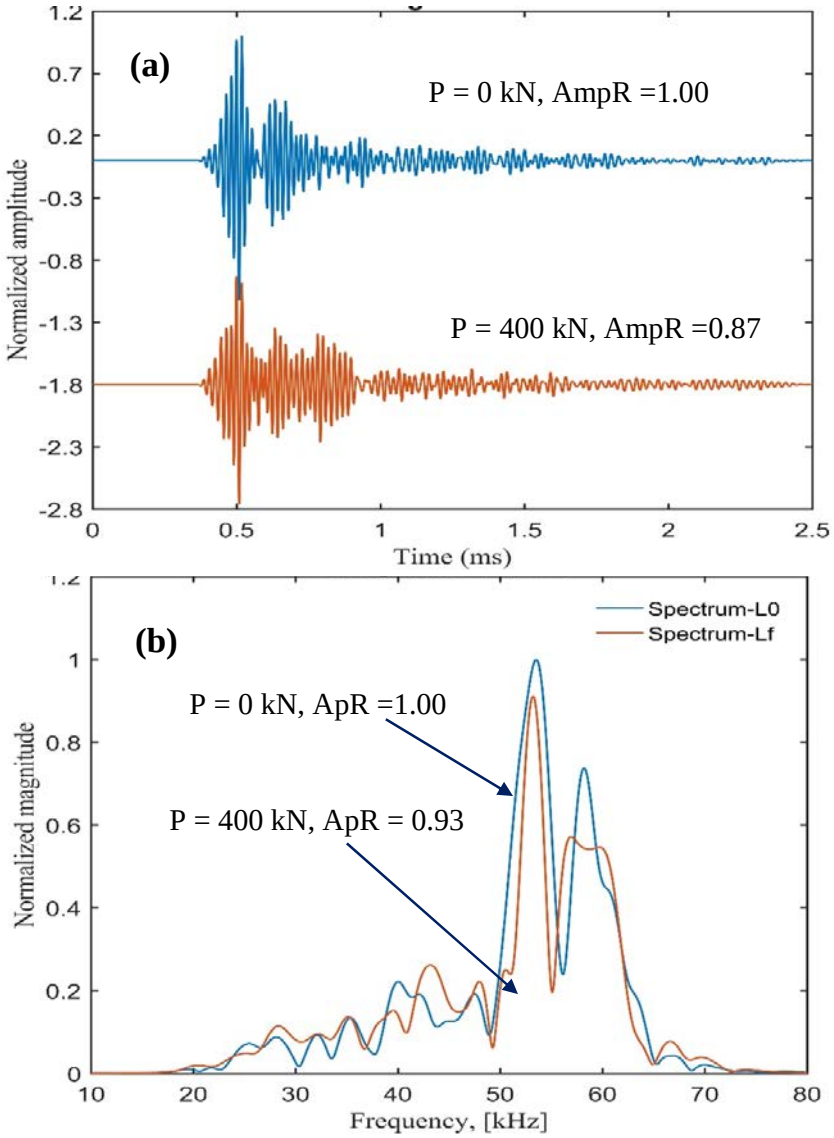

Figure 7-19. Typical waveform signals using aluminum disc with 54 kHz (C) and received at transducer (P6) embedded in Model MA-SP during compression load, (a) in time domain, (b) in frequency domain. L0 and Lf are initial and final load steps.

The attenuation analysis of the testing measurement dataset is also performed. Figure 7-23 shows the total attenuation of the waveforms received using the embedded transducers in model MA-SP. The transmission of pulse procedures in this example include acrylic tube (52 kHz, location A) and direct contact (54 kHz, location C). Figure 7-23(a) reveals a gradual detection of the cracks developed under compression at even lower load values using the acrylic tube procedure with 52 kHz, the observed range of attenuation are between 1.5 and 7 (dB).

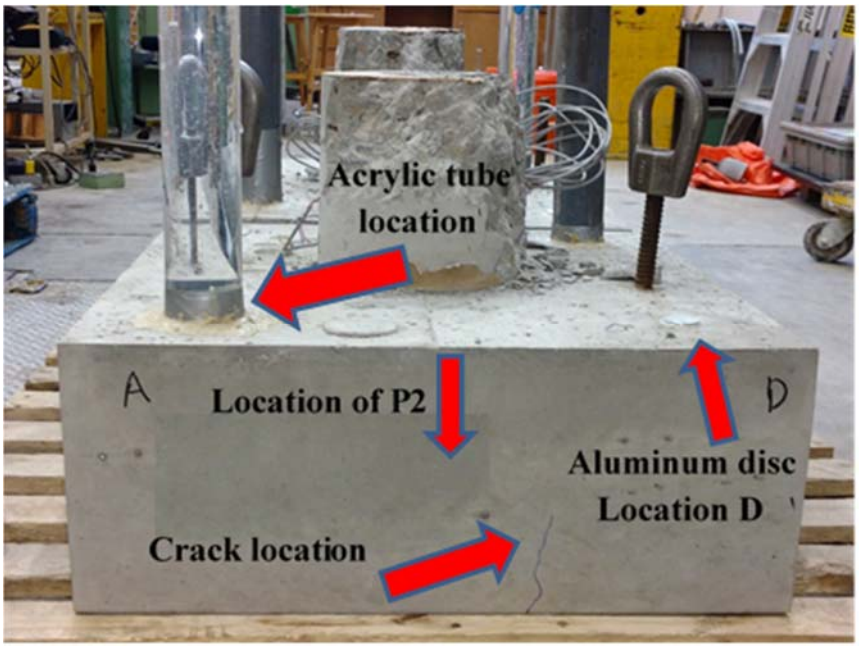

Figure 7-20. Picture of the model MC-SDR shown a crack marked with blue color beside the location of transducer (P2).

In Figure 7-23(b), the case is different in which the results are not consistent especially with transducers (P1, P3, P8) in contrast to the observed values using the acrylic tube procedure. Figure 7-24 shows the results of the total attenuation obtained from the ultrasonic measurments of cocnrete model MC-SDR reinforced with dense rebar and using two pulse trasmission techniques, using 52 kHz through acrylic tube and using 54 kHz through aluminum disc. These results also computed based on the peak amplitude of the recorded waveforms under compression load. The obseved results uisng both pulse trasmission methods reveal similar trend of crack detection as the results of model MA-SP (3.5 - 11 dB). Sending the excitation pulse through the acrylic tube provide better indication of crack grwoth in comparison to the direct method.

In which, the late procedure reveal inconsistent attenuation values that may attributed to the presence of rebar distract the propgation of wave. Also, another procedure is used to compute the attenuation using the spectrum area. Figure 7-25 illustrates the results obtained from the ultrasonic measurements of the same model MA-SP.

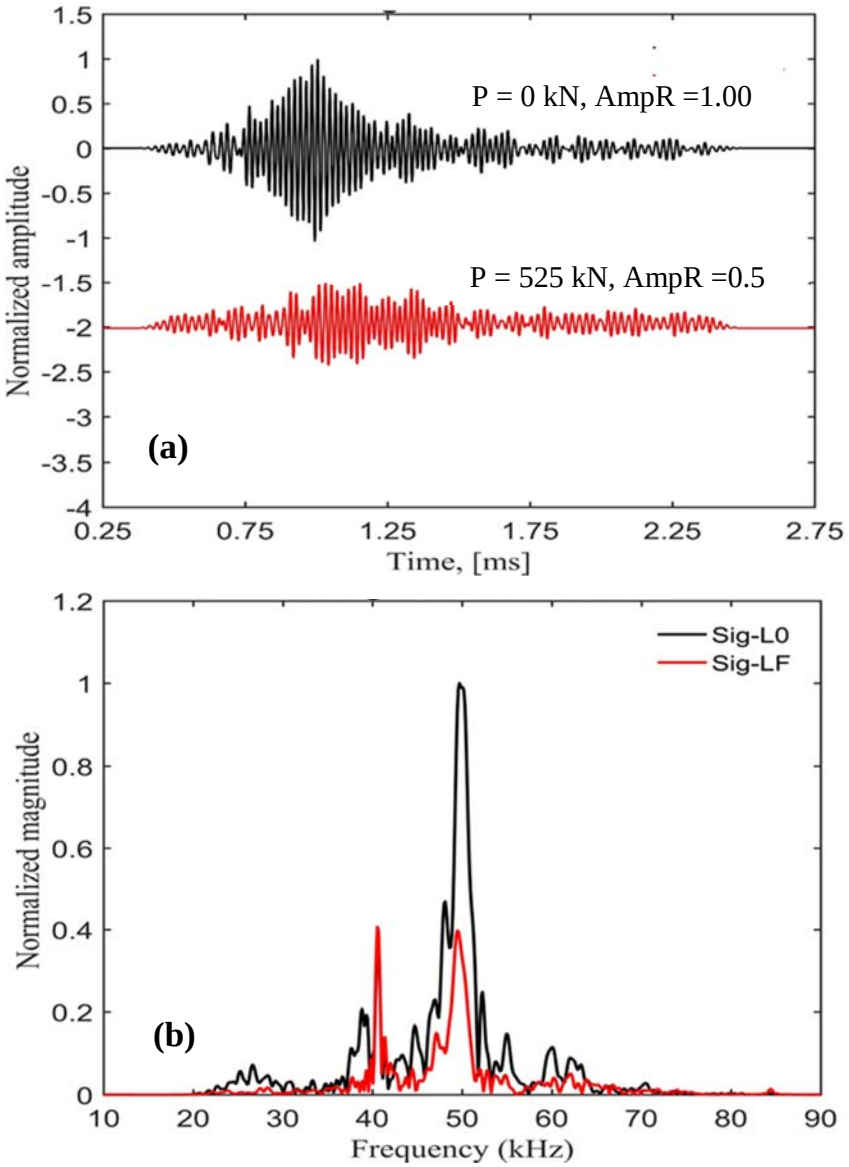

Figure 7-21. Typical waveform signals send using acrylic tube (A) with 52 kHz and received at transducer (P2) embedded in Model MC-SDR during compression load, (a) in time domain, (b) in frequency domain.

It can also be found in this figure that the attenuation of signals received by transducers (P3-4, P5, P7, P9) using the direct procedure with 54 kHz varies under compression load, the situation is different with other transducers which show good damage indication and this in a good agreement with the results obtained by using acrylic tube. The observed attenuation range for acrylic tube method was found to be between 1 to 5.5 (dB).

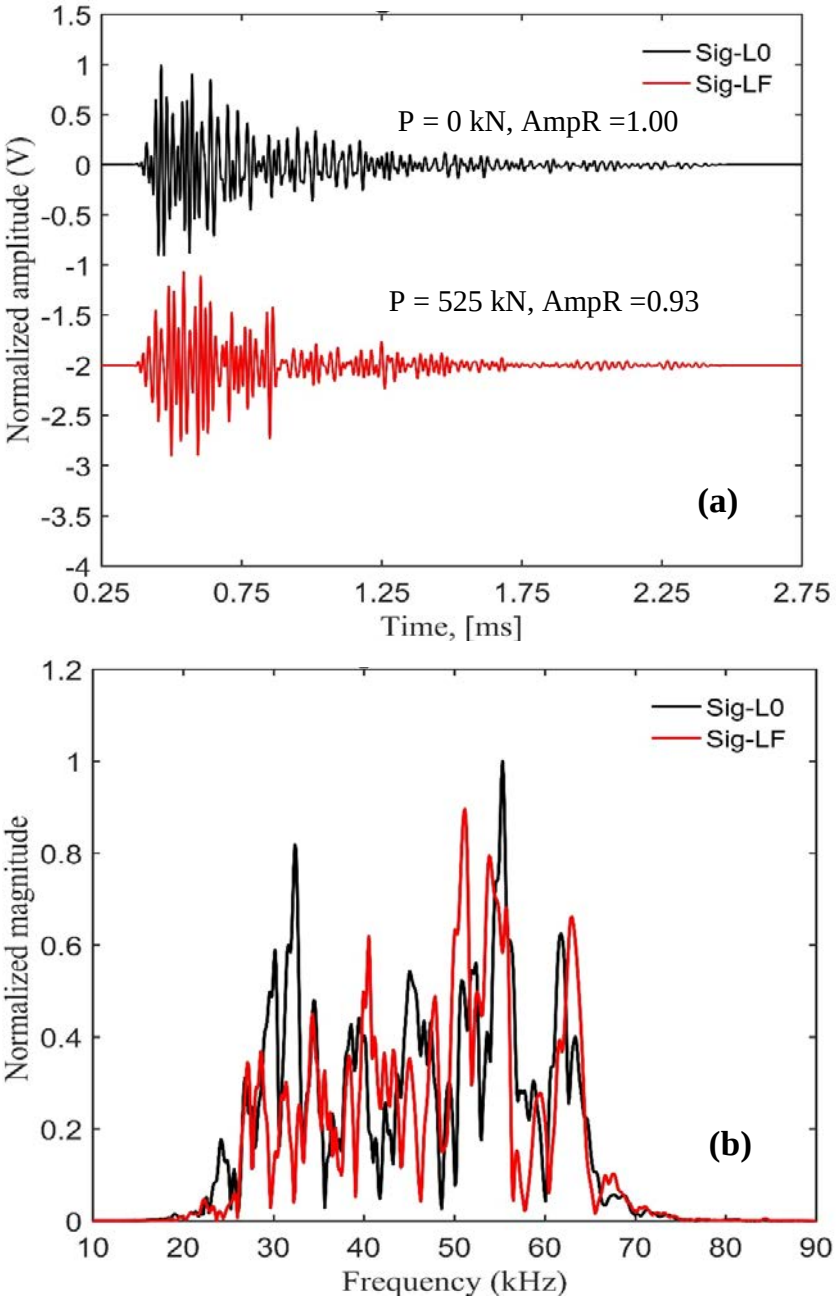

Figure 7-22. Typical waveform signals using aluminum disc with 54 kHz (D) and received at transducer (P2) embedded in Model MC-SDR during compression load, (a) in time domain, (b) in frequency domain.

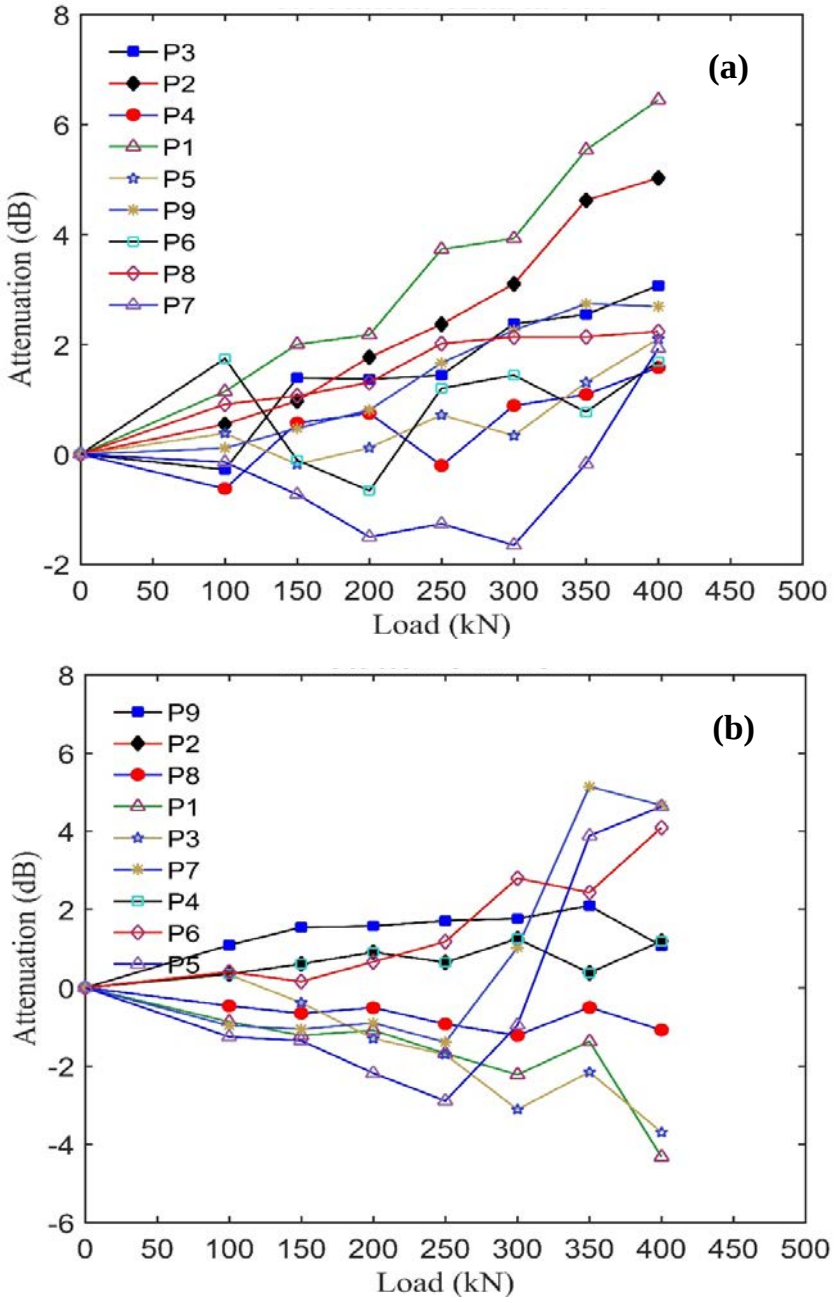

Figure 7-23. Typical attenuation results of model MA-SP computed based on peak amplitude of the waveform signals received using the nine embedded transducers during compression load, (a) using acrylic tube with 52 kHz (location A), (b) using direct contact with 54 kHz (location C).

The results of attenuation measurements computed using spectrum method and obtained from ultrasonic measurements during testing concrete model MC-SDR are shown in Figure 7-26. The figure reveals that acrylic tube method to send the excitation pulse highlights the feasibility

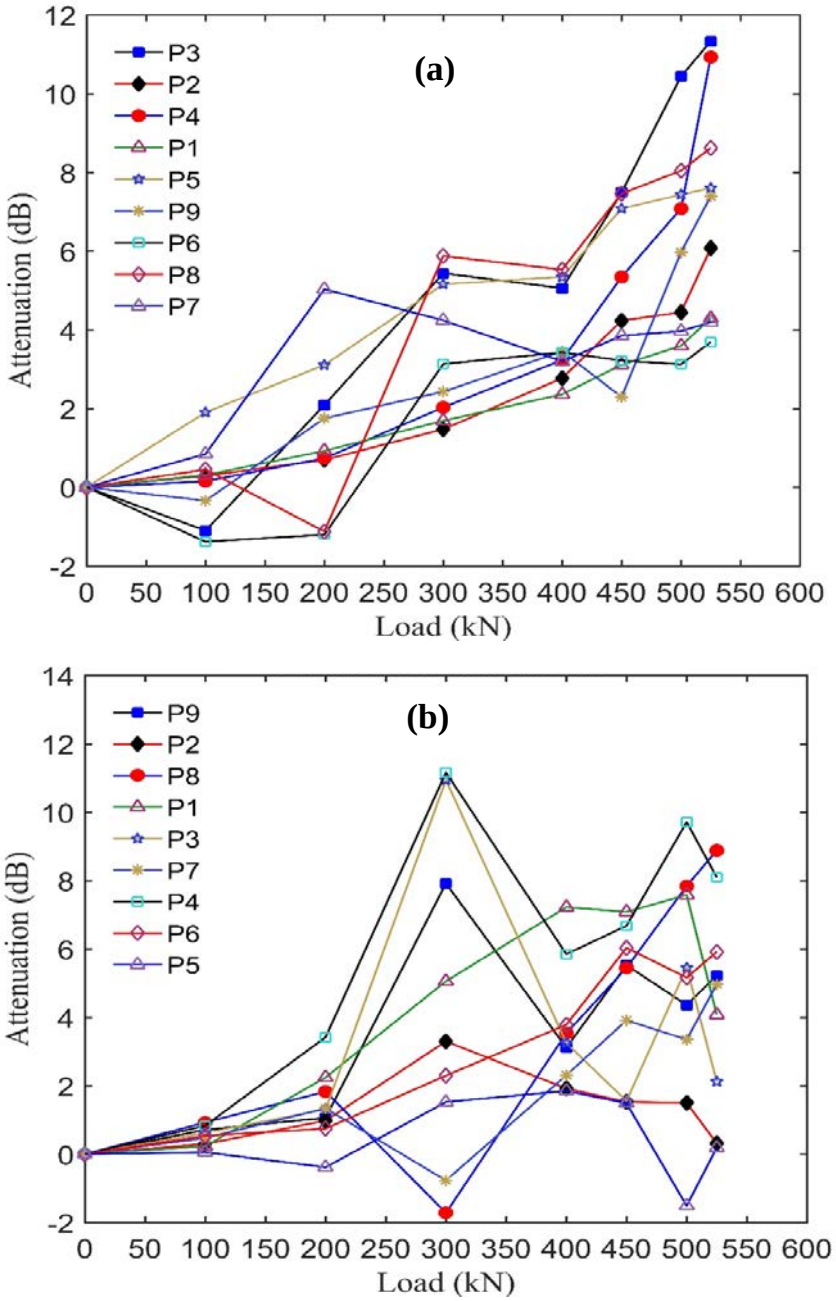

Figure 7-24. Typical Attenuation results of model MC-SDR computed based on peak amplitude of the waveform signals received using the embedded transducers during compression load, (a)using acrylic tube with 52 kHz (location A), (b) using direct contact with 54 kHz (location C).

of this technique to detect early cracks in concrete model reinforced with dense rebar. In contrast, the direct method using 54 kHz transducer shown inconsistent results, even some transducers are performed better, the total performance is lower than the tube method.

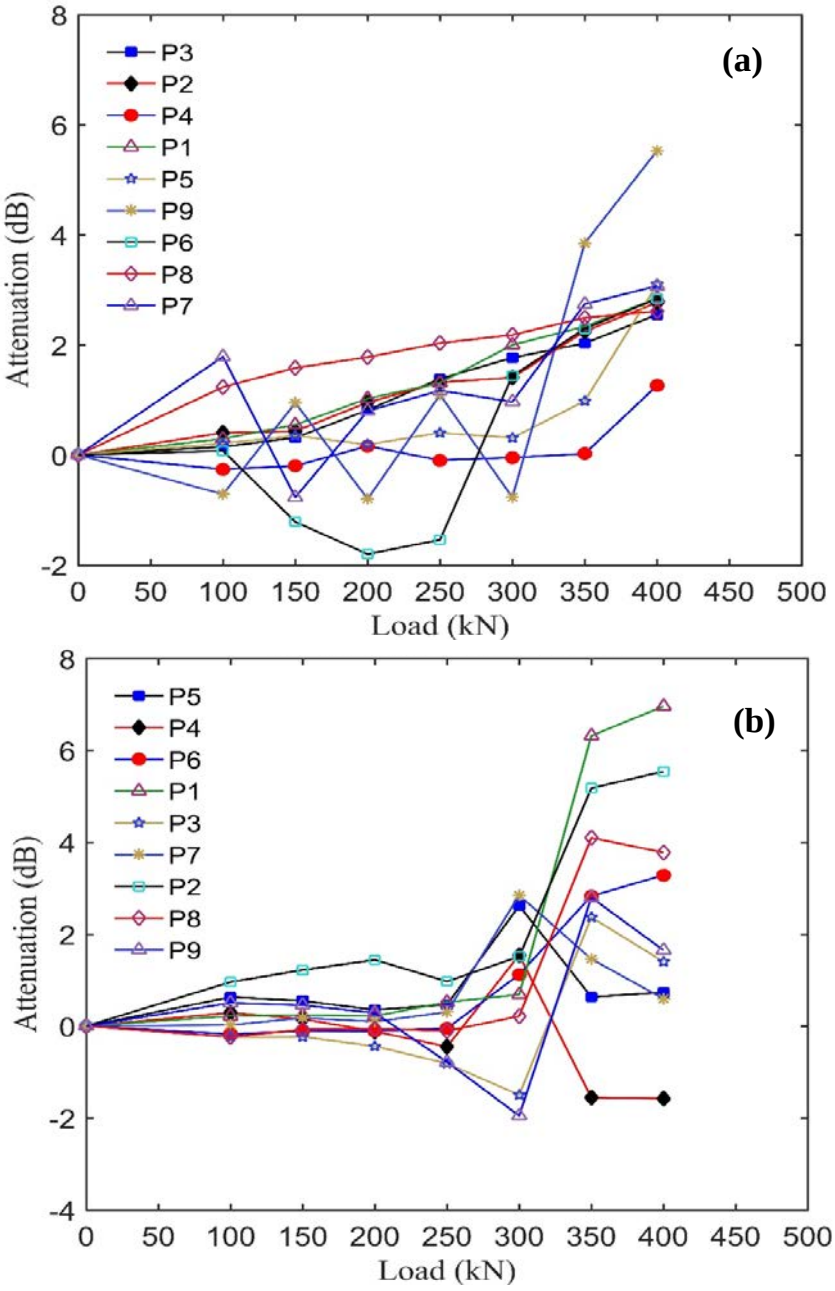

Figure 7-25. Typical Attenuation results of model MA-SP computed based on spectrum area of the waveform signals received using the nine embedded transducers during compression load, (a) using acrylic tube with 52 kHz (location A), (b) using direct contact with 54 kHz (location C).

The findings of this section highlight the efficiency of the proposed NDT procedure to monitor damage in concrete of shallow foundation lab-scale models. Also, it observed the reliability of the technique of using a tube filled with water for pulse transmission in comparison with the

direct contact procedure. Another important observation is the possibility to monitor the damage induced under compression load even when rebar is present in concrete.

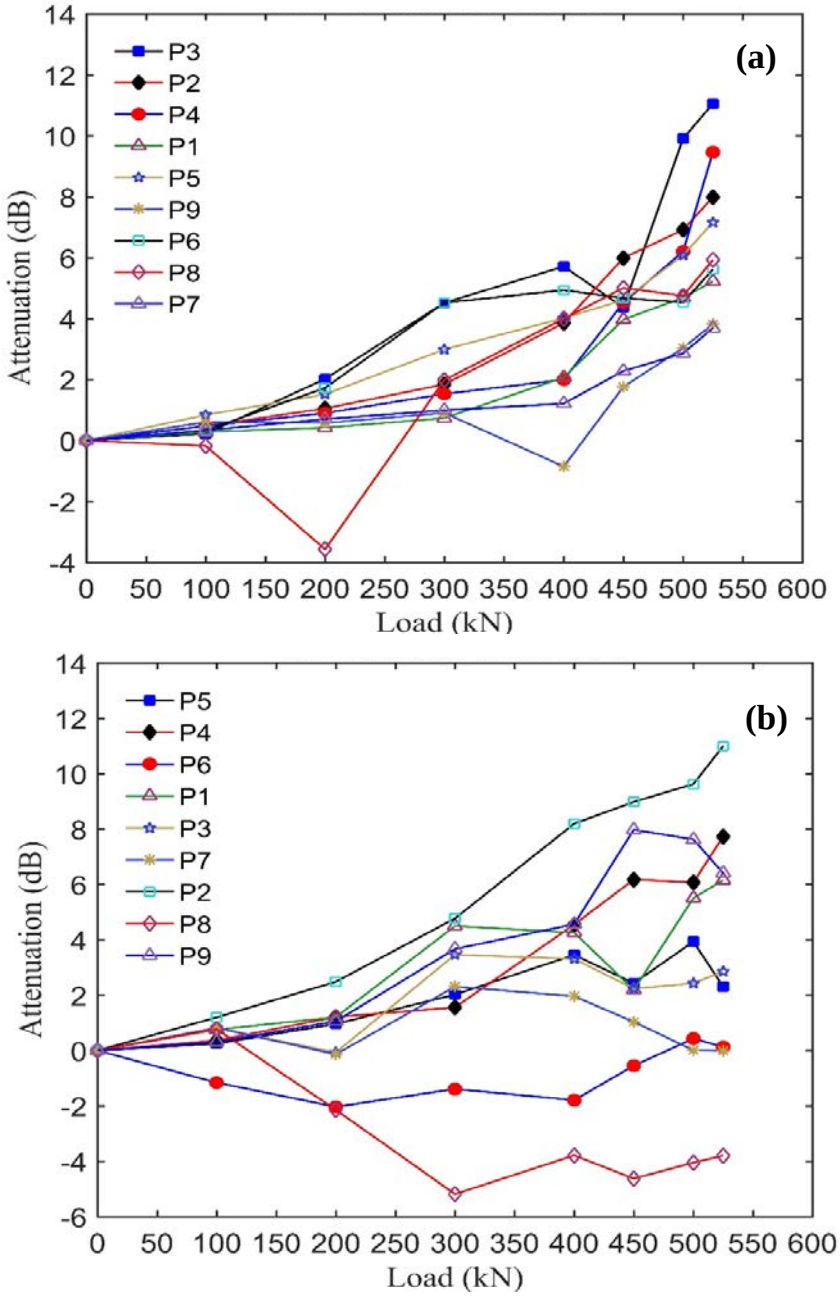

Figure 7-26. Typical Attenuation results of model MC-SDR computed based on spectrum area of the waveform signals received using the nine embedded transducers during compression load, (a) using acrylic tube with 52 kHz (location A), (b) using direct contact with 54 kHz (location C).

7.4 Summary

This chapter included the findings of quality control phase and the damage evaluation under compression load phase of four shallow foundation lab-scale models. One model is plain concrete and three are reinforced with rebar. Thirty-six radial transducers are fabricated and embedded in the four models. Two transmission pulse procedures were proposed, one using tubes filled with water and the other aluminum discs glued to the surface of the model. In the quality phase, the tube procedure was used to monitor the development of the concrete strength, while both transmission procedures are used in the damage evaluation phase.

The results of the quality assessment phase showed good indication of concrete durability during four weeks of curing. The was assessment performed by monitoring the P-wave velocities that were computed from the ultrasonic measurements received by the embedded transducers. Most of the observed wave velocities are above 4000 (m/s) which may be considered good according to the documented reference values. Also, waveform amplitude and spectrum area were investigated to observe the strength progress of the concrete model, the gain noticed in a typical waveform and spectrum areas reach up to 85%. On the other hand, the results of phase two indicate the efficiency of the proposed NDT procedure to evaluate the damage evolution under uniaxial compression load. The assessment of damage was performed by observing the signal amplitudes and the spectrum area. For example, the observed reduction of waveform signal of model MA-SP in the time domain and frequency domain were found to be 65% and 66% respectively, while in model MC-SDR, which contains rebar, the reductions noticed were 50% and 43% respectively. Similar trends were observed with the attenuation computed using the amplitude and spectrum area.

The findings of this chapter highlight the efficiency of the proposed NDT procedure to monitor damage in concrete of shallow foundation lab-scale models. Also, it observed the reliability of the tube technique that was filled with water for pulse transmission in comparison with the direct contact procedure. Another important observation, the possibility to monitor the damage induced under compression load even when rebar is present in concrete.

Chapter 8: Conclusions and Recommendations

In this project, a new NDT procedure is proposed based on fabricated transducers, which are waterproofed and cost-effective, embedded at the base of lab-scale concrete foundation models. Although there is enormous literature about using embedded transducers to assess the integrity of concrete structures, there is no reference to their use in shallow foundations. Currently there is no comprehensive technique to assess reinforced concrete of shallow foundations. In this study, two procedures are used to generate the excitation pulse; one uses a transmitter on an aluminum plate glued to concrete surface; and the other uses a tube filled with water; which is partially embedded in the concrete. This second option has good potential for practical applications as the transducer does not have to touch the foundation surface. The new testing procedure can be used during construction to monitor the uniformity, curing, and quality of the concrete; as well as during the in-service life to assess the condition of the foundation, especially after any significant event such as an earthquake or overloading.

This project includes an extensive literature review and a comprehensive experimental program on the use of ultrasonic testing for damage detection. The literature review focused on the condition assessment methods for concrete elements, the use of the ultrasonic and laser-vibrometer tests for structural evaluation, and the characterization of ultrasonic transducers. The literature review highlighted the limitations of the current condition assessment methods and the required steps to improve them. This information is used to define the fundamental aspects to be studied in the subsequent experimental program. The experimental program addressed important issues such as transducer characterization, testing setup, damage evaluation, and finally the improvement of the system. The experimental program included the casting of lab-scale models shallow foundation and fabrication ultrasonic transducers. The main findings of the research are summarized in the following sections. In this work, all ultrasonic measurements are averaged 16 times to ensure the consistency of the results and to eliminate high frequency noise. The average coefficient of variance obtained is less than 3.5%; which is considered acceptable in this type of measurements (typical measurement error ~5%). Also, different tests were repeated more than three times by removing and putting back all the ultrasonic transducers to enhance the statistical significance of the results.

8.1 Characterization of ultrasonic transducer

The characterization measurements were performed for different types of piezoelectric transducers using conventional methods to determine the characteristic time delay of the

system; and a state-of-the-art laser Doppler vibrometer to measure the actual the frequency response of the transducers. In addition, the selection of the couplant for laboratory testing was described.

The laser characterization of the transducers showed that the frequency response is not flat; hence, the nominal frequency given by the manufacturer is not an adequate value for the characterization of transducers. The resonance frequencies of these transducers differed with the nominal values reported by the manufacturer by only 5%; however, significant resonances were also found at different frequencies. The resonance frequencies of the calibrated transducers obtained from laser measurements are identified to be used in subsequent ultrasonic testing in this research project.

8.2 Fracture evaluation in a homogenous medium

A new fabrication technique is used to generate a stable fracture growth at the fused PMMA specimens. Complementary ultrasonic pulse velocity and signal attenuation measurements are used to characterize the fracture growth in a homogenous media (PMMA specimens).

The UPV results show that wave velocity and fracture length are practically independent (compressional wave velocity decreased only by 4% for different fracture lengths). Nevertheless, time signal amplitudes and corresponding frequency spectra indicated that a significant amplitude change occurs with fracture growth in the selected frequency bandwidth (≈ 60% increase in attenuation). The readability of frequency spectrum peaks obtained from strain-controlled tests is improved by using a time window technique. The frequency spectra of damaged PMMA specimens show that spectral amplitudes at high frequencies (f > 50 kHz) are more susceptible to fracture propagation than lower frequencies (f < 40 kHz) because of the associated wavelengths. The dynamic Young's modulus of the PMMA specimens, obtained from UPV measurements, are about three times greater than static modulus because of the orders of magnitude difference in the strain levels used in each test.

The new fabrication method of fused PMMA specimens provides an effective procedure for monitoring fracture growth. The study reveals that the determination of arrival time requires a careful revision as there is a misleading use of wave velocity in the literature to identify material damage. The results presented here clearly indicate that changes in wave attenuation from material damage are significant. Thus, previous results indicating that wave velocity changed with material damaged are likely incorrect; the reported change in wave velocity is likely due

to the incorrect selection of the arrival time as the real first arrival was removed by the effect of wave attenuation. An interesting finding of this study is the observed sensitivity of wave attenuation for the detection of fracture lengths even smaller than half the main wavelength of the propagating pulse; whereas, traditionally it has been accepted that the fracture length should be as minimum equal to one wavelength to significantly affect wave attenuation.

8.3 Characterization of cement-based specimens

Two procedures of tests, immersion through transmission and Laser Doppler vibrometer, are used to characterize cement-based materials. The characterization includes; materials' acoustic parameters, P-wave and S-wave velocities, materials' elastic moduli, and attenuation parameters. Two groups of specimens are tested; homogenous (acrylic, nylon, and mortar) and heterogeneous (concrete, and mortar with 15 %, 35%, 50% glass beads).

For testing with the immersion method, two different procedures (arrival time and peak points) were used to determine the acoustic parameters, wave velocities and attenuation parameters. The results obtained show that grain size plays an important role in the changing process of waveform amplitudes which causes a significance variability to the parameters calculated from this method. Also, the method proved to be a reliable technique to characterize cementitious materials, specifically in estimating the elastic moduli and attenuation coefficient of the cement-based materials being tested.

In the case of the Laser Doppler vibrometer testing, the observed results for P-wave velocities and attenuation measurements exposed different trends. For example, the grain size effect on the propagated wave has less influence than the ones noticed in the immersion test. While, the attenuation results reveal overestimated coefficients which can be attributed to many factors such as laser electronic effect and coupling concern between the transmitter and specimen under investigation. Nevertheless, the estimated P-wave velocities were in good match with the immersion measurements. On the other hand, the laser Doppler technique requires more careful study in characterization of cement-based materials to reduce any uncertainty.

8.4 Study of ultrasonic techniques sensitivity to internal damage

UPV through transmission and Laser Doppler vibrometer are intended to evaluate two types of damage induced using freeze-thaw cycles and compression load. The experimental program includes adding to concrete mixture two set of additives; air-entrained and silica fume. For this

purpose, eight unreinforced concrete specimens (four cylinders and four prisms) are prepared with four percentages of air-entrained to evaluate frost damage. Similar number of specimens are prepared with four percentages of silica fume to investigate the damage induced under compression load.

The sensitivity of wave velocity and wave attenuation is studied using UPV measurements and the results indicate that wave velocity did not show any clear trend about the presence of frost damage. In contrast, wave attenuation shows better indication to frost damage. In the compression load process, the results obtained show that wave velocity also indicates less sensitivity to damage than wave amplitude. Also, the multi-measurements procedure proposed in this study presents a reliable technique to evaluate load damage in different orientations based on a preferable frequency range.

In the case of the Laser Doppler vibrometer testing for freeze-thaw and compression load, the observed results of attenuation measurements exposed very interested findings. For example, the damage areas were identified by computing the total attenuation using two procedures; peak amplitude and spectrum area methods in which the first has shown better results than the latter. The findings of laser vibrometer exhibited a significant indication of zones that were influenced by load damage and this can be a motive to establish a reliable testing program to evaluate internal condition of concrete specimens under lab conditions.

8.5 Health monitoring of concrete shallow foundation lab-scale models

The main objective of the research is to develop a new NDT procedure to evaluate the integrity of shallow foundations. For this purpose, four shallow foundation lab-scale models were inspected for quality control and damage detection under compression load. One model is plain concrete and three are reinforced with rebar. Thirty-six radial transducers are fabricated and embedded in the four models. Two transmission pulse procedures were proposed, one using tubes filled with water and the other aluminum discs glued to the surface of the model. In the quality phase, the tube procedure was used to monitor the development of the concrete strength, while both transmission procedures are used in the damage evaluation phase.

The results of the quality assessment phase showed good indication of concrete durability during four weeks of curing. The assessment performed by monitoring the P-wave velocities that were computed from the ultrasonic measurements received by the embedded transducers. Most of the observed wave velocities are above 4000 (m/s) which may be considered good

according to the documented reference values. Also, waveform amplitude and spectrum area were investigated to observe the strength progress of the concrete model, the gain noticed in a typical waveform and spectrum areas reach up to 85%. On the other hand, the results of phase two indicate the efficiency of the proposed NDT procedure to evaluate the damage evolution under uniaxial compression load. The assessment of damage was performed by observing the signal amplitudes and the spectrum area. For example, the observed reduction of waveform signal of model MA-SP in the time domain and frequency domain were found to be 45% and 55% respectively, while in model MC-SDR, which contains rebar, the reductions noticed were 50% and 43% respectively. Similar trends were observed with the attenuation computed using the amplitude and spectrum area. The reduction process that observed in time and frequency domain can be attributed to the growth of cracks inside concrete models due to the impact of static load even at early stage of the loading process.

The findings of this study are an initial evaluation of the developed testing system, and further testing is required. It is necessary to perform several field tests using the new fabricated transducers and the transmission pulse procedure. Also, it required to develop a portable testing setup which can be used to obtain the ultrasonic measurements in the short term and long term to evaluate the reliability of the new methodology to assess the integrity of shallow foundations. The results obtained to date revealed the novelty of the new NDT procedure to monitor damage in concrete of shallow foundation lab-scale models. Also, it observed the reliability of the tube technique that was filled with water for pulse transmission in comparison with the direct contact procedure. Another important observation, the possibility to monitor the damage induced under compression load even when rebar is present in concrete.

References

Abadjiev, P., Panayotov, K., & Petrov, S. I. (1993). Influence of condensed silica fume as admixture to concrete on the bond to the reinforcement. *Construction and Building Materials, 7*(1), 41-44.

Abdel-Jaber, H., & Glisic, B. (2018). Monitoring of long-term prestress losses in prestressed concrete structures using fiber optic sensors. *Structural Health Monitoring*, 1475921717751870.

Adams, D. E., Koester, D. J., & Underwood, S. (2014). *U.S. Patent No. 8,656,779*. Washington, DC: U.S. Patent and Trademark Office.

Aggelis, D., Shiotani, T., & Polyzos, D. (2009). Characterization of surface crack depth and repair evaluation using rayleigh waves. *Cement and Concrete Composites, 31*(1), 77-83.

Ahn, E., Kim, H., Sim, S. H., Shin, S. W., & Shin, M. (2017). Principles and Applications of Ultrasonic-Based Nondestructive Methods for Self-Healing in Cementitious Materials. *Materials, 10*(3), 278.

Aldred, J. M., Holland, T. C., Morgan, D. R., Roy, D. M., Bury, M. A., Hooton, R. D., & Ozyildirim, H. C. (2006). Guide for the use of silica fume in concrete. *ACI–American Concrete Institute–Committee: Farmington Hills, MI, USA, 234*.

Alexander, E., & Poularikas, D. (1998). The handbook of formulas and tables for signal processing. *Boca Raton, FL, USA: CRC Press, 73*, 79.

Aliabdo, A. A. E., & Elmoaty, Abd Elmoaty Mohamed Abd. (2012). "Reliability of using nondestructive tests to estimate compressive strength of building stones and bricks." *Alexandria Engineering Journal, 51*(3), 193-203.

Aki, K., & Richards, P. G. (1980). Quantitative Seismology-Theory and Methods, volume IWH Freeman and company. *New York.*

American Concrete Institute. (2000). *ACI 365.1R-00: Service-Life Prediction.* Farmington Hills, MI.

American Concrete Institute. (2016). *ACI ITG.9R-16: Report on Design of Concrete Wind Turbine Towers.* Farmington Hills, MI.

American Concrete Institute. (2003). *ACI 228.1R-03: In-place Methods to Estimate Concrete Strength.* Farmington Hills, MI.

American Concrete Institute. (2003). *ACI 437R-03: Strength Evaluation of Existing Concrete Buildings.* Farmington Hills, MI.

American Concrete Institute. (2003). *ACI 228.1R-03: In-place Methods to Estimate Concrete Strength.* Farmington Hills, MI.

American Concrete Institute. (2007). *ACI 364.1R-07: Guide for Evaluation of Concrete Structures before Rehabilitation.* Farmington Hills, MI.

American Concrete Institute. (2011). *ACI 318-11: Building Code Requirements for Structural Concrete and Commentary*. Farmington Mills, MI.

American Concrete Institute. (2013). *ACI 228.2R-13: Report on Nondestructive Test Methods for Evaluation of Concrete in Structures.* Farmington Hills, MI.

American Concrete Institute. (2013). *ACI Concrete Terminology*. Farmington Hills, MI.

American Concrete Institute. (2016). *ACI E4 -16:* Chemical admixtures for concrete. Farmington Hills, MI.

Anugonda, P., Wiehn, J. S., & Turner, J. A. (2001). Diffusion of ultrasound in concrete. *Ultrasonics*, *39*(6), 429-435.

American Society for Testing and Materials. (2016). *ASTM C597-16: Standard Test Method for Pulse Velocity Through Concrete.* West Conshohocken, PA.

American Society for Testing and Materials. (2011). *ASTM E1316-11b: Standard Terminology for Nondestructive Examinations.* West Conshohocken, PA.

ASTM International. (2010). *ASTM C469-10:Standard Test Method for Static Modulus of Elasticity and Poisson's Ratio of Concrete in Compression.* West Conshohocken.

Ayatollahi, M., Torabi, A., & Firoozabadi, M. (2015). Theoretical and experimental investigation of brittle fracture in V-notched PMMA specimens under compressive loading. *Engineering Fracture Mechanics, 135*, 187-205.

Basu, A., & Aydin, A. (2005). Evaluation of ultrasonic testing in rock material characterization. *Geotechnical Testing Journal*, *29*(2), 117-125.

Becker, J., Jacobs, L. J., & Qu, J. (2003). Characterization of cement-based materials using diffuse ultrasound. *Journal of engineering mechanics*, *129*(12), 1478-1484.

Berthelot, J. M., Ben, S. M., & Robert, J. L. (1993). Study of wave attenuation in concrete. *Journal of materials research*, *8*(9), 2344-2353.

Breysse, D. (Ed.). (2012). Non-Destructive Assessment of Concrete Structures: Reliability and Limits of Single and Combined Techniques: State-of-the-Art Report of the RILEM Technical Committee 207-INR (Vol. 1). Springer Science & Business Media.

Breysse, D. (2010). Deterioration processes in reinforced concrete: an overview. In C. R. Maierhofer, *Non-destructive evaluation of reinforced concrete structures* (Vol. 1: Deterioration processes and standard test methods, pp. 28-56). Boca Raton, FL: Woodhead Publishing Limited.

Bungey, J. H., Grantham, M. G., & Millard, S. (2006). Testing of concrete in structures. Crc Press.

Cerrillo, C., Jiménez, A., Rufo, M., Paniagua, J., & Pachón, F. (2014). New contributions to granite characterization by ultrasonic testing. *Ultrasonics*, *54*(1), 156-167.

Chai, H., Momoki, S., Kobayashi, Y., Aggelis, D., & Shiotani, T. (2011). Tomographic reconstruction for concrete using attenuation of ultrasound. *NDT and E International, 44*(2), 206-215.

Chaix, J., Garnier, V., & Corneloup, G. (2003). Concrete damage evolution analysis by backscattered ultrasonic waves. *NDT and E International, 36*(7), 461-469.

Chen, X., & Ansari, F. (1999). Fiber optic stress wave sensor for detection of internal flaws in concrete structures. *Journal of intelligent material systems and structures, 10*(4), 274-279.

Chen, J., Deng, X., Luo, Y., He, L., Liu, Q., & Qiao, X. (2015). Investigation of microstructural damage in shotcrete under a freeze–thaw environment. *Construction and Building Materials, 83*, 275-282.

Cheng, X., Xu, D., Lu, L., Huang, S., & Jiang, M. (2010). Performance investigation of 1-3 piezoelectric ceramic–cement composite. *Materials Chemistry and Physics, 121*(1-2), 63-69.

Çobanoğlu, İ., & Çelik, S. B. (2008). Estimation of uniaxial compressive strength from point load strength, schmidt hardness and P-wave velocity. *Bulletin of Engineering Geology and the Environment, 67*(4), 491-498.

Dang, C., Schmerr Jr, L. W., & Sedov, A. (2002). Modeling and measuring all the elements of an ultrasonic nondestructive evaluation system I: modeling foundations. *Journal of Research in Nondestructive Evaluation, 14*(3), 141-176.

Daponte, P., Maceri, F., & Olivito, R. S. (1995). Ultrasonic signal-processing techniques for the measurement of damage growth in structural materials. *IEEE Transactions on instrumentation and measurement, 44*(6), 1003-1008.

Del Rıo, L., Jimenez, A., Lopez, F., Rosa, F., Rufo, M., & Paniagua, J. (2004). Characterization and hardening of concrete with ultrasonic testing. *Ultrasonics, 42*(1), 527-530.

Detwiler, R. J., Dalgleish, B. J., & Brady, R. (1989). Assessing the durability of concrete in freezing and thawing. *Materials Journal*, *86*(1), 29-35.

Dixit, A., & Bhalla, S. (2018). Prognosis of fatigue and impact induced damage in concrete using embedded piezo-transducers. *Sensors and Actuators A: Physical*, *274*, 116-131.

Duan, A., Jin, W., & Qian, J. (2011). Effect of freeze–thaw cycles on the stress–strain curves of unconfined and confined concrete. *Materials and Structures*, *44*(7), 1309-1324.

Dumoulin, C., Karaiskos, G., Carette, J., Staquet, S., & Deraemaeker, A. (2012). Monitoring of the ultrasonic P-wave velocity in early-age concrete with embedded piezoelectric transducers. *Smart materials and structures*, *21*(4), 047001.

Dumoulin, C., Karaiskos, G., & Deraemaeker, A. (2015). Monitoring of crack propagation in reinforced concrete beams using embedded piezoelectric transducers. In *Acoustic Emission and Related Non-Destructive Evaluation Techniques in the Fracture Mechanics of Concrete* (pp. 161-175).

Ensminger, D., and Bond, L. J. (2011). Ultrasonics: Fundamentals, technologies, and applications CRC Press.

Evans, A. G., Tittmann, B. R., Ahlberg, L., Khuri Yakub, B. T., & Kino, G. S. (1978). Ultrasonic attenuation in ceramics. *Journal of Applied Physics*, *49*(5), 2669-2679.

Ewins, D. J. (1984). *Modal testing: theory and practice* (Vol. 15). Letchworth: Research studies press.

Fereidooni, D. & Khajevand, R. (2018). Determining the Geotechnical Characteristics of Some Sedimentary Rocks from Iran with an Emphasis on the Correlations between Physical, Index, and Mechanical Properties. Geotechnical Testing Journal, Volume 41, Issue 3.

Finas, M., Ali, H., Cascante, G., & Vanheeghe, P. (2016). Automatic Shear Wave Velocity Estimation in Bender Element Testing. *Geotechnical Testing Journal*, *39*(4), 557-567.

Flintsch, G. W., Ferne, B., Diefenderfer, B., Katicha, S., Bryce, J., & Nell, S. (2012). Evaluation of traffic speed continuous deflection devices. In *Proceedings of the 91st Annual Meeting, Transport Research Board*.

Flynn, E. B. (2012). *Frequency-wavenumber processing of laser-excited guided waves for imaging structural features and defects* (No. LA-UR-12-01685; LA-UR-12-1685). Los Alamos National Laboratory (LANL).

Fröjd, P., & Ulriksen, P. (2016). Continuous wave measurements in a network of transducers for structural health monitoring of a large concrete floor slab. *Structural Health Monitoring*, *15*(4), 403-412.

Gaydecki, P., Burdekin, F., Damaj, W., & John, D. (1992). The propagation and attenuation of medium-frequency ultrasonic waves in concrete: A signal analytical approach. *Measurement Science and Technology*, *3*(1), 126.

Gerstle, W. (2010). Progress in developing a standard fracture toughness test for concrete. *Structures Congress 2010*, 1915-1926.

Ghandehari, M., Sidelev, A., Liu, E., Brückner, C., & Khalil, G. (2018). Sensing Hygrothermal Processes in Calcium Silicate Hydrates. In *Optical Phenomenology and Applications* (pp. 123-129). Springer, Cham.

Ginzel, E., & Turnbull, B. (2016). Determining Approximate Acoustic Properties of Materials. *NDT. net Dec*.

Gomez Rodriguez, D. M.., Dusseault, M. B., & Gracie, R. (2016). Cohesion and Fracturing in a Transparent Jointed Rock Analogue. *50th US Rock Mechanics / Geomechanics Symposium*.

Grinzato, E., Marinetti, S., Bison, P., Concas, M., & Fais, S. (2004). Comparison of ultrasonic velocity and IR thermography for the characterisation of stones. *Infrared Physics and Technology*, *46*(1), 63-68.

Haeri, H., Shahriar, K., Marji, M. F., & Moarefvand, P. (2013). A coupled numerical–experimental study of the breakage process of brittle substances. *Arabian Journal of Geosciences*, *8*(2), 809-825.

Hasan, M., Okuyama, H., Sato, Y., & Ueda, T. (2004). Stress-strain model of concrete damaged by freezing and thawing cycles. *Journal of Advanced Concrete Technology*, *2*(1), 89-99.

Hasan, M., Ueda, T., & Sato, Y. (2008). Stress-strain relationship of frost-damaged concrete subjected to fatigue loading. *Journal of Materials in Civil Engineering*, *20*(1), 37-45.

Hasanian, M., & Lissenden, C. J. (2017). Assessment of coating layers on the accuracy of displacement measurement in laser Doppler vibrometry. In *AIP Conference Proceedings* (Vol. 1806, No. 1, p. 050006). AIP Publishing.

Hatano, H., Chaya, T., Watanabe, S., & Jinbo, K. (1998). Reciprocity calibration of impulse responses of acoustic emission transducers. *IEEE transactions on ultrasonics, ferroelectrics, and frequency control*, *45*(5), 1221-1228.

Hellier, C. (2001). Handbook of nondestructive evaluation. New York, United States: McGraw-Hill.

Hertlein, B. H. (2013). Stress wave testing of concrete: A 25-year review and a peek into the future. *Construction and Building Materials*, *38*, 1240-1245.

Hobbs, B., & Kebir, M. T. (2007). Non-destructive testing techniques for the forensic engineering investigation of reinforced concrete buildings. *Forensic Science International*, *167*(2), 167-172.

Hooton, R. D. (1993). Influence of silica fume replacement of cement on physical properties and resistance to sulfate attack, freezing and thawing, and alkali-silica reactivity. *materials Journal*, *90*(2), 143-151.

Hutchins, D. A., & Hayward, G. (1990). Radiated fields of ultrasonic transducers. In *Physical acoustics* (Vol. 19, pp. 1-80). Academic Press.

Hwang, E., Kim, G., Choe, G., Yoon, M., Gucunski, N., & Nam, J. (2018). Evaluation of concrete degradation depending on heating conditions by ultrasonic pulse velocity. *Construction and Building Materials*, *171*, 511-520.

Ishimaru, A. (1999). *Wave propagation and scattering in random media* (Vol. 12). John Wiley & Sons.

Jiefan, H., Ganglin, C., Yonghong, Z., & Ren, W. (1990). An experimental study of the strain field development prior to failure of a marble plate under compression. *Tectonophysics, 175*(1-3), 269-284.

Kahraman, S. (2001). Evaluation of simple methods for assessing the uniaxial compressive strength of rock. *International Journal of Rock Mechanics and Mining Sciences, 38*(7), 981-994.

Kirlangic, A. S. (2013). Condition assessment of cemented materials using ultrasonic surface waves. (Doctoral dissertation, University of Waterloo).

Kim, Y. H., Lee, S. E. K. Y. U. N. G., & Kim, H. C. (1991). Attenuation and dispersion of elastic waves in multi-phase materials. *Journal of Physics D: Applied Physics*, *24*(10), 1722.

Knab, L. I., Blessing, G. V., & Clifton, J. R. (1983). Laboratory evaluation of ultrasonics for crack detection in concrete. In *Journal Proceedings* (Vol. 80, No. 1, pp. 17-27).

Kozlov, V.N., Shevaldykin, V.G., & Yakovlev, N.N. (1988). Experimental determination of an ultrasonic wave in concrete. Scientific Research Institute for NDT, Moscow,2:67-75.

Krautkrämer, J., & Krautkrämer, H. (1990). *Ultrasonic testing of materials* Springer Science and Business Media.

Kudela, P., Wandowski, T., Malinowski, P., & Ostachowicz, W. (2017). Application of scanning laser Doppler vibrometry for delamination detection in composite structures. *Optics and Lasers in Engineering, 99*, 46-57.

Lamond, J. F., & Pielert, J. H. (2006). Significance of tests and properties of concrete and concrete-making materials. West Conshohocken, PA: ASTM.

Landis, E. N., & Shah, S. P. (1995). Frequency-dependent stress wave attenuation in cement-based materials. *Journal of Engineering Mechanics*, *121*(6), 737-743.

Li, Z., & Shah, S. P. (1994). Localization of microcracking in concrete under uniaxial tension. *Materials Journal*, *91*(4), 372-381.

Li, Z., Li, F., Li, X. S., & Yang, W. (2000). P-wave arrival determination and AE characterization of concrete. *Journal of Engineering Mechanics*, *126*(2), 194-200.

Liu, M. H., & Wang, Y. F. (2012). Damage constitutive model of fly ash concrete under freeze-thaw cycles. *Journal of Materials in Civil Engineering*, *24*(9), 1165-1174.

Longo, R., Vanlanduit, S., Vanherzeele, J., & Guillaume, P. (2010). A method for crack sizing using Laser Doppler Vibrometer measurements of Surface Acoustic Waves. *Ultrasonics*, *50*(1), 76-80.

Ludovico-Marques, M., Chastre, C., & Vasconcelos, G. (2012). Modelling the compressive mechanical behaviour of granite and sandstone historical building stones. *Construction and Building Materials*, *28*(1), 372-381.

Lu, S. W., & Xie, H. Q. (2006). Real-time Monitoring and Simulating the Load Effects of Smart" CFRP-Strengthened RC Beams. In *Key Engineering Materials* (Vol. 324, pp. 129-132). Trans Tech Publications.

Lu, Y., & Li, Z. (2010). Crack detection using embedded cement-based piezoelectric sensor. *Korea Concrete Institute, Seoul*.

Lutzmann, P., Göhler, B., Van Putten, F., & Hill, C. A. (2011). Laser vibration sensing: overview and applications. In *Electro-Optical Remote Sensing, Photonic Technologies, and Applications V* (Vol. 8186, p. 818602). International Society for Optics and Photonics.

Jacobs, L. J., & Owino, J. O. (2000). Effect of aggregate size on attenuation of Rayleigh surface waves in cement-based materials. *Journal of engineering mechanics*, *126*(11), 1124-1130.

MacPherson, W. N., Reeves, M., Towers, D. P., Moore, A. J., Jones, J. D., Dale, M., & Edwards, C. (2007). Multipoint laser vibrometer for modal analysis. *Applied optics*, *46*(16), 3126-3132.

Maio, L., Ricci, F., Memmolo, V., Monaco, E., & Boffa, N. D. (2018). Application of laser Doppler vibrometry for ultrasonic velocity assessment in a composite panel with defect. *Composite Structures*, *184*, 1030-1039.

Malhotra, V. M., & Carino, N. J. (2003). *Handbook on Nondestructive Testing of Concrete Second Edition*. CRC press.

Malek, J., & Kaouther, M. (2014). Destructive and non-destructive testing of concrete structures. *Jordan Journal of Civil Engineering, Volume No8.PP432-441., Year2014*,

Malekjafarian, A., Martinez, D., & OBrien, E. J. (2018). The Feasibility of Using Laser Doppler Vibrometer Measurements from a Passing Vehicle for Bridge Damage Detection. *Shock and Vibration*, *2018*.

Martarelli, M. (2001). *Exploiting the laser scanning facility for vibration measurements* (Doctoral dissertation, University of London).

Mazloom, M., Ramezanianpour, A. A., & Brooks, J. J. (2004). Effect of silica fume on mechanical properties of high-strength concrete. *Cement and Concrete Composites*, *26*(4), 347-357.

Mehta, P. K. & Monteiro P. J. (1993). Concrete. Structure, properties and materials.

Meyendorf, N. G., Nagy, P. B., & Rokhlin, S. I. (Eds.). (2013). *Nondestructive materials characterization: With applications to aerospace materials* (Vol. 67). Springer Science & Business Media.

Miao, C., Mu, R., Tian, Q., & Sun, W. (2002). Effect of sulfate solution on the frost resistance of concrete with and without steel fiber reinforcement. *Cement and Concrete Research*, *32*(1), 31-34.

Mikulić, D., Pauše, Ž., & Ukrainčik, V. (1992). Determination of concrete quality in a structure by combination of destructive and non-destructive methods. *Materials and Structures*, *25*(2), 65-69.

Naik, Tarun R., V. Mohan Malhotra, & John S. Popovics. (2004). The ultrasonic pulse velocity method. *In Handbook of Nondestructive Testing of Concrete (Malhotra, V.M. and Carino, N.J.Editors)Boca Raton, Florida: CRC Press*,

Neville, A. M. (2011). Properties of Concrete, 4th. *London Pearson Education Limited*, *443*(846), 444.

Nogueira, C. L., & Willam, K. J. (2001). Ultrasonic testing of damage in concrete under uniaxial compression. *Materials Journal*, *98*(3), 265-275.

OBrien, E. J., Sevillano, E., & Martinez, D. (2016). Monitoring the condition of a bridge using a traffic speed deflectometer vehicle travelling at highway speed.

Ono, K. (2016). Calibration methods of acoustic emission sensors. *Materials*, *9*(7), 508.

Ostachowicz, W., Wanddowski, T., & Malinowski, P. (2010). Damage detection using laser vibrometry. In *2nd international symposium on NDT in aerospace* (Vol. 2010, pp. 1-8).

Otsuki, N., Iwanami, M., Miyazato, S., & Hara, N. (2000). Influence of aggregates on ultrasonic elastic wave propagation in concrete. *Non-destructive testing in civil engineering. Elsevier, Amsterdam*, 313-322.

Owens, C. T., Swenson, E. D., & Allen, C. (2011). *Visualization of Lamb wave interaction with a 5 mm fatigue crack using 1D ultra high frequency laser Doppler vibrometry*. air force inst of tech wright-patterson afb oh school of engineering and management.

Pai, P. F., Oh, Y., & Lee, S. Y. (2002). Detection of defects in circular plates using a scanning laser vibrometer. *Structural Health Monitoring*, *1*(1), 63-88.

Parker, E. R. (1967). *Materials data book. For Engineers and Scientists*. McGraw-Hill.

Philippidis, T. P., & Aggelis, D. G. (2005). Experimental study of wave dispersion and attenuation in concrete. *Ultrasonics*, *43*(7), 584-595.

Polytec GmbH. (2013). *User manual: Fiber-coupled vibrometer sensor head OFV-534*. Waldbronn, GR.

Popovics, S., Bilgutay, N. M., Caraoguz, M., & Akgul, T. (2000). High-frequency ultrasound technique for testing concrete. *Materials Journal*, *97*(1), 58-65.

Popovics, S., Rose, J. L., & Popovics, J. S. (1990). The behaviour of ultrasonic pulses in concrete. *Cement and Concrete Research*, *20*(2), 259-270.

Proceq. (2017). *Pundit Lab: Operating instructions*. Schwerzenbach, SA.

Pour-Ghaz, M. (2011). *Detecting damage in concrete using electrical methods and assessing moisture movement in cracked concrete*. Purdue University.

Punurai, W. (2006). *Cement-based materials' characterization using ultrasonic attenuation* (Doctoral dissertation, Georgia Institute of Technology).

Puri, S., & Weiss, J. (2006). Assessment of localized damage in concrete under compression using acoustic emission. *Journal of materials in civil engineering*, *18*(3), 325-333.

Qasrawi, H. Y., & Marie, I. A. (2003). The use of USPV to anticipate failure in concrete under compression. *Cement and Concrete Research*, *33*(12), 2017-2021.

Ranz, J., Aparicio, S., Romero, H., Casati, M. J., Molero, M., & González, M. (2014). Monitoring of freeze-thaw cycles in concrete using embedded sensors and ultrasonic imaging. *Sensors*, *14*(2), 2280-2304.

Ren, L., Li, H. N., Li, X., Zhou, J., & Xiang, L. (2006). Application of FBG sensors in rolled concrete dam model. In *Smart Structures and Materials 2006: Sensors and Smart Structures Technologies for Civil, Mechanical, and Aerospace Systems* (Vol. 6174, p. 617436). International Society for Optics and Photonics.

Rodríguez Roblero, M. J. (2017). Condition Assessment of Concrete Elements through Two Nondestructive Ultrasonic Techniques. (Doctoral dissertation, University of Waterloo).

Rubin, M. (1983). Experimental study of hydraulic fracturing in an impermeable material. *Journal of Energy Resources Technology*, *105*(2), 116-124.

Ruzzene, M., Jeong, S. M., Michaels, T. E., Michaels, J. E., & Mi, B. (2005). Simulation and measurement of ultrasonic waves in elastic plates using laser vibrometry. In *AIP Conference Proceedings* (Vol. 760, No. 1, pp. 172-179). AIP.

S. H., Kerkhoff, B., & Panarese, W. C. (2002). *Design and Control of Concrete Mixtures* (14th edition ed.). Illinois: Portland Cement Association.

Saboori, A. (2015). *Application of damage mechanics to describe the behavior of concrete under fatigue and freeze-thaw processes* (Doctoral dissertation, North Dakota State University).

Santhanam, M. (2010). Ultrasonic characterization of damage in concrete. *Structural Longevity*, *3*(1-2), 111-125.

Santamarina, J. C., Klein, A., & Fam, M. A. (2001). Soils and waves: Particulate materials behavior, characterization and process monitoring. *Journal of Soils and Sediments*, *1*(2), 130-130.

Santamarina, J. C., & Fratta, D. (1998). Introduction to discrete signals and inverse problems in civil engineering

Santamarina, J. C., Klein, A., & Fam, M. A. (2001). Soils and waves: Particulate materials behavior, characterization and process monitoring. *Journal of Soils and Sediments*, *1*(2), 130-130.

Schmerr, L. W., Lopez-Sanchez, A., & Huang, R. (2006). Complete ultrasonic transducer characterization and its use for models and measurements. *Ultrasonics*, *44*, e753-e757.

Selleck, S. F., Landis, E. N., Peterson, M. L., Shah, S. R., & Achenbach, J. D. (1998). Ultrasonic investigation of concrete with distributed damage. *ACI Materials Journal*, *95*, 27-36.

Selfridge, A. R. (1985). Approximate material properties in isotropic materials. *IEEE transactions on sonics and ultrasonics*, *32*(3), 381-394.

Sfikas, I. P., & Trezos, K. G. (2013). Effect of composition variations on bond properties of self-compacting concrete specimens. *Construction and building materials*, *41*, 252-262.

Shah, A. A., & Ribakov, Y. (2009). Non-destructive evaluation of concrete in damaged and undamaged states. *Materials & Design*, *30*(9), 3504-3511.

Shang, H. S., & Yi, T. H. (2013). Freeze-thaw durability of air-entrained concrete. *The Scientific World Journal*, *2013*.

Shang, H., Song, Y., & Ou, J. (2009). Behavior of air-entrained concrete after freeze-thaw cycles. *Acta Mechanica Solida Sinica*, *22*(3), 261-266.

Shang, H. S., & Song, Y. P. (2008). Behavior of air-entrained concrete under the compression with constant confined stress after freeze–thaw cycles. *Cement and Concrete Composites*, *30*(9), 854-860.

Shields, Y., Garboczi, E., Weiss, J., & Farnam, Y. (2018). Freeze-thaw crack determination in cementitious materials using 3D X-ray computed tomography and acoustic emission. *Cement and Concrete Composites*, *89*, 120-129.

Shiotani, T., & Aggelis, D. G. (2009). Wave propagation in cementitious material containing artificial distributed damage. *Materials and Structures*, *42*(3), 377-384.

Siddique, R. (2011). Utilization of silica fume in concrete: Review of hardened properties. *Resources, Conservation and Recycling*, *55*(11), 923-932.

Sih, G. C., & Ditomasso, A. (Eds.). (2012). *Fracture mechanics of concrete: Structural application and numerical calculation: Structural Application and Numerical Calculation* (Vol. 4). Springer Science & Business Media.

Silk, M. G. (1984). *Ultrasonic transducers for nondestructive testing*. Bristol, United Kingdom, Adam Hilger Ltd.

Slawinski, M. A. (2010). *Waves and rays in elastic continua*. Singapore, World Scientific Publishing Co. Pte. Ltd.

Sohn, H., Dutta, D., Yang, J. Y., Desimio, M. P., Olson, S. E., & Swenson, E. D. (2010). *A wavefield imaging technique for delamination detection in composite structures*. korea advanced inst of science and technology daejeon (korea).

Sonia M., Simranjit S., Amit A., & Hemant S. (2015). A Comparative Study of Varying Dosage of Different Air Entraining Agents for M35 & M40 Concrete Grades. Indian journal of research volume 4 issue 8.

Sriram, P., Craig, J. I., & Hanagud, S. (1992). Scanning laser Doppler techniques for vibration testing. *Experimental Techniques*, *16*(6), 21-26.

Staszewski, W. J., Lee, B. C., Mallet, L., & Scarpa, F. (2004). Structural health monitoring using scanning laser vibrometry: I. Lamb wave sensing. *Smart Materials and Structures*, *13*(2), 251.

Stanbridge, A. B., & Ewins, D. J. (1999). Modal testing using a scanning laser Doppler vibrometer. *Mechanical systems and signal processing*, *13*(2), 255-270.

Tattersall, H. G., & Tappin, G. (1966). The work of fracture and its measurement in metals, ceramics and other materials. *Journal of Materials Science*, *1*(3), 296-301.

Tharmaratnam, K., & Tan, B. S. (1990). Attenuation of ultrasonic pulse in cement mortar. *Cement and Concrete research*, *20*(3), 335-345.

Treiber, M., Kim, J. Y., Qu, J., & Jacobs, L. J. (2010). Effects of sand aggregate on ultrasonic attenuation in cement-based materials. *Materials and structures*, *43*(1), 1-11.

Trtnik, G., Kavčič, F., & Turk, G. (2009). Prediction of concrete strength using ultrasonic pulse velocity and artificial neural networks. *Ultrasonics*, *49*(1), 53-60.

Turner, C. W., & Arif, M. Z. (1991). Novel composite transducer for ultrasonic NDE of concrete. In *Ultrasonics Symposium, 1991. Proceedings., IEEE 1991* (pp. 757-761). IEEE.

Ulusay, R. (2015). The ISRM suggested Methods for Rock Characterization, Testing and Monitoring: 2007-2014. DOI 10.1007/978-3-319-07712-3, *SPRINGER*, 290 pp.

Vasconcelos, G., Lourenço, P., Alves, C., & Pamplona, J. (2008). Ultrasonic evaluation of the physical and mechanical properties of granites. *Ultrasonics, 48*(5), 453-466.

Washabaugh, P., & Knauss, W. (1995). The effect of aligned defects on the propagation speed of a dynamic crack in PMMA. *International Journal of Solids and Structures, 32*(17), 2481-2496.

Yang, S. (2011). Crack coalescence behavior of brittle sandstone specimens containing two coplanar fissures in the process of deformation failure. *Engineering Fracture Mechanics, 78*(17), 3059-3081.

Yang, S., & Allen, M. S. (2012). Output-only modal analysis using continuous-scan laser Doppler vibrometry and application to a 20 kW wind turbine. *Mechanical Systems and Signal Processing, 31*, 228-245.

Yang, Z. (2004). Assessing cumulative damage in concrete and quantifying its influence on life cycle performance modeling.

Yasar, E., & Erdogan, Y. (2004). Correlating sound velocity with the density, compressive strength and young's modulus of carbonate rocks. *International Journal of Rock Mechanics and Mining Sciences, 41*(5), 871-875.

Yim, H. J., Kwak, H., & Kim, J. H. (2012). Wave attenuation measurement technique for nondestructive evaluation of concrete. *Nondestructive Testing and Evaluation, 27*(1), 81-94.

Waldron, K., Ghoshal, A., Schulz, M. J., Sundaresan, M. J., Ferguson, F., Pai, P. F., & Chung, J. H. (2002). Damage detection using finite element and laser operational deflection shapes. *Finite Elements in Analysis and Design, 38*(3), 193-226.

Wen, Y., Li, P., & Huang, S. (1998). Readout of a piezoelectric distributed sensing network embedded in concrete. In *Smart Structures and Materials 1998: Sensory Phenomena and Measurement Instrumentation for Smart Structures and Materials* (Vol. 3330, pp. 67-75). International Society for Optics and Photonics.

Wiggenhauser, H., Helmerich, R., Taffe, A., Kraise, M., Kind, T., Lai, W. L., & Niederleithinger, E. (2003). Non-Destructive Testing in Civil Engineering. *Proceedings Berlin*.

Wong, H. S., Pappas, A. M., Zimmerman, R. W., & Buenfeld, N. R. (2011). Effect of entrained air voids on the microstructure and mass transport properties of concrete. *Cement and Concrete Research, 41*(10), 1067-1077.

Xu, K., Deng, Q., Cai, L., Ho, S., & Song, G. (2018). Damage detection of a concrete column subject to blast loads using embedded piezoceramic transducers. *Sensors (Basel, Switzerland), 18*(5).

Appendix A

Numerical data

A.1 Characterization results of bar reference method

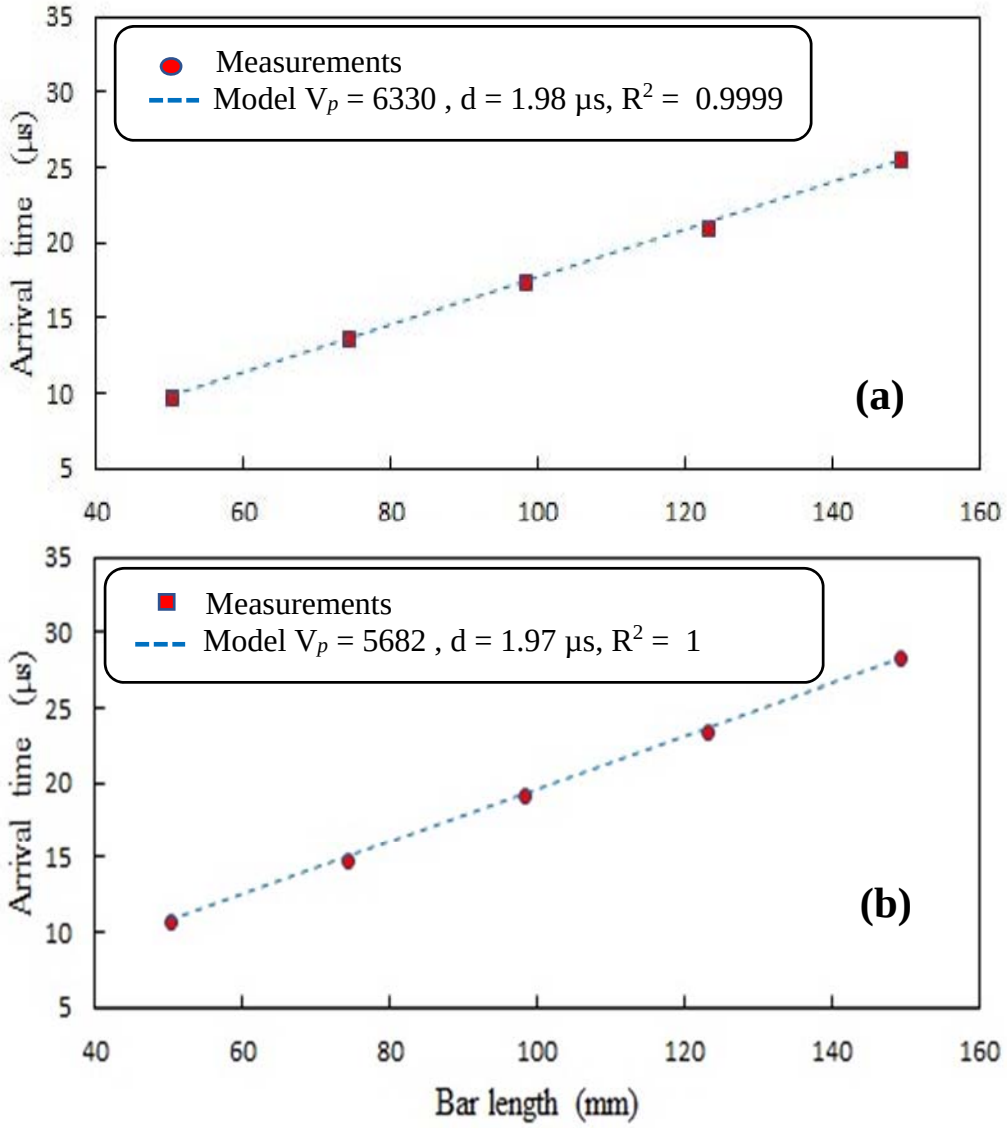

Figure A-1: Characterization results of 54 kHz transducer (54O). (a) using aluminum rods, (b) using steel rods. where V_p is wave velocity (m/s), d is delay time, and R^2 is correlation coefficient.

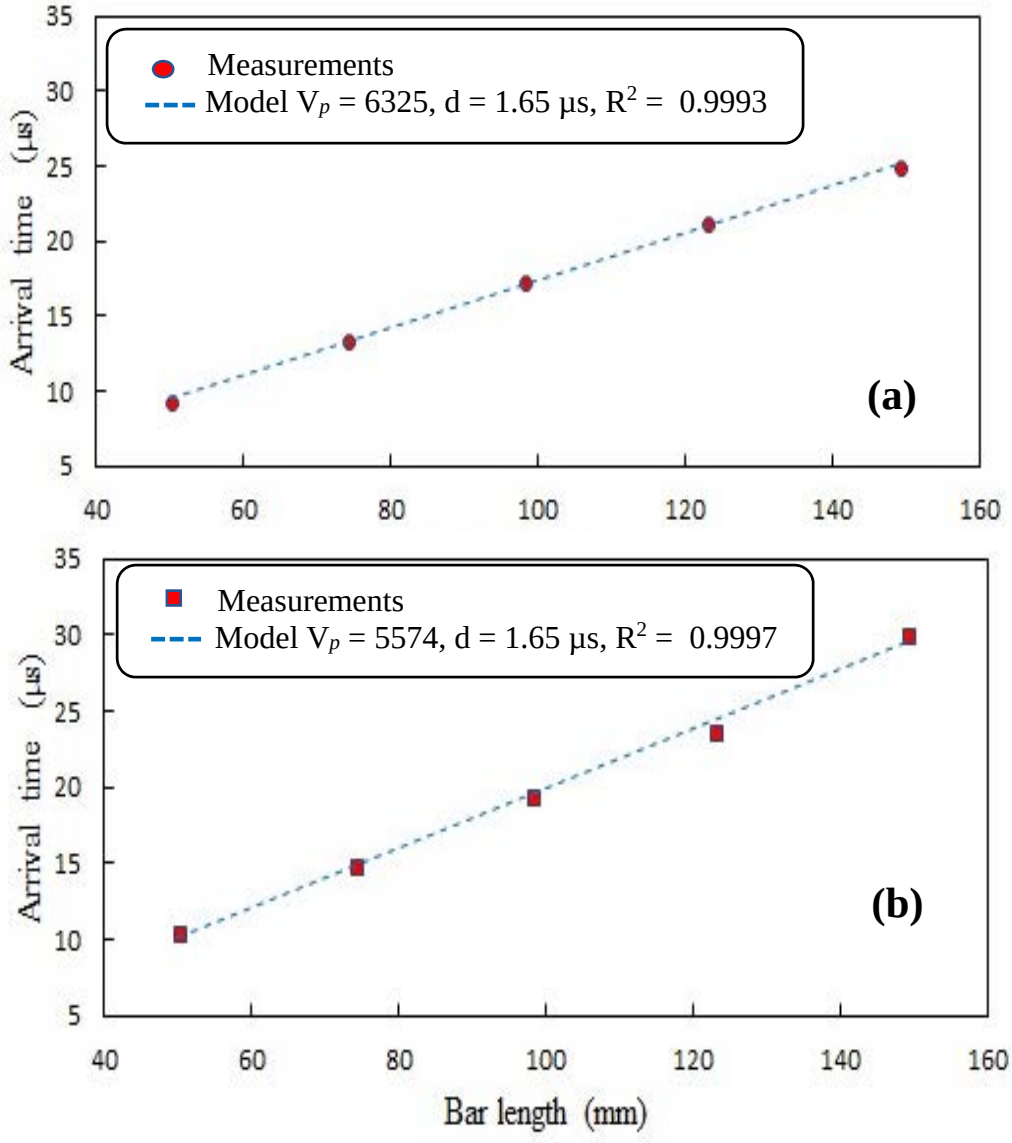

Figure A-2: Characterization results of 150 kHz transducer (150N). (a) using aluminum rods, (b) using steel rods. where V_p is wave velocity (m/s), d is delay time, and R^2 is correlation coefficient.

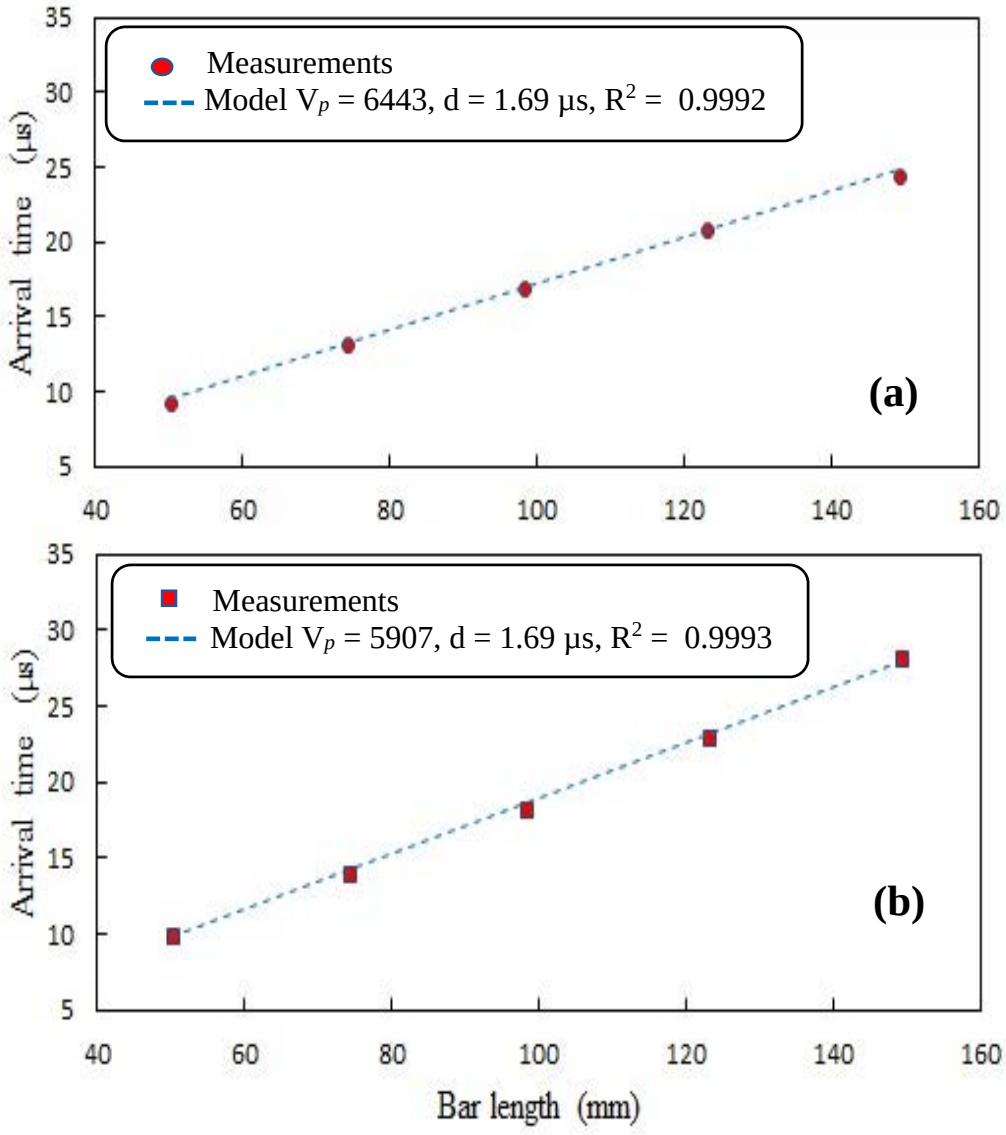

Figure A-3: Characterization results of 250 kHz transducer (250N). (a) using aluminum rods, (b) using steel rods. where V_p is wave velocity (m/s), d is delay time, and R^2 is correlation coefficient.

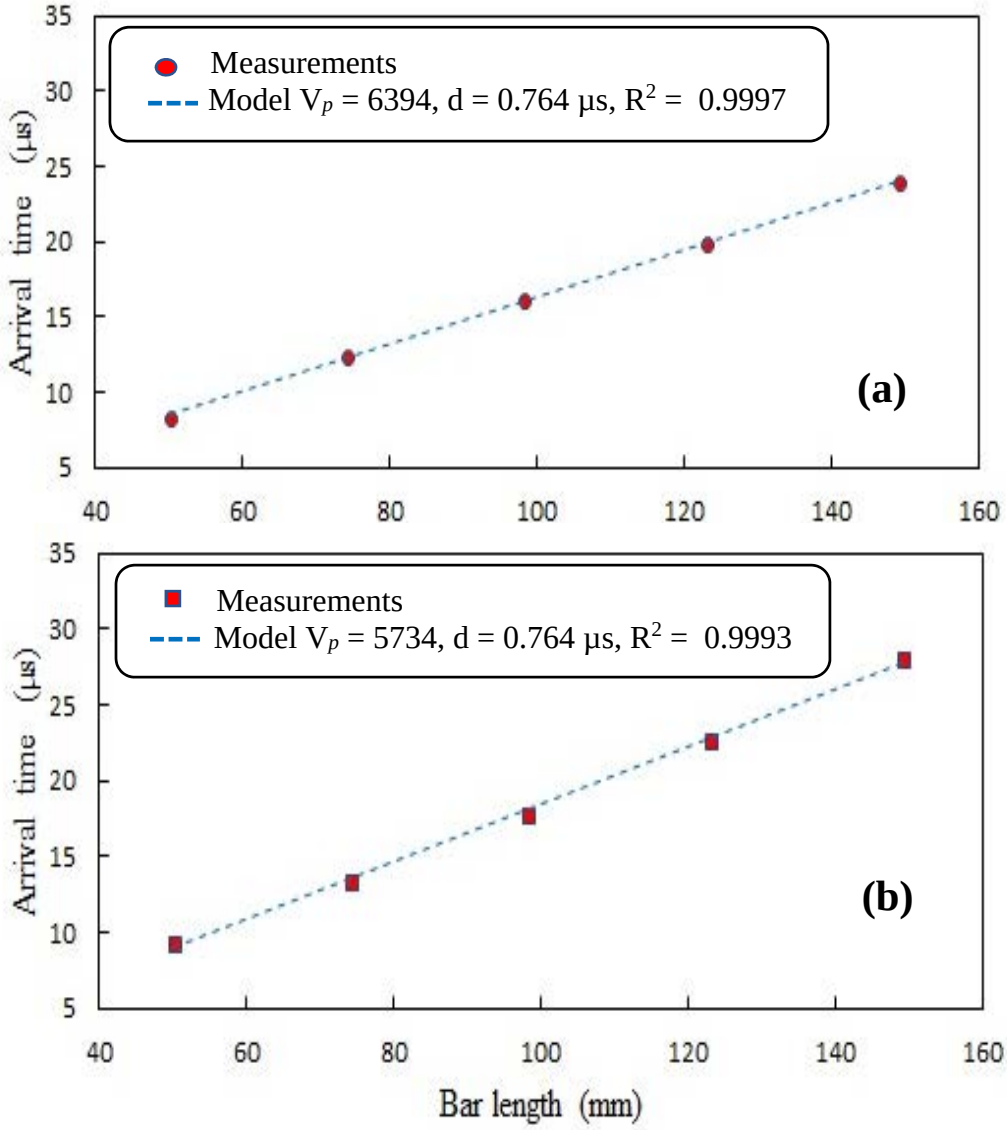

Figure A-4: Characterization results of 500 kHz transducer (500Oy). (a) using aluminum rods, (b) using steel rods. where V_p is wave velocity (m/s), d is delay time, and R^2 is correlation coefficient.

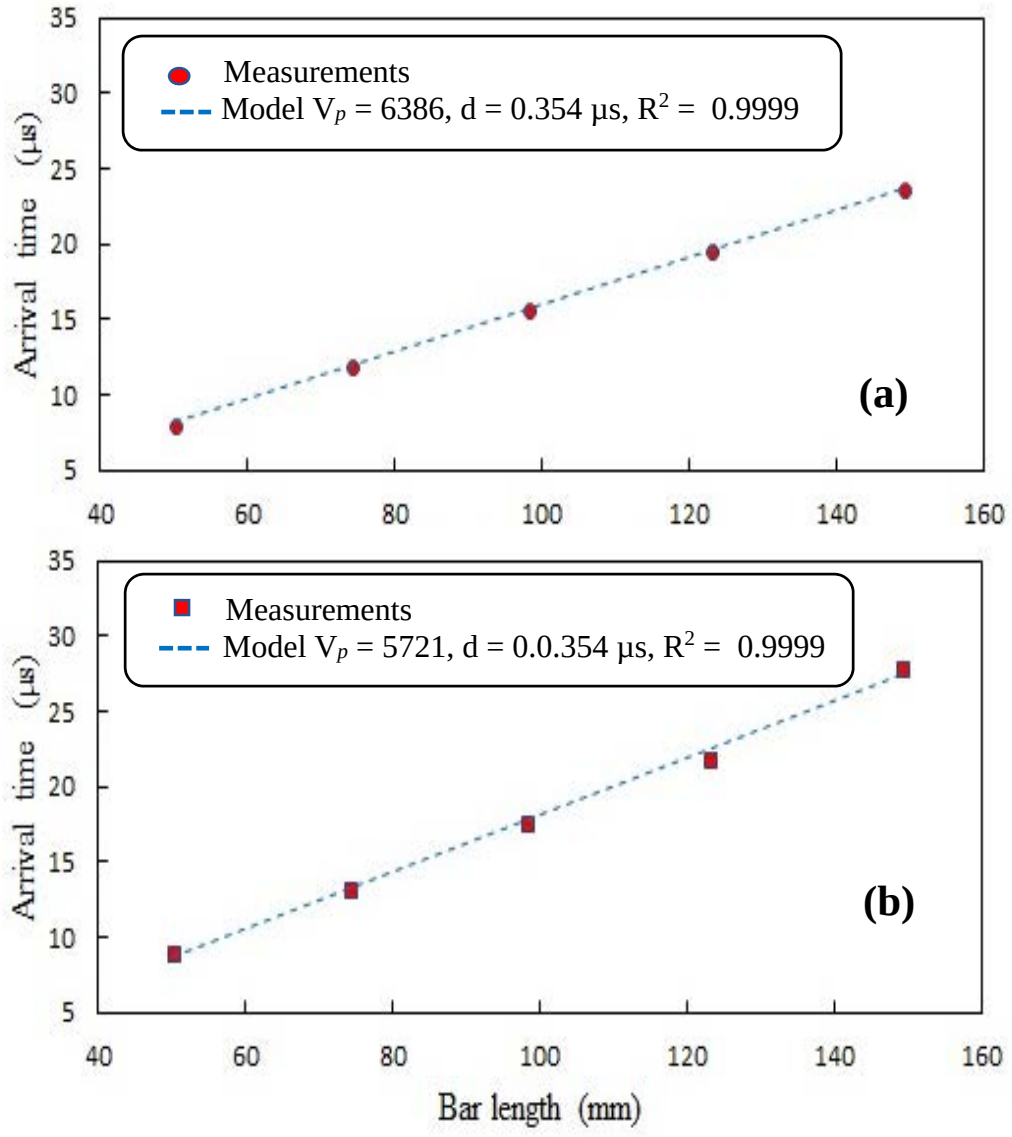

Figure A-5: Characterization results of 500 kHz transducer (500Ut). (a) using aluminum rods, (b) using steel rods. where V_p is wave velocity (m/s), d is delay time, and R^2 is correlation coefficient.

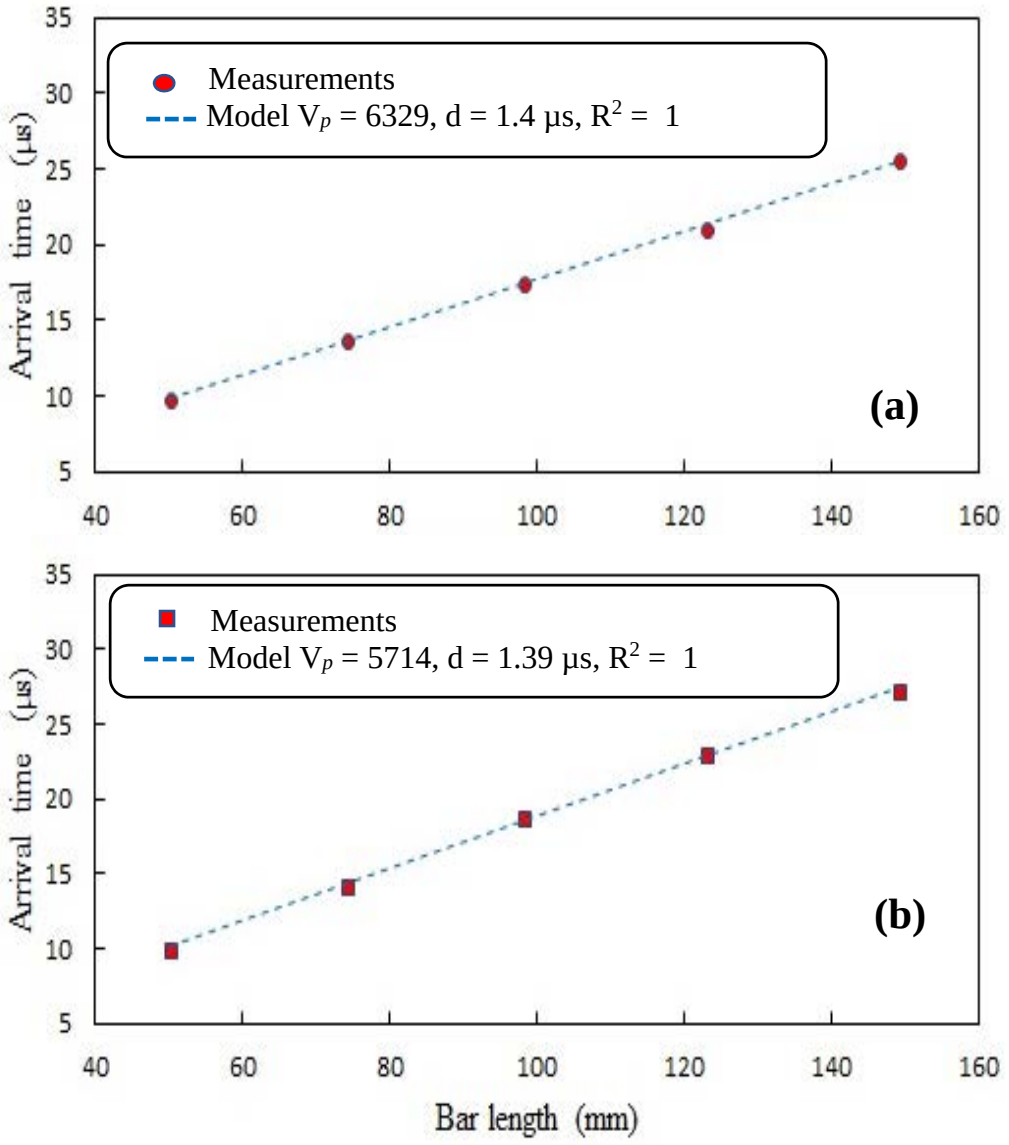

Figure A-6: Characterization results of 500 kHz immersion transducer (500MN). (a) using aluminum rods, (b) using steel rods. where V_p is wave velocity (m/s), d is delay time, and R^2 is correlation coefficient.

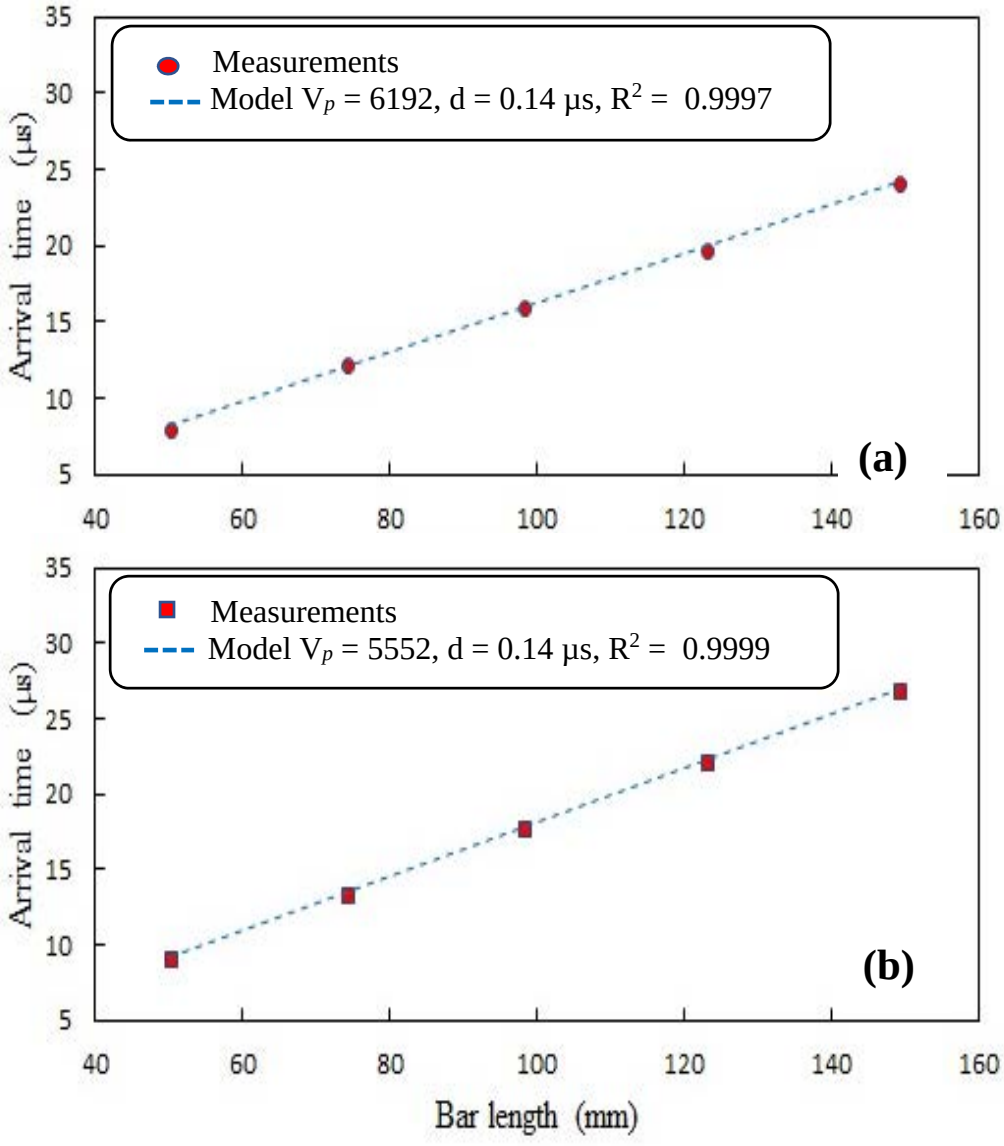

Figure A-7: Characterization results of 1 MHz S-wave transducer (1MSN). (a) using aluminum rods, (b) using steel rods. where V_p is wave velocity (m/s), d is delay time, and R^2 is correlation coefficient.

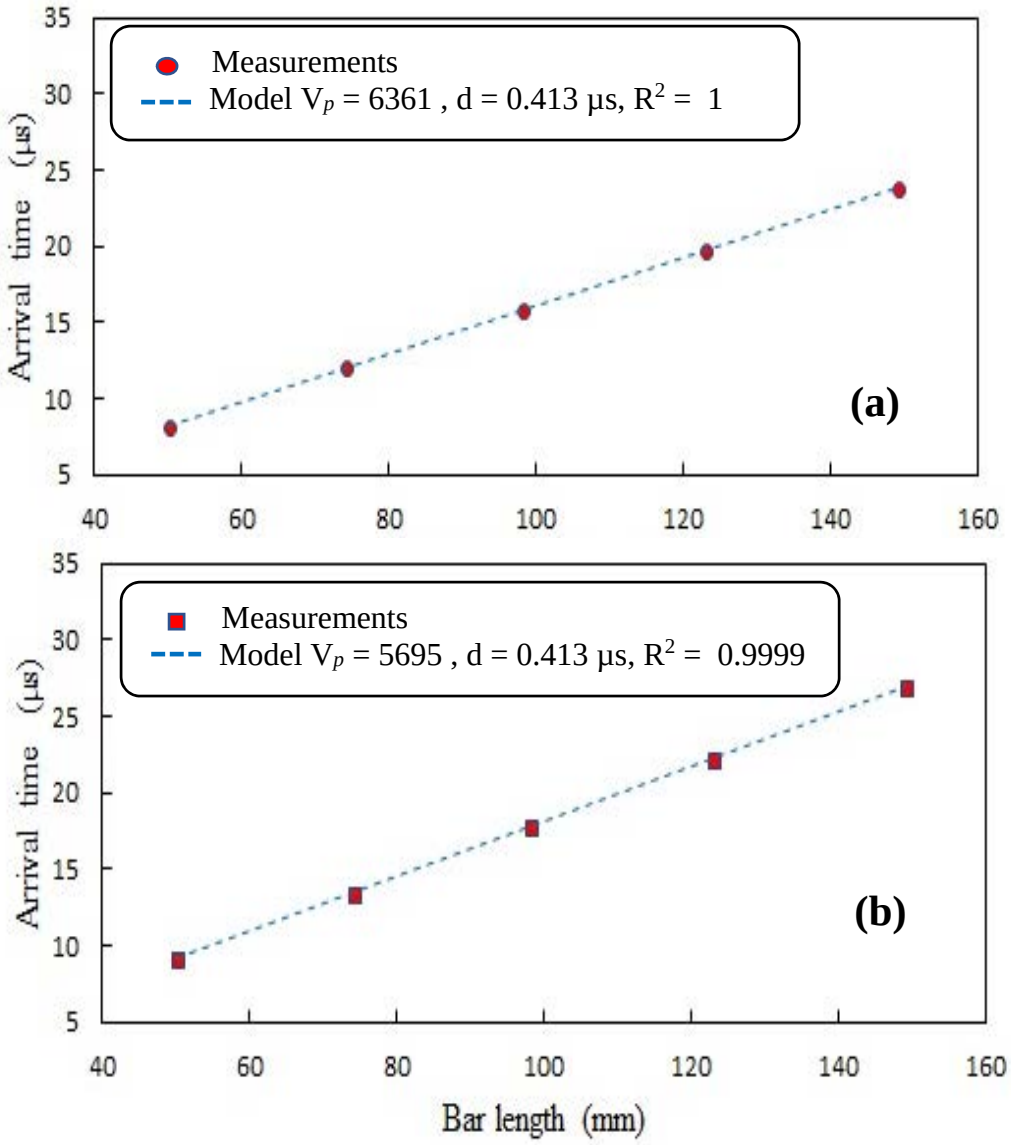

Figure A-8: Characterization results of 1 MHz P-wave transducer (1MPO). (a) using aluminum rods, (b) using steel rods. where V_p is wave velocity (m/s), d is delay time, and R^2 is correlation coefficient.

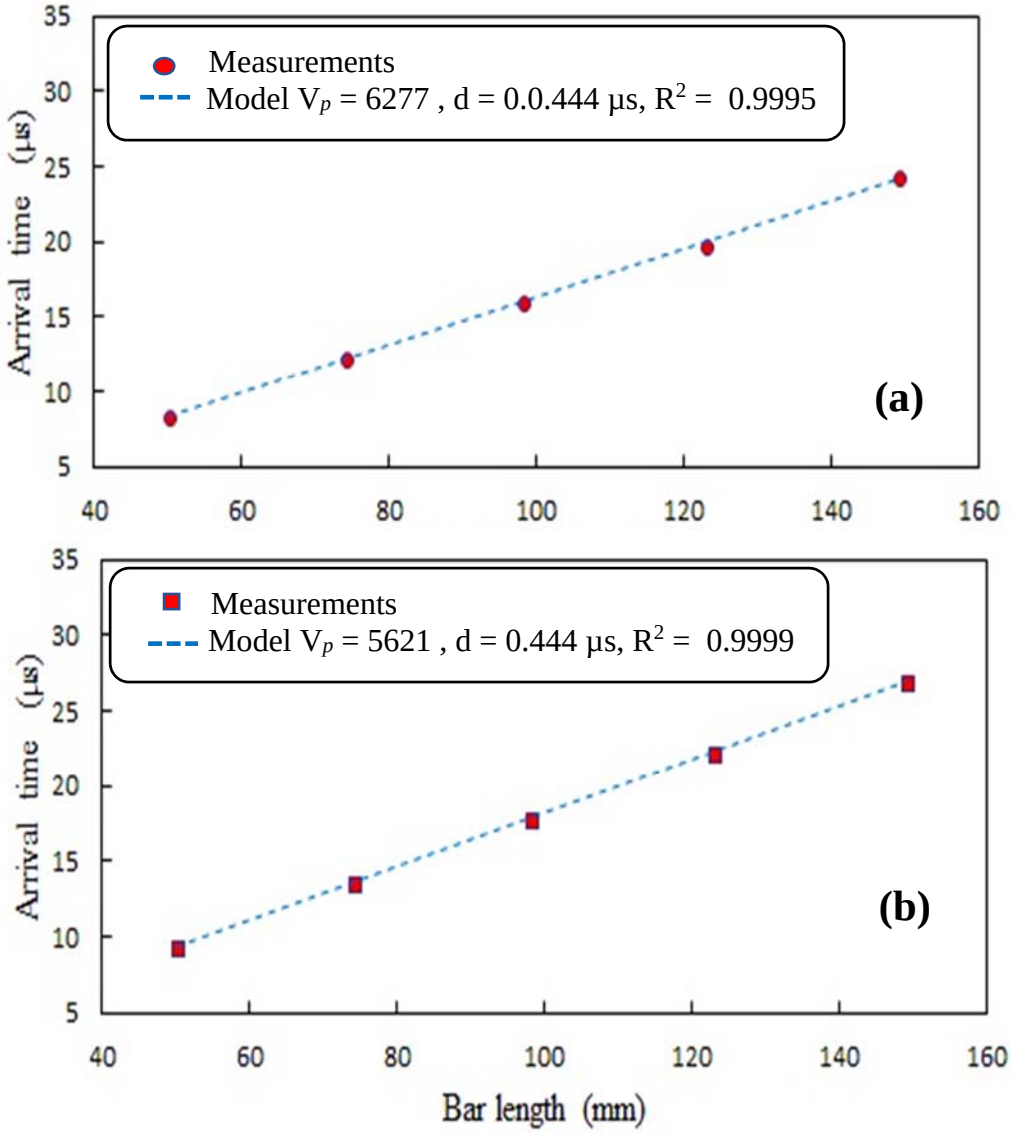

Figure A-9: Characterization results of 1 MHz S-wave transducer (1MSO). (a) using aluminum rods, (b) using steel rods. where V_p is wave velocity (m/s), d is delay time, and R^2 is correlation coefficient.

A.2 Distribution scheme of scanned points with laser

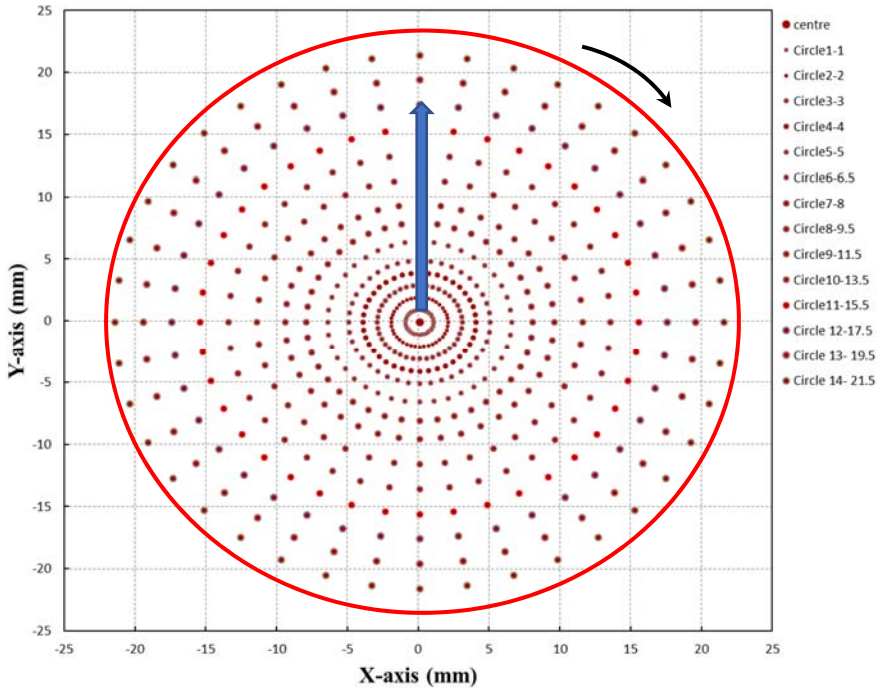

Figure A-10: Distribution laser points scheme of 54 kHz transducer (arrows represent the direction of scanning).

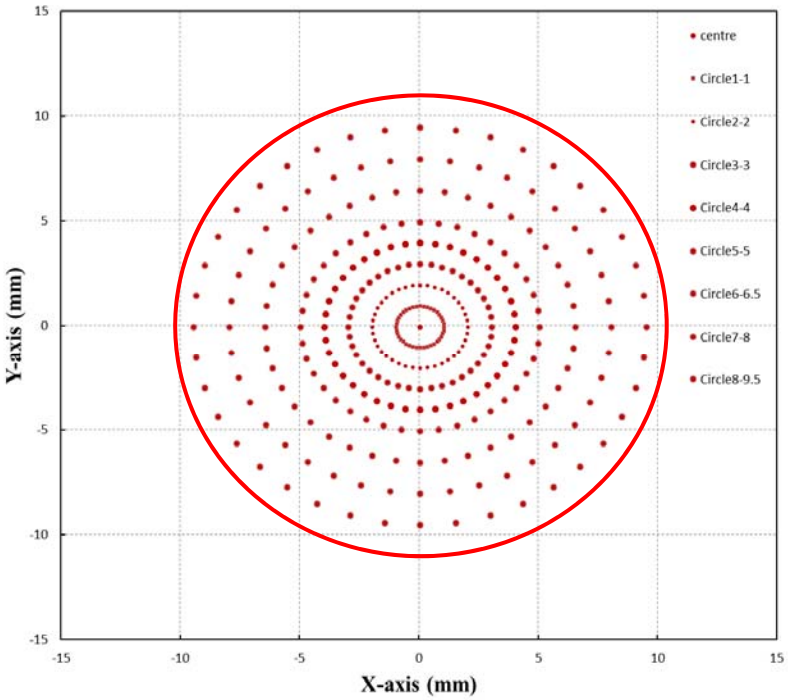

Figure A-11: Distribution laser points scheme of other transducers.

A.3 Mode vibrations of characterized transducers with laser vibrometer

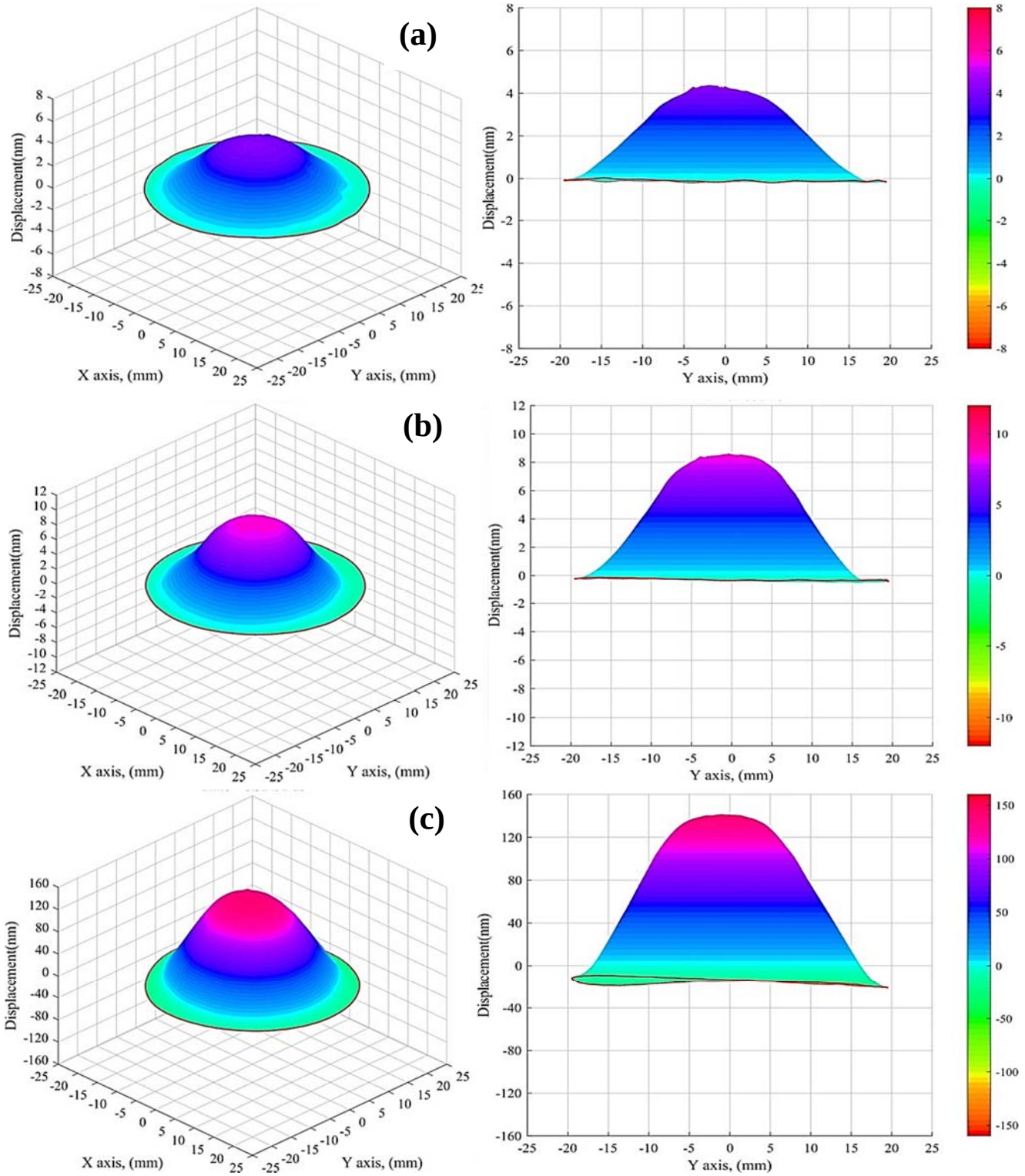

Figure A-12: Perspective and side views of 54 kHz transducer (54O) vibration modes. (a) under 5 volts excitation, (b) under 10 volts excitation, (c) under 150 volts excitation.

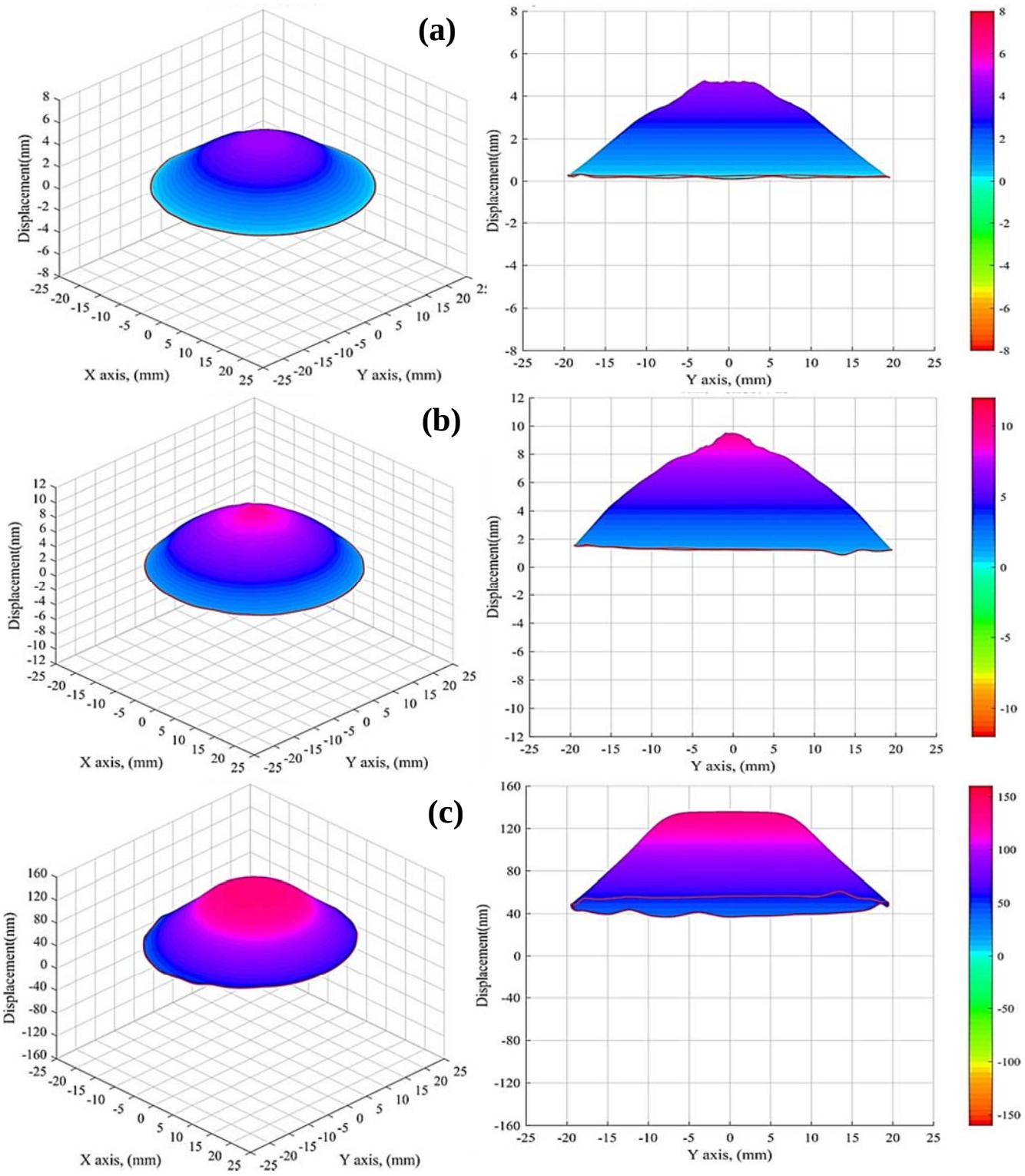

Figure A-13: Perspective and side views of 54 kHz transducer (54N) vibration modes. (a) under 5 volts excitation, (b) under 10 volts excitation, (c) under 150 volts excitation.

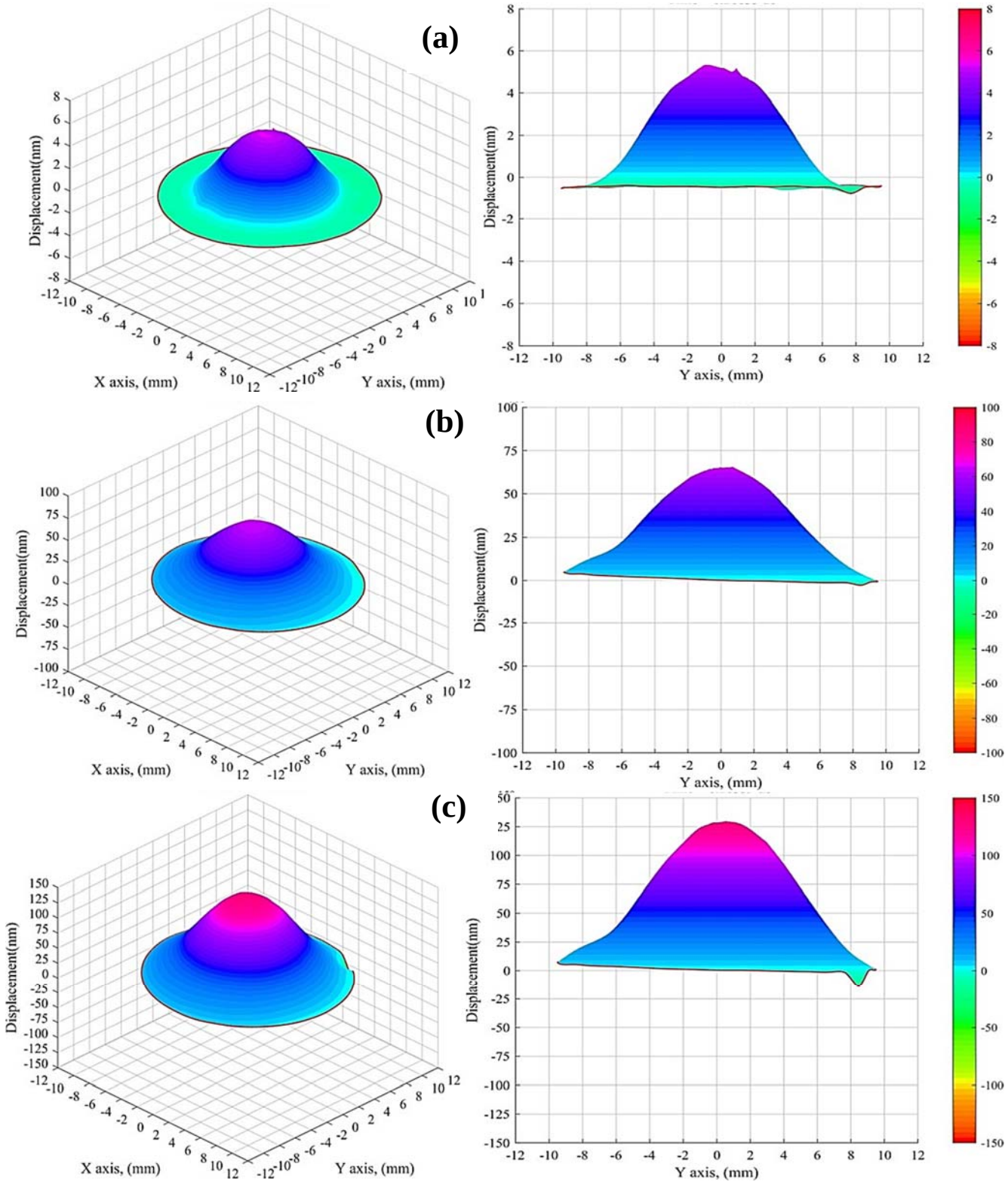

Figure A-14: Perspective and side views of 150 kHz transducer (150N) vibration modes. (a) under 10 volts excitation, (b) under 100 volts excitation, (c) under 200 volts excitation.

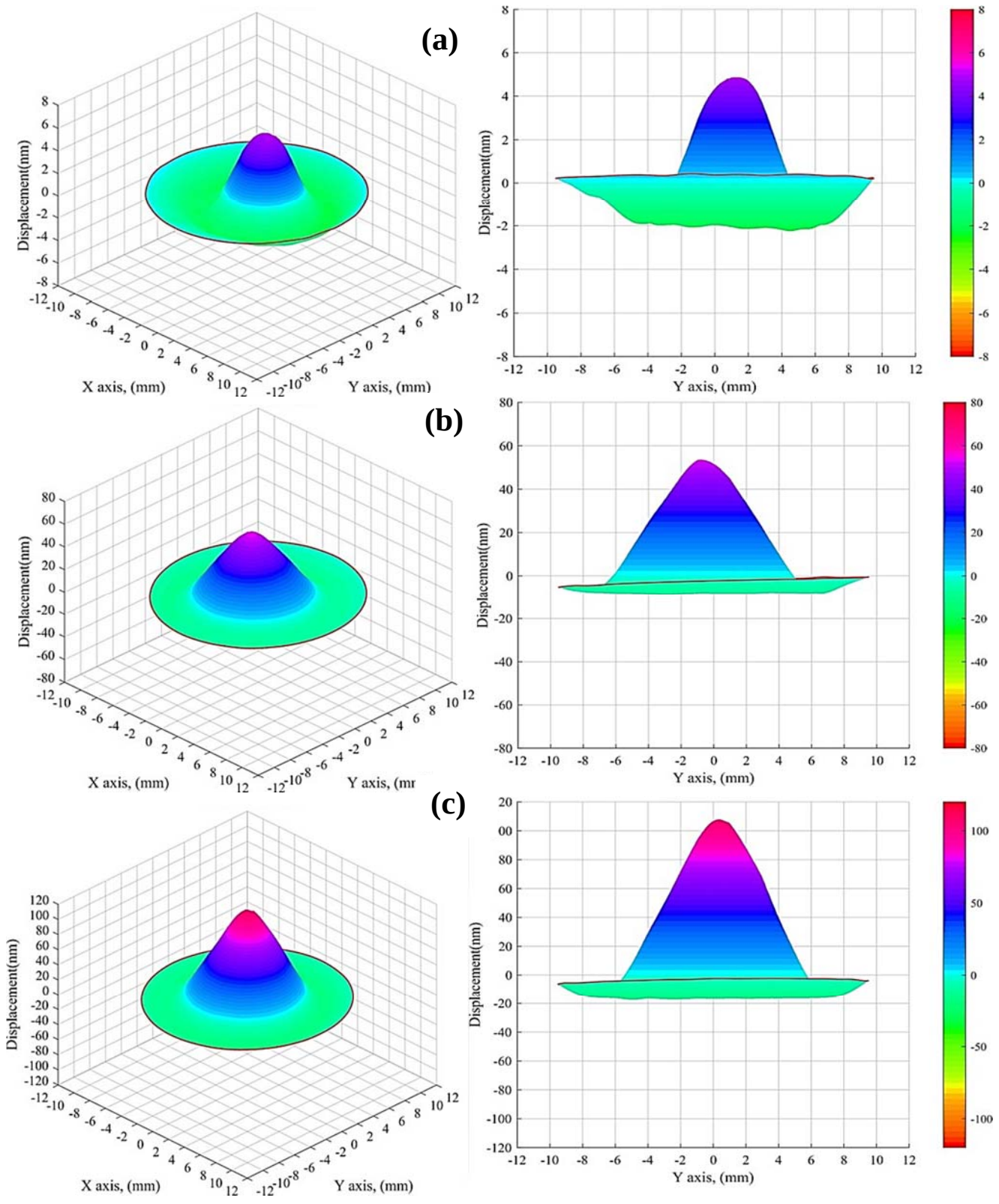

Figure A-15: Perspective and side views of 250 kHz transducer (250N) vibration modes. (a) under 10 volts excitation, (b) under 100 volts excitation, (c) under 200 volts excitation.

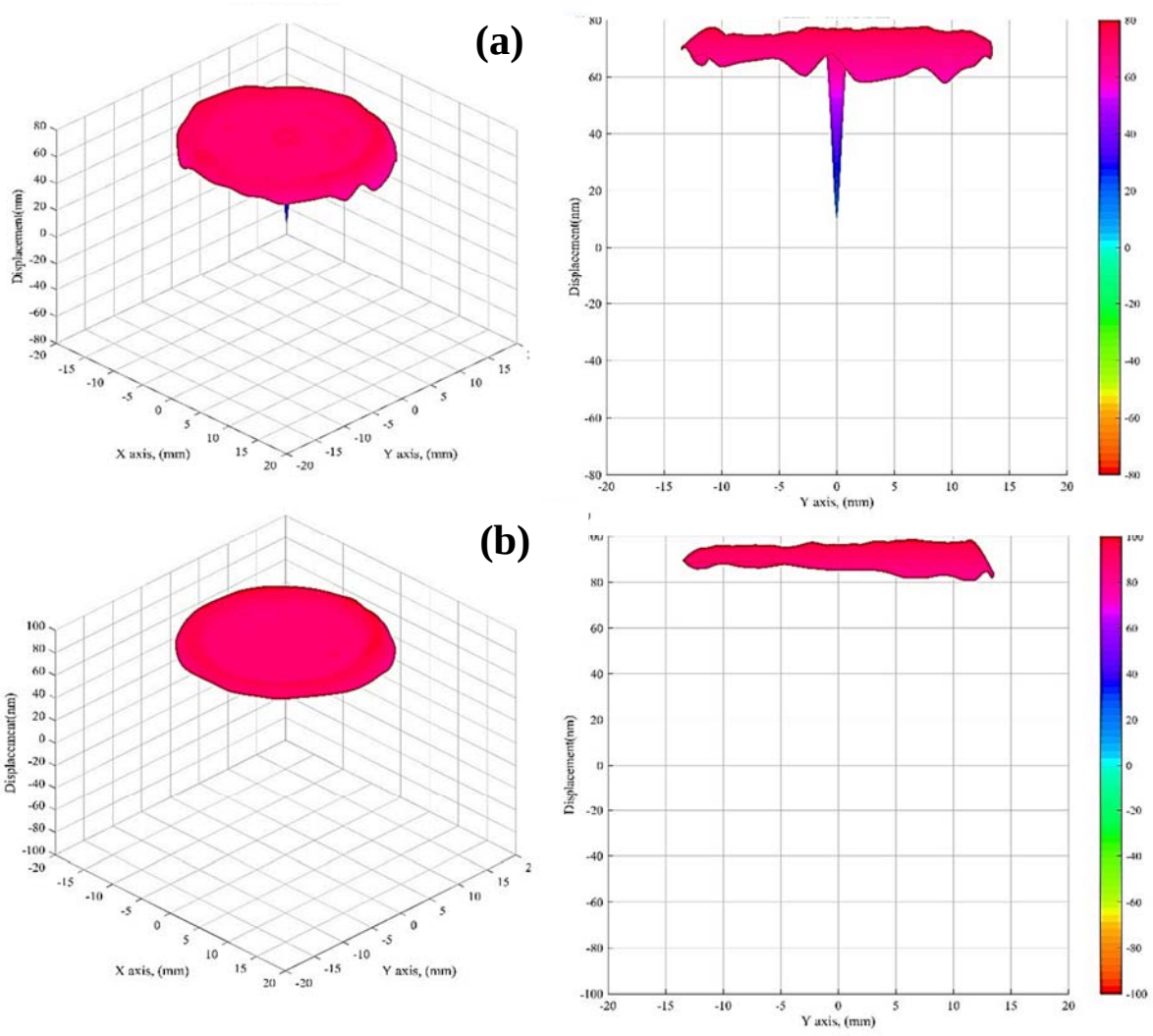

Figure A-16: Perspective and side views of 500 kHz transducer (500Oy) vibration modes. (a) under 100 volts excitation, (b) under 200 volts excitation.

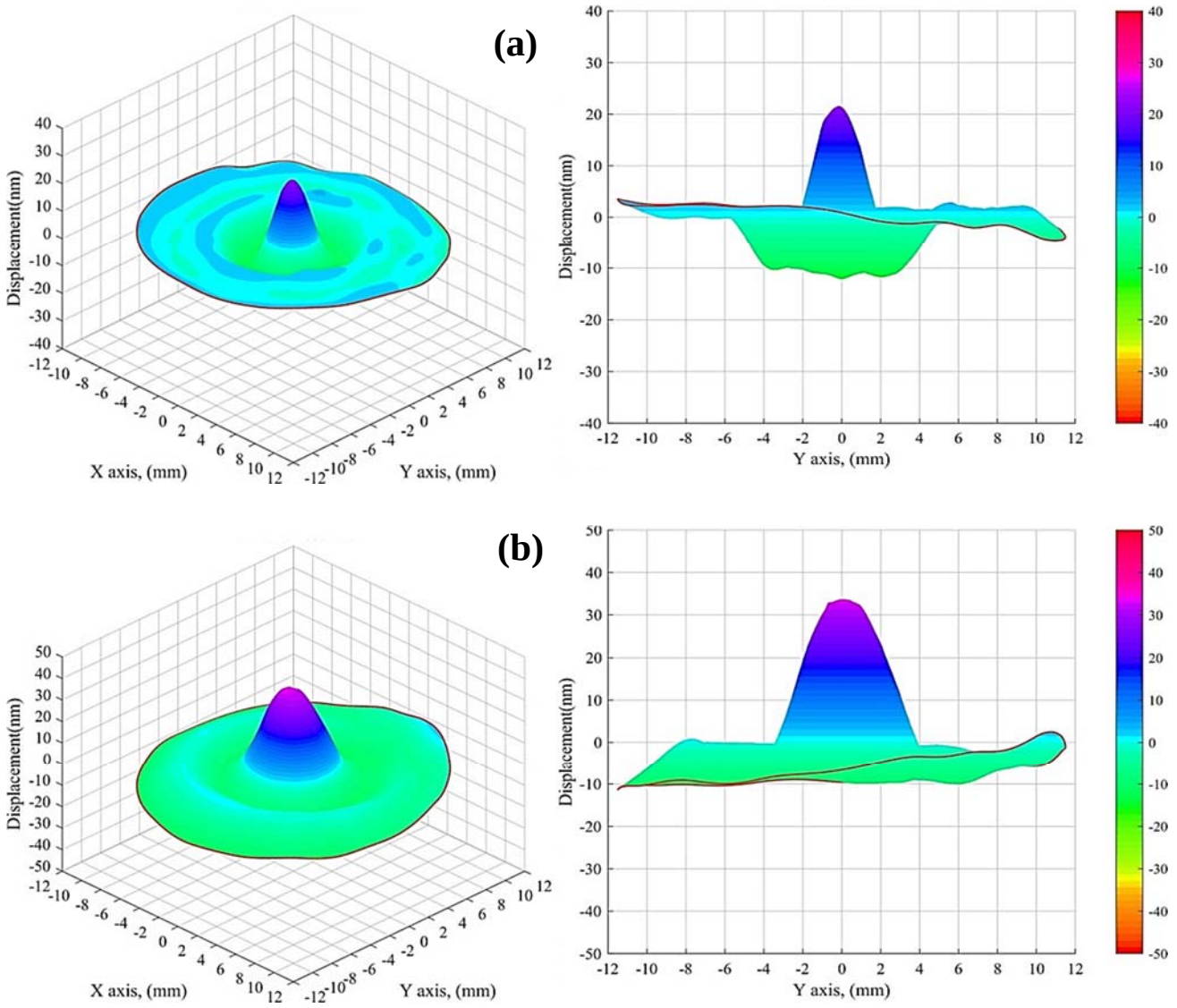

Figure A-17: Perspective and side views of 500 kHz transducer (500Ut) vibration modes. (a) under 100 volts excitation, (b) under 200 volts excitation.

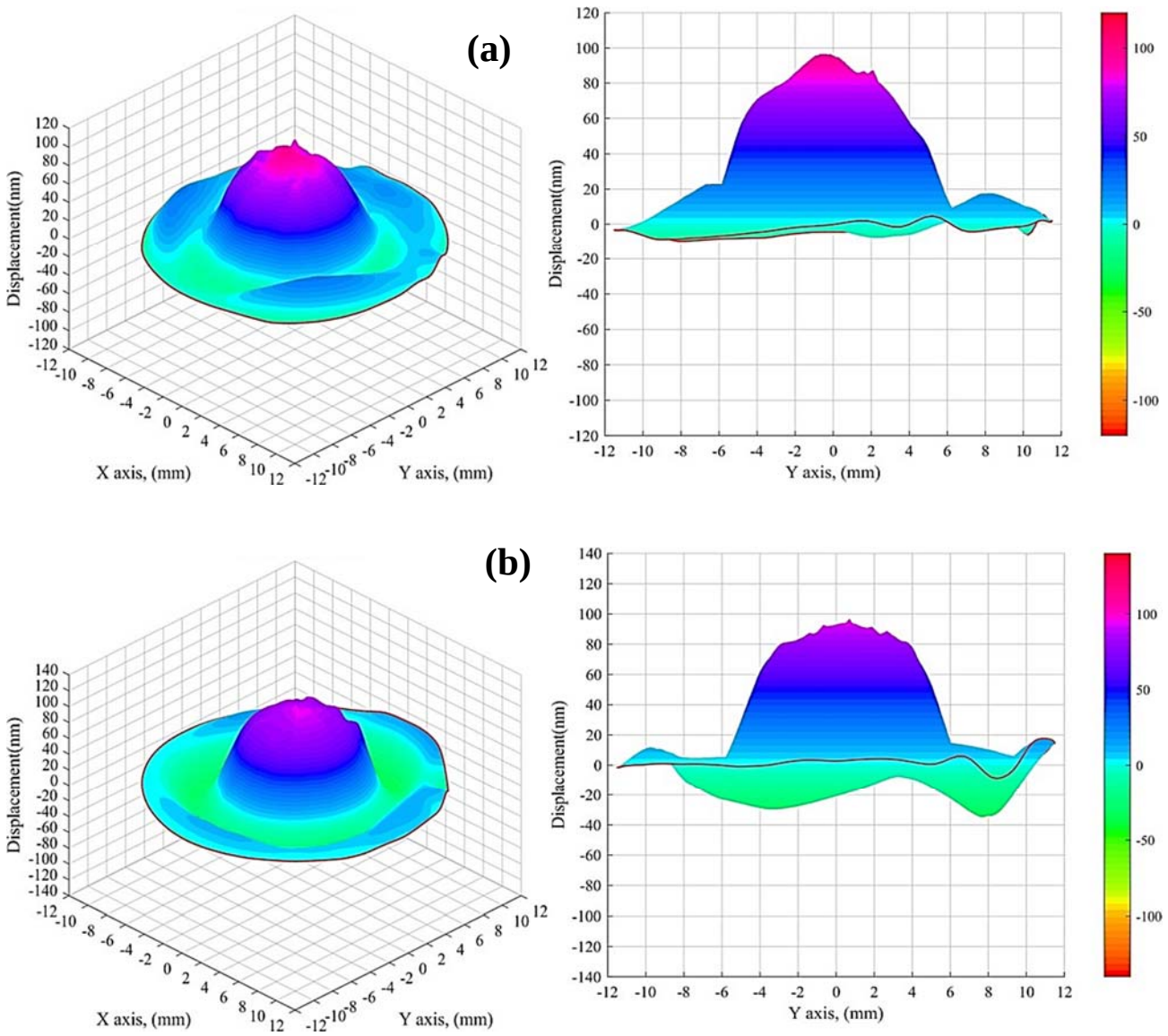

Figure A-18: Perspective and side views of 500 kHz transducer (500MN) vibration modes. (a) under 100 volts excitation, (b) under 200 volts excitation.

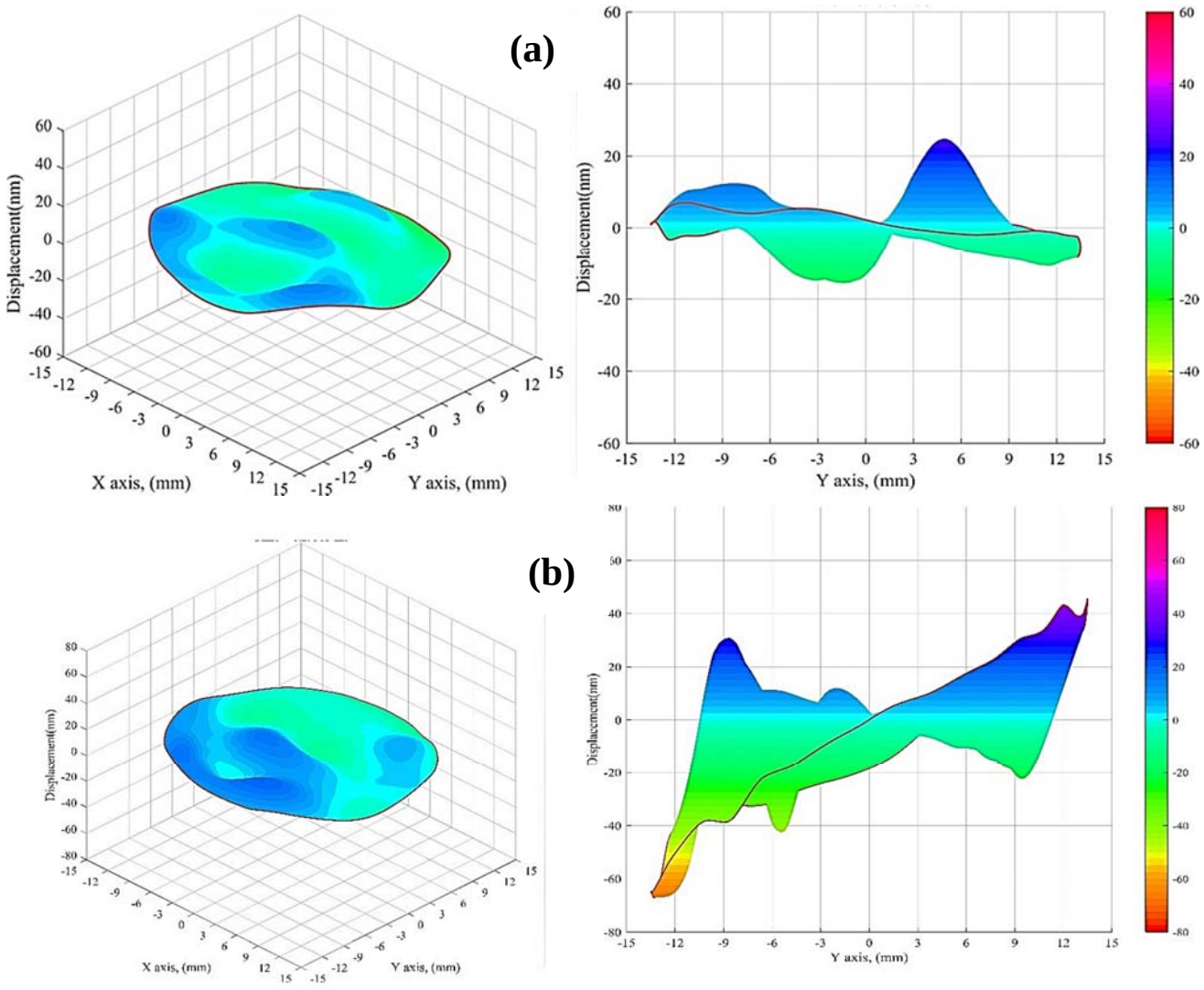

Figure A-19: Perspective and side views of 1 MHz transducer (1MSN) vibration modes. (a) under 100 volts excitation, (b) under 200 volts excitation.

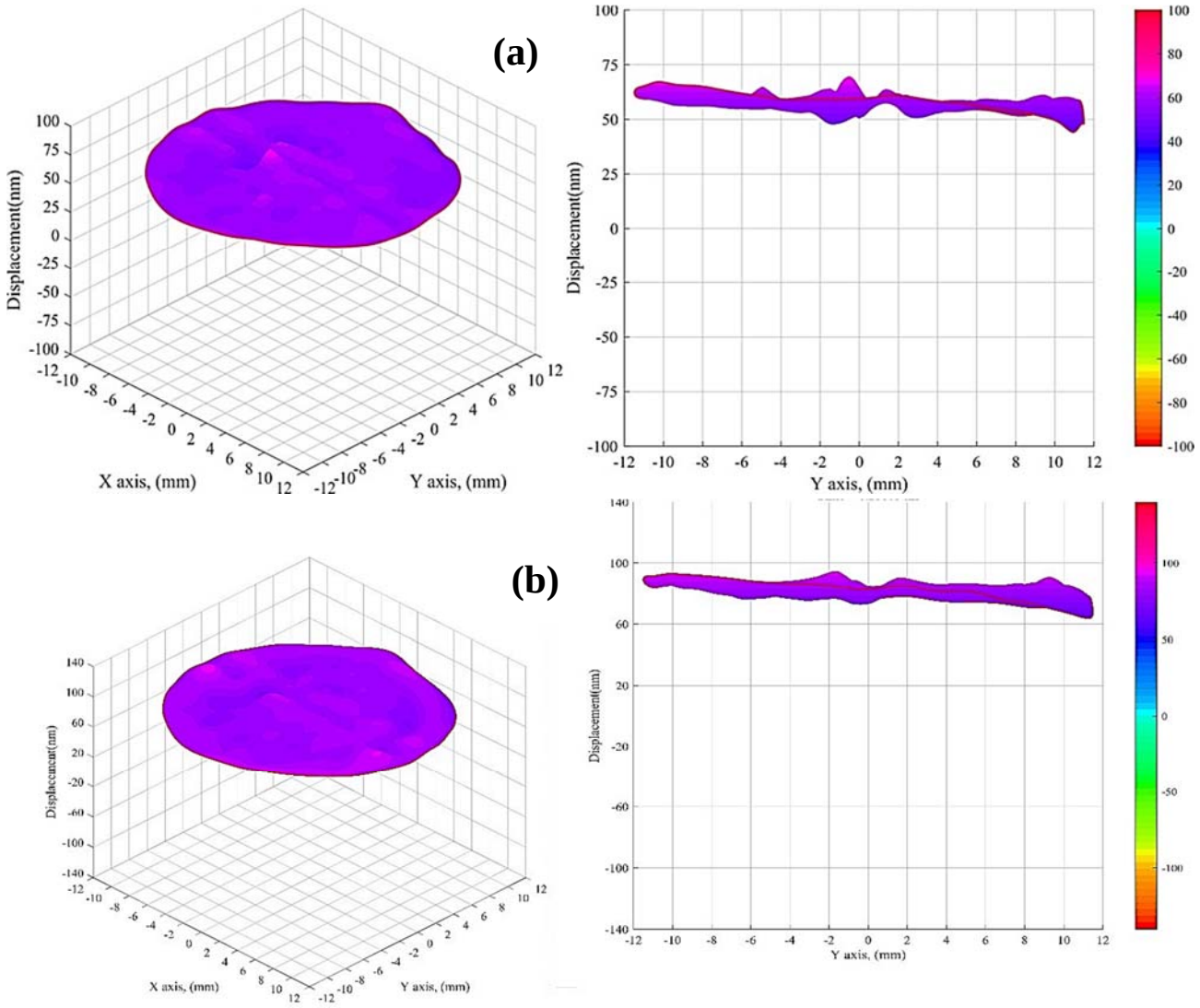

Figure A-20: Perspective and side views of 1MHz transducer (1MPO) vibration modes. (a) under 100 volts excitation, (b) under 200 volts excitation.

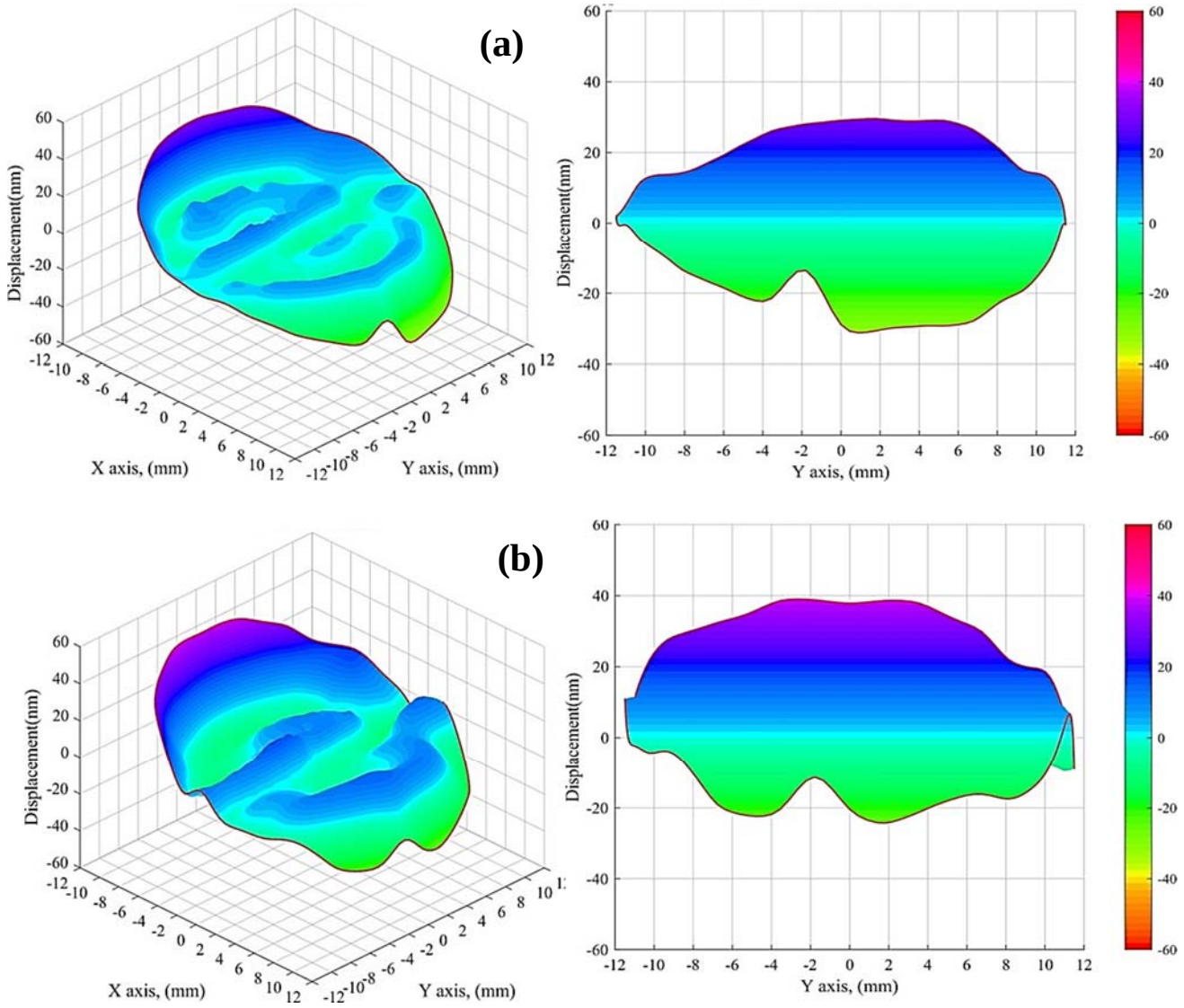

Figure A-21: Perspective and side views of 1MHz transducer (1MSO) vibration modes. (a) under 100 volts excitation, (b) under 200 volts excitation.

Appendix B

B.1 Immersion results – P-wave signals

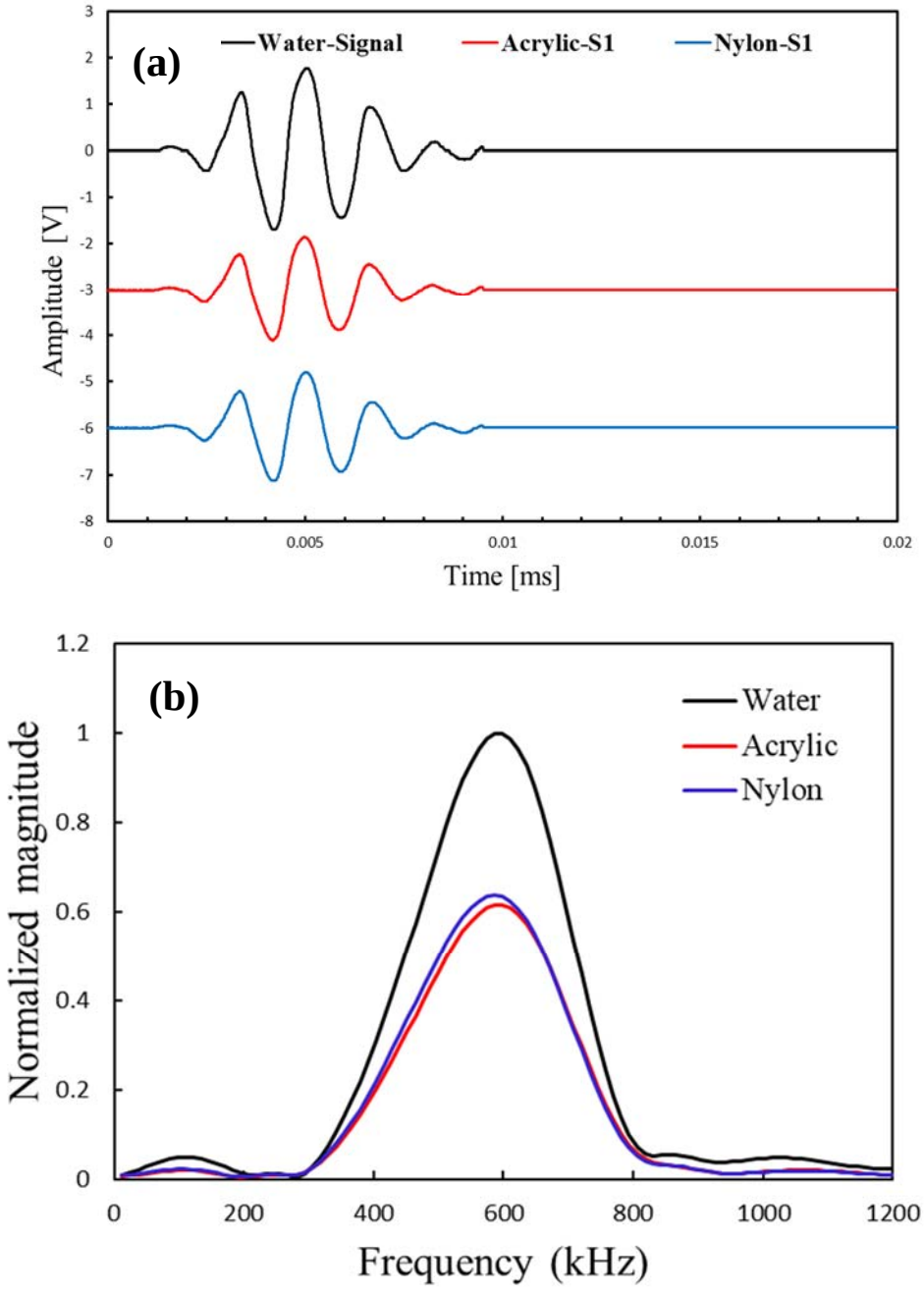

Figure B-1: Typical P-wave waveforms of water, acrylic and nylon. (a) time signals, (b) Fourier spectra.

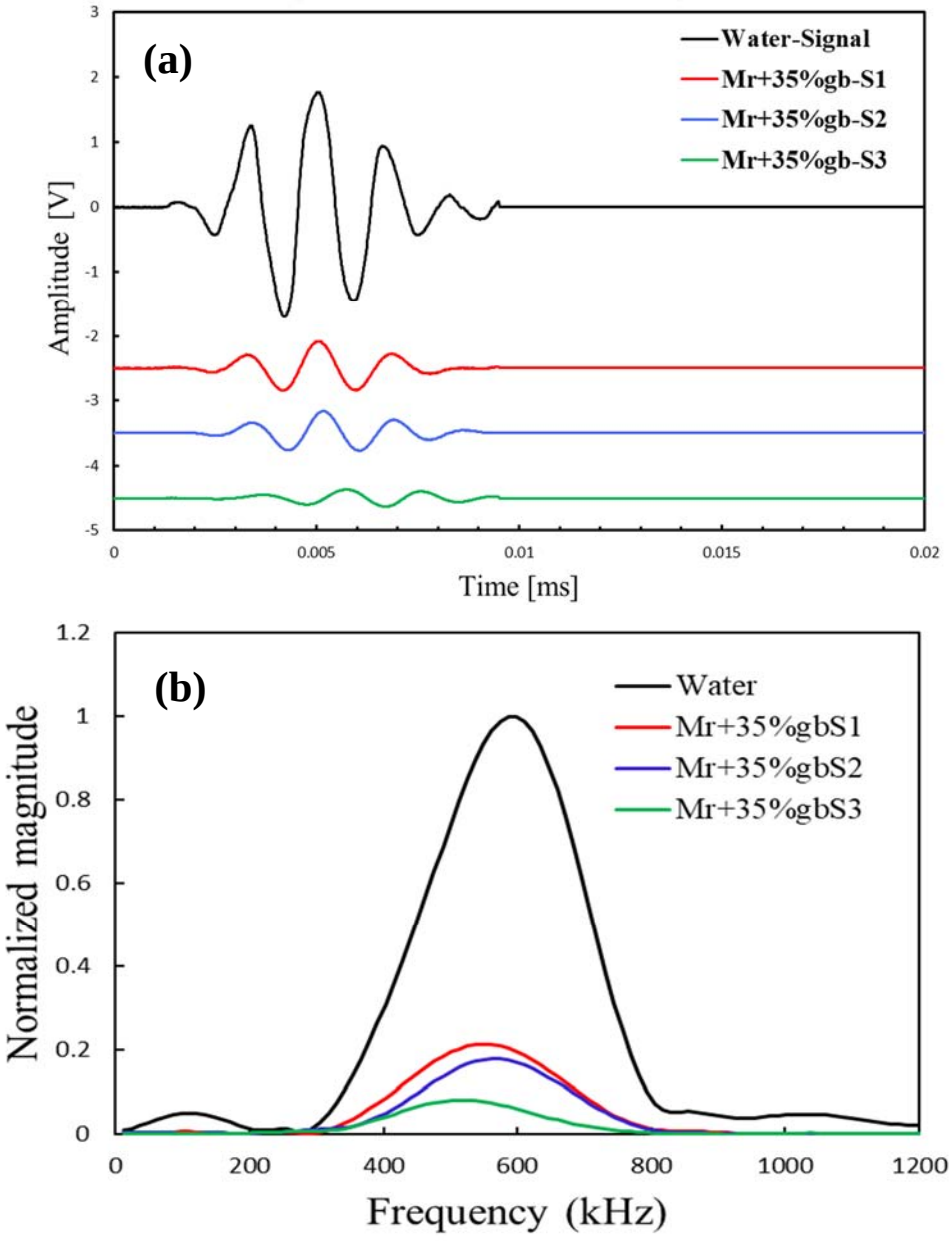

Figure B-2: Typical P-wave waveforms of water and mortar with 35%gb specimens. (a) time signals, (b) Fourier spectra.

B.2 Immersion results – S-wave signals

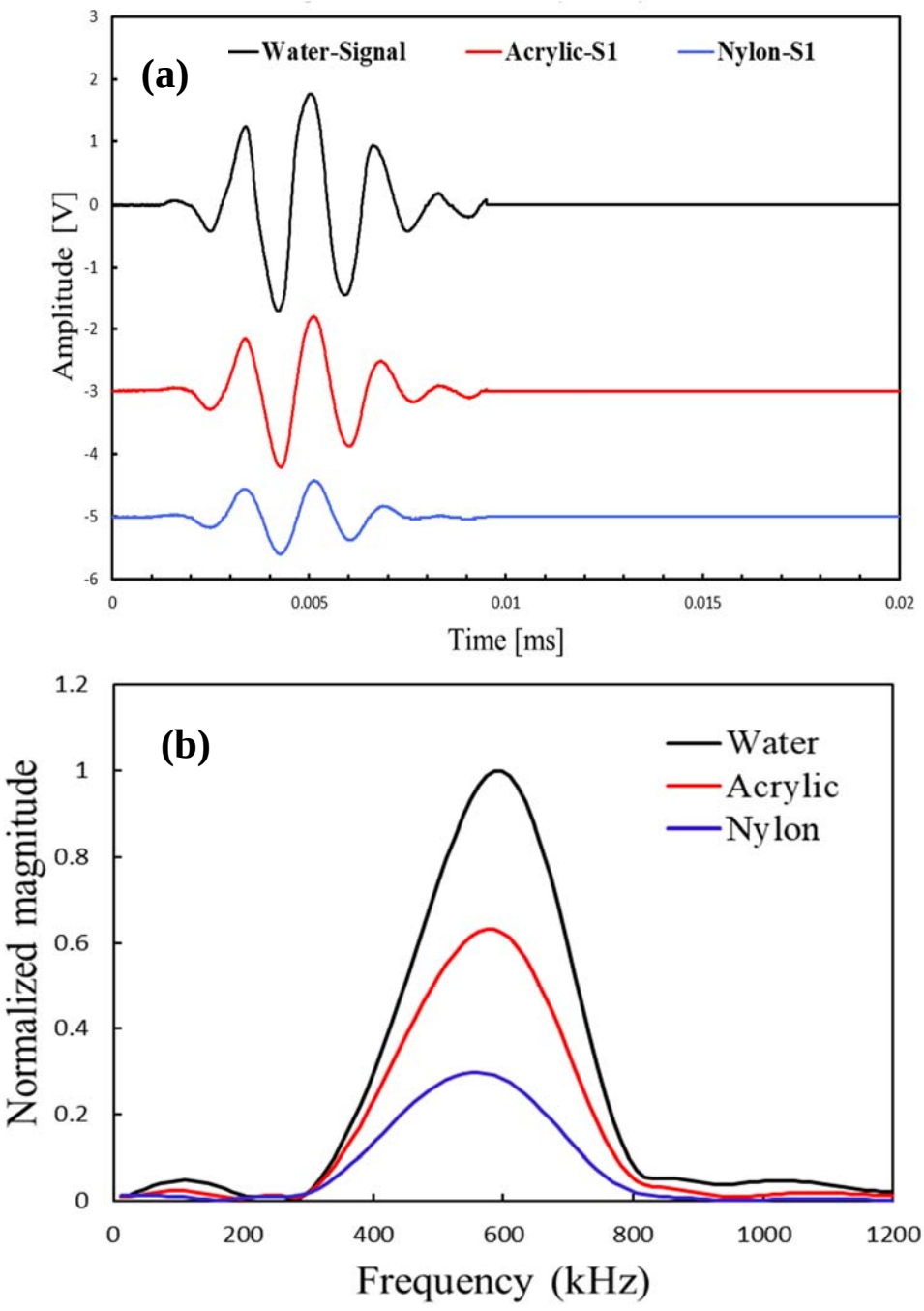

Figure B-3: Typical S-wave waveforms of water, acrylic and nylon. (a) time signals, (b) Fourier spectra.

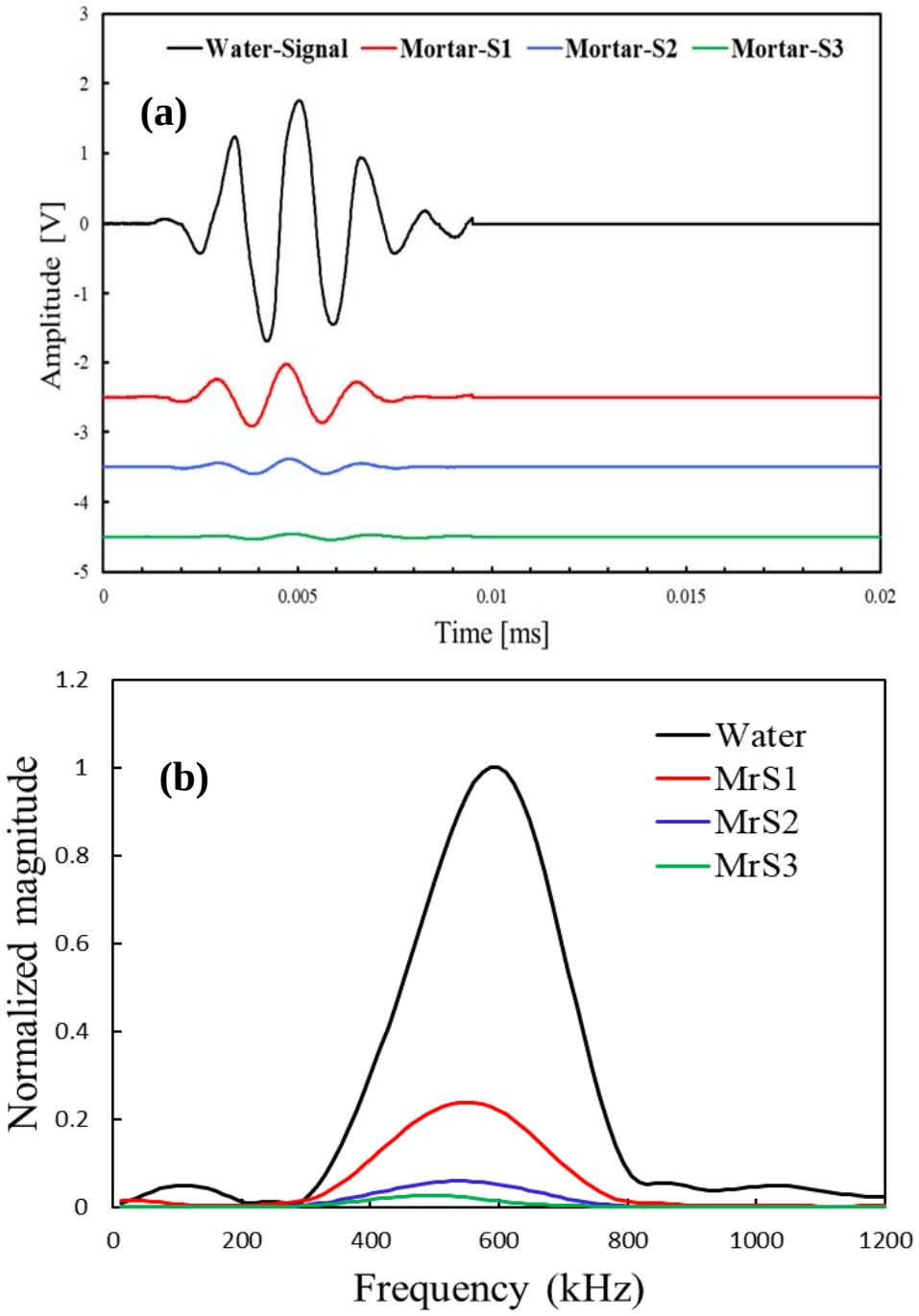

Figure B-4: Typical S-wave waveforms of water and mortar specimens. (a) time signals, (b) Fourier spectra.

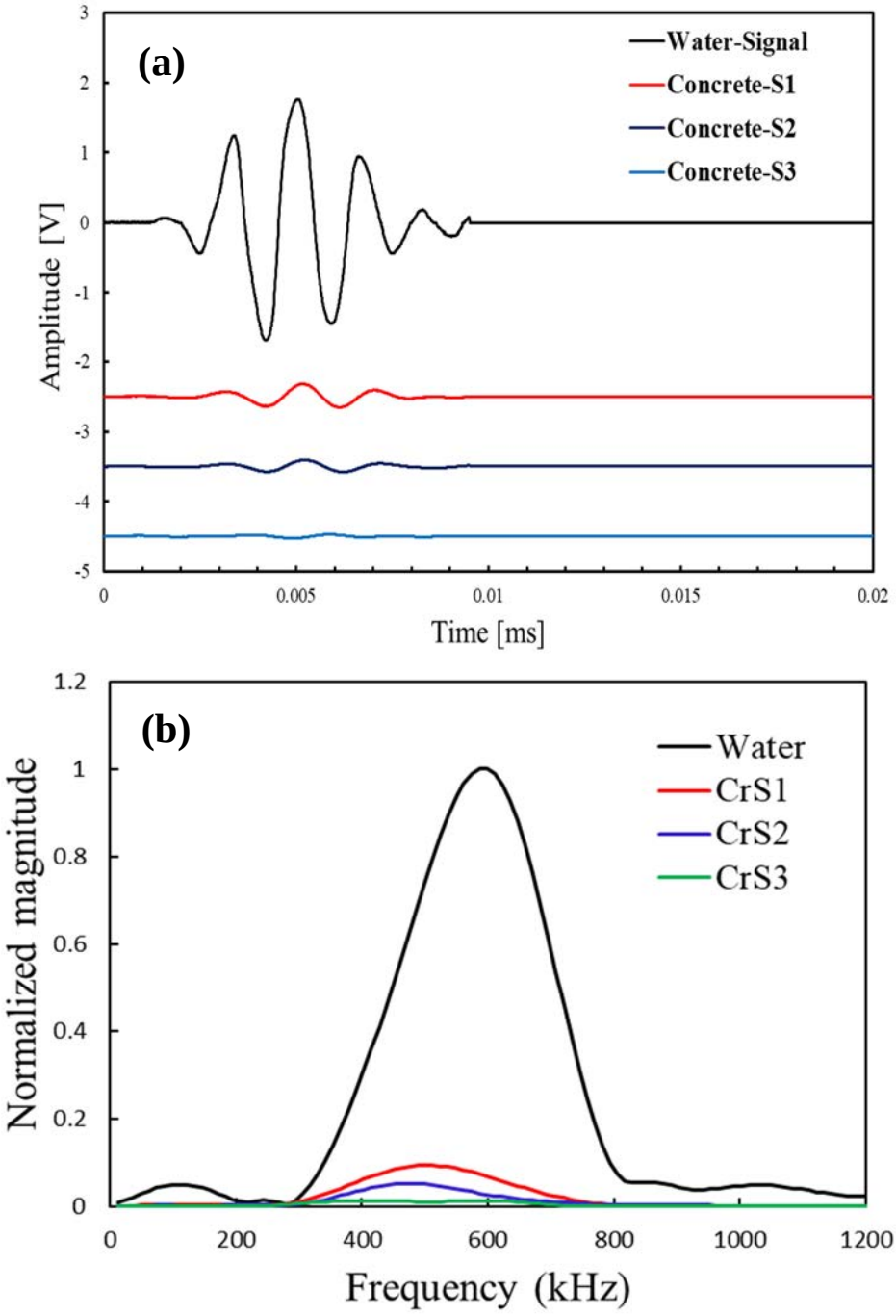

Figure B-5: Typical S-wave waveforms of water and concrete specimens. (a) time signals, (b) Fourier spectra.

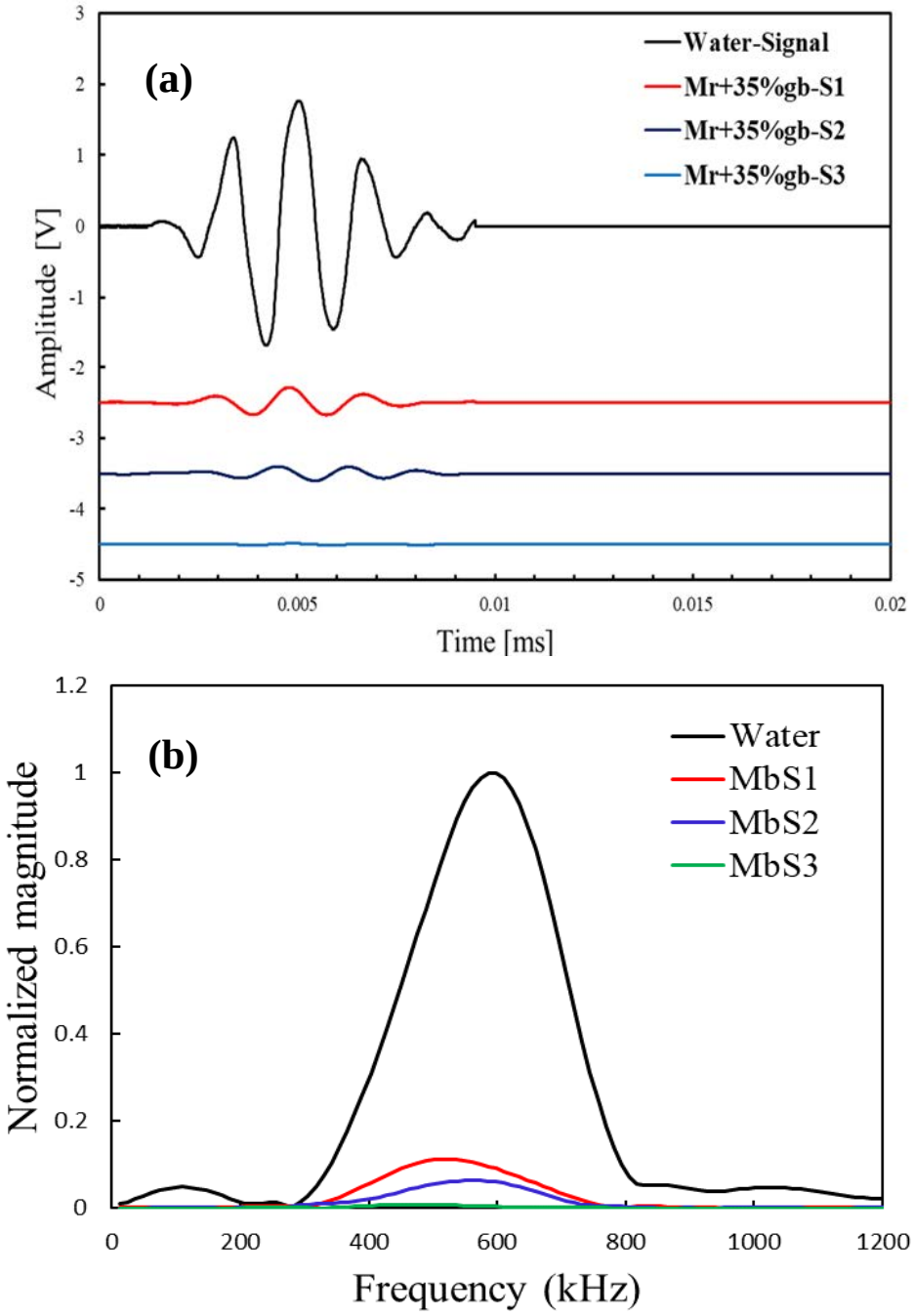

Figure B-6: Typical S-wave waveforms of water and mortar with 35%gb specimens. (a) time signals, (b) Fourier spectra.

B.3 Laser results – P-wave signals

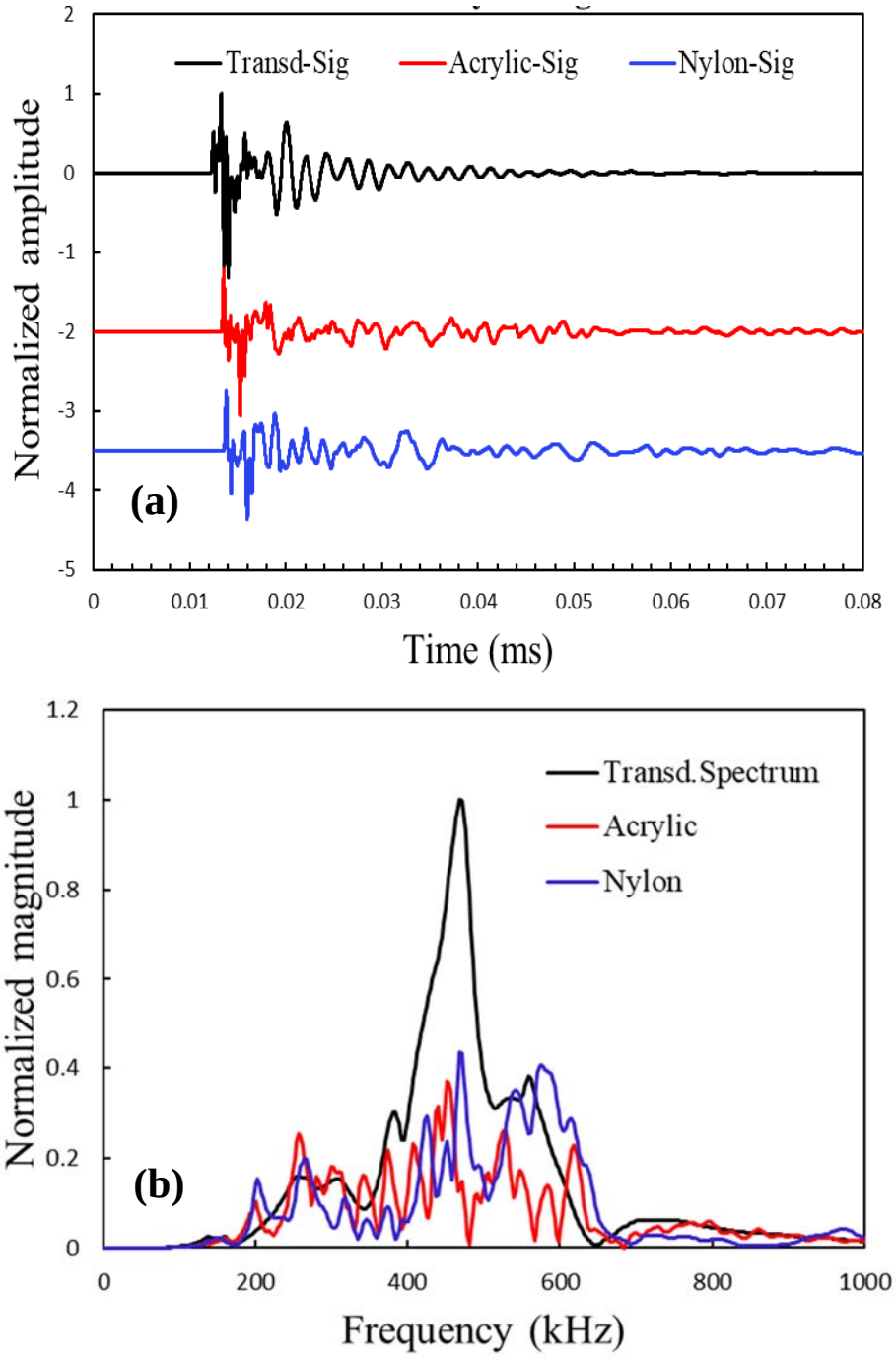

Figure B-7: Typical P-wave waveforms of water, acrylic and nylon. (a) time signals, (b) Fourier spectra.

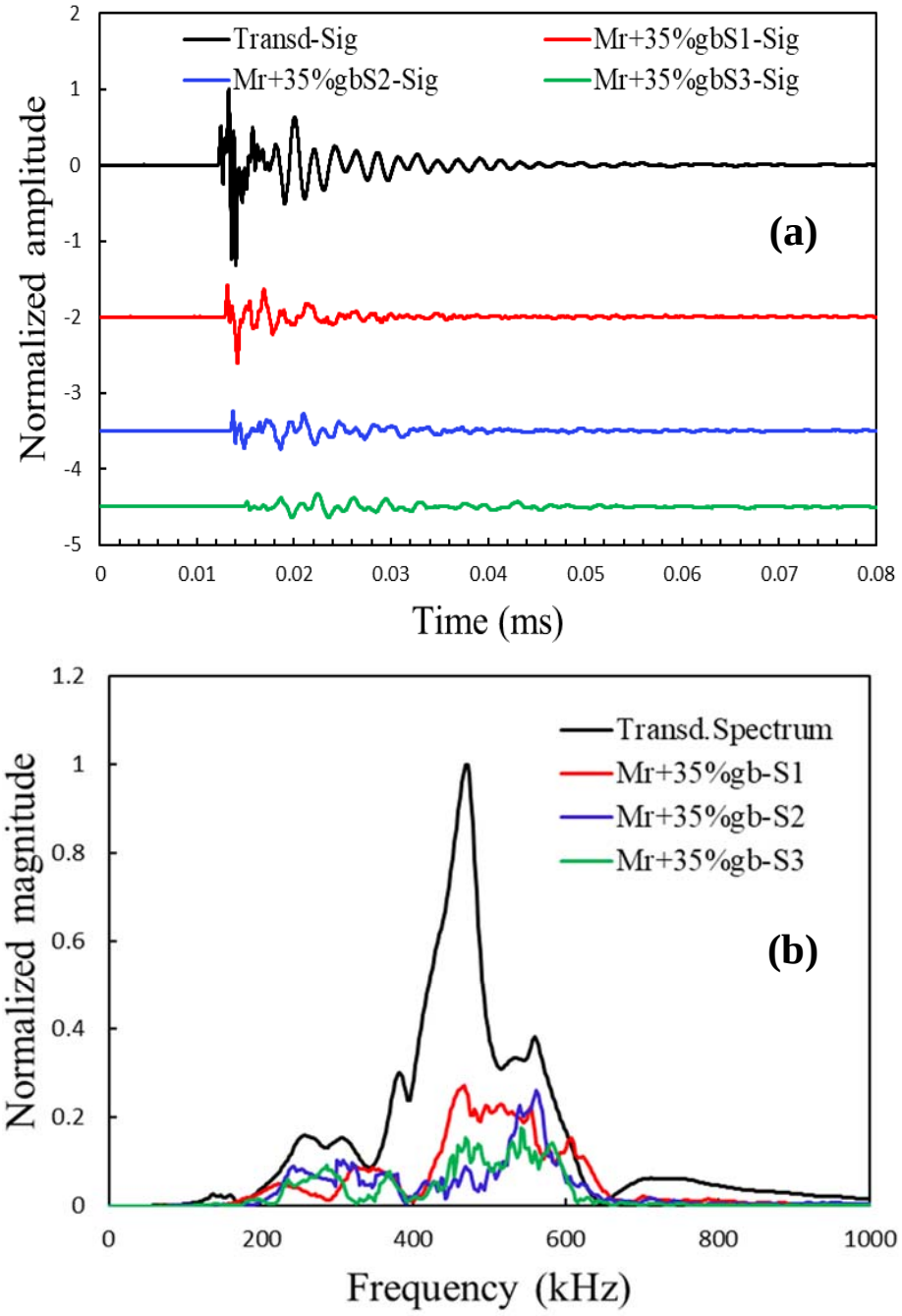

Figure B-8: Typical P-wave waveforms of water and mortar with 35%gb specimens. (a) time signals, (b) Fourier spectra.

Appendix C

C.1 Freeze-thaw results

C.1-1 Freeze-thaw UPV results (concrete cylinders)

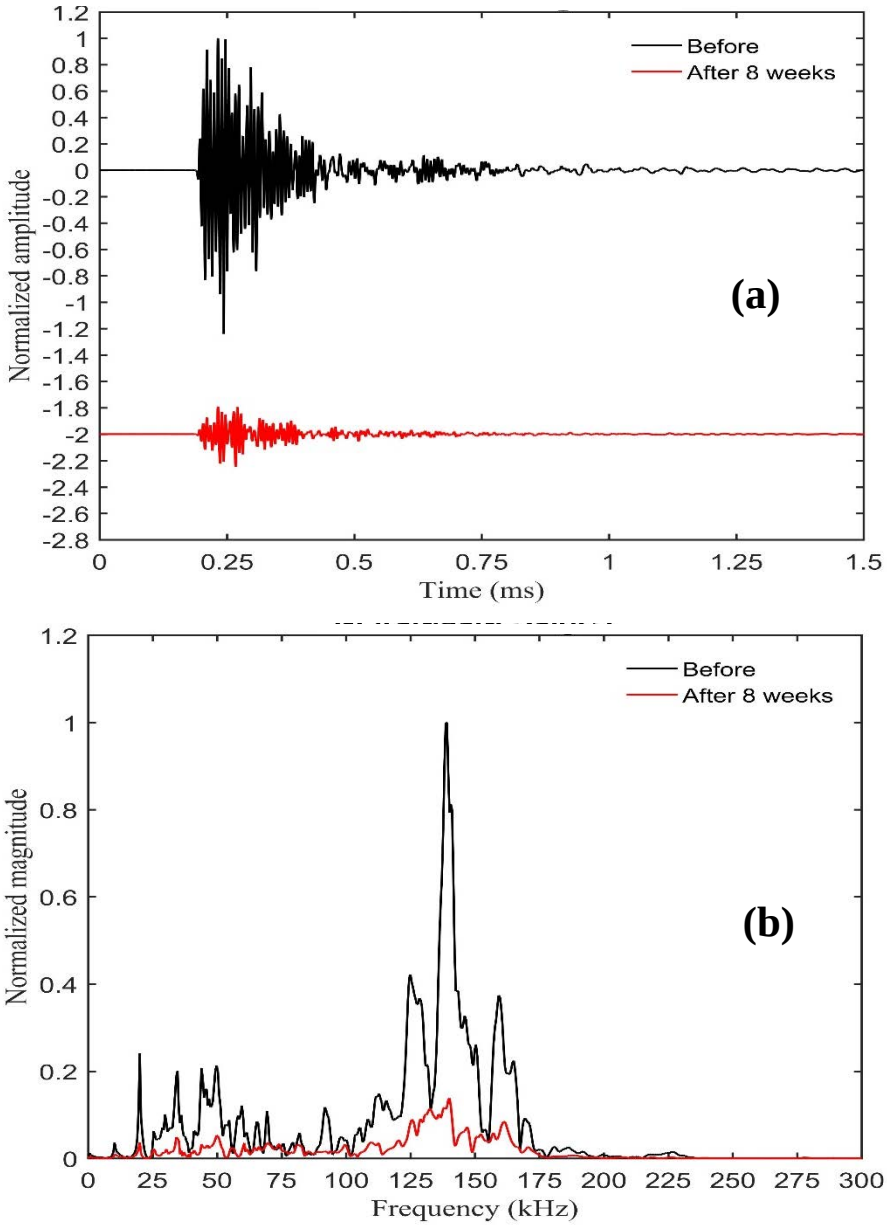

Figure C-1: Typical waveforms of untreated cylinder concrete specimen before and at the end of the period of study using 150 kHz. (a) time signals, (b) Fourier spectra.

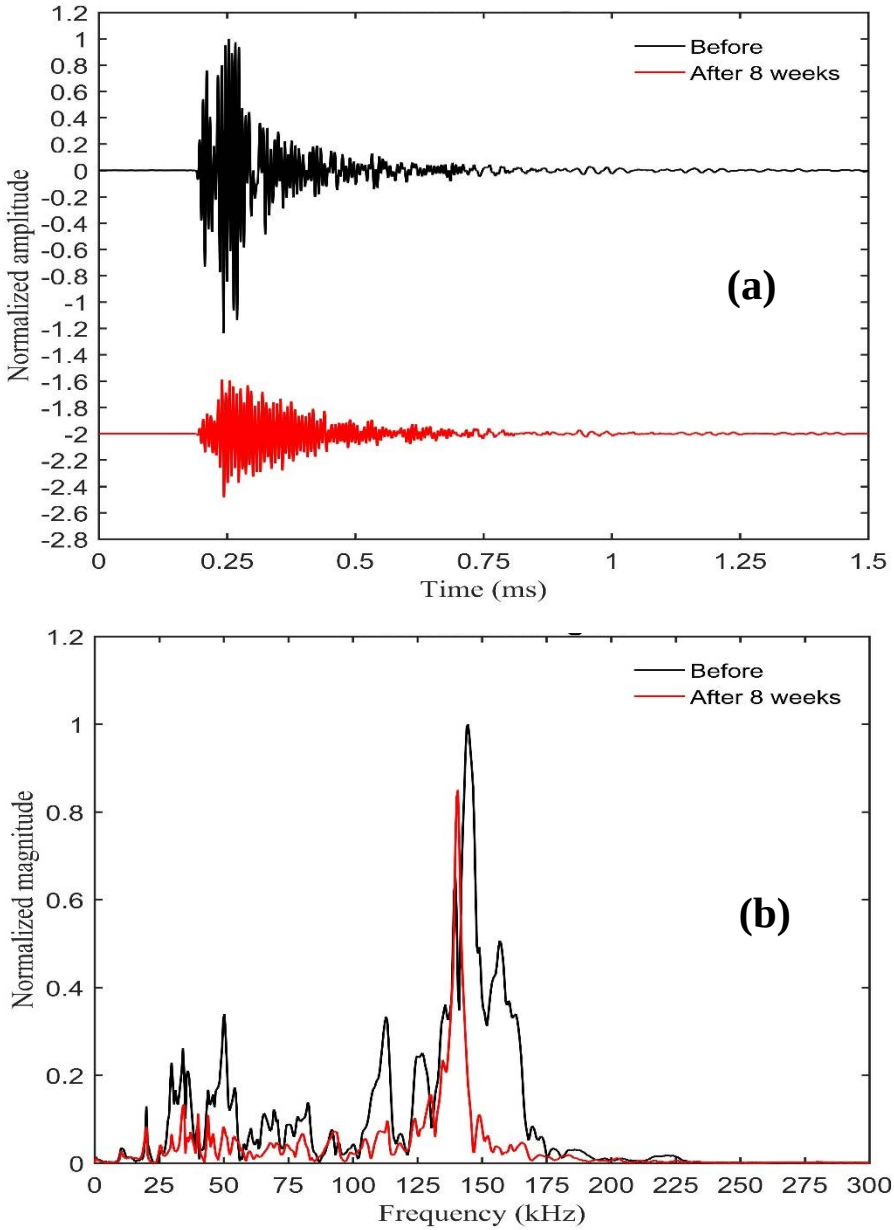

Figure C-2: Typical waveforms of treated cylinder concrete specimen with 0.1% air-entrained before and at the end of the period study using 150 kHz. (a) time signals, (b) Fourier spectra.

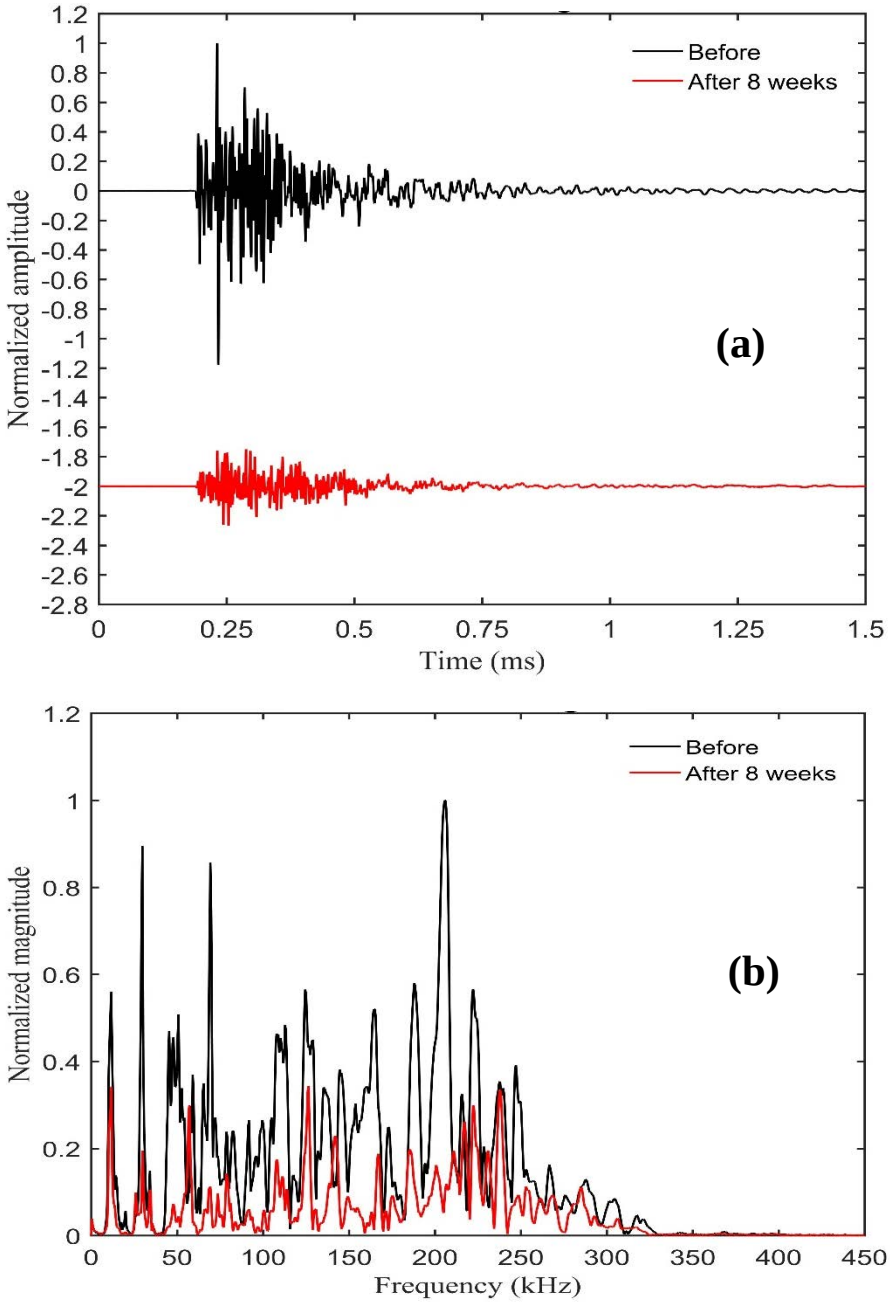

Figure C-3: Typical waveforms of treated cylinder concrete specimen with 0.1% air-entrained before and at the end of the period study using 250 kHz. (a) time signals, (b) Fourier spectra.

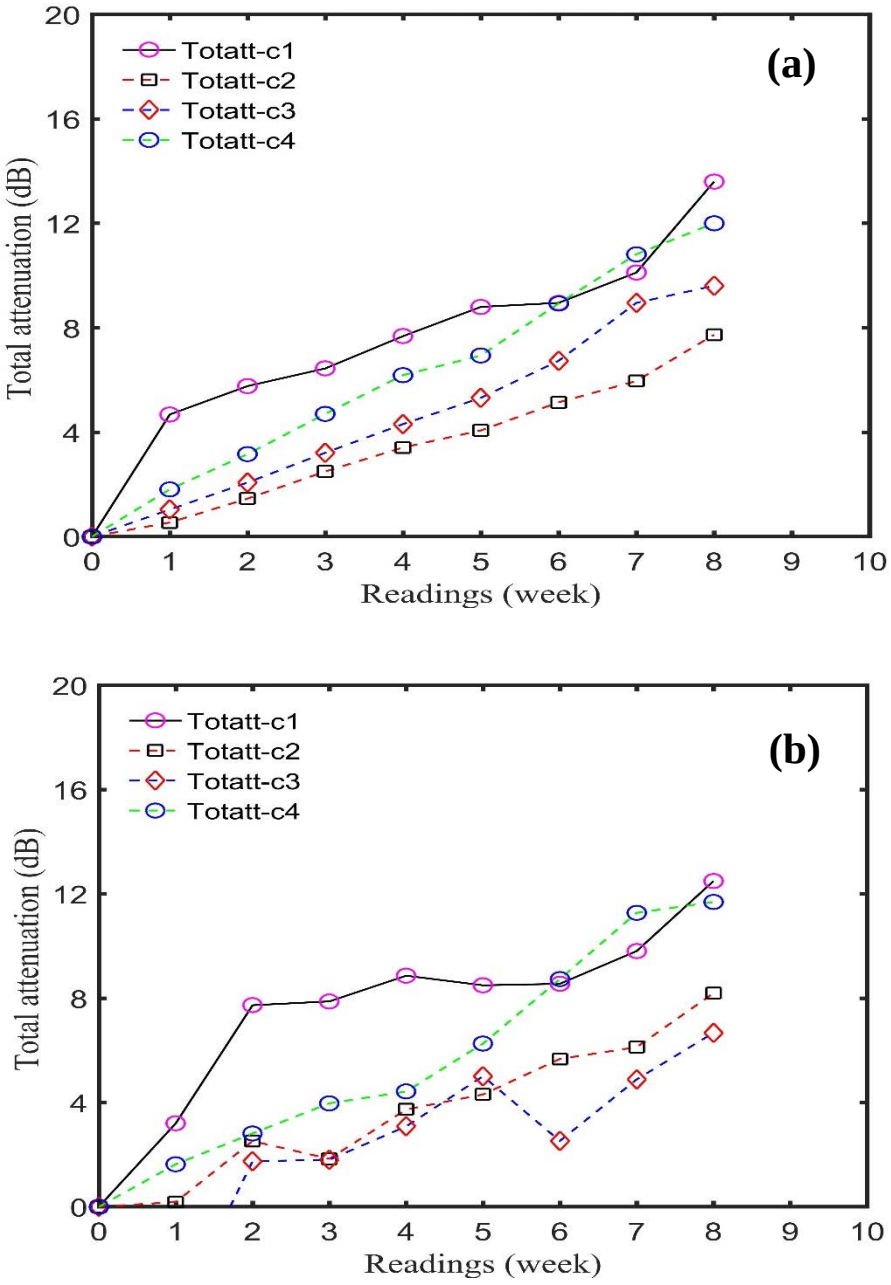

Figure C-4: Typical total attenuation of cylinder concrete specimens using 150 kHz transducer. (a) amplitude method, (b) spectrum area method.

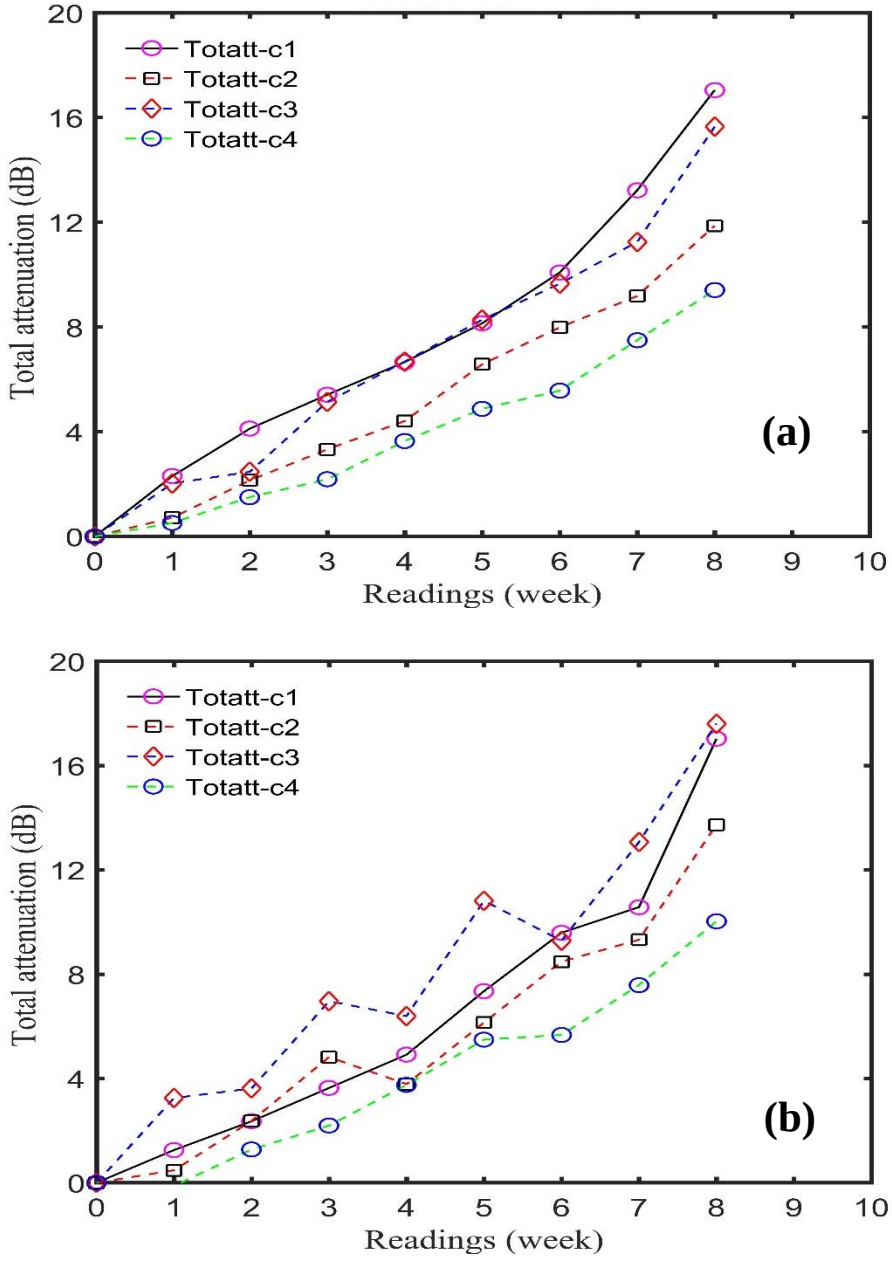

Figure C-5: Typical total attenuation of cylinder concrete specimens using 500 kHz transducer. (a) amplitude method, (b) spectrum area method.

C.1-2 Freeze-thaw laser vibrometer results (concrete cylinders)

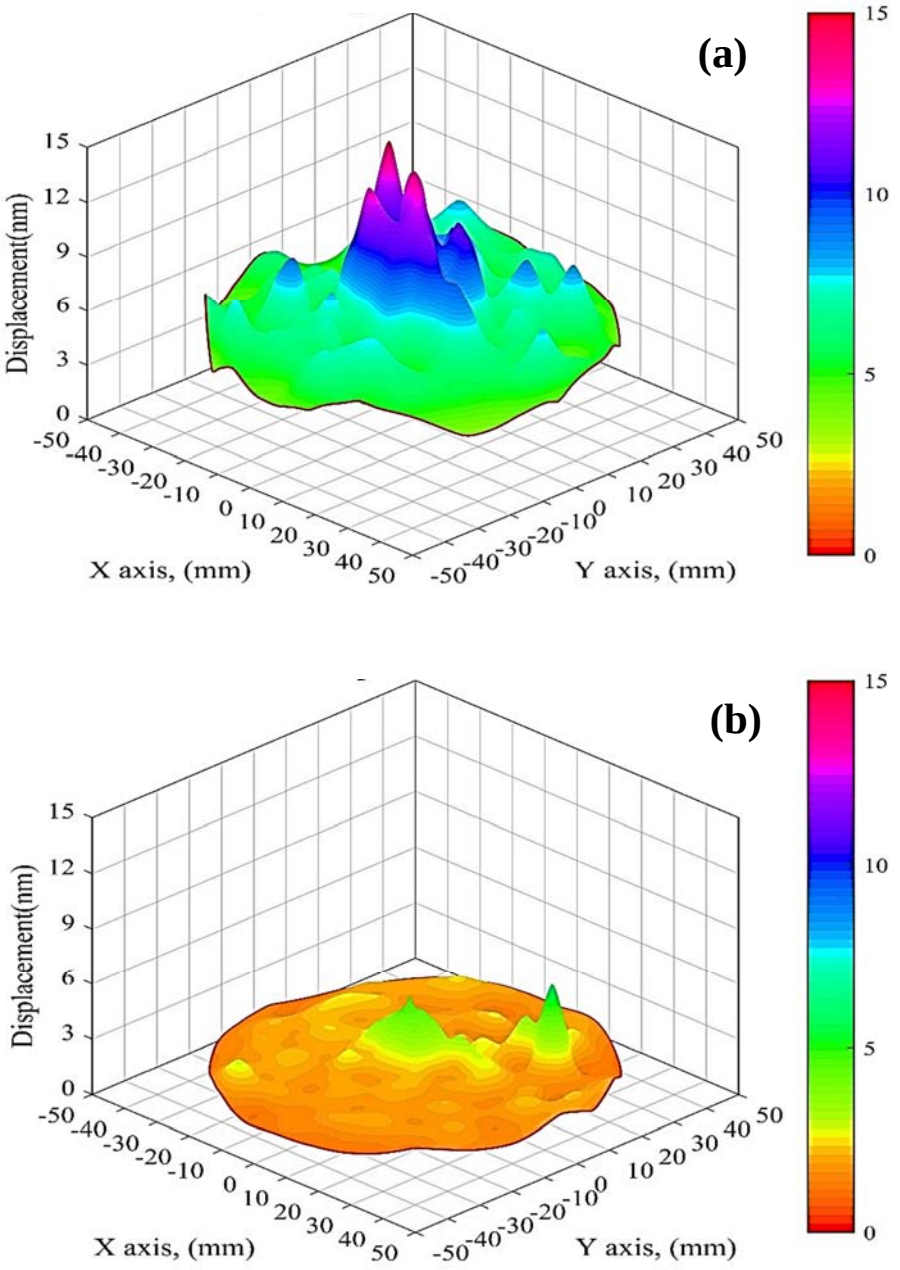

Figure C-6. Typical vibration modes of untreated cylinder specimen using 250 kHz. (a) before freeze-thaw process, (b) after 56 freeze-thaw cycles.

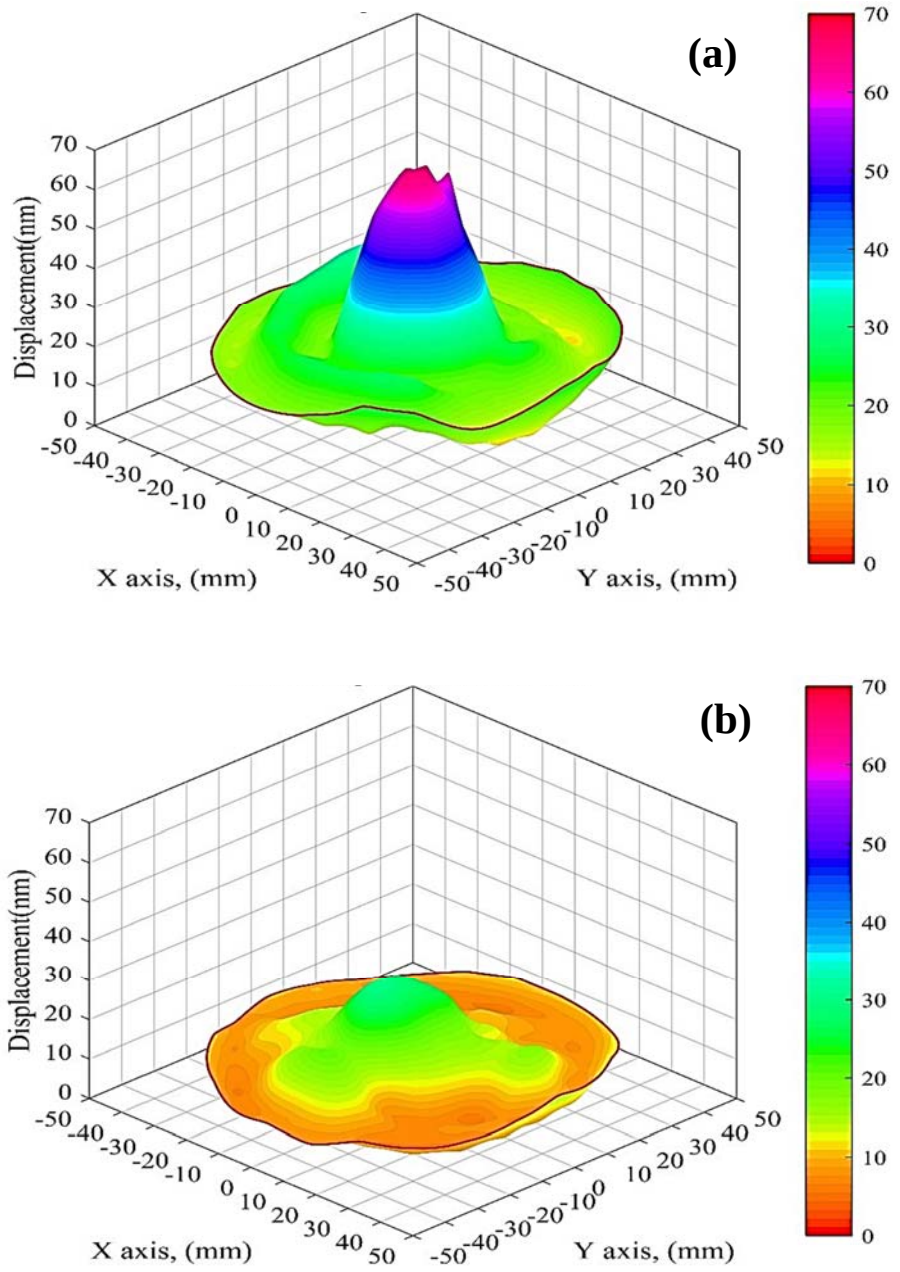

Figure C-7. Typical vibration modes of treated cylinder specimen with 0.1% air-entrained scanned with laser using 54 kHz. (a) before freeze-thaw process, (b) after 56 freeze-thaw cycles.

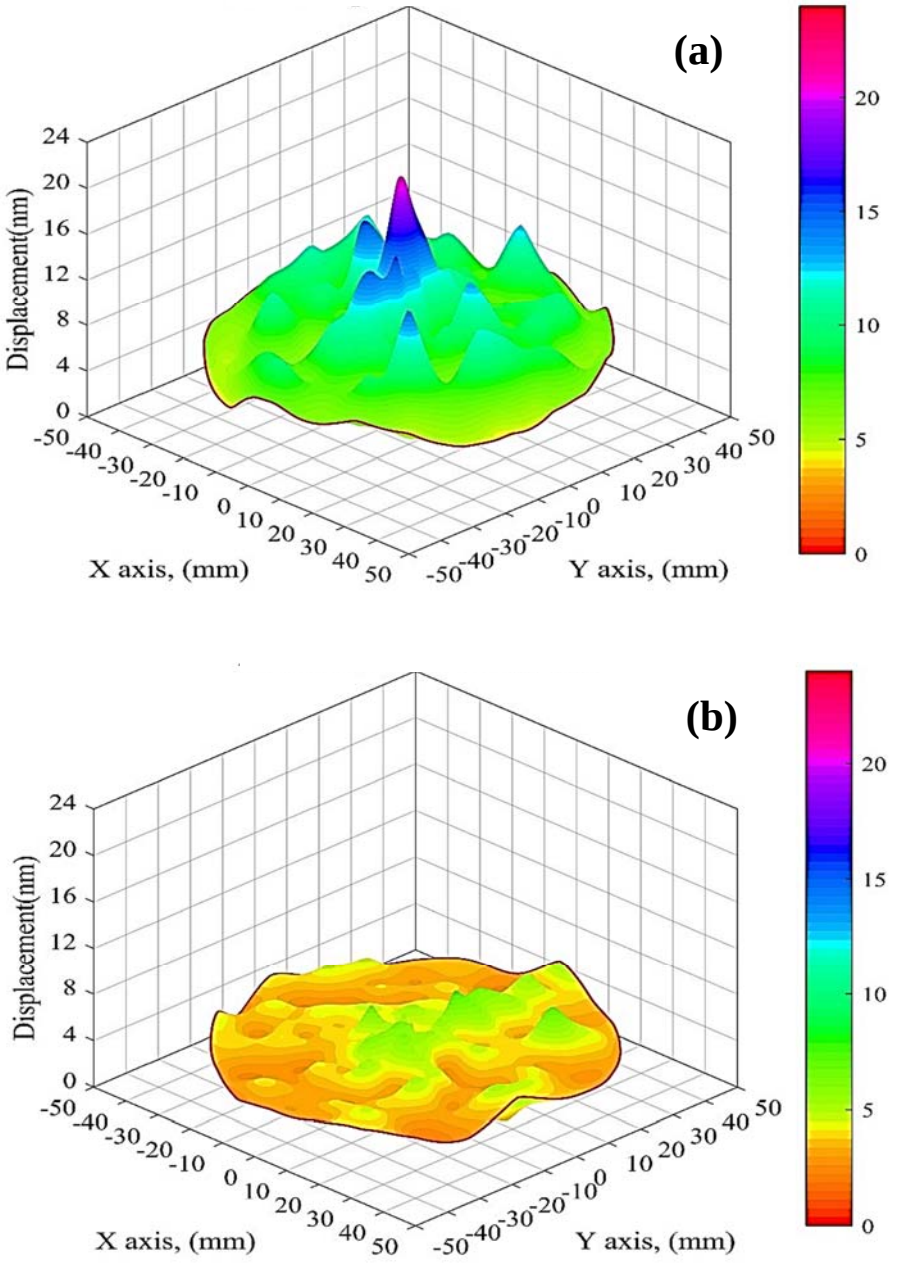

Figure C-8. Typical vibration modes of treated cylinder specimen with 0.1% air-entrained scanned with laser using 250 kHz. (a) before freeze-thaw process, (b) after 56 freeze-thaw cycles.

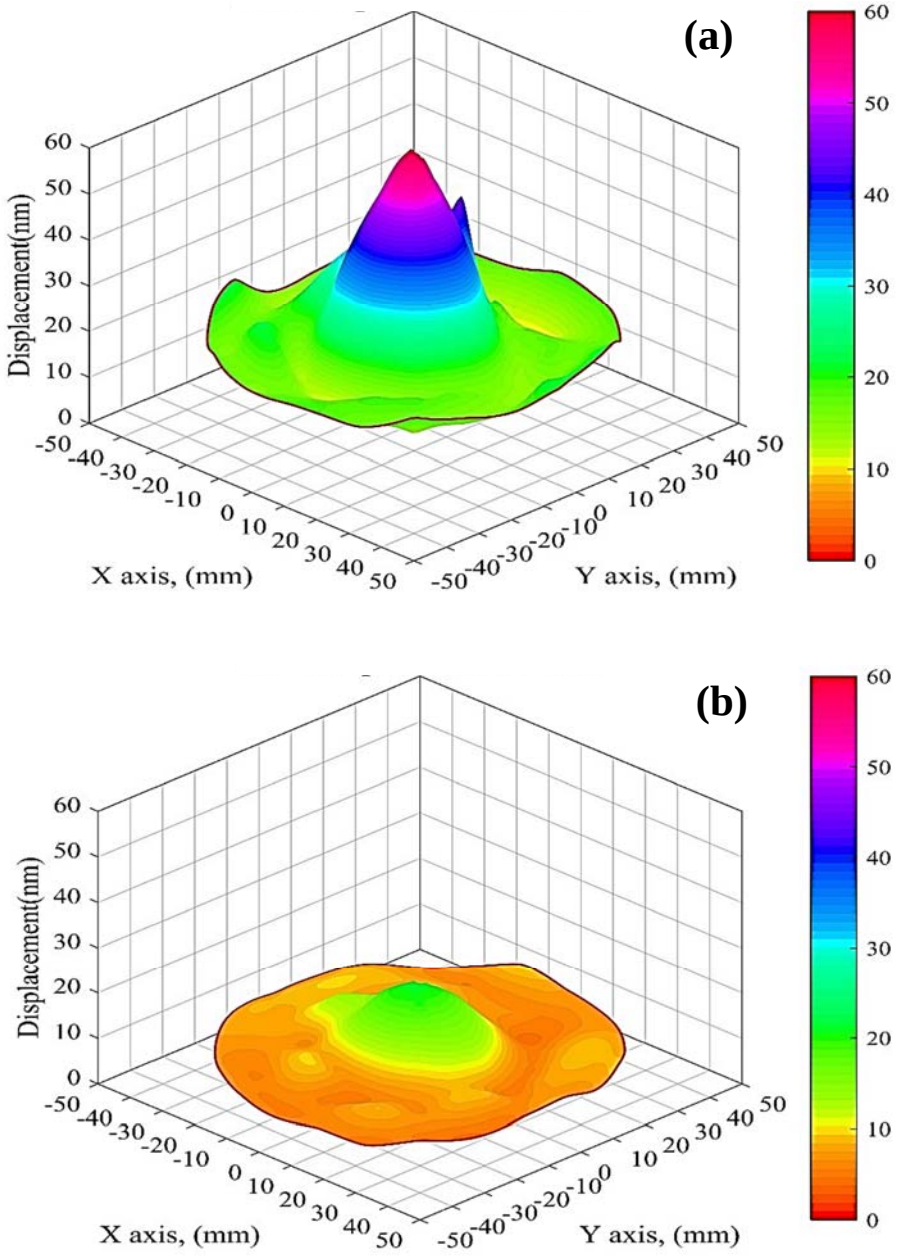

Figure C-9. Typical vibration modes of treated cylinder specimen with 0.25% air-entrained scanned with laser using 54 kHz. (a) before freeze-thaw process, (b) after 56 freeze-thaw cycles.

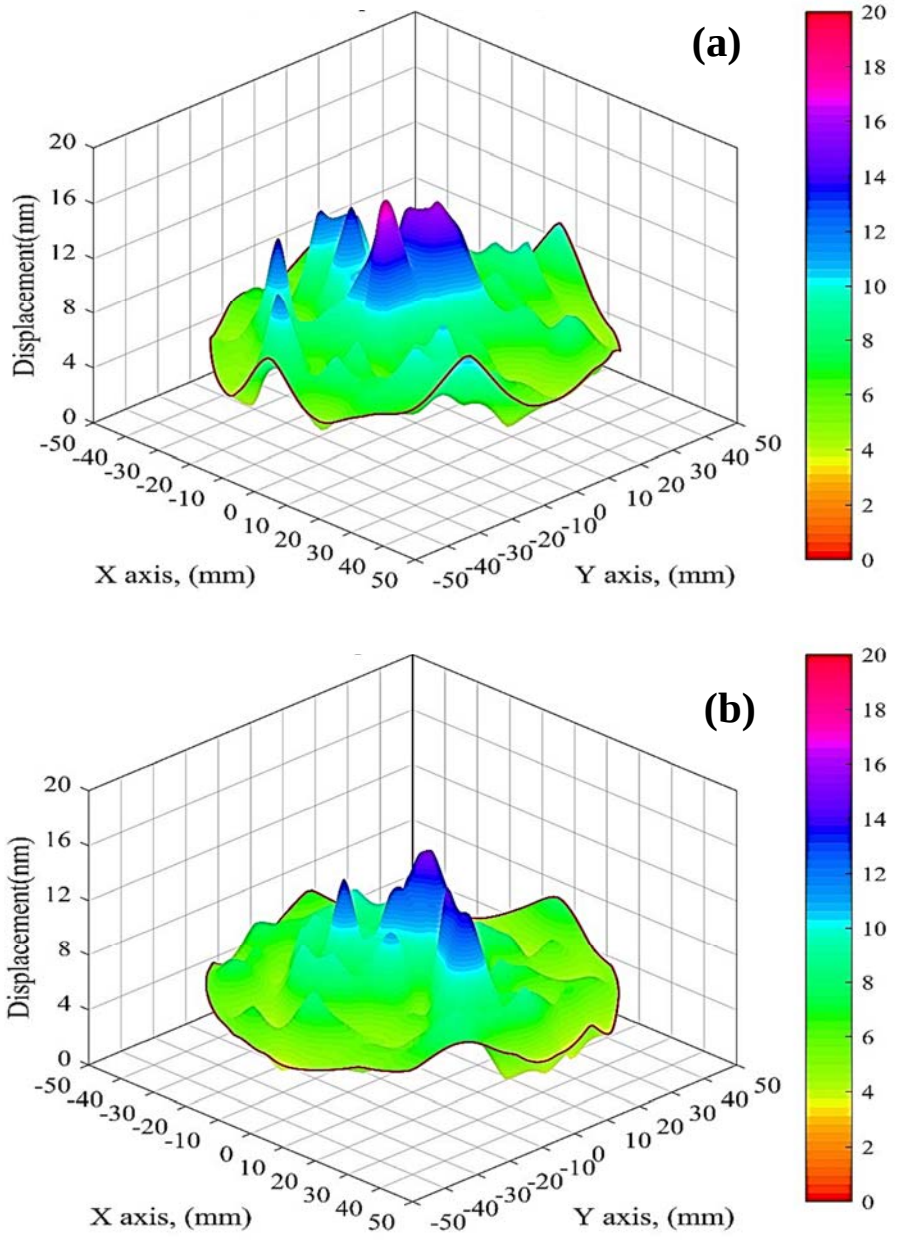

Figure C-10. Typical vibration modes of treated cylinder specimen with 0.25% air-entrained scanned with laser using 150 kHz. (a) before freeze-thaw process, (b) after 56 freeze-thaw cycles.

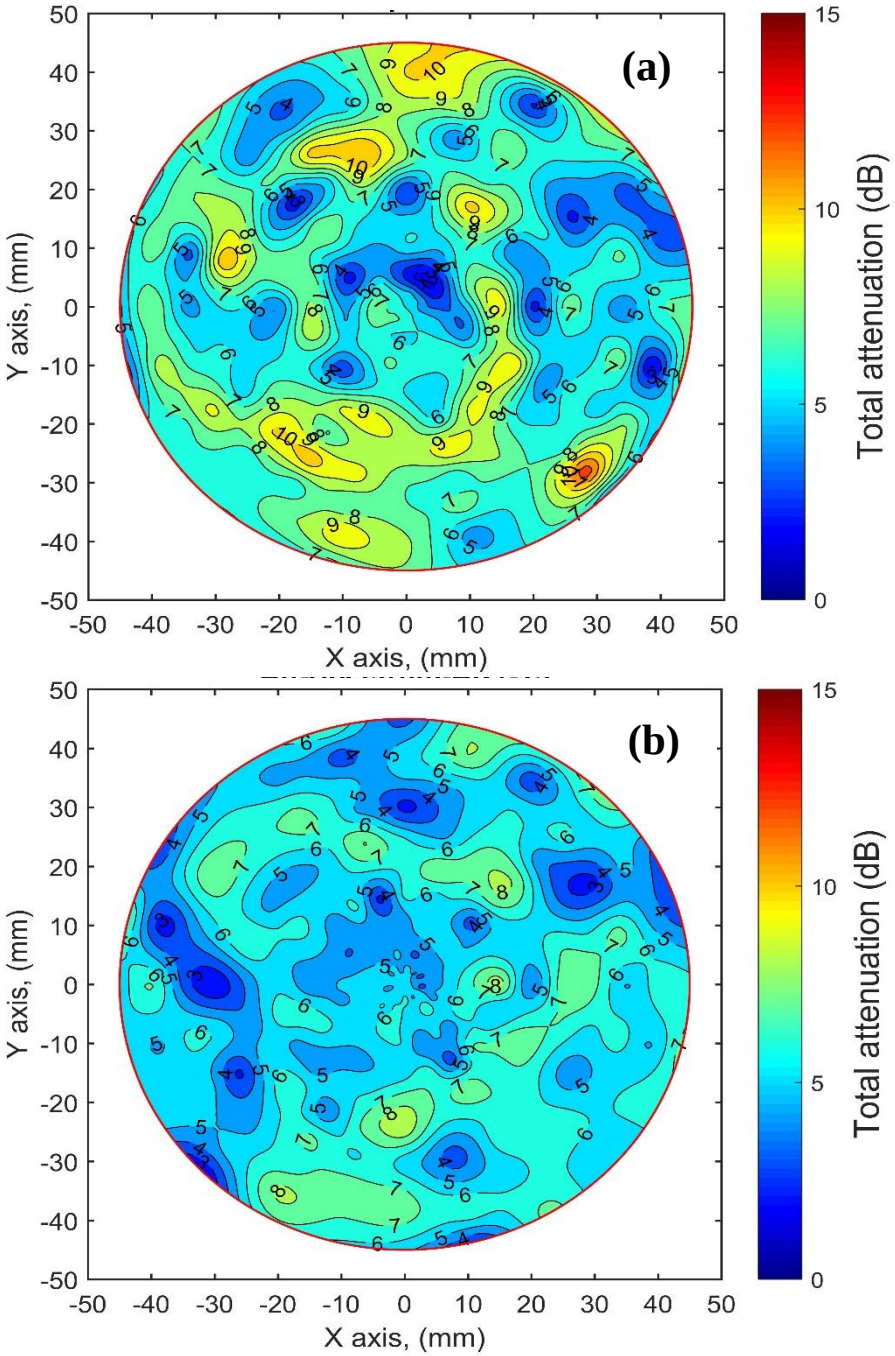

Figure C-11. Typical contour lines of total attenuation results of untreated cylinder specimen scanned with laser using 150 kHz. (a) using peak amplitude, (b) using spectrum area.

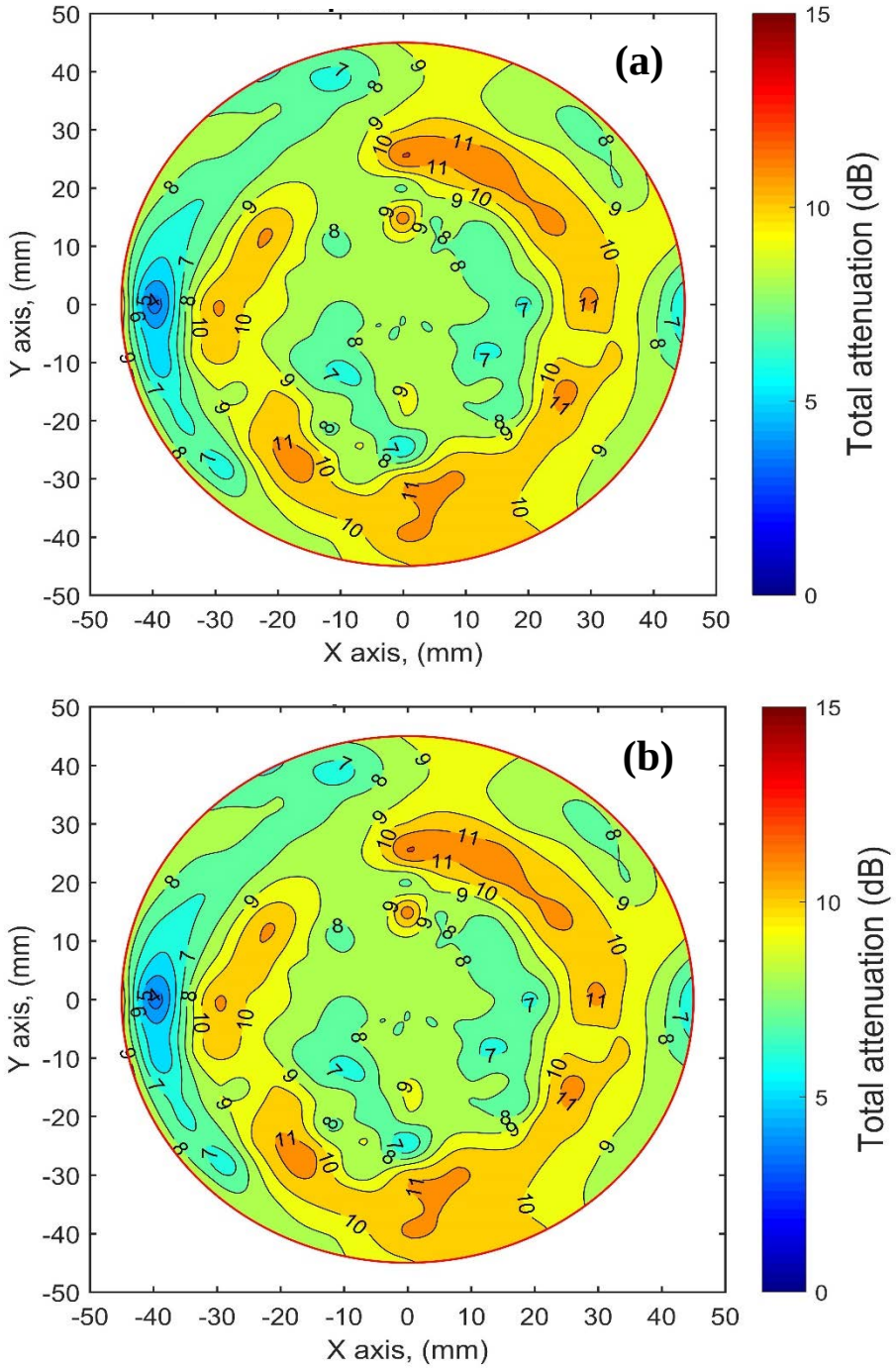

Figure C-12. Typical contour lines of total attenuation results of treated cylinder specimen with 0.25% air-entrained scanned with laser using 54 kHz. (a) using peak amplitude, (b) using spectrum area.

C.1-3 Freeze-thaw UPV results (concrete prisms)

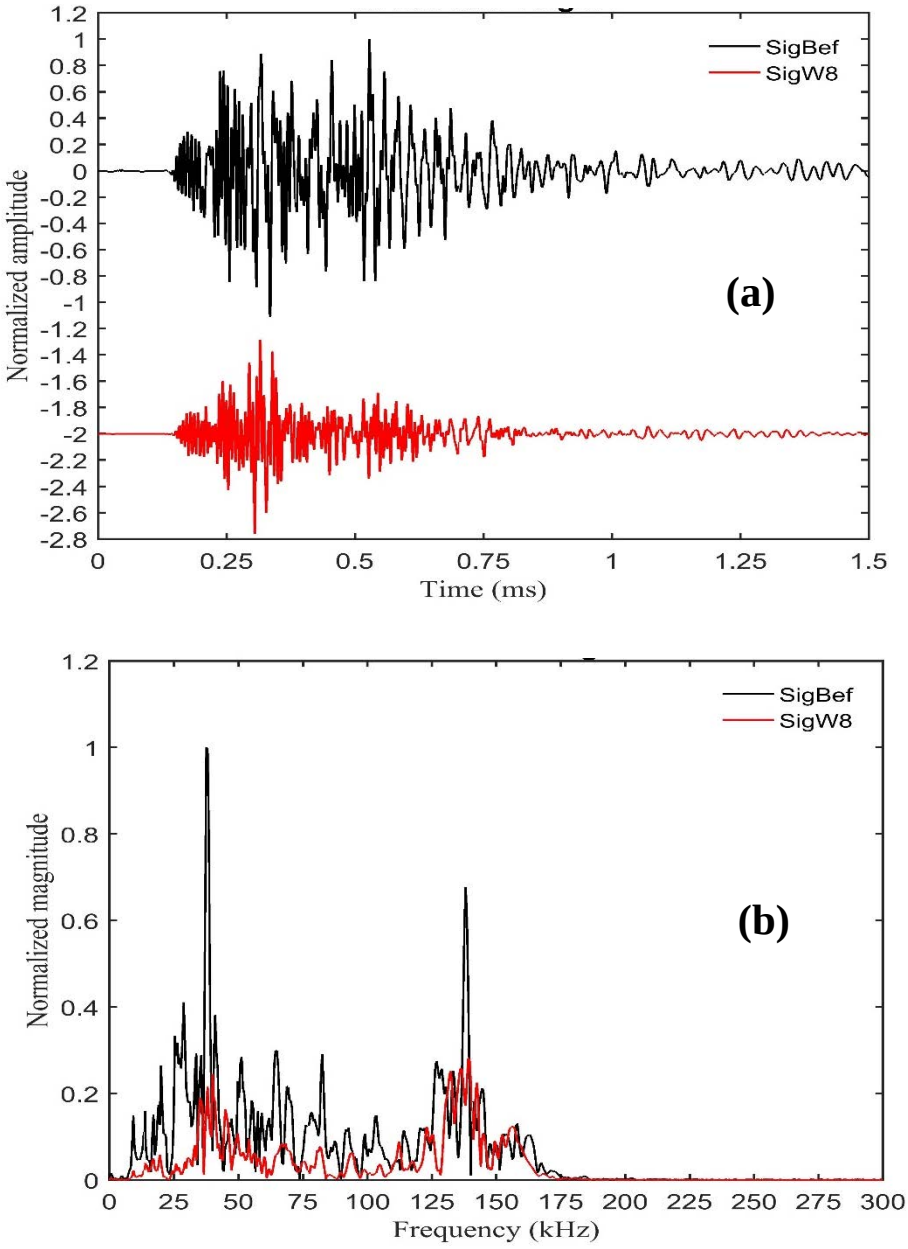

Figure C-13: Typical waveforms of treated prism concrete specimen with 0.1% air-entrained before and at the end of the period study using 150 kHz. (a) time signals, (b) Fourier spectra.

C.1-4 Freeze-thaw laser vibrometer results (concrete prisms)

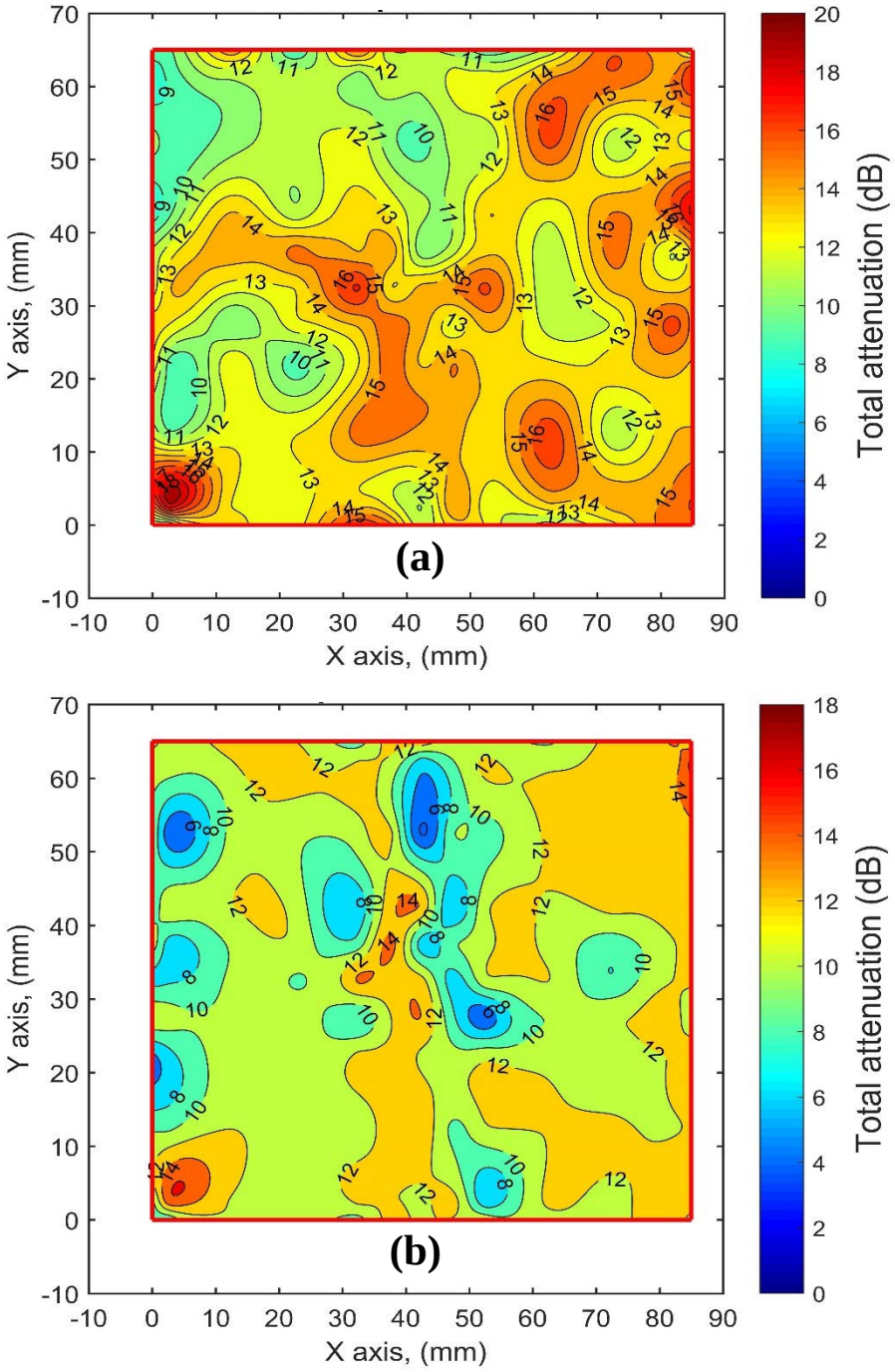

Figure C-14. Typical contour lines of total attenuation results of untreated prismatic specimen scanned with laser using 500 kHz. (a) using peak amplitude, (b) using spectrum area.

C.2 Compression test results

C.2-1 Single UPV testing results (concrete cylinders)

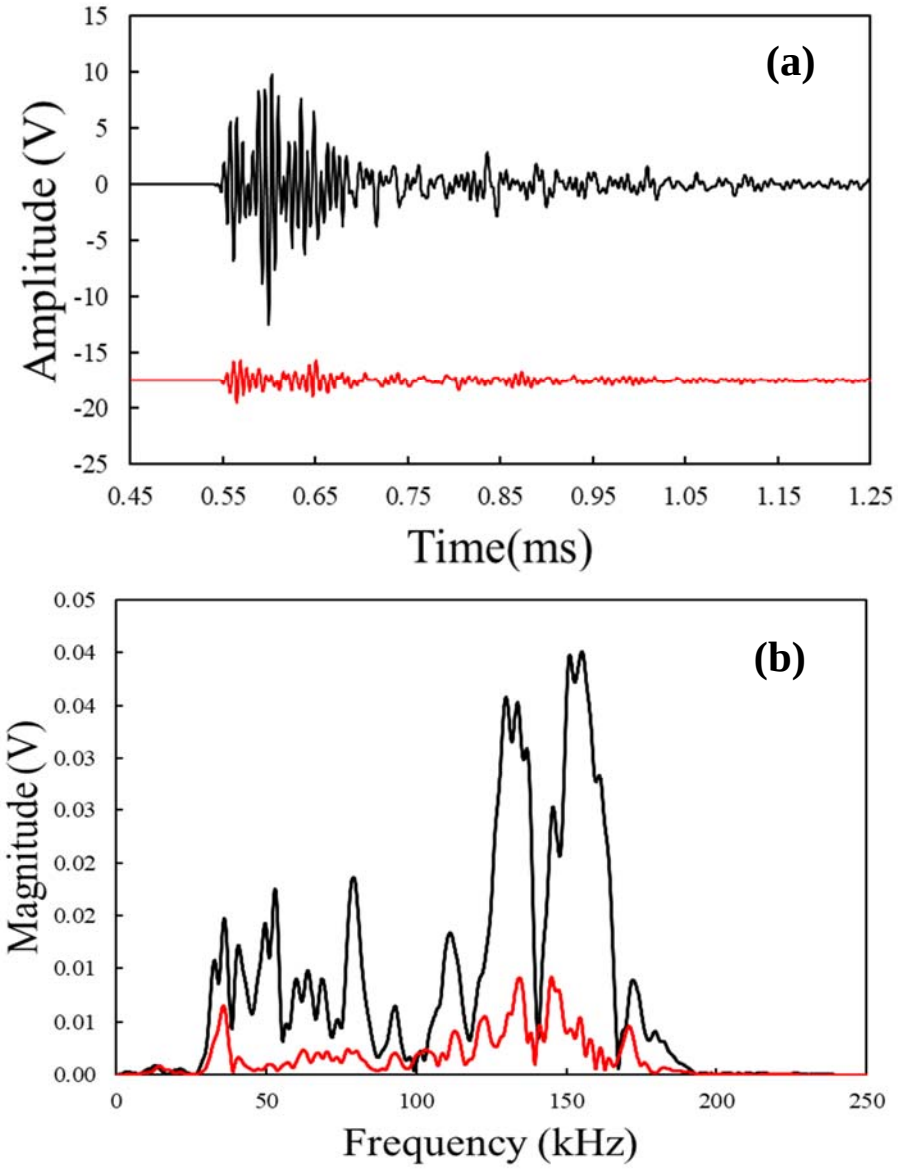

Figure C-15: Typical waveforms of untreated cylinder concrete specimen before and after compression load using 150 kHz. (a) time signals, (b) Fourier spectra.

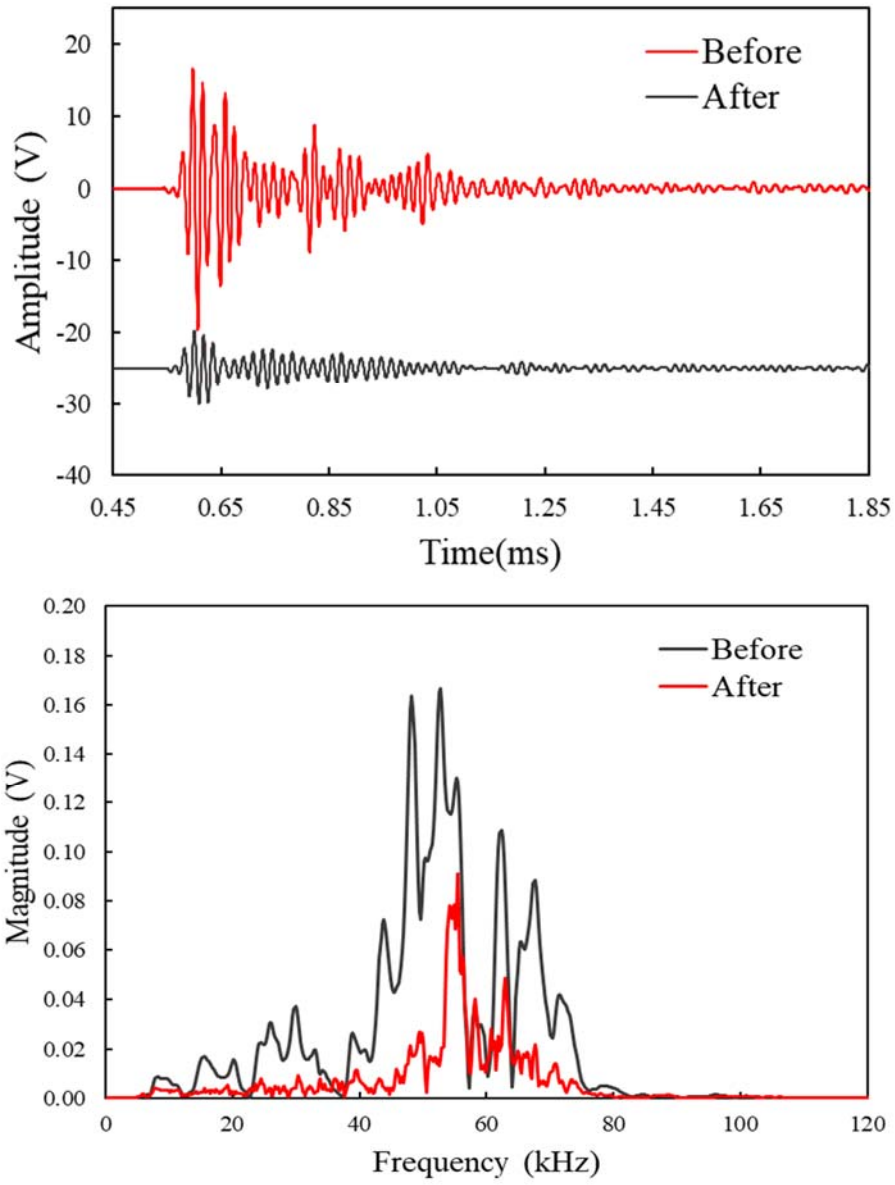

Figure C-16: Typical waveforms of treated cylinder concrete specimen with 20% air-entrained before and at the end of the period study using 54 kHz. (a) time signals, (b) Fourier spectra.

C.2-2 Multi UPV testing results (concrete cylinders)

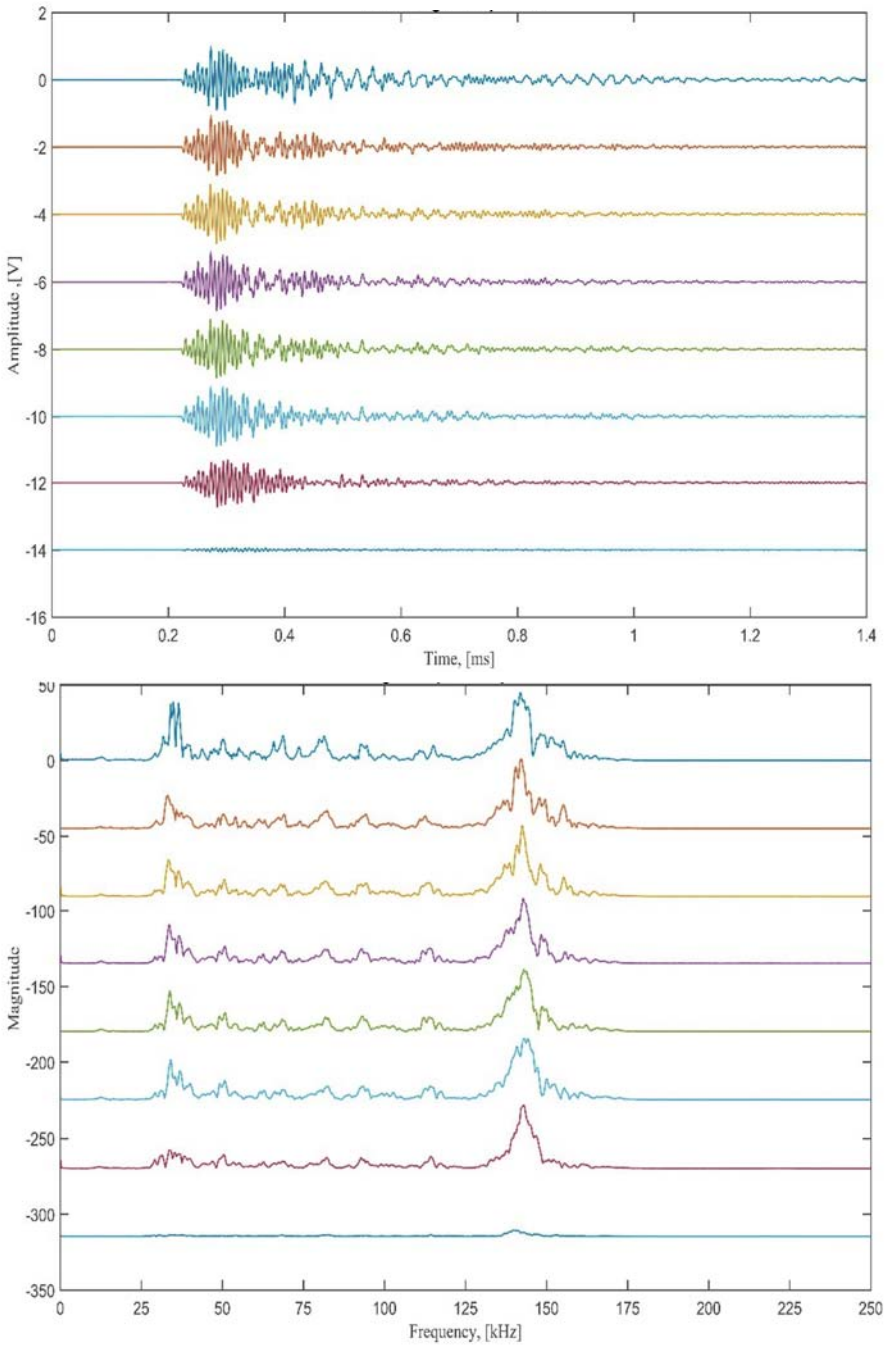

Figure C-17: Typical waveform results of untreated cylinder specimen subjected to compression load and using 150 kHz transduces at different load steps. (a) in time domain, (b) in frequency domain.

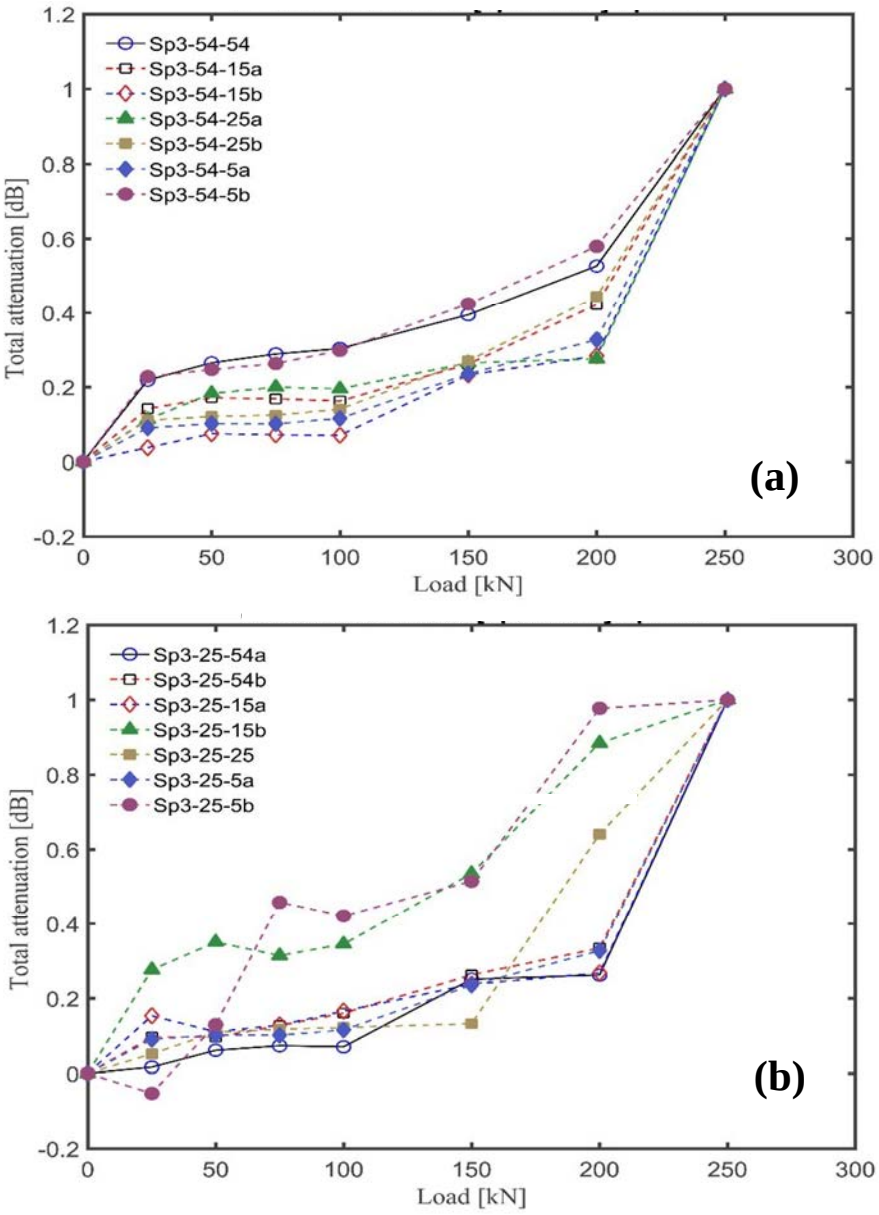

Figure C-18: Typical total attenuation results of treated cylinder specimen with 20% silica fume subjected to compression load and tested using different orientations. (a) using 54 kHz as transmitter, (b) using 250 kHz as transmitter.

C.2-3 Compression test laser vibrometer results (concrete cylinders)

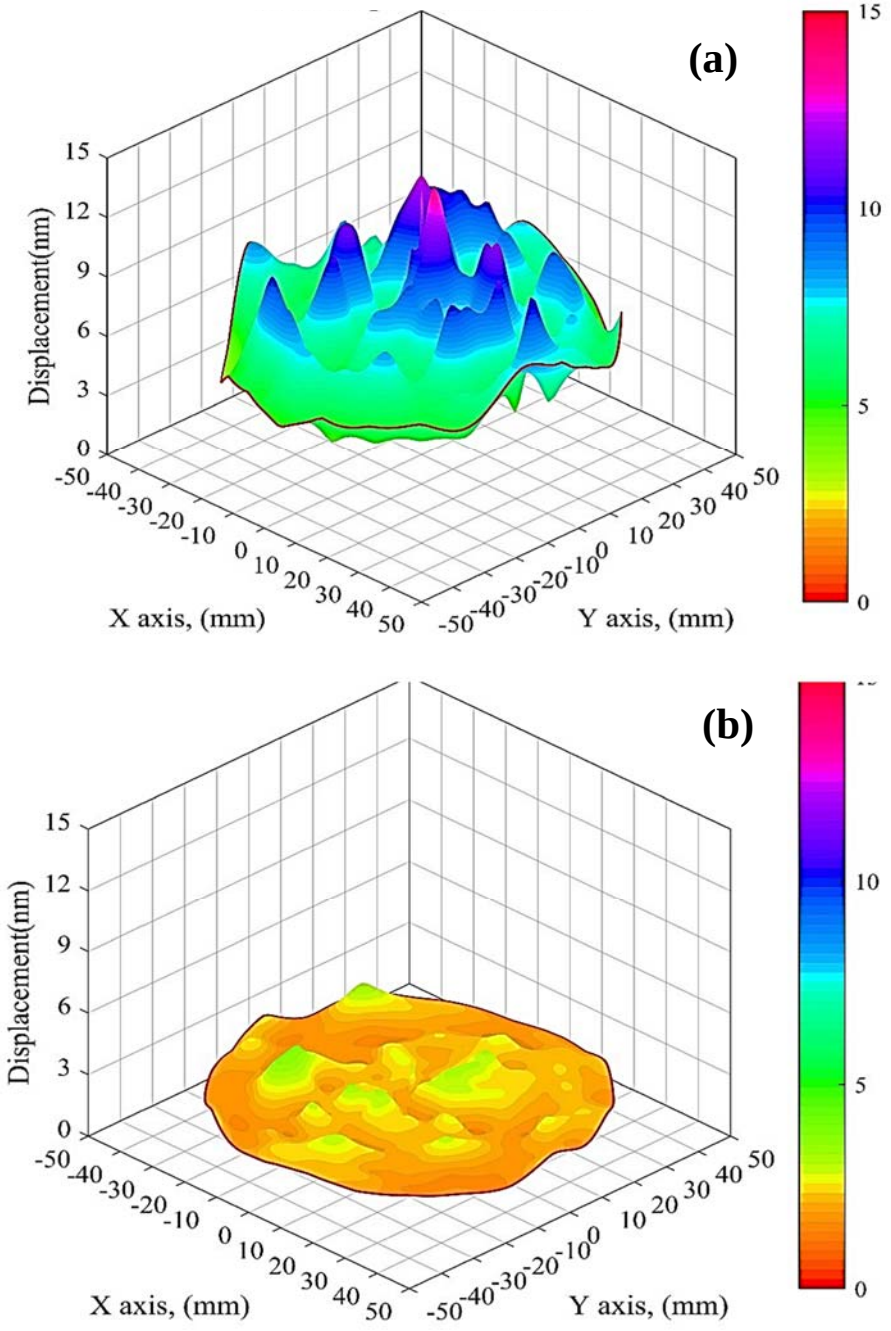

Figure C-19. Typical vibration modes of untreated cylinder specimen using 250 kHz. (a) before applying the load, (b) after applying the load.

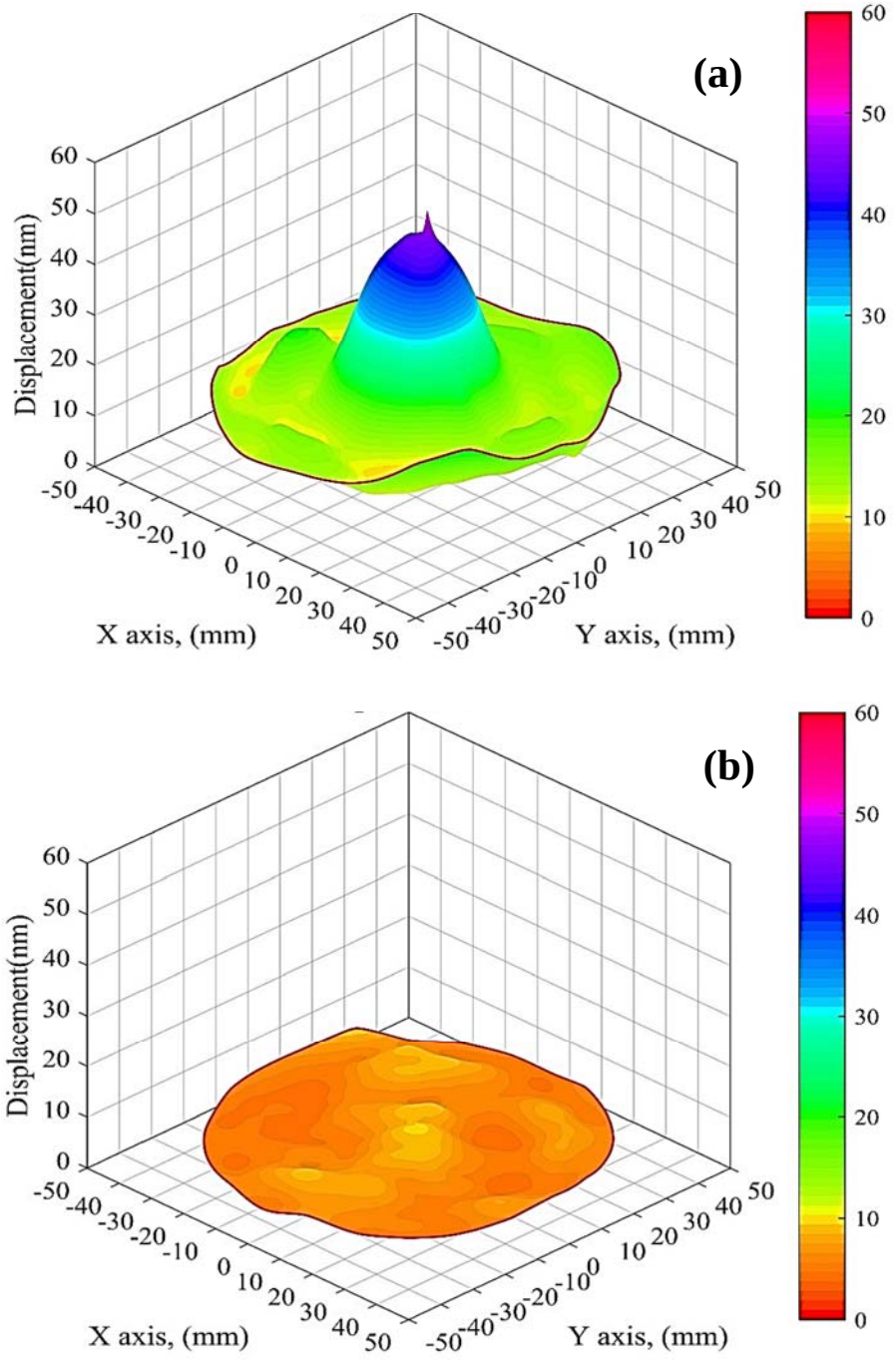

Figure C-20. Typical vibration modes of treated cylinder specimen with 5% silica fume using 54 kHz. (a) before applying the load, (b) after applying the load.

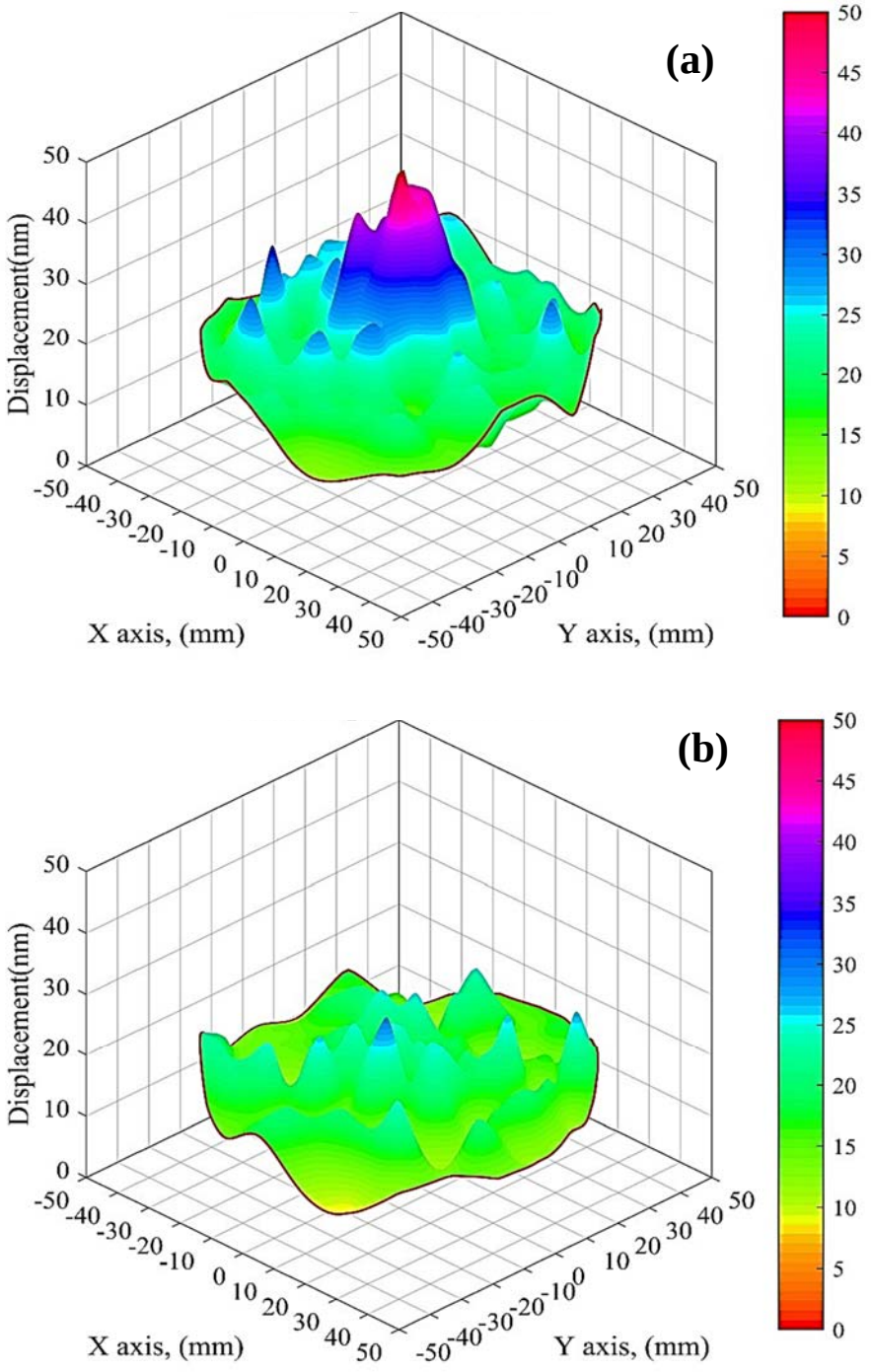

Figure C-21. Typical vibration modes of treated cylinder specimen with 10% silica fume using 150 kHz. (a) before applying the load, (b) after applying the load.

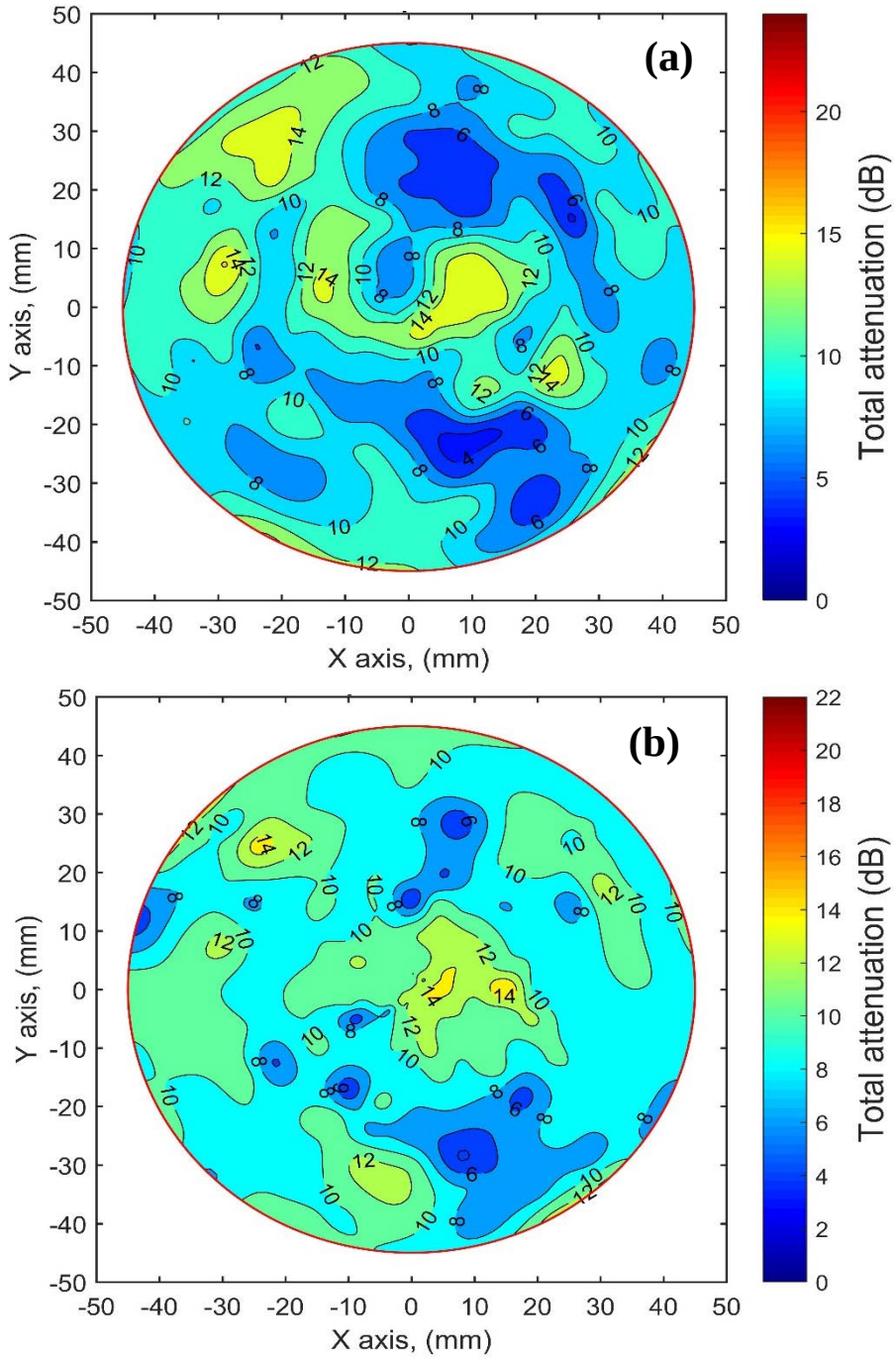

Figure C-22. Typical contour lines of total attenuation results of untreated cylinder specimen scanned with laser using 500 kHz. (a) using peak amplitude, (b) using spectrum area.

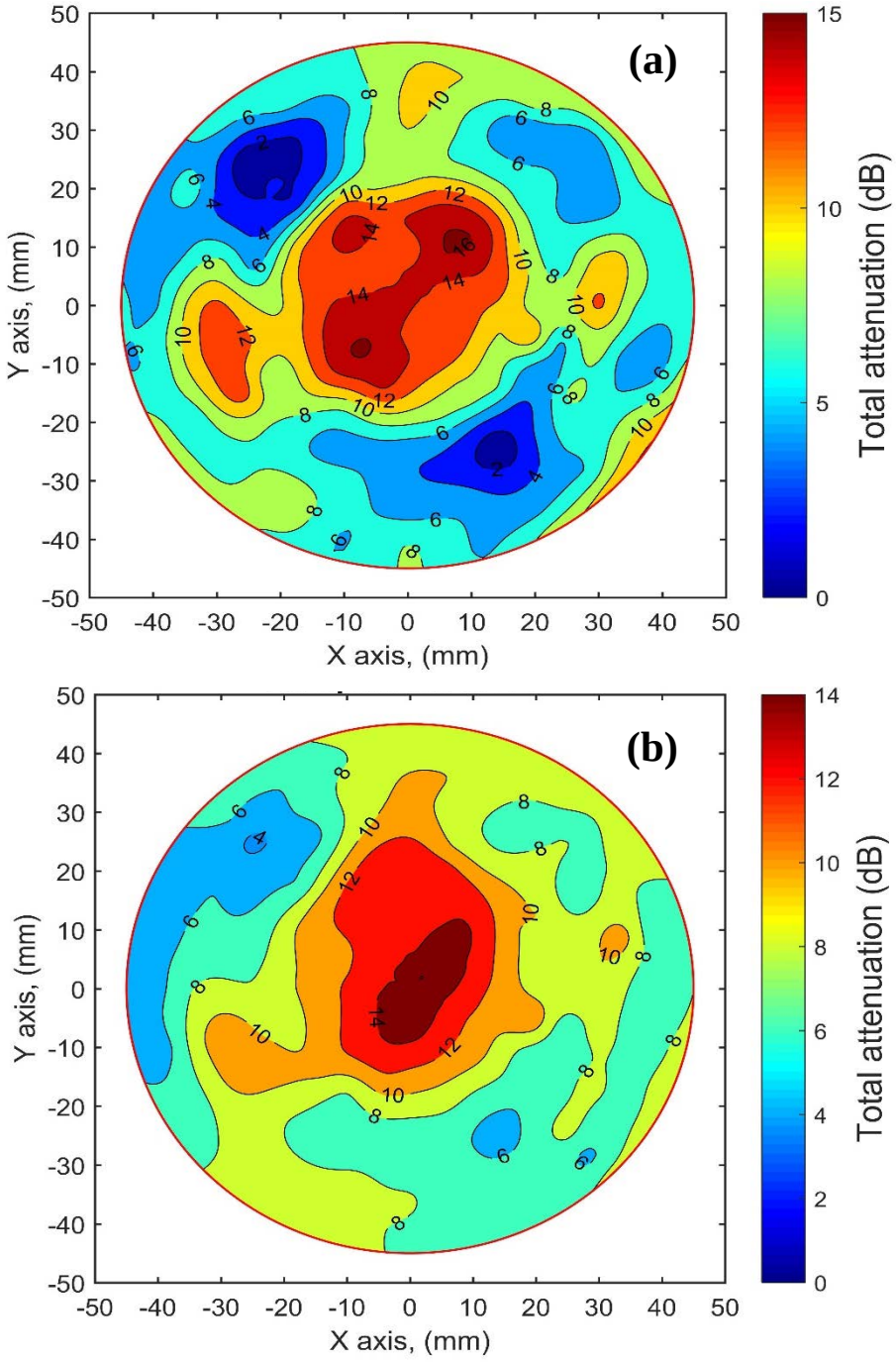

Figure C-23. Typical contour lines of total attenuation results of treated cylinder specimen with 5% silica fume and scanned with laser using 54 kHz. (a) using peak amplitude, (b) using spectrum area.

C.2-4 Single UPV testing results (concrete prisms)

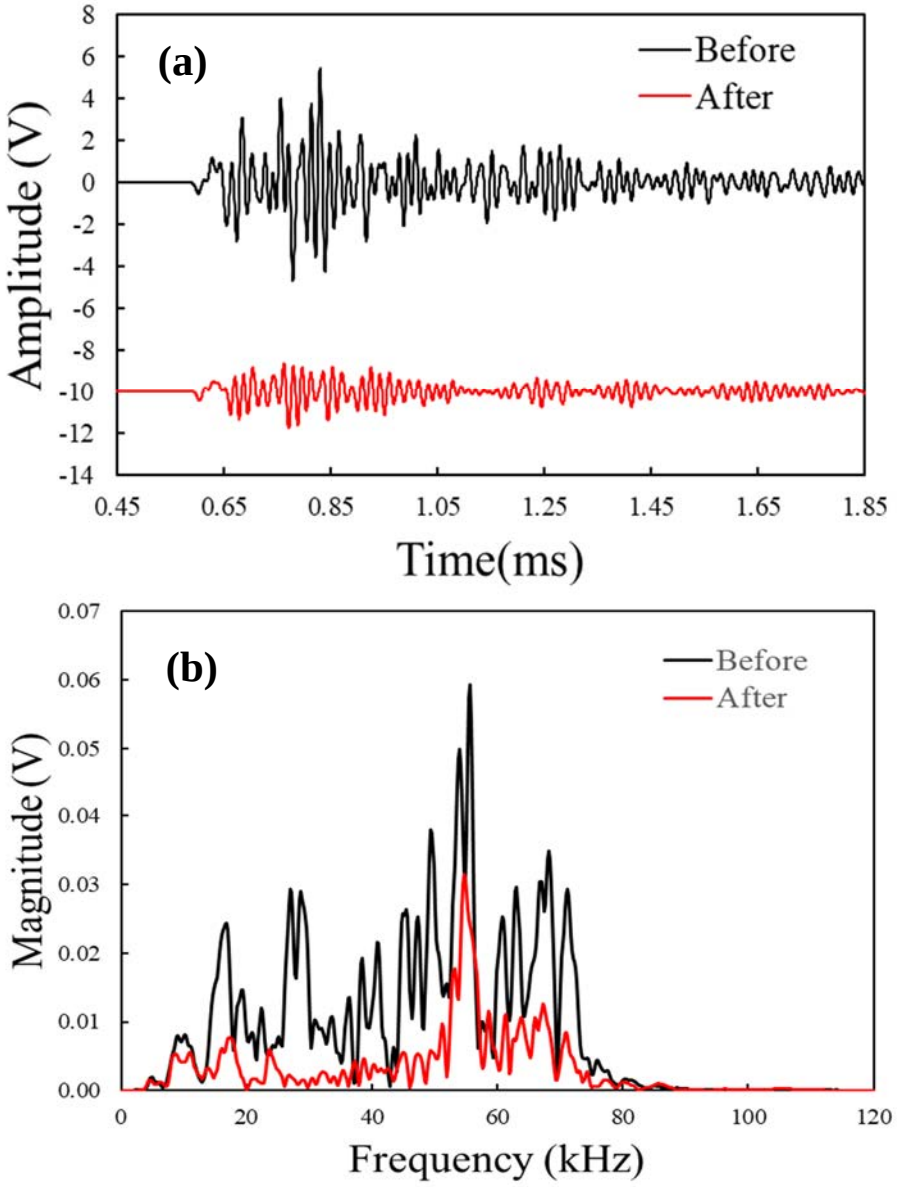

Figure C-24: Typical waveforms of untreated prism concrete specimen before and after compression load using 54 kHz. (a) time signals, (b) Fourier spectra.

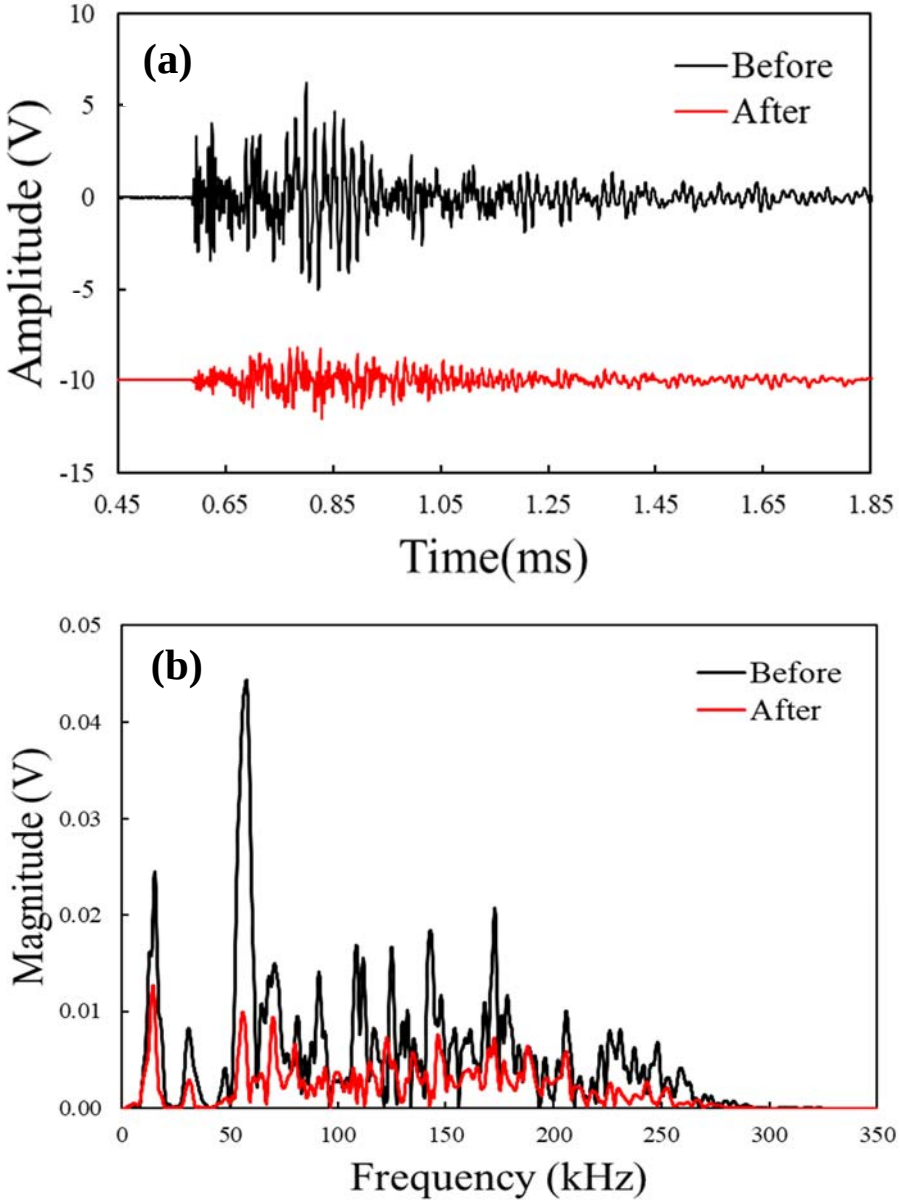

Figure C-25: Typical waveforms of untreated prism concrete specimen before and after compression load using 150 kHz. (a) time signals, (b) Fourier spectra.

C.2-5 Multi UPV testing results (concrete prisms)

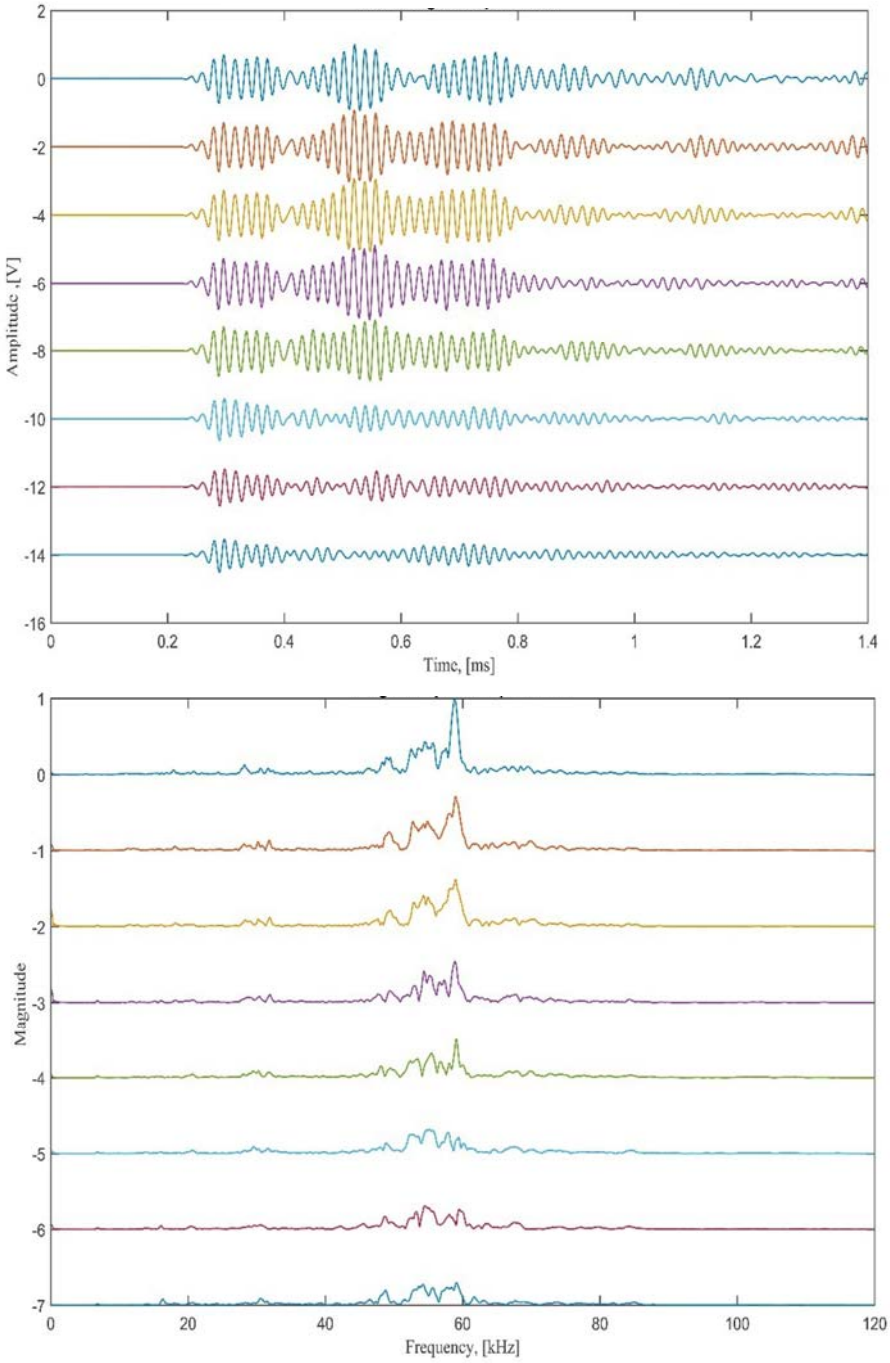

Figure C-26: Typical waveform results of untreated prismatic specimen subjected to compression load and using 54 kHz - 250 kHz transduces at different load steps. (a) in time domain, (b) in frequency domain.

C.2-6 Compression test laser vibrometer results (concrete prisms)

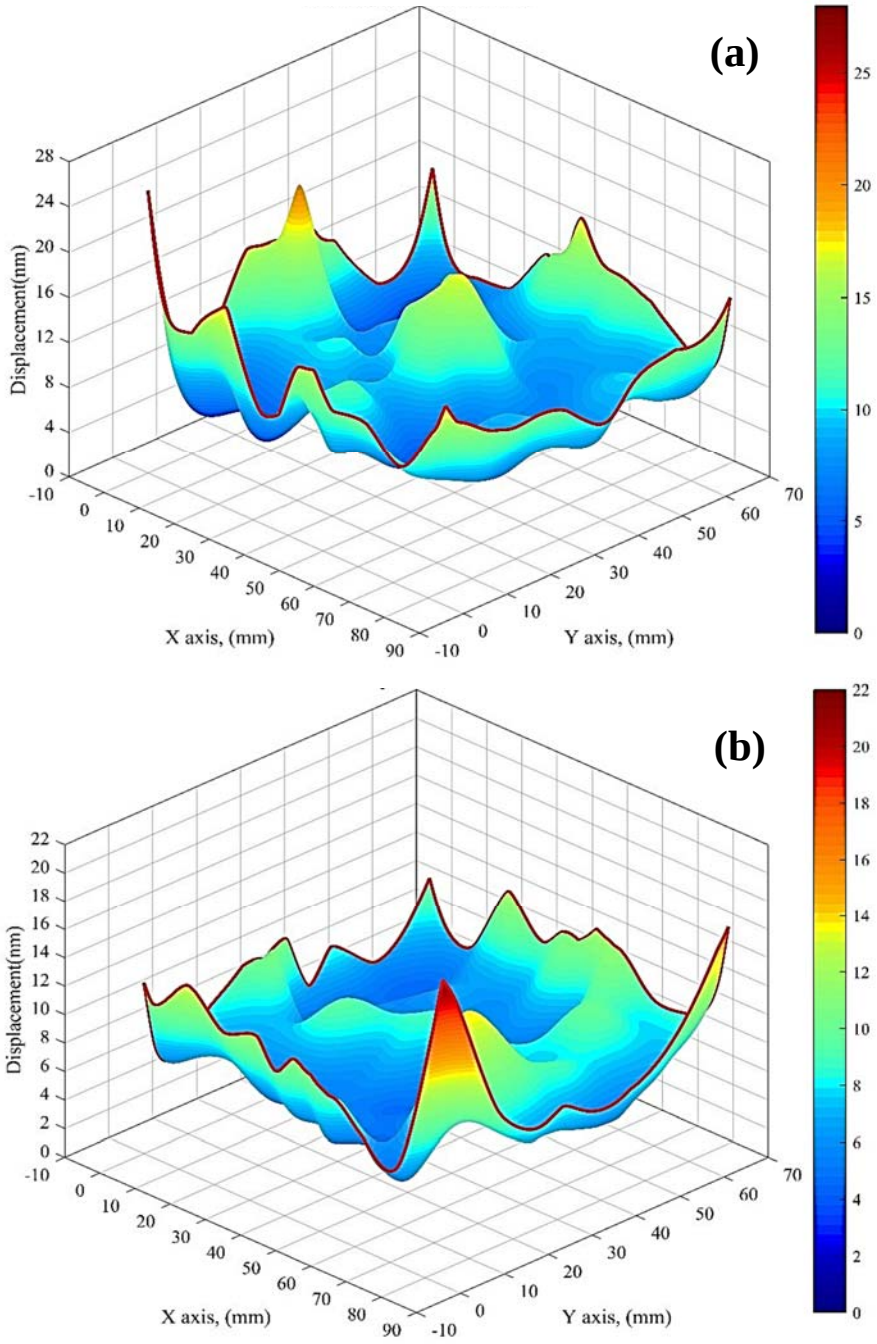

Figure C-27. Typical vibration modes of untreated prismatic specimen using 54 kHz. (a) before applying the load, (b) after applying the load.

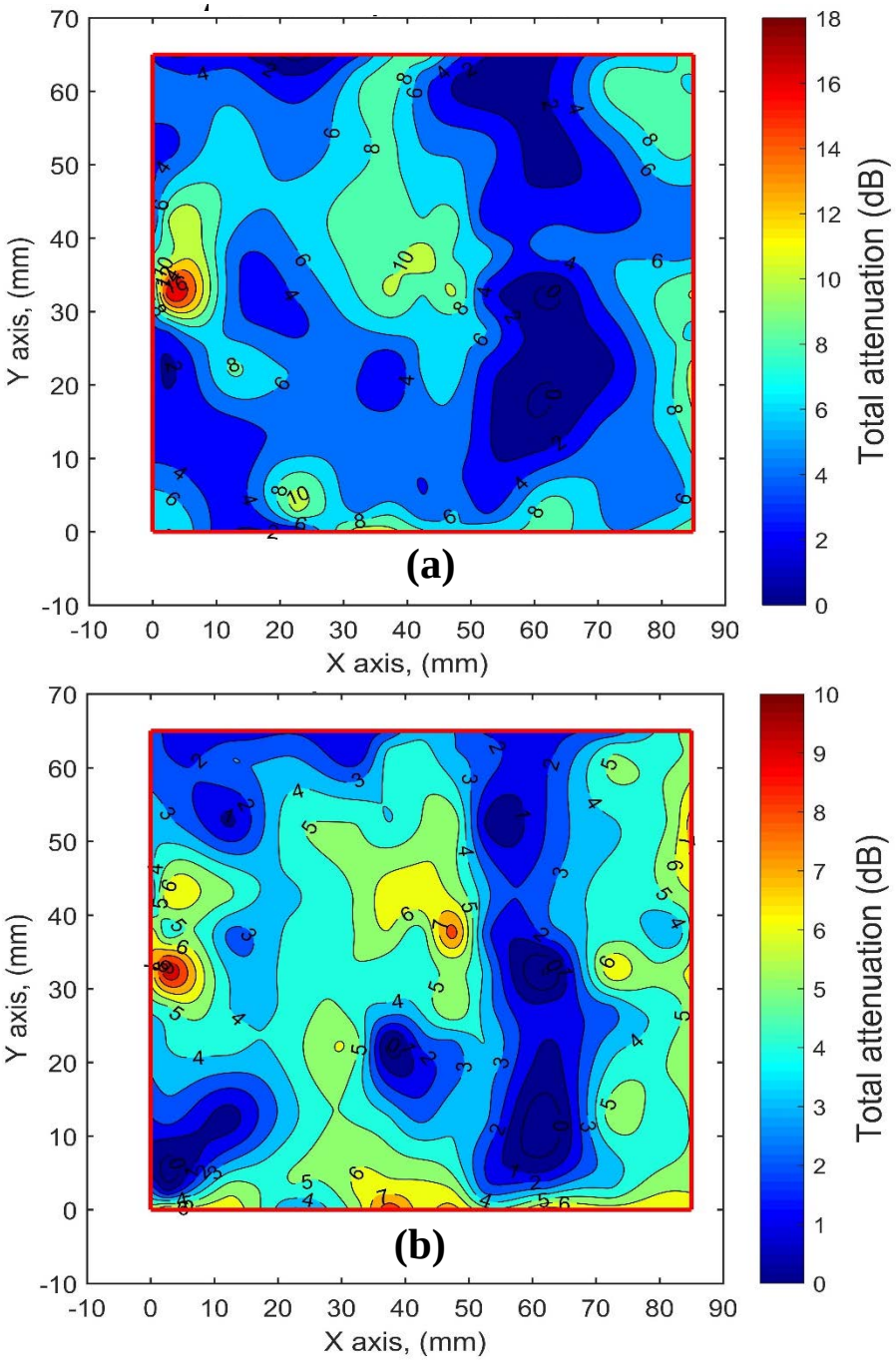

Figure C-28. Typical contour lines of total attenuation results of untreated prismatic specimen scanned with laser using 150 kHz. (a) using peak amplitude, (b) using spectrum area.

Appendix D

D.1 Fabricated transducers

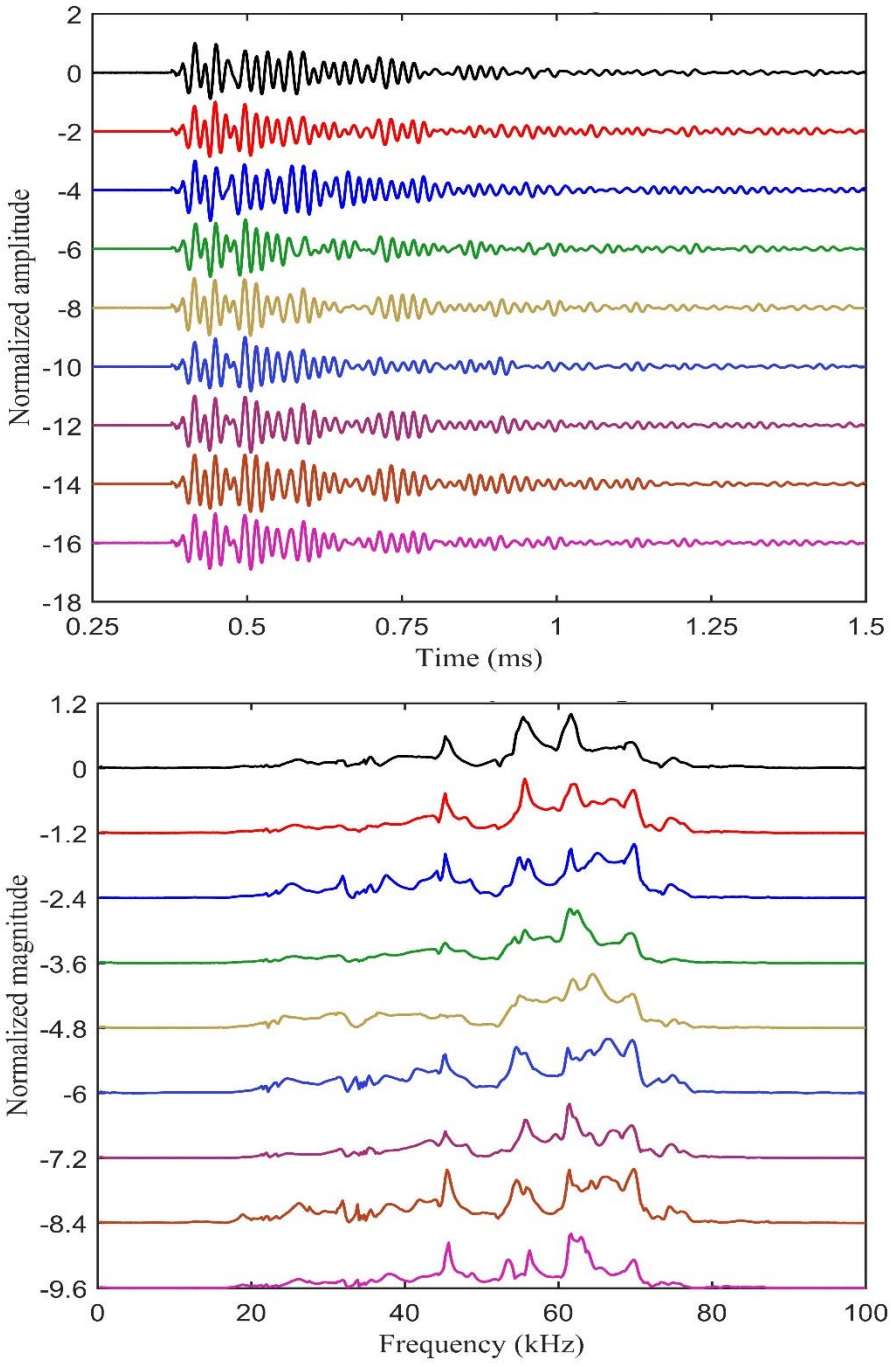

Figure D-1: Typical waveform signals of the fabricated radial transducers (model MC-SDR transdcuers). (a) in time domian, (b) in frequency domain.

D.2 Langevin transducers

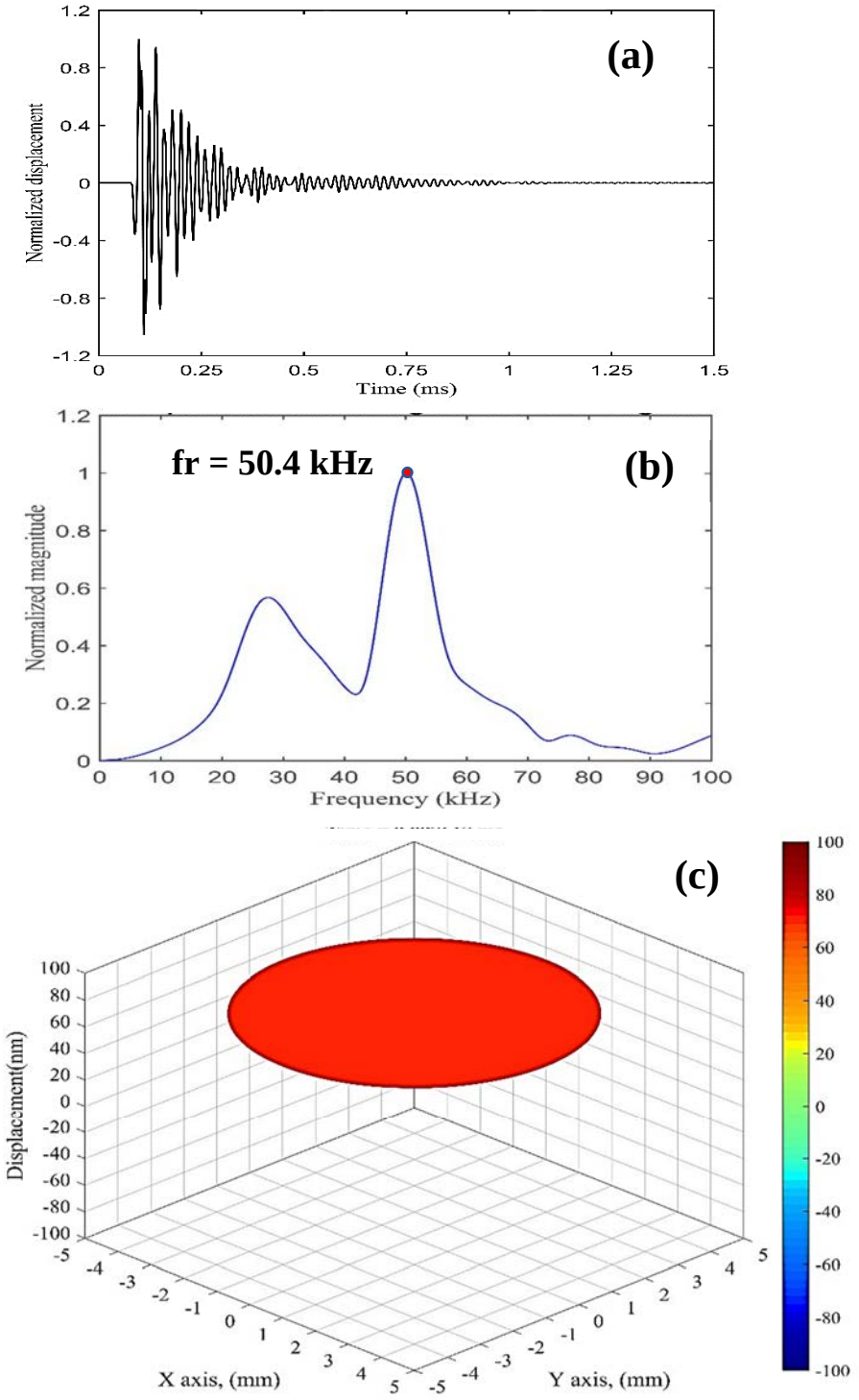

Figure D-2: Typical laser calibration results of Langevin 52 kHz transducer. (a) time signal, (b) Fourier spectrum, (c) 3D view perspective. fr is resonance frequency.

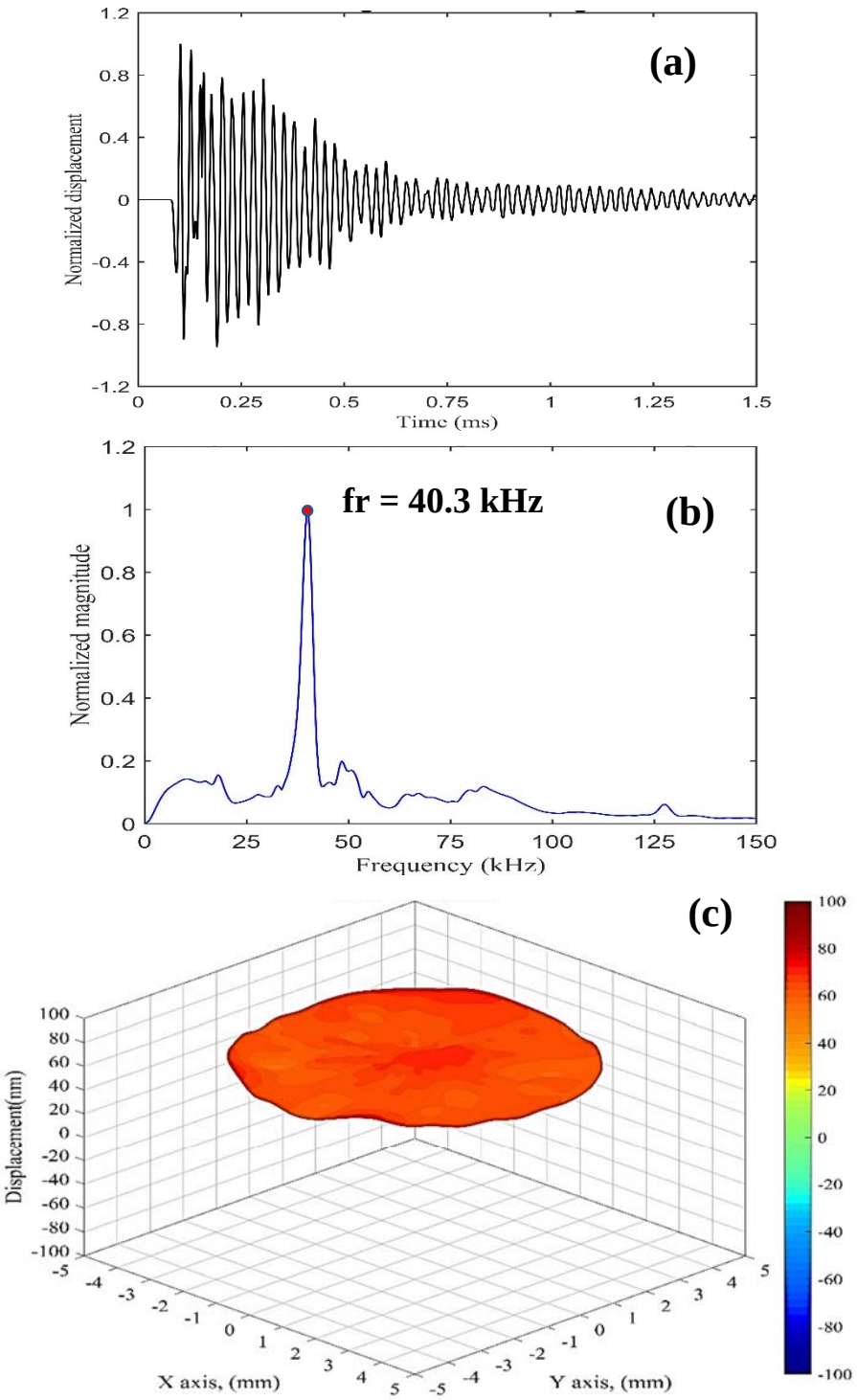

Figure D-3: Typical laser calibration results of Langevin 40 kHz transducer. (a) time signal, (b) Fourier spectrum, (c) 3D view perspective.

D.2 Quality control test results

D-2-1 UPV results

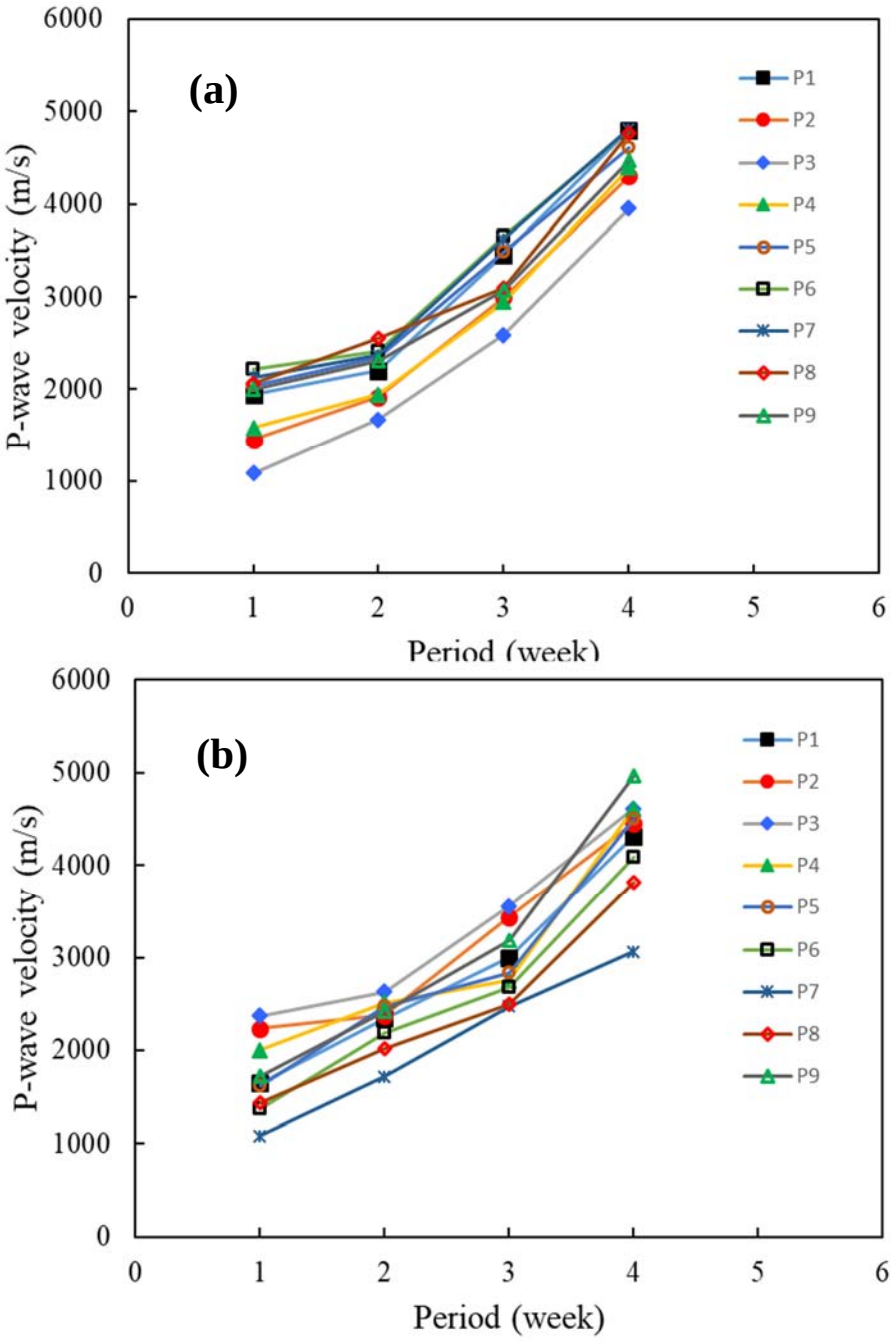

Figure D-4: Typical P-wave velocities computed for selected transducers in concrete model MA-SLR reinforced with light rebar, (a) excitation from tube A (acrylic) (b) excitation from tube B (nylon).

D-2-2 Evolution of waveform signals results

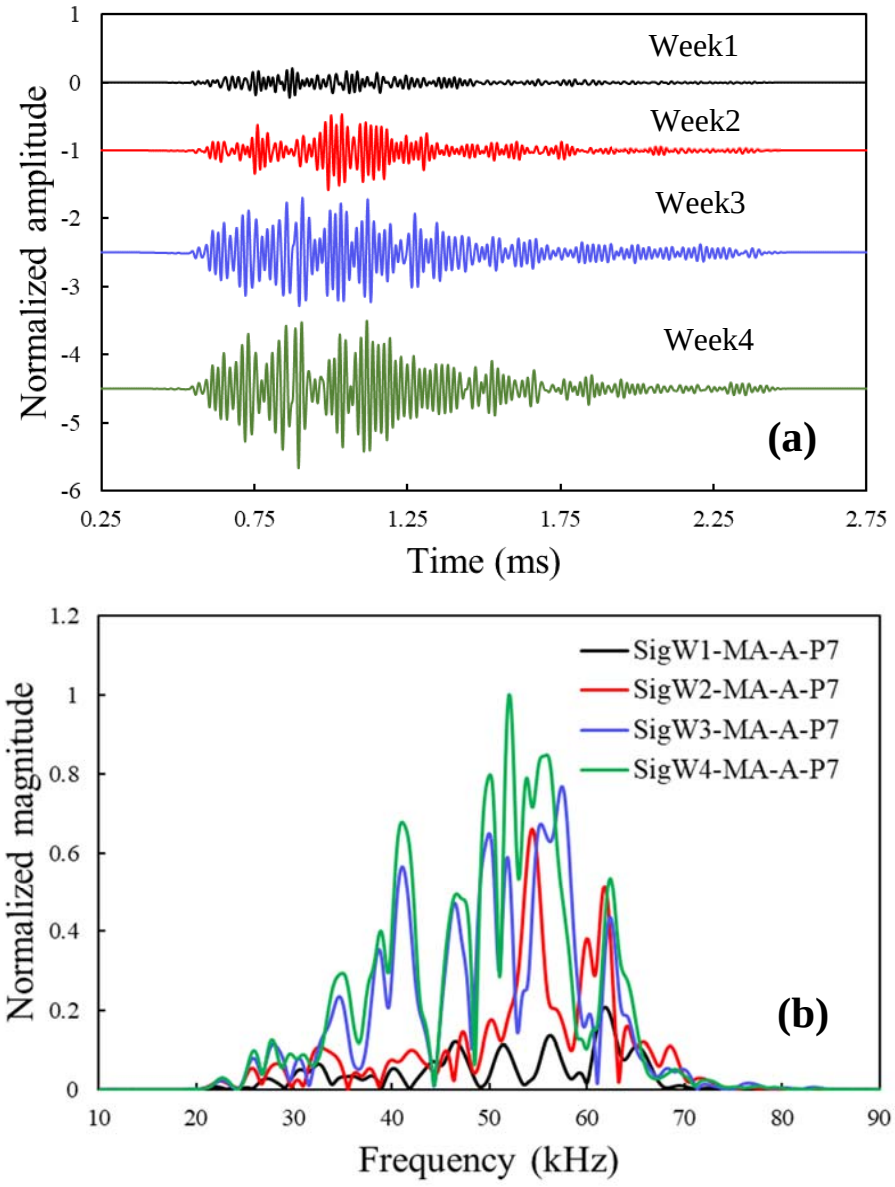

Figure D-5: Typical waveform signals received at the transducer P7 embedded in Model MA-SP during the curing period using 52 kHz through acrylic tube (B), (a) in time domain, (b) in frequency domain.

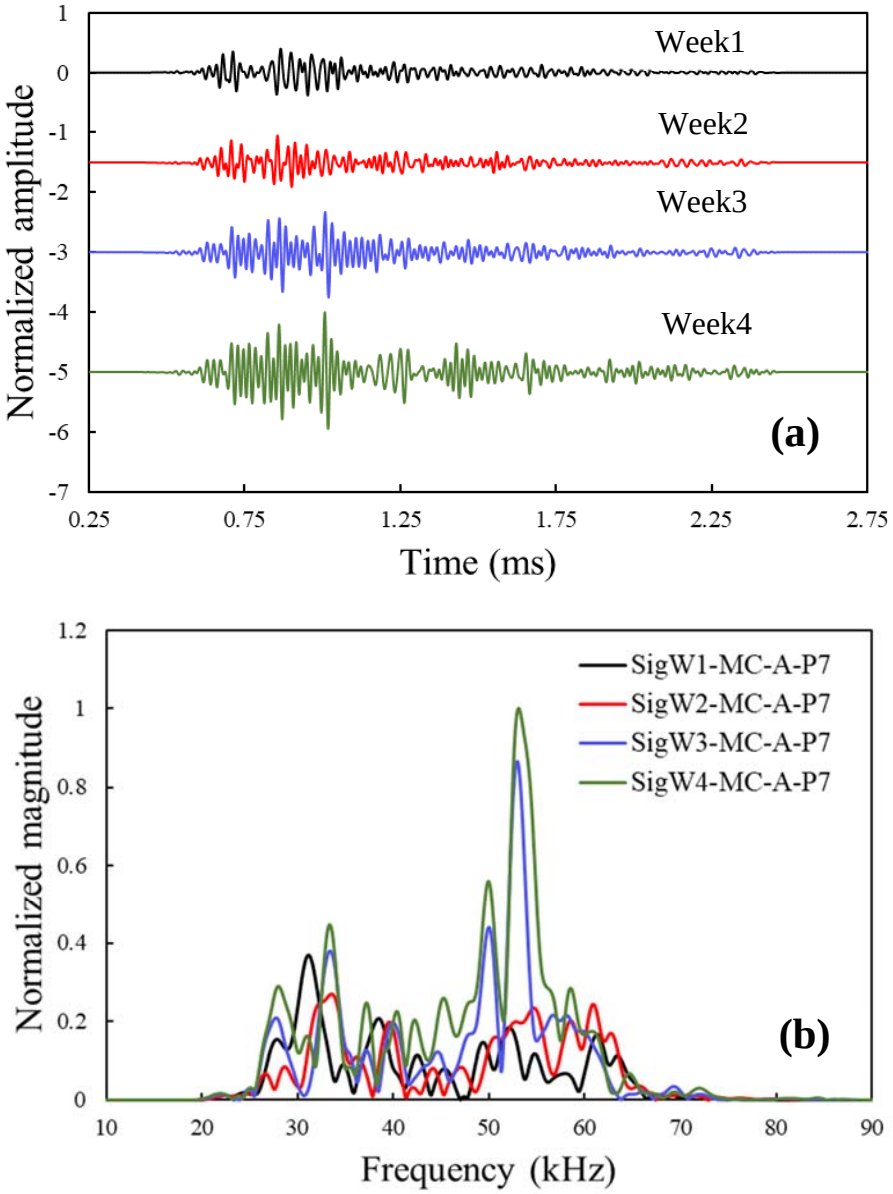

Figure D-6: Typical waveform signals received at the transducer P7 embedded in Model MA-SDR during the curing period using 54 kHz through aluminum disc (C), (a) in time domain, (b) in frequency domain.

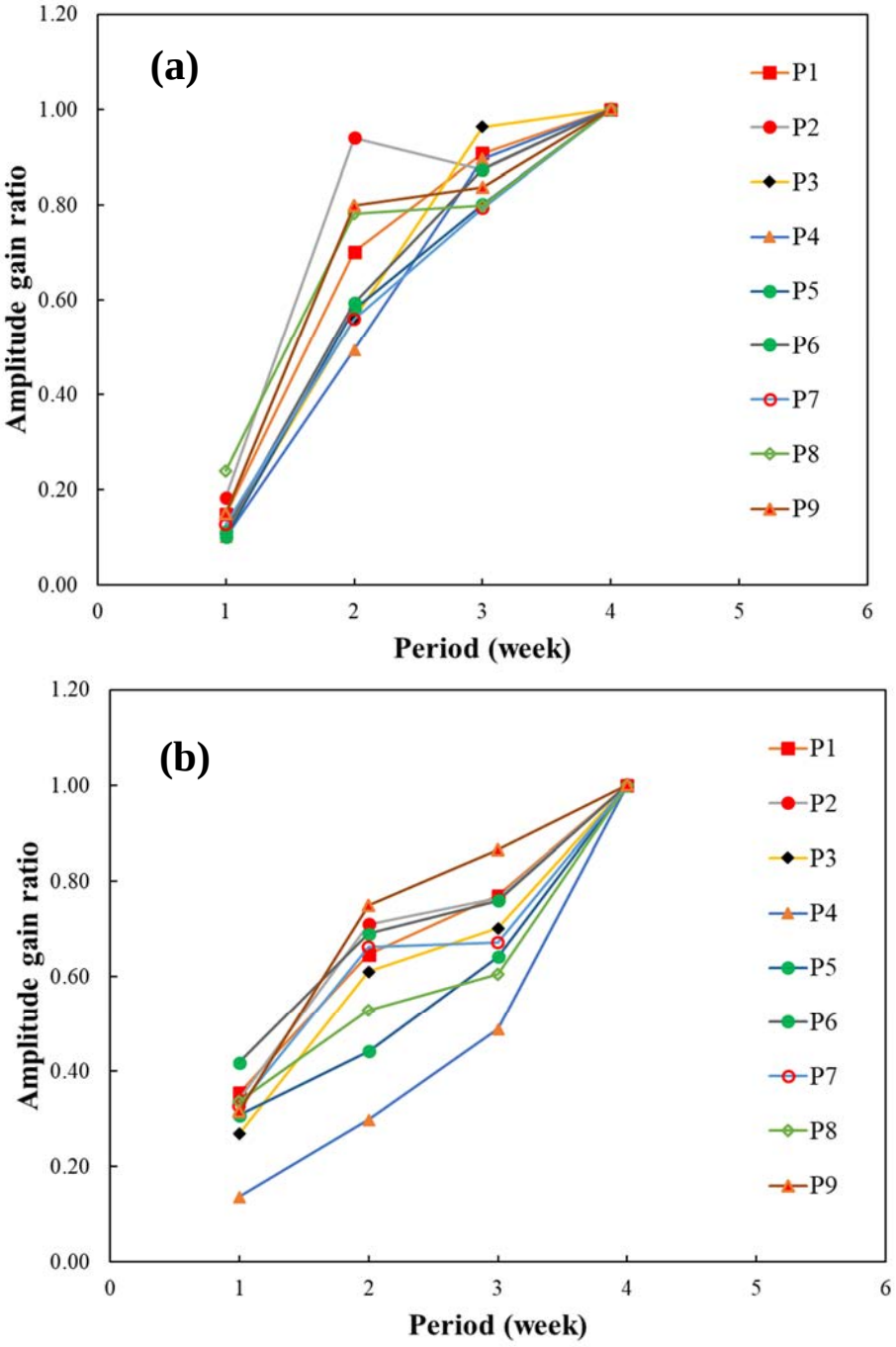

Figure D-7: Typical maximum amplitude gain of selected embedded transducers in concrete models during curing period. (a) model MA-SP excited from tube B (nylon), (b) model MB-SLR excited from tube A (acrylic).

D.3 Damage monitoring test results

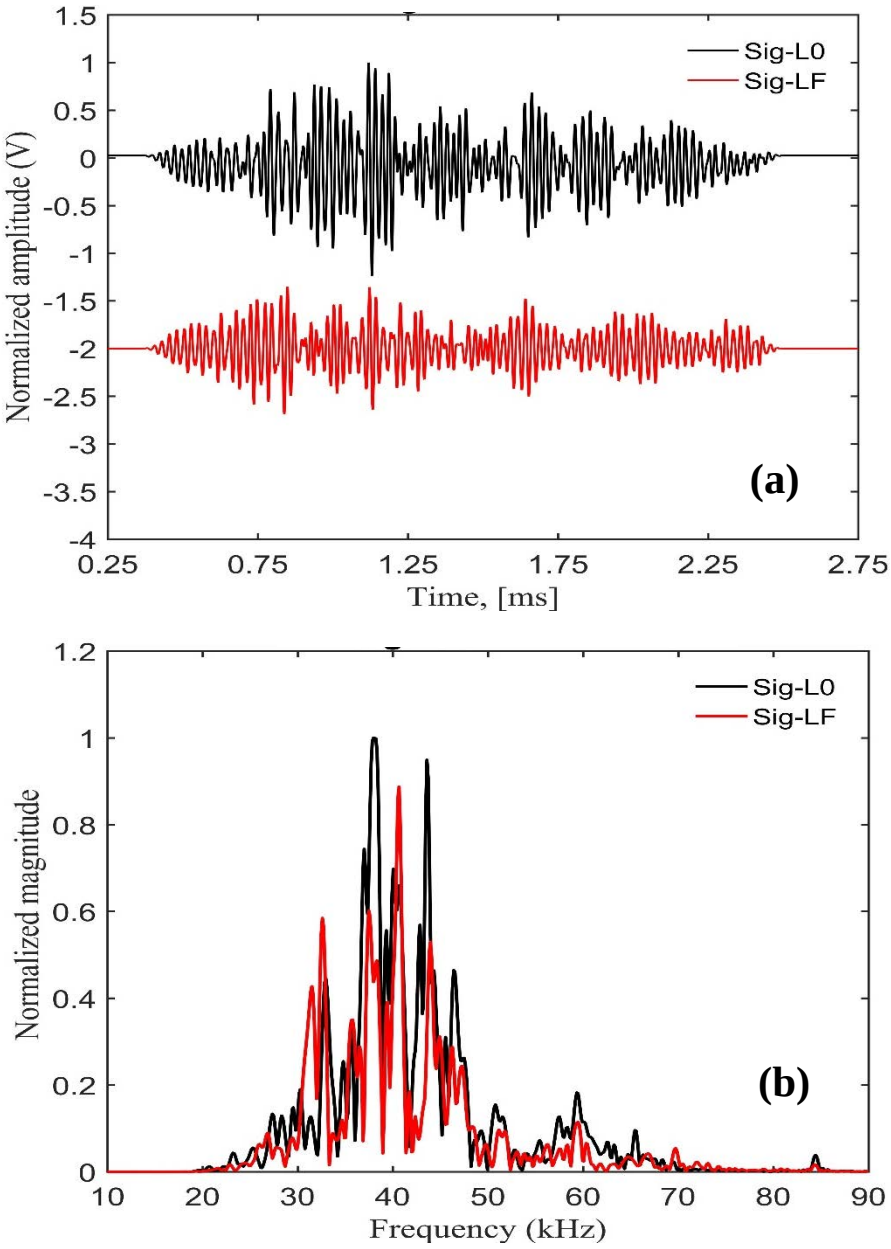

Figure D-8: Typical waveform signals obtained at transducer P5 embedded in concrete model MA-SP by exciting from tube B (nylon) using Langevin 40 kHz transducer. (a) in time domain, (b)in frequency domain. L0 and LF are initial and failure loads.

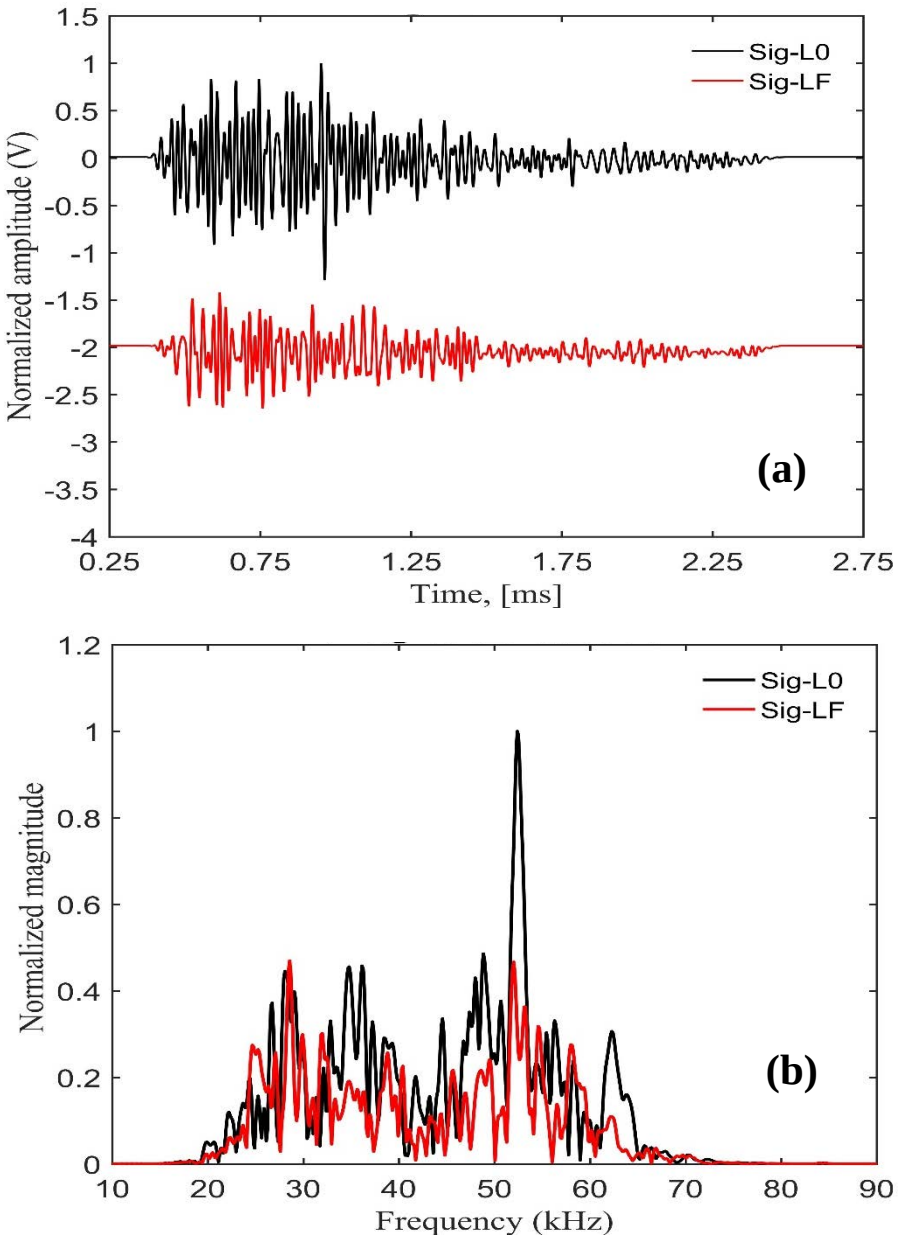

Figure D-9: Typical waveform signals obtained at transducer P9 embedded in concrete model MA-SP by exciting from tube A (acrylic) using Langevin 52 kHz transducer. (a) in time domain, (b) in frequency domain.

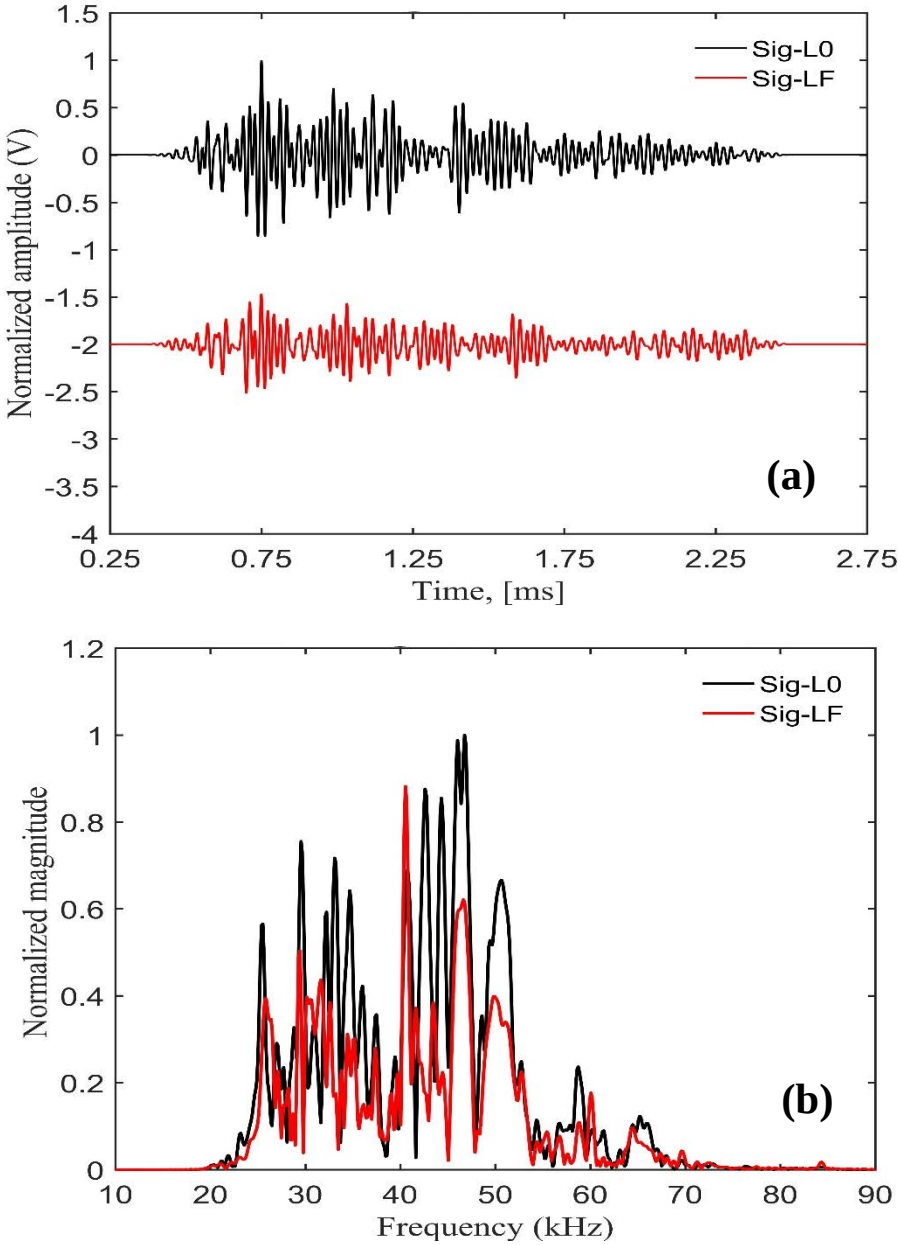

Figure D-10: Typical waveform signals obtained at transducer P7 embedded in concrete model MA-CLR by exciting from tube B (nylon) using Langevin 40 kHz transducer. (a) in time domain, (b) in frequency domain.

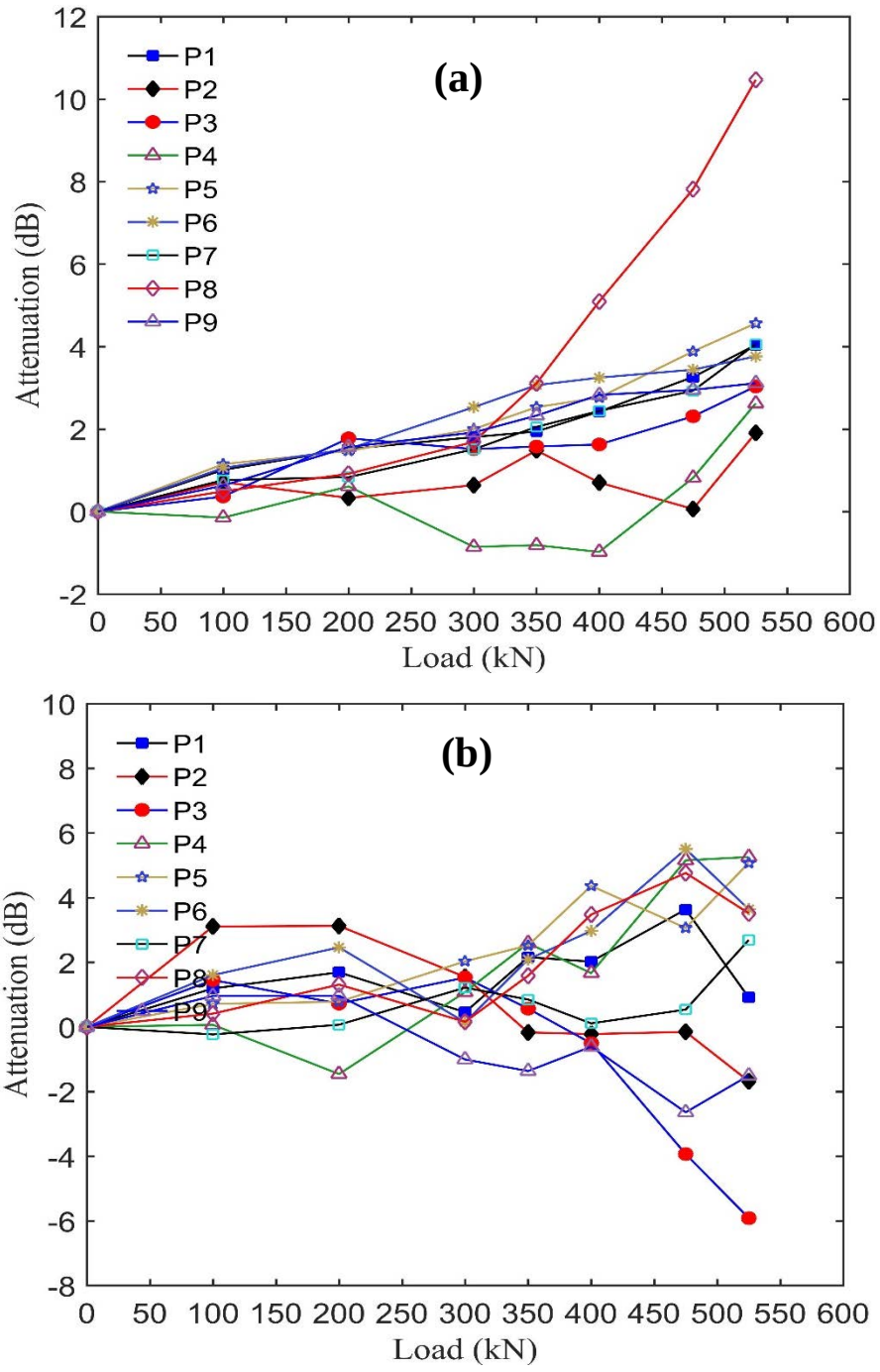

Figure D-11. Typical attenuation results of model MB-SLR computed based on peak amplitude of the waveform signals received at the embedded transducers during compression load, (a)using nylon tube with 40 kHz (location B), (b) using direct contact with 54 kHz (location D).

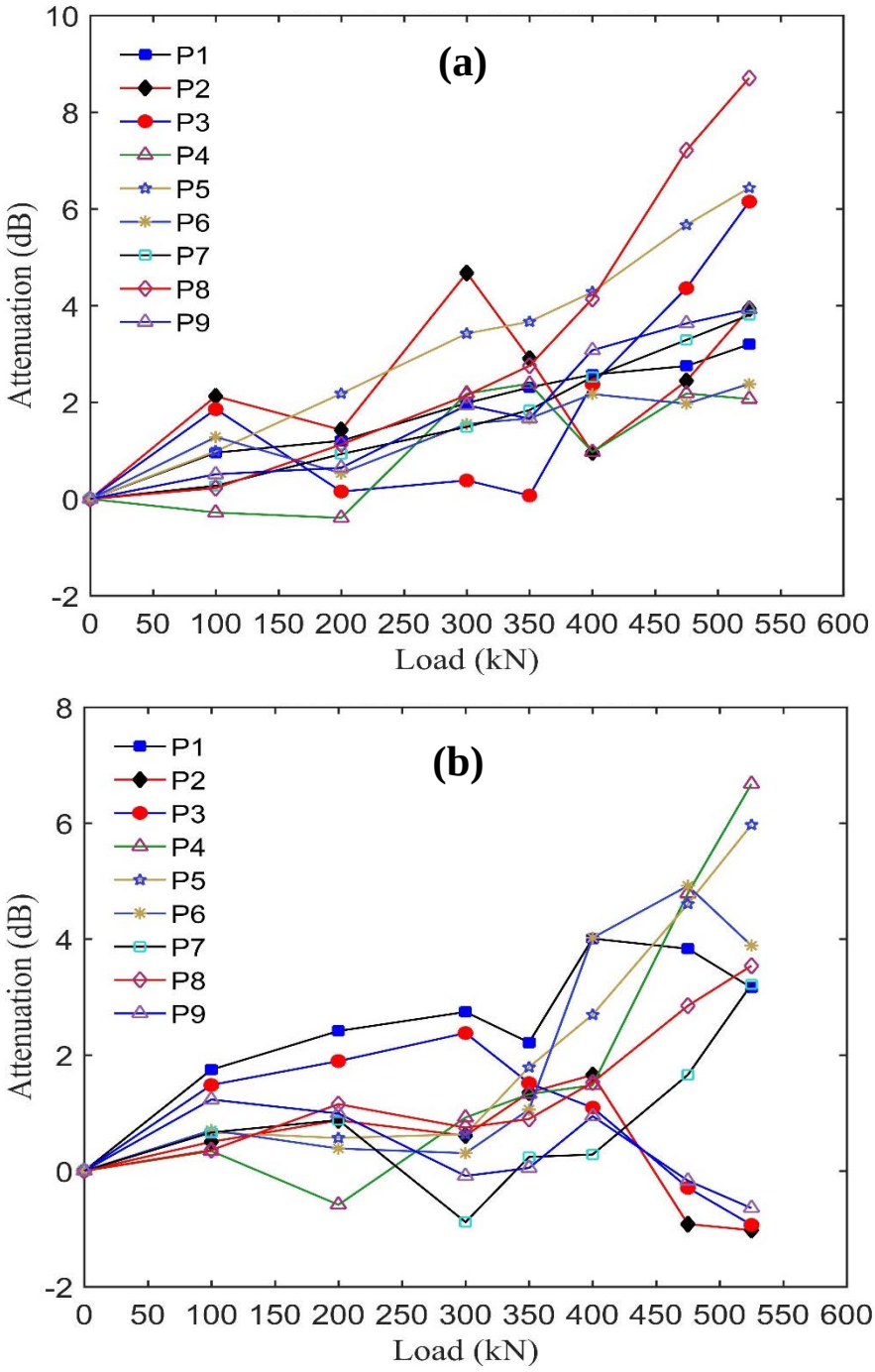

Figure D-12. Typical Attenuation results of model MB-SLR computed based on spectrum area of the waveform signals received at the embedded transducers during compression load, (a)using nylon tube with 40 kHz (location B), (b) using direct contact with 54 kHz (location D).